Study of electromagnetic wave propagation and scattering in Low-THz automotive radar

Emidio Marchetti

School of Engineering

University of Birmingham

This dissertation is submitted for the degree of

Doctor of Philosophy

College of Engineering and

Physical Sciences

September 2019

"Ma non ho ancora capito, con la mia cultura fasulla

chi avesse capito la vita chi non capisse ancor nulla..."

F. G.

Abstract

The development of a new generation of sensors for autonomous vehicles requires the increase of the number of automotive radars on the roads, leading to an inevitable problem of overcrowding of the electromagnetic spectrum in the allocated 77 GHz band. The solution proposed in this research is the migration of the automotive radar operation frequency towards the low-THz band.

This thesis reports, firstly, an experimental study on the feasibility of deploying automotive radars working at frequencies above 100 GHz. The study analyses the possible additional attenuation of the electromagnetic waves in adverse weather conditions and the differences in targets reflectivities, in comparison to the performances of current automotive radars. A comprehensive library of reflectivity signatures of a number of road actors is established, to provide a basis for the development of low-THz automotive radars.

Secondarily, the thesis discusses and demonstrates the advantages of the employment of low-THz signals to improve the imaging capability of automotive radars, to allow identification and classification of road targets based on high resolution images and micro-Doppler signatures.

Acknowledgements

I would like to thank the following people, who contributed to make the work presented in this thesis possible.

I would like to express my sincere gratitude to my supervisors Professor Marina Gashinova and Professor Mikhail Cherniakov for the continuous support, for their motivation and guidance. I also would like to thank the members of my doctoral committee: Professor Andrew Stove and Professor Paul Brennan, for their insightful suggestions to improve this thesis.

I would like to thank Dr. Edward Hoare, Dr. Fatemeh Norouzian and Dr. Liam Daniel who provided invaluable advice and support and the essential instruments to conduct a productive research. My sincere thanks also goes to Dr. Rui Du, Dr. Ben Willetts, Ms. Yang Xiao and Mr. Alan Yates for the constructive discussions and their fundamental role in the experimental part of the research. Many thanks also to the rest of MISL group, past and present, for their support and friendship.

Last but not the least, I would like to thank my family for their precious support throughout the time of my PhD.

Furthermore, I would like to thank Jaguar Land Rover for funding and sponsoring my PhD project. This work was supported by Jaguar Land Rover in association with the UK-EPSRC grant EP/N012372/1 as part of the jointly funded Towards Autonomy: Smart and Connected Control (TASCC) Programme.

Publications

Publications which incorporate work outlined within the thesis

- Emidio Marchetti, Rui Du, Ben Willetts, Fatemeh Norouzian, Edward G. Hoare, Thuy Yung Tran, Nigel Clarke, Mikhail Cherniakov, and Marina Gashinova. "Radar cross-section of pedestrians in the low-THz band." IET Radar, Sonar and Navigation, 2018.

- Emidio Marchetti, Rui Du, Fatemeh Norouzian, Edward G. Hoare, Thuy Yung Tran, Mikhail Cherniakov, and Marina Gashinova. "Radar reflectivity and motion characteristics of pedestrians at 300 GHz." In 2017 European Radar Conference (EURAD), 2017.

- Emidio Marchetti, Rui Du, Fatemeh Norouzian, Edward G. Hoare, Thuy Yung Tran, Mikhail Cherniakov, and Marina Gashinova. "Comparison of pedestrian reflectivities at 24 and 300 GHz." In 2017 18th International Radar Symposium (IRS), 2017.

- Emidio Marchetti, Liam Daniel, Edward G. Hoare, Fatemeh Norouzian, Mikhail Cherniakov, and Marina Gashinova. "Radar Reflectivity of a Passenger Car at 300 GHz." In 2018 19th International Radar Symposium (IRS), 2018.

- Emidio Marchetti, Scott Cassidy, Fatemeh Norouzian, Edward G. Hoare, Mikhail Cherniakov, and Marina Gashinova. "Automotive Targets Characterization in the Low-THz Band." In 2019 20th International Radar Symposium (IRS), 2019.

- Fatemeh Norouzian, Emidio Marchetti, Edward G. Hoare, Marina Gashinova, Costas Constantinou, Peter Gardner, and Mikhail Cherniakov. "Rain Attenuation at Millimetre Wave and Low-THz Frequencies." IEEE Transactions on Antennas and Propagation, 2019.

- Fatemeh Norouzian, Emidio Marchetti, Edward G. Hoare, Marina Gashinova, Costas Constantinou, Peter Gardner, and Mikhail Cherniakov. "Experimental study on low-THz automotive radar signal attenuation during snowfall." IET Radar, Sonar and Navigation, 2019.
- Rui Du, Emidio Marchetti, Fatemeh Norouzian, Marina Gashinova, and Mikhail Cherniakov. "Micro Doppler signature of pedestrian walking on spot at low-teraHertz frequencies." In International Conference on Radar Systems (Radar 2017), 2017.
- Fatemeh Norouzian, Emidio Marchetti, Edward Hoare, Marina Gashinova, Costas Constantinou, Peter Gardner, and Mikhail Cherniakov. "Low-THz Wave Snow Attenuation." In International Conference on Radar Systems (Radar 2018), 2018.
- Yang Xiao, Fatemeh Norouzian, Edward G. Hoare, Emidio Marchetti, Marina Gashinova and Mikhail Cherniakov. "Modelling and Experiment Verification of Transmissivity of Low-THz Radar Signal through Vehicle Infrastructure," in IEEE Sensors Journal, 2020.
- Rui Du, Fatemeh Norouzian, Emidio Marchetti, Ben Willetts, Marina Gashinova, and Mikhail Cherniakov. "Characterisation of attenuation by sand in low-THz band." In 2017 IEEE Radar Conference (RadarConf), 2017.
- Fatemeh Norouzian, Rui Du, Emidio Marchetti, Marina Gashinova, Edward G. Hoare, Costas Constantinou, Peter Gardner, and Mikhail Cherniakov. "Transmission through uniform layer of ice at low-THz frequencies." In 2017 European Radar Conference (EURAD), 2017.
- Fatemeh Norouzian, Rui Du, Emidio Marchetti, Marina Gashinova, Edward G. Hoare, Costas Constantinou, Peter Gardner, and Mikhail Cherniakov. "Low-THz transmission through liquid contaminants on antenna radome." In 12th European Conference on Antennas and Propagation (EuCAP 2018), 2018.

- Fatemeh Norouzian, Edward G. Hoare, Emidio Marchetti, Mikhail Cherniakov, and Marina Gashinova. "Next Generation, Low-THz Automotive Radar – the potential for frequencies above 100 GHz." In 2019 20th International Radar Symposium (IRS), 2019.

- Yang Xiao, Fatemeh Norouzian, Emidio Marchetti, Scott Cassidy, Edward G. Hoare, Mikhail Cherniakov, and Marina Gashinova. "Transmissivity Through Automotive Bumpers at mm-wave and Low-THz Frequencies." In 2019 20th International Radar Symposium (IRS), 2019.

Other publications

- Suzanne Melo, Emidio Marchetti, Scott Cassidy, Edward G. Hoare, Antonella Bogoni, Marina Gashinova, and Mikhail Cherniakov. "24 GHz Interferometric Radar for Road Hump Detections in Front of a Vehicle." In 2018 19th International Radar Symposium (IRS), 2018.

- Alexander Gureev, Mikhail Cherniakov, Emidio Marchetti, and Ilya Gureev. "Channel description in the low-THz wireless communications." In 2017 IEEE Conference of Russian Young Researchers in Electrical and Electronic Engineering (EIConRus), 2017.

- Alexander Gureev, Mikhail Cherniakov, Emidio Marchetti, Fatemeh Norouzian, and Ilya Gureev. "Analysis of interferences in wideband low-THz wireless systems." In 2018 IEEE Conference of Russian Young Researchers in Electrical and Electronic Engineering (EIConRus), 2018.

- Alexander Gureev, Ilya Gureev, Mikhail Cherniakov, Emidio Marchetti, and Aleksandr Bystrov. "Performance Evaluation of Wideband Indoor Wireless Communication Systems Occupying the Frequency Range of 650–690 GHz." In 2019 IEEE Conference of Russian Young Researchers in Electrical and Electronic Engineering (EIConRus), 2019.

- Ben Willetts, Marina Gashinova, Andy Stove, Costas Constantinou, Edward G. Hoare, and Emidio Marchetti. "Low-THz overhead power cable signatures: The effect of surface features on Low-THz reflectivities." In 2016 17th International Radar Symposium (IRS), 2016.

Table of contents

List of figures

List of tables

Nomenclature

Roman Symbols

c	Speed of light
f	Frequency
f_d	Doppler frequency shift
F_p	Propagation factor
h_{rms}	Surface Root Mean Square height
I	Image
I_i	Integral image
k	Wavenumber
R	Range profile
r	Range
R_i	Integral range profile
r_{un}	Unambigous range
t	time
v_r	Radial velocity

Greek Symbols

$\Delta\omega$	Frequency resolution
Δr	Range resolution
Δt	Time resolution
ε_r	Relative permittivity
Γ	Reflection coefficient
λ	Wavelength
μ D	micro-Doppler
ϕ	Azimuth angle
τ	Time delay
θ	Scanning angle

Acronyms / Abbreviations

ACC	Adaptive cruise control
AEB	Auto Emergency Braking
AVP	Automated Valet Parking
BSD	Blind spot detection
BW	Bandwidth
CDF	Cumulative distribution function
CPI	Coherent processing interval
CTA	Cross traffic alert

CW Continuous wave

EMSL European Microwave Signature Laboratory

EMW Electromagnetic wave

FCW Forward collision warning

FFT Fast Fourier Transform

FoV Field of view

HRI High resolution image

HRR High range resolution

HRRP High resolution range profile

IF BW Bandwidth of the filter at intermediate frequency

IFFT Inverse fast Fourier transform

InSAR Interferometric Synthetic Aperture Radar

ISAR Inverse synthetic aperture radar

ITU-R International Telecommunications Union Radio-communication Sector

LCA Lane-change assist

LOS Line of sight

Low-THz Low-TeraHertz

MISL Microwave Integrated Systems Laboratory

MRR Medium range radar

PA Parking assistant

PDF Probability density function

PEC Perfect Electric Conductor

PRF Pulse repetition frequency

RCS Radar Cross Section

RCW Rear collision warning

SAR Synthetic Aperture Radar

SBR Signal to background ratio

SNR Signal to noise ratio

SRF Sweep repetition frequency

CRF Chirp repetition frequency

SRI Sweep repetition interval

LRR Long range radar

SRR Short range radar

THz TeraHertz

USR Ultra short range radar

VNA Vector Network Analyzer

Chapter 1

Introduction

1.1 Motivations

The European commission recently pushed for the entry into the market of self-driving cars to reduce the number of death every year in road accidents [1]. According to statistics the 95% of accidents are caused by human errors. With cars and lorries equipped with the technology for autonomous driving, the number of accidents could significantly decrease improving road safety. Furthermore, digital technologies can reduce traffic jams, and consequently pollution, improve access to mobility and guarantee new jobs for the automotive and electronic sectors.

To address the increasing request to develop the sensors necessary for systems with high level of automation, the automotive industry has found its interest in deploying radars, in conjunction with LIDARs and cameras, to increase reliability and correct situation awareness. With respect to electro-optical sensors, radars offer the advantage of robust operation in adverse weather conditions and harsh environments. This is, due to the ability of electromagnetic (EM) waves at frequencies below the infra-red band to propagate through optically non-transparent media such as fog, smoke and spray, with much lower loss. Moreover, radars offer the possibility of direct measurements of range and speed.

The main function of a radar is to provide detection, parameter estimation and recognition of multiple targets by exploiting information on the range, angle and motion relative to the radar. Current automotive radars, operating at the bands of 24 and 79 GHz, provide parking and adaptive cruise control assistance to the driver and also collision avoidance and pre-crash warning as measures to prevent or reduce accidents. Figure 1.1 illustrates the different applications provided by current automotive radars.

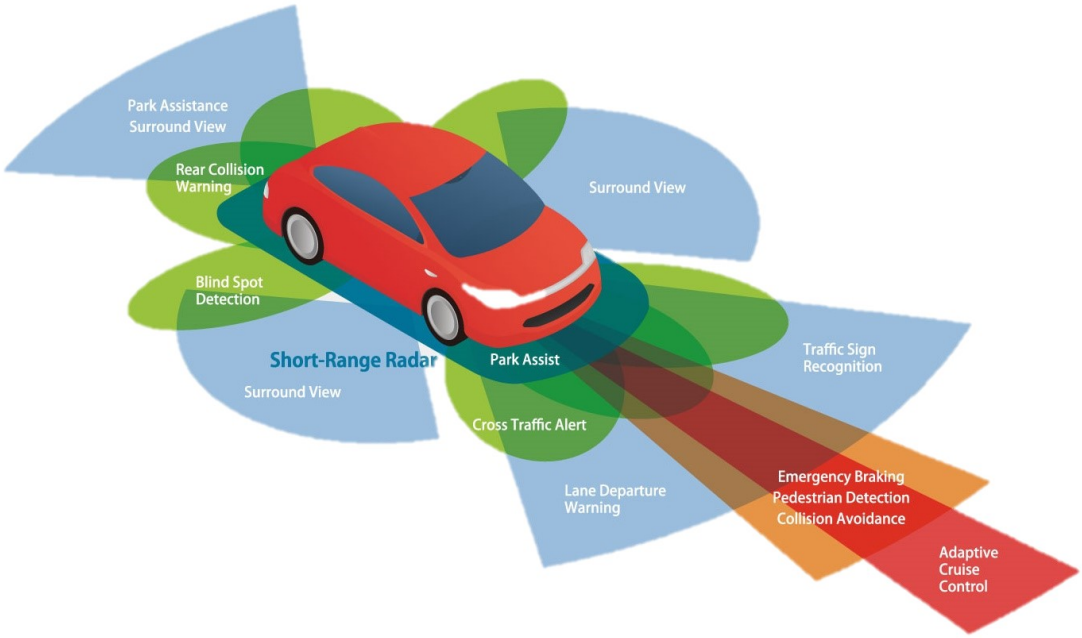

Fig. 1.1 Current automotive sensors application [2]

A roadmap of some of the driver-assistance functions and radar features that are expected to appear in the coming years is shown in Figure 1.2. The goal is to reach level 5 autonomy, removing the driver completely from the loop and enabling the car to handle all driving situations.

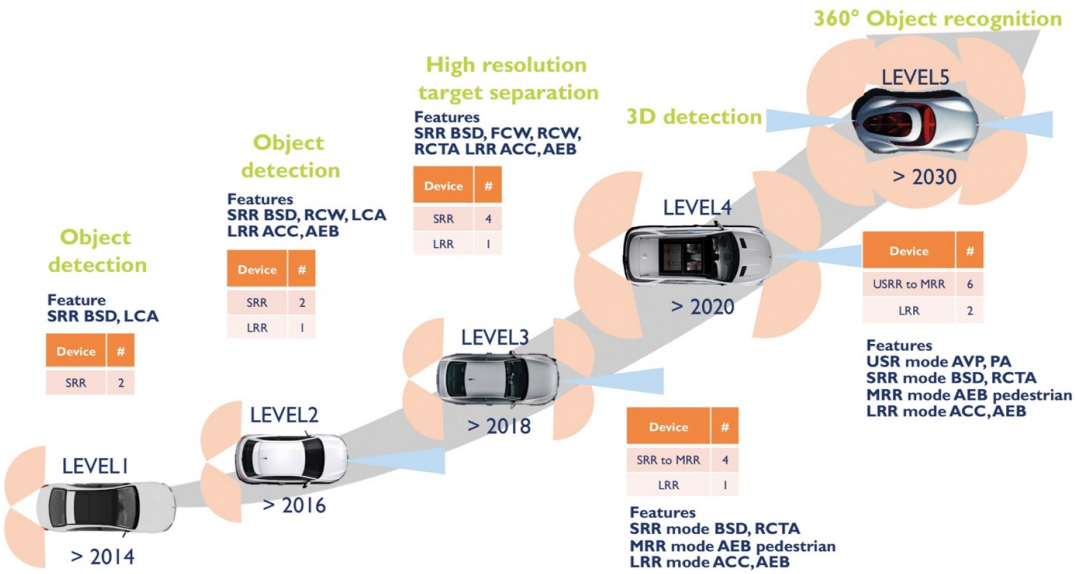

Fig. 1.2 Roadmap for driver assistance functions [3]

It is possible to identify a list of key aspects, where today's radar sensors need to be improved to address future requirements [4]:

- Higher range resolution and angular resolution in both azimuth and elevation, to be able to provide much more detailed information about detected objects. This is especially important to determine object properties like height, size, or type.
- Improved velocity estimation and resolution, as well as micro-movement assessment, to reliably detect vulnerable road users like pedestrians or cyclists.
- A flexible field of view (FoV) to allow a broad FoV for pedestrian detection, as well as a narrow FoV for highway driving.
- Reliable detection of all relevant objects, and assertion of failure, due to component defects or environmental influence like heavy rainfall.
- Adhere to cost and size restrictions while still addressing the required performance improvements.

It would be unrealistic to think to fulfil all the requirements for designing radars for autonomous driving systems by using a single sensor. The requirement to integrate

high number of radars in the system means that the number of radars per car and the number of cars equipped with radars will dramatically increase, tens of millions of radar sensors will be fielded annually raising the question of mutual interference and co-existence. The increase of available bandwidth is one of the methods that can be used to mitigate some of these effects. As answer to the request to enlarge the allocated bandwidth, a new generation of radars is making its way as a new research trend and is the subject of the current research and development work taking place at the Microwave Integrated System Laboratory (MISL), University of Birmingham [5]: Low-TeraHertz (Low-THz) radar systems operating within the 0.3-1 THz frequency spectrum. This band, currently unallocated, offer the possibility of using large absolute bandwidths, with the same fractional bandwidth occupied by the commercial automotive radars, and therefore potentially reduce the problem of mutual interferences between radars [6].

Before the advantages of low-THz radars can be exploited, we need to answer the question of whether fundamental physical limitations affects the propagation and reflections of such high frequency signals. The well-known graph of atmospheric attenuation in clear air versus frequency in Figure 1.3, between 100 GHz and 1 THz, shows regions of local minima attenuation between absorption peaks at frequencies referred to as “atmospheric windows”. The operation of Low-THz sensors lies in these windows. Specifically, this work focus on two frequency bands: 150 GHz and 300 GHz. The clear-air attenuation is around 3 dB/km at 150 GHz and 10 dB/km at 300 GHz. Taking into account that automotive radar operates for distances up to 200 m, the loss over this range is tolerable in these two bands.

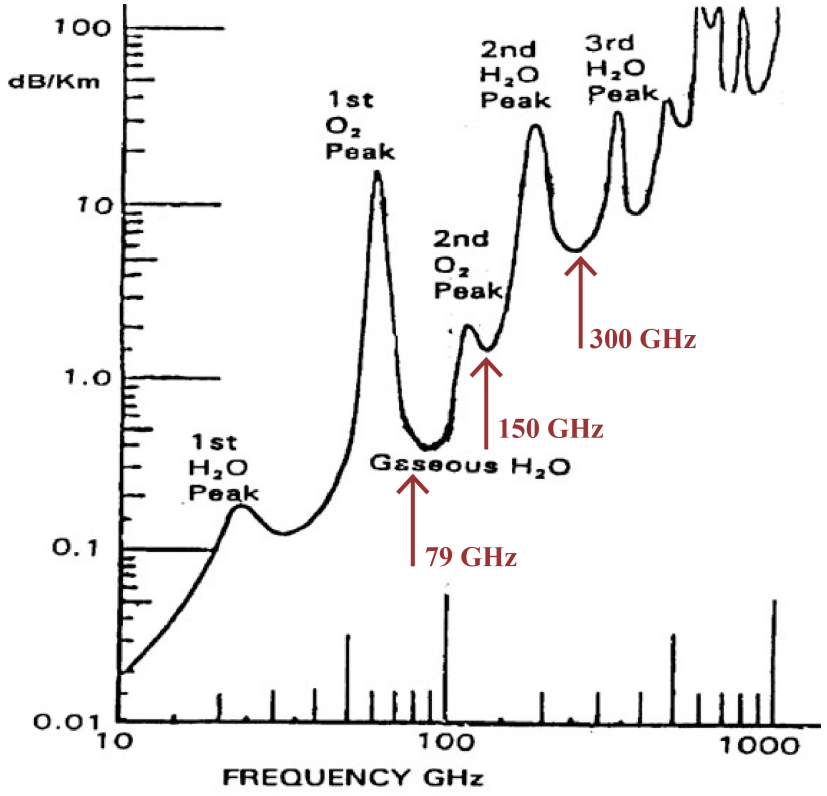

Fig. 1.3 Atmospheric attenuation in clear air [7]

Other factors affecting the signal energy dissipation, introduced by the atmosphere, are the particles present in rain, snow, fog, dust, sand etc, which increase the attenuation as the wavelengths becomes comparable with the particles sizes, in the order of few millimetres, and reduces it for higher frequencies, when the particles are larger than the wavelength. **The first objective of this work is the investigation of the additional attenuation, caused by adverse weather conditions, of signals at low-THz frequencies** and the comparison with the performances of sensors operating at the current automotive frequencies (77 GHz).

Let us now to examine the additional advantages of moving to low-THz frequencies for automotive radar operation. As a direct consequence of increasing the available bandwidth, the range resolution increases. The increase in the carrier frequency is also responsible for a potential increase of the angular resolution, as antennas' sizes are directly proportional to the wavelength: higher resolution can be achieved using

the same antennas' size of standard automotive radars and vice versa the antennas' dimensions can be reduced without affecting the resolution. Next advantage is that extremely small wavelengths show an increased sensitivity to surface texture.

Improved resolution in both range and azimuth and high sensitivity to rough surfaces have the potential to provide high resolution images of the scene surrounding the vehicle, resulting in the feasibility of using imaging radars for automotive applications. The concept of imaging radar is rather new in the automotive industry, being usually associated to remote sensing applications using synthetic aperture radar (SAR) and inverse SAR (ISAR) techniques [8]. Automotive imaging radar currently relates to two-dimensional (2D) maps of detected targets created with a real aperture. Unlike target detection sensors, such as ACC, which can only give information on the presence or absence of objects, an imaging radar provides the spatial distribution of reflectivity corresponding to an extended object, which is more detailed and similar to an optical image, as the resolution increases. An optical-like radar image allows the application of computer vision techniques to identify and classify different targets, techniques that were reserved for optical or light detection and ranging (LIDAR) images until now. The image in Figure 1.4 shows a radar image of a person using a 300 GHz system made at the Fraunhofer Institute, Germany [9]. Although the image is produced using the ISAR technique and required few hours of integration, which is not a feasible technique for automotive applications, where the detection and recognition of targets is required in fractions of seconds, it shows the enormous potential of low-THz radar to produce images with optical quality.

Fig. 1.4 Radar image of a person at 300GHz using ISAR [10]

The development of low-THz imaging automotive radars requires the complete knowledge of the road objects and actors reflectivities and their distribution in space and time. There are a number of reasons to acquire these information, related to the operations of target detection and recognition:

- The need to assess quantitatively the detection performance of radars operating at high frequencies.
- The establishment of reference libraries of the overall reflectivity of all the road objects and actors, using the concept of radar cross section (RCS), to define the minimum signal to noise ratio (SNR) required to design effective sensors.
- The extrapolation of statistical models for target RCS fluctuations at different aspect angles, to produce robust detection algorithms.

- The analysis of the fluctuations at different ranges and angles of reflectivities of extended objects, to be used in object recognition systems which use radar images as an identifier unique to a particular object.

- The building of libraries of road targets images to be used in classification algorithms based on machine learning.

- The analysis of the fluctuation of the target reflectivities over time as the targets move relative to the radar, by exploring the Doppler effect and in particular the micro-Doppler phenomenon: the frequency modulation on the returned signal induced by the mechanical vibration or rotation of the target or any structure on the target in addition to its bulk translation. The micro-Doppler signatures are used as additional feature for identification and classification of road targets.

- The determination of the size of the targets and the position of scattering centres, useful to develop simulators for complex traffic scenarios for determining responses of radar sensors.

The characterization of automotive targets reflectivity and micro-Doppler signatures is the second objective of this work, the study is made at low-THz frequencies, but simultaneously also at the current allocated automotive frequencies, 24 GHz and 79 GHz, to compare their performances and have a reference with the results already available in literature, so as to validate the methodology employed. To the best of the author's knowledge, there is no previous researche about road target reflectivities at low-THz frequencies. Moreover, for some of the targets characterised, such as wheelchairs, pushchairs and bikes, the literature lacks of information even at lower frequencies, therefore in this case this study is also useful for the development of radars operating at standard automotive frequencies.

1.2 Contributions

To obtain the data to form radar images, the low-THz waves, transmitted from the radar positioned on the vehicle, propagate through the surrounding environment and is scattered from the targets and surfaces. Scattered waves propagating back to the radar are used to generate images and signatures related to the objects motion. The research work outlined in this thesis relates to these physical aspects of the radar and is based on experimental characterization. The attenuation of low-THz waves through different media and atmospheric precipitation is investigated to show the feasibility of Low-THz sensing for outdoor applications in presence of adverse weather conditions. Then, the reflectivity and motion properties of typical road targets is analysed to determine the most appropriate parameters and waveforms, to be used in the development of low-THz radars and for the generation of robust algorithms for target detection and classification.

The original contribution from the author regards the investigation of the reflectivities and temporal signatures of the road targets, while results on the attenuation study have been obtained in collaboration with other team members as part of the laboratory research.

The doctoral work consisted in the development of the methodologies employed for the experimental characterization, involving the design of the experiments, the collection and processing of reliable data obtained from a combination of measurements in controlled environments created in the laboratory and outdoor trials in real road scenarios; and in the elaboration of the tools necessary to the analysis and statistical interpretation of the radar outputs.

1.3 Thesis outline

- Chapter 2 provides a background for the topics covered in the later sections, such as an overview on current automotive radars and THz sensing, the physical phenomena affecting the electromagnetic wave propagation and scattering, and the concepts of radar cross section, radar imaging and micro-Doppler, which are used to characterise typical road targets.

- Chapter 3 describes the methodology utilised in the experimentation and to analyse the data collected to produce significant results, which can be used for the design of Low-THz radars for future autonomous vehicles. The chapter outlines the waveforms and signal processing needed for automotive radar operations and the radar systems used in the experimentation. The definitions of the signatures and statistics used to characterize road targets are presented. The experimental sites and methodologies used for the measurements are described and characterized.

- Chapter 4 presents the experimental results obtained in the study of attenuation of low-THz signals through the potential car infrastructure behind which the radar is placed, due to radome contamination and in the atmosphere due to common precipitations, rain and snow. To assess the feasibility of low-THz radars in respect to current automotive radars, simultaneous measurements at 77 GHz have also been performed and presented in this chapter.

- Chapter 5 presents a comprehensive study on the radar characteristics of pedestrians in the low-THz band and for comparison at the standard automotive frequencies. The results are presented in terms of high range resolution profiles, radar cross sections statistics and micro-Doppler signatures.

- Chapter 6 illustrates the study of the reflectivity of a popular passenger car at 300 GHz and 24 and 79 GHz to validate the experimental setup, carried out in a typical

road environment. The results are presented with high range resolution profiles, radar cross sections statistics and images of the car. Analysis of the reflectivity and motion characteristics of other common road objects in the low-THz band is also provided.

Chapter 2

Background

2.1 Overview

The purpose of this chapter is to provide a background for the topics covered in the thesis. Firstly, a brief overview of the state of the art of automotive radars is given to put the novel Low-THz radar in context. Secondarily, basics on the physical phenomena affecting the electromagnetic wave propagation are provided. Next, an overview on current uses of THz sensing is given and Low-THz radar for automotive applications is introduced. Finally, three sections define the concepts of radar cross section, radar imaging and micro-Doppler, which are used to characterise typical road actors.

2.2 Automotive radars: state of the art

The main objectives of a radar system are to detect the presence of one or more targets of interest and estimate their range, angle, and motions relative to the radar. The concept of Radio Detection and Ranging (radar) arises between the end of the 19th and the beginning of the 20th from the experiments realized by Hertz on the reflections of electromagnetic waves (EMW) and the invention of the Telemobiloscope by Hülsmeyer; the first developments of radar dating back to the world war second were limited

to military applications. Radar is now used in many applications, including civilian aviation, navigation, mapping, meteorology, radio astronomy, medicine and many others.

To go into details of automotive radars, their development started in the '70s, but it was not before the '90, with the progress in semiconductor microwave sources, microcontrollers and digital signal processing algorithms and units, that automotive radars started to be commercialized; since then they had a rapid growth up to acquire a key role in the technology of driving assistant systems before and self-driving cars in the nearest future. Also other sensing technologies, such as LIDAR, video camera-based sensors, are currently used to provide path planning for autonomous driving. But *only radar offer the advantage of robust operation in adverse weather conditions and harsh environments*, in addition to the inherent ability to measure targets range and velocity directly. This is due to the ability of electromagnetic (EM) waves at frequencies below the IR band to propagate through optically non-transparent media such as fog, smoke and spray, with much lower loss.

Current majority of automotive radars are based on the principle of frequency-modulated continuous-wave (FMCW) radar [11]. Increase of hardware capabilities permits the use of higher carrier frequencies and bandwidth and the fast development of MIMO systems offer additional degrees of freedom to traditional FMCW radar system design and signal processing. Two carrier frequency are predominantly used: 24 and 77 GHz, with the latter, also refereed as millimetre-waves, that have almost completely replaced the first. In the mm-waves two bands have emerged: 76–77 GHz, which is used for long range sensors (up to 250 m), and 77–81 GHz, introduced to replace the ultrawide-band at 24 GHz. It is employed in medium range sensors (up to 100 m) providing a larger bandwidth of 4 GHz instead of 1 GHz, increasing, therefore, the range resolution, however with the drawback of lower transmitted power. Table 2.1 summarises the key parameters for current automotive radars, by classifying them in three categories:

- Long Range Radar (LRR) for applications, like ACC, which are relatively narrow beam forward-looking systems to control driving path in front of the car to determine distance of vehicle driving ahead.
- Medium Range Radar (MRR) for applications with a medium distance and speed profile, like Cross Traffic Alert (CTA).
- Short Range Radar (SRR) for applications sensing in direct proximity of the vehicle, like blind spot detection, parking aid, stop and go functionality.

Table 2.1 Classification of current automotive sensors characteristics [12]

Type	LRR	MRR	SRR
Maximum trnasmitted power (EIRP)	55 dBm	-9 dBm/MHz	-9 dBm/MHz
Frequency band	76-77 GHz	77-81 GHz	77-81 GHz
Bandwidth	600 MHz	600 MHz	2 GHz
Distance range	10-250 m	1-100 m	0.15-30 m
Range resolution	0.25 m	0.25 m	0.075 m
Velocity accuracy	0.6 m/s	0.6 m/s	0.6 m/s
Angular accuracy	0.1°	0.5°	1°
Antennas azimuth 3dB beamwidth	±15°	±40°	±80°
Antennas elevation 3dB beamwidth	±5°	±5°	±10°

The great challenge of FMCW radar systems is mutual interference which will become a severe problem with the increasing number of radar-sensor equipped vehicles in dense traffic situations in the near future and a solution to the expected increase in interference is still an open question [13]. One of the proposed solution is the use of alternative radar waveforms such as pseudo-random or orthogonal-frequency division multiplexing (OFDM) [14]. The solution proposed in this work is the migration to

higher frequencies (low-THz band), which are currently unallocated, to take advantage of the possibility to use larger bandwidths.

2.3 Electromagnetic wave propagation mechanisms

Radar waves are electromagnetic waves (EMW) that convey energy from one point in space to another. These waves properties can directly be inferred by the Maxwell equations [15]: (i) EMW travel in vacuum at a maximum speed equal to the speed of light, (ii) EMW propagates transversely to electric and magnetic fields, (iii) Electric and magnetic fields vectors are always perpendicular to each other. An EMW travelling in free space is an oscillatory propagation phenomenon which characteristic parameters are: wavelength, propagation velocity and energy. Propagation is affected by media leading to phenomena such as attenuation, refraction, diffraction, reflection, scattering and interference. Attenuation is the reduction of energy of the wave due to the absorption from particles, gases or ionized atoms present in the atmosphere and depends on the frequency of the EMW. Refraction, diffraction, reflection and scattering are physical phenomena which occur when the EMW impacts an obstacle and in general depend on the shape, size and material of the object if compared with the EMW wavelength. These varied phenomena's lead to large scale and small scale propagation losses and constitute the basic principles of operation of radars.

2.3.1 Atmospheric attenuation

Some gases in the atmosphere, like water vapour, oxygen and CO_2, cause attenuation as their molecules, not electrically balanced, resonate at certain frequencies dissipating energy; therefore, atmospheric attenuation depends on the concentration of such gases and is highly dependant on frequency. The International Telecommunication Union (ITU) in [16] recommended a model to estimate the specific attenuation at frequencies

up to 1 THz, due to dry air and water vapour at any value of pressure, temperature and humidity. Attenuation constants as a function of frequency are defined usually in units of dB/km. Figure 2.1 shows the specific attenuation for a pressure of 1013.25hPa, temperature of 15°C for the cases of a water-vapour density of 7.5g/m^3 (Standard) and a dry atmosphere (Dry). For propagation paths that are mostly horizontal, such as the operation of automotive radars, the attenuation constants are fairly constant, and the total attenuation is simply found by multiplying the attenuation constant by the path distance.

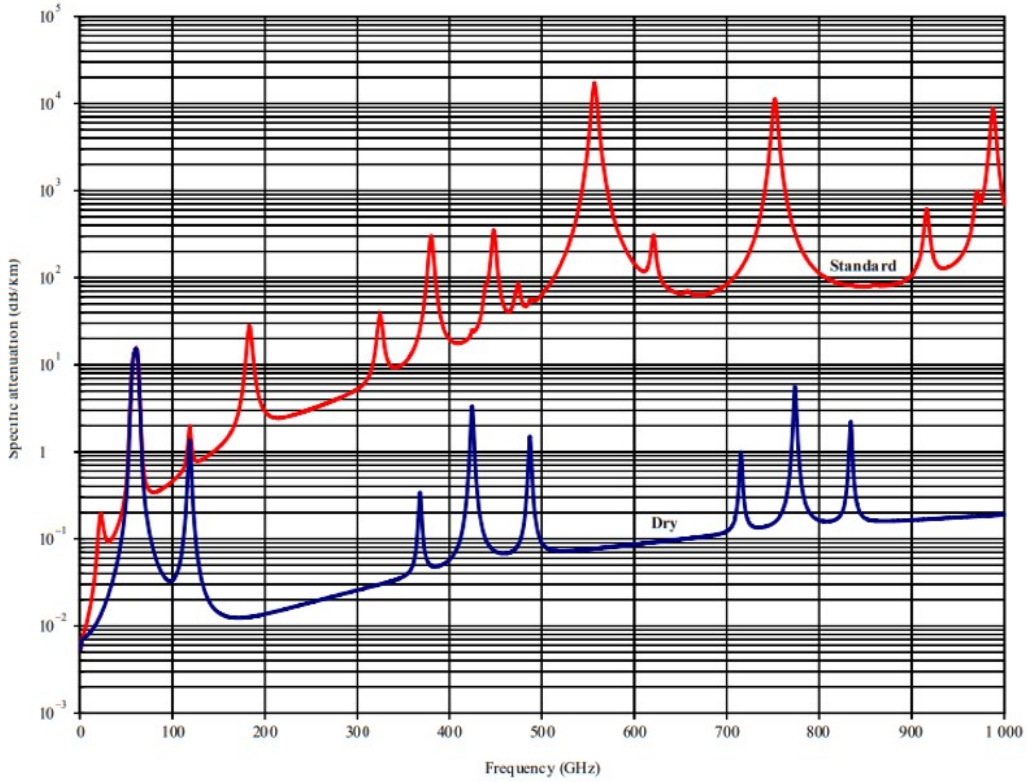

Fig. 2.1 Atmospheric attenuation as a function of frequency [16]

Additional attenuation of signals propagating in the atmosphere are caused by the precipitations, the most common being rain, fog or snow. When a plane wave intercept a raindrop or a snowflakes, some of its energy wave is absorbed by the water (since it is a highly lossy dielectric), while some of it is scattered. These two phenomena leads to an overall effect called “extinction”. Empirical formulas are useful for predicting the

attenuation constant, which is multiplied to the atmospheric attenuation and the path distance to estimate the total attenuation during the propagation path. The ITU [17] uses a power-law relationship which takes into account the falling rate R_r measured in mm/h and depends on two empirical constants, k and α, dependant on frequency and incident wave polarization.

2.3.2 Interference

The result of overlapping two or more waves is called interference. Two waves are said to be in-phase when their maximum, minimum and null amplitudes are reached at the same time, otherwise they are out of phase. When in-phase, two waves constructively interfere producing a wave of the same frequency but having an amplitude given by the sum of the amplitudes of the single waves. If out of phase the two waves interfere and if their phase difference is $\lambda/2$ they cancel each other [18].

Diffraction is a phenomenon of interference that allows the EMW to propagate over an aperture or the edge of an obstacle of size comparable with its wavelength, permitting the penetration of the EMW in shadow regions for the radar signal. Refraction occurs when a wave travels from one medium to another, with different density, so that its velocity and its direction of propagation are subject to variations. Since density and temperature of normal atmosphere vary with altitude, the EMW bend down, permitting the detection of objects placed over the geometric horizon [19].

2.3.3 Reflection

Reflection occurs when the EMW impacts an obstacle which dimension is much greater than the wavelength and there is a variation of the relative permittivity (ε_r) between the propagation media and the object. The reflection of a EMW from an obstacle can be studied using the Huygens principle, from which is obtained the important property that the reflection angle is the same of the incident one. The amplitude of the reflected

wave depends upon the nature of the obstacle and the incident wave. When the obstacle absorbs all or part of the energy, as in the case of a dielectric materials, the reflected wave amplitude is small or zero. Otherwise, if the object matter is a perfect conductor the reflected wave amplitude is the same of that of the incident wave. The ratio between the amplitude of incident and reflected waves is defined as the reflection coefficient (Γ), it depends on the incident angle, the physical characteristics of the point of reflection, the polarization and the frequency [15].

2.3.4 Scattering

Scattering occurs when the medium through the wave is travelling contains objects which are smaller than the wavelength of the EMW. The definition of reflection assumes that the wave incises on a flat, smooth surface. Figure 2.2 shows as the reflected and incident waves of constant phase fronts in this case are in phase with each other and have the same path length (l). However, if the surface is rough the reflected waves from different points of the surface have different path lengths, producing a phase difference:

$$\Delta\phi = 2kh_{rms}cos(\theta_i) \tag{2.1}$$

where, $k = \frac{2\pi}{\lambda}$ is the wavenumber (λ is the wavelength), θ_i is the incident angle of the i-th wave of the wavefront and h_{rms} is called surface root mean square height and it is the deviation in the direction of the normal vector of a rough surface from a smooth surface.

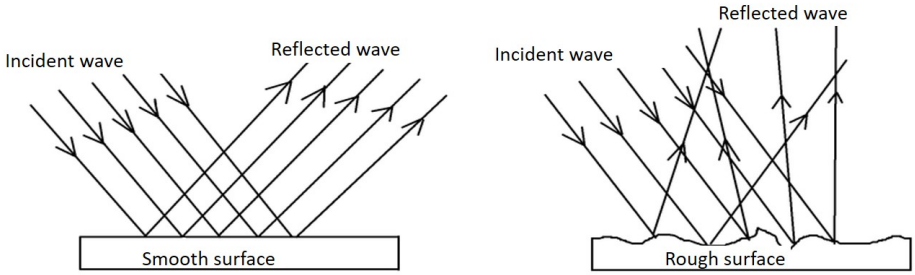

Fig. 2.2 Difference between smooth and rough surface scattering

The phase difference will cause the diffraction or the cancellation of part of the reflected waves due to the interference between them. The Rayleigh criterion determine a boundary between the possible definition of smooth and rough surfaces for an EMW, the surface is regarded as rough if [20]:

$$h_{rms} > \frac{\lambda}{8} cos\theta_i \tag{2.2}$$

For extremely small wavelength most of surfaces are accounted as very rough ($hrms >> \frac{\lambda}{8} cos\theta_i$), in this case the incident waves are scattered in all directions causing the so-called diffuse scattering. As it will shown in the results reported in this thesis, low-THz sensors take advantage of the diffuse scattering to obtain large amount of information from targets and surfaces [21].

2.3.5 High frequency scattering by complex objects

High frequency scattering occurs when the wavelength of the transmitted signal is much smaller than the target sizes and also than the scattering centers constituting the target. In this case there are a number of scattering mechanism that determine the total scattering from the target [22]:

- Specular scattering from planar and curved surfaces when the normal to the surface points back toward the radar, in this case the scattering mechanism is a bright flash return
- Multiple bounce corner reflectors
- Diffraction from edges and tips
- Surface wave scattering due to travelling wave reflection from planar or curved surfaces or wires
- Creeping wave scattering from uninterrupted paths around curved surfaces

- Scattering from rough surfaces
- Scattering from surfaces discontinuities such as gaps, cracks or joints

2.3.6 Mie Scattering

The first quantitative study on the scattering of waves caused by small particles was conducted by Rayleigh in 1871. The scattered radiation from a particle much smaller than λ is in-phase with the incident wave and forward scattering and backward scattering have the same intensity. Mie theory (1908) describes the scattering mechanism in relation to a single spherical particle with finite dimensions, which size is of the same order of magnitude or greater than the wavelength of the incident radiation. As shown in figure 2.3, the angular distribution of diffuse radiation exhibits a high concentration around the direction of the incident wave propagation, with a lower intensity in the opposite direction. The directivity of the scattered wave in the same direction of the incident wave increases as the particle size increases [23]. Mie theory is fundamental to model the propagation mechanisms through particles present in the atmosphere and the reflection from spherical targets.

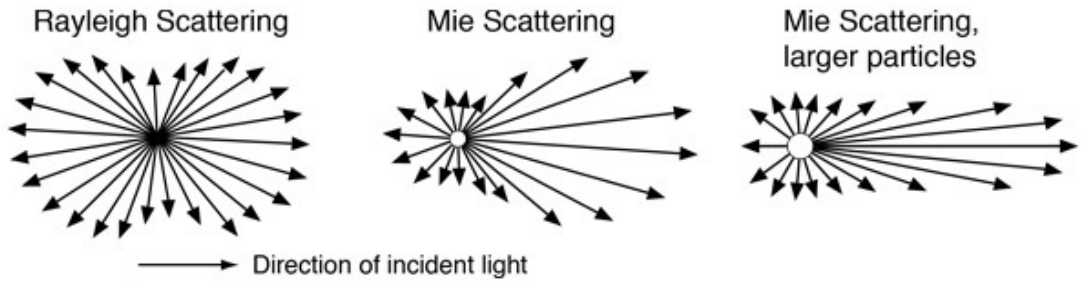

Fig. 2.3 Difference between Rayleigh and Mie scattering [24]

2.4 TeraHertz sensing

In the electromagnetic spectrum, Terahertz (THz) radiation is located between the microwave and infra-red regions and represent an effective bridge between electronic

and photonic technologies. THz radiation interacts little with matter and its absorption is low, therefore like radio is transparent to non-conductive materials, however it cannot penetrate metals and is strongly attenuated by water. Moreover, this radiation can propagate through optically non-transparent media such as fog, smoke and spray, with low losses and effects of diffraction are not significant as the wavelength is much smaller than ordinary sized objects. Further, THz photon energies have much less amplitude of x-rays and are thus non-ionising and therefore less dangerous for humans. THz sources can be used to illuminate non-metallic objects and in some cases see through them: it is possible to obtain images, where materials appear to be darker as their are opaque for THz waves. Therefore they find application in a variety of fields, like biomedicine [25], environmental studies [26], material science [27], art conservation [28] and radar imaging. Moreover, the enormous amount of bandwidth available makes THz frequencies object of research for the communication community [29–32] as it allows for high capacity for data transmission.

2.4.1 Low-THz radar

In this thesis we refer as Low-TeraHertz (Low-THz) the lower part of the THz region, with wavelengths in the range 0.5-2 mm, with corresponding frequencies of 150 GHz to 670 GHz. In this sub-region of the THz band not only attenuation is lower as it doesn't exceed 1 dB/100m, but radar technology is already in development [7]. With the rapid development of Monolithic Millimetre-Wave Integrated Circuits (MMICs), performance of semiconductor electron devices, especially transistors and diodes, operating at these frequencies has been constantly improved [33, 34] . This technology permits the realisation of several components, including mixers, amplifiers, oscillators, modulators/demodulators and phase locked loops essential for radar systems architectures. Meanwhile, efforts have being put with the objective of developing designs based on compact transceivers [35, 36]. Currently low-THz radars are employed in

the security field for the detection of concealed weapons and perimeter surveillance [37], military fighter jets [38], overhead power cable detection [39] and, as mentioned early, the automotive industry is moving from the traditional standardised frequencies to higher bands for autonomous vehicles technologies.

2.4.2 Low-THz radar technology for autonomous vehicles

Development of future autonomous vehicles requires the complete knowledge of the obstacle around the vehicle in order to define free areas to which the vehicle movement would be safe. Although other sensing technologies, such as LIDAR, stereo, video and infrared cameras, are currently used to provide path planning for autonomous driving, only radar offer the advantage of robust operation in adverse weather conditions and harsh environments. In this sense, the goal for automotive radar systems is to obtain radar images with resolutions as close as possible to those of cameras and lidar that can be used for surface identification, passable region identification and development of algorithms for obstacles identification and classification. Low-terahertz (THz) radar systems fit these requirements, λ is much smaller using these carrier frequencies if compared with sensor operating at standard automotive frequencies, offering the following advantages:

- very fine range resolution is achievable due to the large bandwidth available
- according to equation2.2, the smaller λ leads to an increase of roughness of the surfaces encountered by the transmitted wave and thus, a high amount of diffuse scattering is received from the full extent of an object
- more compact components and first of all antennas sizes
- for a given antenna aperture size, a higher operating frequency results in a beam with a smaller angular size

- reduced susceptibility to interference due to large bandwidths available. In fact, if the allocated bandwidth is much larger than the radar operating bandwidth, the probability that the spectra of two or more individual radars overlap is reduced.

Fine range and angular resolution and diffuse scattering at low-THz frequencies entails an increasing of the sensor to produce high-quality images from real physical apertures, as shown in the example in Figure 2.4.

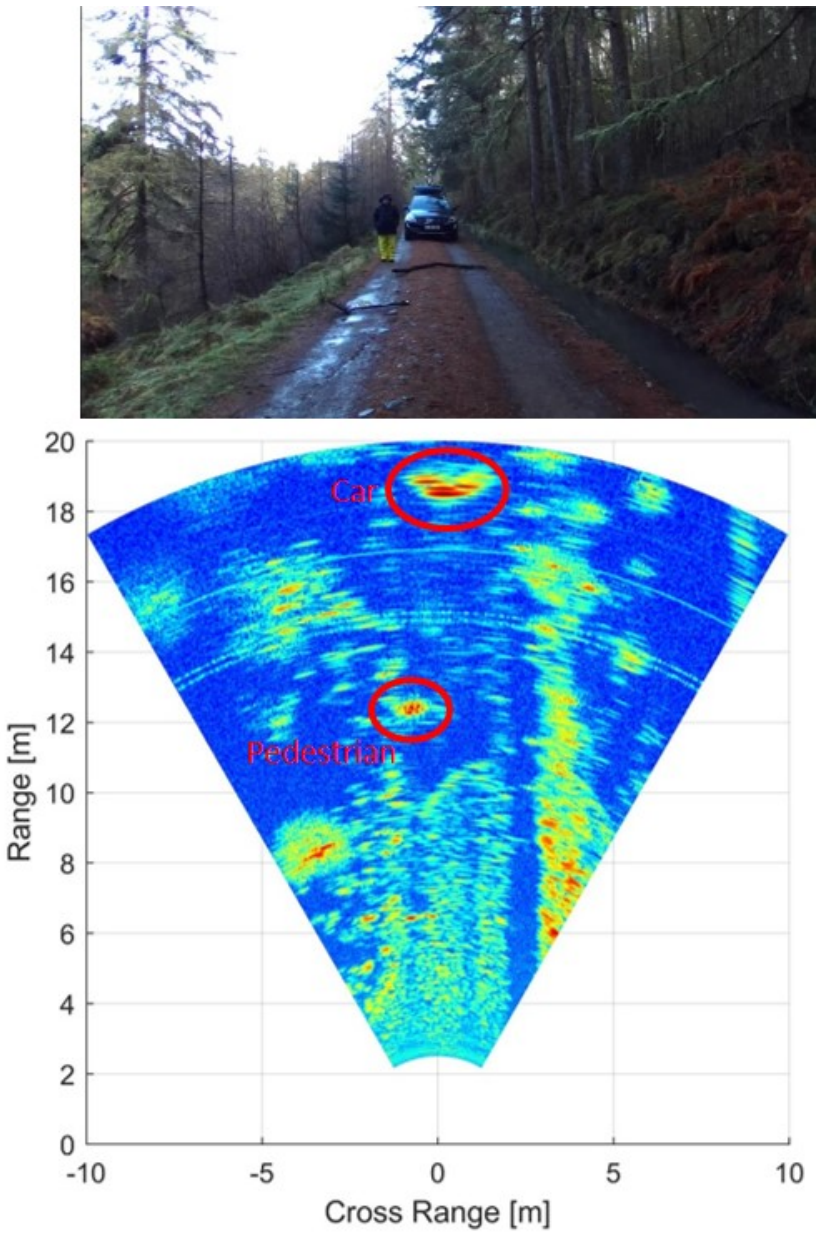

Fig. 2.4 150 GHz Radar Image of an off-road scene [40]

The figure shows a radar image obtained at 150 GHz of an off road scenario. Beside the car and pedestrian present in the scene that can be easily identified, the radar image is rich of information and it is potentially feasible to label all the objects in the field of view. It includes several features, like the images of the tree formations on the side of the road or the low reflectivity vertical stripe on the right caused by the water filled street gutter. The texture of the country road constituted by a very rough surface is identified by its high reflectivity.

2.5 Radar Cross Section

During the development process, the designer of an automotive sensor system needs to assess quantitatively the detection performance of objects and also to quantify the maximum detection range. This requires the knowledge of objects reflectivities at low-THz frequencies and in this thesis we will use the concept of Radar Cross Section (RCS) as a measure of such reflectivities. RCS is a measure of the power scattered in a given direction when a target is illuminated by an incident wave and does not depend on the distance between the target and illumination source. The 'IEEE Standard Radar Definitions' [41] defines RCS as:

$$\sigma = \lim_{r \to \infty} 4\pi r^2 \frac{P_s}{P_i} \tag{2.3}$$

Where P_s is the power per unit solid angle scattered in a specified direction and P_i the power per unit area in a plane wave incident on the scatterer from a specified direction.

There is a number of different factors that determine the RCS of an object, such as the material, the size compared with the wavelength, the transmitted electromagnetic wave, the angle at which the transmitted wave hits the target and the polarization of transmitted and the received radiation in respect to the orientation of the target.

The limit for the range r in 2.3 defines mathematically the condition of plane wave and therefore is related to the concept of far field, the RCS test community has adopted the rule that, in order to ensure an accuracy of 1 dB or better in the measurements, the range to a target with maximum dimension D has to be:

$$r \geq \frac{2D^2}{\lambda} \tag{2.4}$$

The use of Low-THz frequencies rarely permits to fulfilment of the far field criterion as most of targets are large if compared with λ, and in a strict sense we should use the term reflectivity in this case. However, we will retain the RCS term meaning the object characterization and methodology of the measurements, even because we will always consider the average RCS which varies little with the distance chosen for testing, as suggested by Knott [42] in this case the collection of near-field data is often defensible. Moreover the far field criterion should be used considering the longest flat feature on the target, not the maximum target dimension. Indeed, the fine resolution and the roughness at low-THz frequencies leads to the consideration that the majority of objects should be assumed to be a collection of point scatterers without any dominant long straight scattering feature and therefore the optimum distance should depend on the distribution of scattering centres over the target. This issue has been addressed for example by Pouliguen [43].

2.5.1 RCS of a perfectly conductive sphere

As it will be argued in Chapter 3, calibration is a an essential procedure allowing for a precise estimation of targets' RCS and a sphere made of perfect electric conductor (PEC) is the most common target used for calibration of RCS test ranges. The exact solution for the RCS of a PEC sphere of radius a is well known in literature [44] and has been developed starting for the Mie theory. The scattering cross section from a

metal sphere can be expressed in the simple form [42]:

$$\sigma = \frac{\lambda^2}{\pi}\left|\sum_{n=1}^{\infty}(-1)^n(n+\frac{1}{2})(b_n - a_n)\right|^2 \tag{2.5}$$

where:

$$a_n = \frac{j_n(ka)}{h_n(ka)} \tag{2.6}$$

$$b_n = \frac{kaj_{n\_1}(ka) - nj_n(ka)}{kah_{n-1}(ka) - nh_n(ka)} \tag{2.7}$$

$$h_n(x) = j_n(x) + jy_n(x) \tag{2.8}$$

j_n and h_n are the n-th order spherical Bessel and Hankel function, respectively.

By computing 2.5 at different frequencies, the trend in Figure 2.5 is obtained.

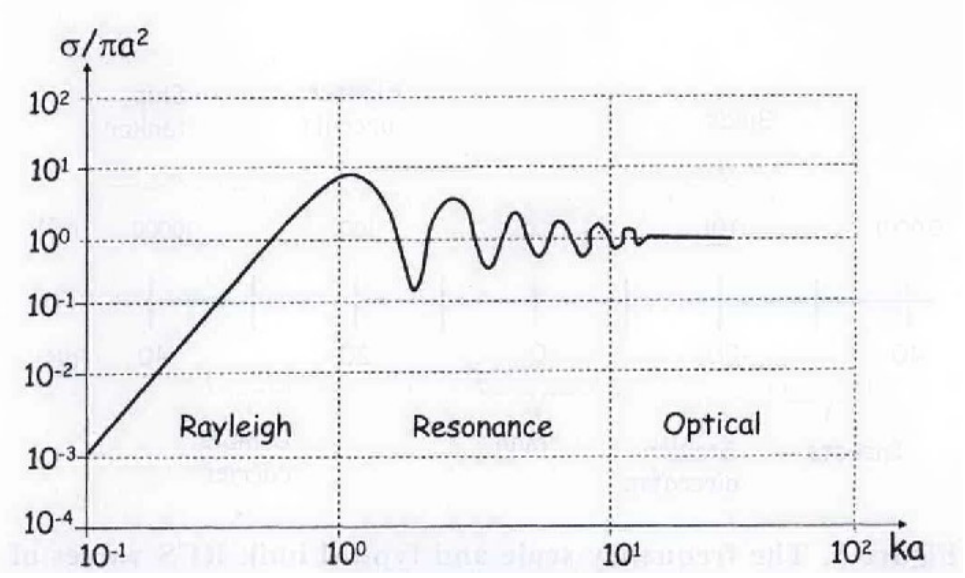

Fig. 2.5 Theoretical RCS of a sphere [45]

Three regions can be identified in the plot: for $\lambda >> a$ the scattering is of Rayleigh type, for $\lambda \sim a$ the scattering has an oscillatory behaviour, being characterized by interference between specular backscatter and creeping waves (the wave diffracted around the shadowed surface of the sphere). Finally, in the optical region ($\lambda << a$) the

RCS is frequency independent and only defined by the sphere's projected area:

$$\sigma = \pi a^2 \tag{2.9}$$

2.6 Radar imagery

Radar imagery generally refers to the resolution of target's scattering centres in both the range and azimuth (or cross-range) dimensions. An imaging radar is a system that elaborate the backscattered signal from a scene in order to build a reflectivity map. We can distinguish three classes of imaging radars.

2.6.1 Radar systems with rotating antennas

These are classic surveillance pulsed radars using rotating antennas with limited scanning angles and small azimuth aperture. The use of pulse compression techniques permits to obtain small resolution cells size and therefore produce images with relatively high resolution. These radars are used for example in airports for ground traffic control [46].

2.6.2 Synthetic aperture radar

The synthetic aperture radar (SAR) technique is primarily used for long range application to mapping of large areas on the ground, but its application is nowadays also studied for short range sensors for automotive applications [47, 48]. The radar is mounted on a moving platform that uses its motion to increase the length of the antenna and thus define a synthetic antenna. The backscatter signals received at each position of the antenna are coherently processed and the azimuthal resolution results to be half of the length of the actual antenna and independent from the distance of between the sensor

and the ground. By reducing the antenna's aperture the beamwidth broaden, but at the same time the resolution increase.

An improvement of the SAR technique which uses the phase difference between two images collected at different viewing angles (the interferometric phase) is used to generate elevation map of the terrain and improve the range resolution [49]. In principle, by coherently comparing the backscattered signals from a target, collected by the same antenna in two different position or by two antennas it is possible to calculate the height of the target. Interferometric SAR (InSAR) finds mainly application in geodesy and remote sensing but has also been proposed for automotive applications [50] and is the subject of our recent study [51].

2.6.3 Real aperture radar

In this kind of radar a narrow beam illuminates the scene and the received backscattered signal used to build a 1-D map of the scene. Then, by scanning the antenna, mechanically, electronically, or using an array of narrow beam antennas, a 2-D intensity map is obtained. As it will be shown later, the azimuth resolution directly depends upon the beamwidth and reduces as the range increase. The range resolution depends on the bandwidth of the transmitted signal, in particular it will be shown as a frequency modulated continuous wave (FMCW) with large bandwidth will dramatically increase the resolution if compared to a pulsed waveform.

2.7 Features for classification - The micro-Doppler effect in radar

Early it was mentioned as one of the goal for a low-THz automotive radar is ultimately to produce images with resolution as high as possible that can be used for identification and classification of road objects and actors. Alongside with this approach, another

feature obtained through radar data can be used for identification and classification: the micro-Doppler (μD) signatures.

Radar systems using continuous wave (CW) waveform are designed to acquire information on the movement of targets exploiting the Doppler effect: the frequency shift caused by the change in the frequency observed by the radar receiver as compared to the transmission frequency, when an object is moving relative to the radar. Micro-Doppler is a variant of the Doppler effect that uses the micro-motions of the target superimposed on the main motion [52]. Common targets, in fact, are made of several components, each having a separate motion which will induce a frequency modulation on the reflected signal that generates sidebands besides the Doppler due to bulk motion of the target. Radar signals reflected from targets with oscillating vibrating or rotating parts, such as drones' propellers, birds' wings, or limbs in case of humans, contain μD features related to these structures. These features, usually expressed in terms of μD signatures, are distinctive for each class of target and potentially offers a different approach for the detection and recognition by radar systems, they can be integrated to information obtained with existing methods enhancing the capability of such systems. In the automotive context, the μD effect can potentially be employed to recognise specific types of vehicles as well as their engine type or speed and more importantly, for pedestrian recognition, the human signature can be deployed to classify people against other targets, the direction of their motion.

In our study the aim is to provide better identification and motion parameters estimation of the pedestrian by obtaining a clearer pattern in the μD signatures, taking advantage of the diffuse scattering behaviour of EMW at low-THz frequencies.

Chapter 3

Methodology and characterization

3.1 Overview

The work carried out to characterize the performances of Low-THz radars for automotive application has been mainly based on experimentation. This chapter aims to describe the methodology utilised in the experimentation and to analyse the data collected to produce significant results, which can be used to advise the design of Low-THz radars for future autonomous vehicles. In some occasions, the measurement methodologies have been specifically developed for this research.

In the following sections, firstly, the waveforms and signal processing needed for automotive radar operations and used in the experimentation are described in detail. Sections 3 and 4 are dedicated to the methodologies to characterize the attenuation of low-THz waves in different atmospheric conditions and to achieve signatures of typical road targets. Successively, the radar system hardware used in this work to collect data are described. Finally, the experimental sites in which measurements have been carried out will be described and characterized.

3.2 Automotive radars waveforms and signal processing

Fundamental radar operation involves the estimation of range and radial velocities of targets. The range (r) is estimated by measuring the roundtrip time delay (τ) of the propagation of the electromagnetic wave (EMW) to and from the target. The target radial velocity (v_r) is estimated based on the the Doppler frequency shift induced on the EMW from the motion of the target relative to the radar. The form of the EMW transmitted by the radar (waveform) is important to determine the accuracy with which targets' range and radial velocities are estimated. Automotive radar waveforms determine several fundamental performance metrics, such as range resolution, velocity resolution, angular direction, SNR, through the gain introduced by the time-bandwidth product [53], and the probability of target detection. The waveforms can be classified as pulsed, continuous wave (CW), frequency or phase modulated.

Pulse radars generate short rectangular shape pulses modulating a sine wave carrier. These radars require high peak power to concentrate all the energy in a short period of time. As opposite, a continuous wave (CW) radar constantly transmits and receive simultaneously low peak power EMW, permitting to overcome to the limitations of pulsed systems regarding the high peak power transmitted. However the maximum detectable range is shorter than for a pulsed radar and this kind of waveform only gives information on the velocity of the target without any resolution in range. A common way to overcome these limitations are pulse compression techniques in which the power is spread across different frequencies. Two main technique have been used in this work and will be presented in details in the next sections: the stepped frequency waveforms (SFW), where pulses at increasing frequencies are transmitted, and frequency modulated continuous wave (FMCW) waveforms, where a CW signal is frequency modulated [54]. Due to the ability to measure both range and speed with high resolution, FMCW

and SFW radar are widely used in the automotive industry [55]. Moreover, hybrid waveform types with combination of SFW and FMCW can be employed to achieve additive performance [54]. Finally, it is worth to mention the application of orthogonal frequency division multiplexing (OFDM) to radar systems [56], this technique can offers the features of the joint implementation of automotive radar and vehicle-to-vehicle communications [57].

3.2.1 CW waveform

CW radars are used for velocity estimation using the concept of Doppler frequency shift. The frequency of the transmitted signal is constant and the received signal frequency is continuously compared with it as shown in Figure 3.1.

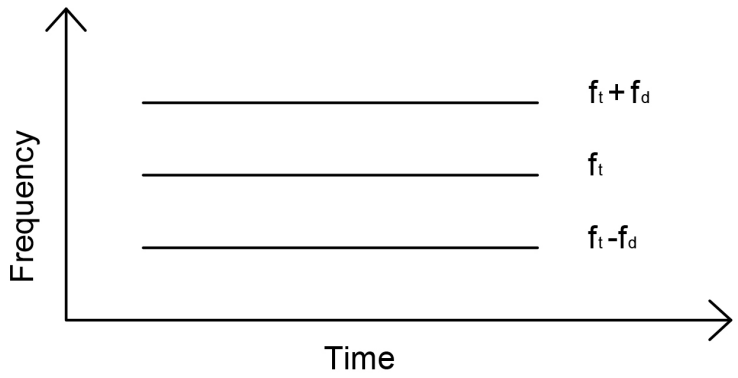

Fig. 3.1 CW Radar: transmitted and received waveforms

The Doppler frequency shift f_d is obtained by the difference between the transmitted and received frequencies and the object radial velocity v_r (the projection of the velocity vector on the radial direction) is calculated according to the equation:

$$v_r = f_d \frac{\lambda}{2} \tag{3.1}$$

As shown in the block diagram in Figure 3.2, the signal received from the target is mixed to the transmitted signal.

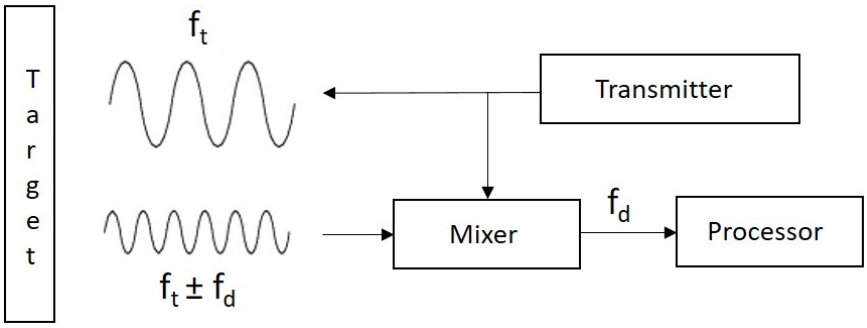

Fig. 3.2 Simple block diagram of a CW Radar

The mixed signal is subsequently sampled and digitally processed through Fast Fourier Transform (FFT) codes [58]. From equation 3.1 follows that the minimum velocity - velocity resolution - that can be measured by a CW radar is function of the wavelength and the minimum detectable Doppler frequency. The latter depends on how the signal received and combined with the transmitted signal is sampled: as the Nyquist sampling theorem suggests, the sampling frequency has to be at least twice that the highest Doppler frequency aimed to measure.

In this work, CW waveforms have been generated, transmitted and received by Vector Network Analyzers (VNA). The VNA is widely used for RF applications and microwave measurements. Among the numerous features provided, the VNA permits to measure the time variation of scattering parameter S_{21}, determined by the magnitude and phase of the ratio between the transmitted and incident voltage signals at two ports of the VNA. The output data are sampled S_{21} parameters, the maximum achievable sampling frequency is determined by the number of data points and the length of the time sweep (τ) which is function of the bandwidth of the filter at intermediate frequencies (IF BW). The IF BW is a crucial setting on modern VNAs: decreasing IF BW will reduce noise floor by filtering out noise that is outside the bandwidth of the digital filter, on the other hand it will increase the time sweep for a given number of data points and therefore, reduce the sampling frequency. For instance the maximum radial velocity (v_r) for the segments of the walking human gait, produced by the arms swing,

is $\pm 3m/s$ and, according to the Nyquist criterion, its measurement would require a sampling frequency f_s which is twice the produced Doppler frequency shift (according to equation 3.1):

$$f_s = 2f_d = \frac{4v_r}{\lambda} \tag{3.2}$$

The sampling frequency required is 3 KHz at 79 GHz and 12 KHz at 300 GHz. In the experimentation an effort had to be made to find the maximum distance at which the noise floor was low enough to permit the measurement of μD produced by a human arms swing.

The traditional method to process CW signals is to apply a Fourier transform to the signal. However, the time variation of the spectrum of signals received from moving targets cannot be interpreted by using classic Fourier transform methods. The most used approach is the Short Time Fourier transform (STFT) [52]. This method (illustrated in Figure 3.3) is straightforward and consists on dividing the signal into time intervals where the target is assumed to be stationary, by multiplication with a window function, and applying the Fourier transform to each of windowed segments separately.

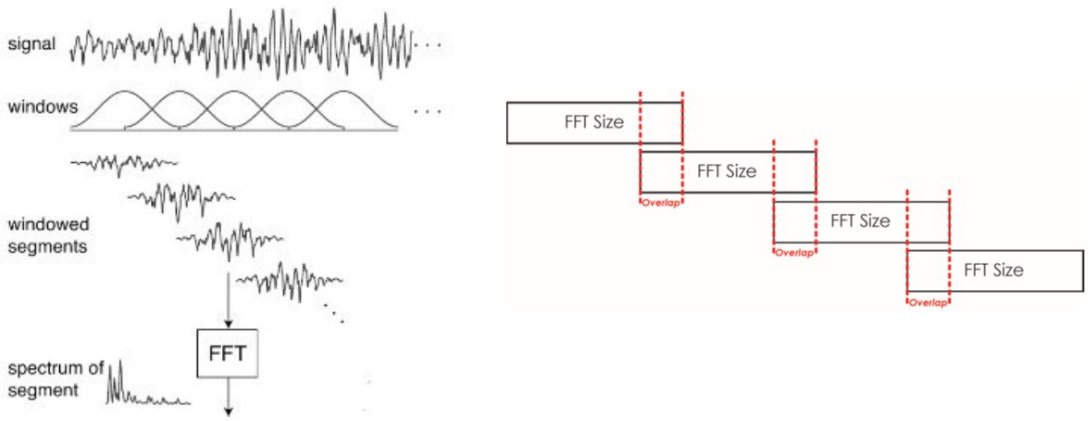

Fig. 3.3 Process of the STFT algorithm [59]

Formally the STFT can be expressed with the equation:

$$STFT(t,f) = \int_{-\infty}^{+\infty} s(\tau)w(\tau - t)e^{-\frac{j2\pi f\tau}{T}}d\tau \tag{3.3}$$

where $w(t)$ is a window function, of length T_w.

The length of the window impacts on the time and frequency resolution, longer windows will increase the frequency resolution, but degrade the time resolution. The window length should be small enough so that the windowed signal is essentially stationary over the window interval and large enough so that the Fourier transform of the windowed signal provides a reasonable frequency resolution. The type of window also affects the time-frequency resolution of the STFT. As shown in Figure 3.4 the rectangular window will produces higher frequency resolution $\Delta\omega$ compared to other windows: $\Delta\omega = 4\pi/T_w$, while for example for a Hamming window $\Delta\omega = 8\pi/T_w$ and for the Blackman $\Delta\omega = 16\pi/T_w$ however, the latter present lower sidelobes, which will degrade the signatures in the spectrogram [60].

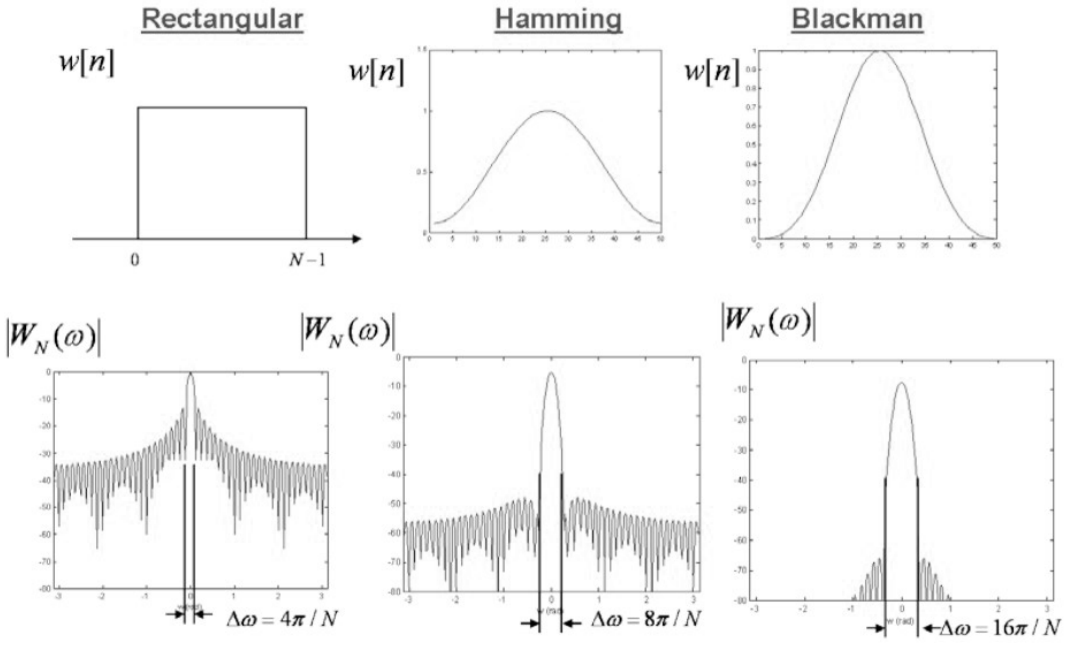

Fig. 3.4 Time domain and frequency spectra for three commonly used time windows [60]

Moreover, in order to avoid the discontinuity caused by the windowing, the window functions are overlapped in time (as shown in Figure 3.3). The STFT is calculated by increasing t with step sized ΔT chosen according to the wanted overlap between the windows. High percentage of overlap between the windows will produce smooth signatures along the time axes, but requires high computation time and memory.

3.2.2 FMCW waveform

FMCW waveforms consist of a CW signal modulated with a periodic signal. In the case of linear modulation the waveform is called chirp, the CW signal can be modulated in frequency by increasing the frequency linearly (up-chirp), decreasing the frequency linearly (down-chirp) or with a triangular wave. In Figure 3.5 it is shown the transmitted FMCW waveform in the case of up-chirp.

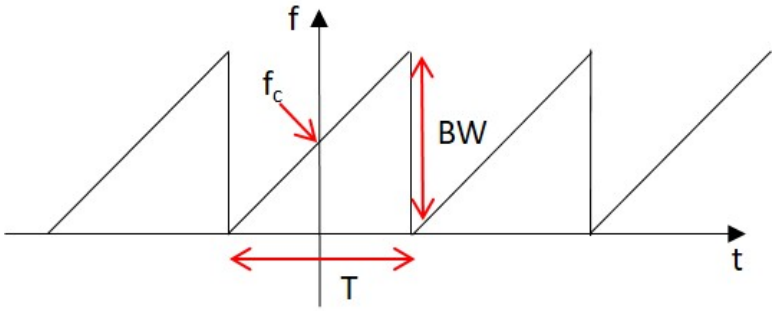

Fig. 3.5 Waveform of a linear FMCW radar

BW is the maximum frequency deviation (bandwidth), A_t the signal amplitude, f_c the carrier frequency, T the chirp duration. Mathematically a single transmitted chirp can be express as:

$$\begin{aligned} s_t(t) &= A_t cos(2\pi f_c t \pm \pi \frac{BW}{T} t^2) \\ t &\in [-\frac{T}{2}, \frac{T}{2}] \end{aligned} \tag{3.4}$$

Where the notation $\pm$ is used to discriminate between up and down chirp. FMCW signals can be processed through matched filter or homodyne detection. A matched filter is a filter with transfer function equal to the conjugated time-reversed version of the transmitted signal, and delayed to ensure causality. In this case the signal is compressed in time and thus it needs to be sampled with fast digitizers. In the heterodyne detection, the signal reflected from a target at range r from the radar is mixed to a replica of the transmitted signal and then low-pass filtered [61]. This process generates a signal which frequency (beat-frequency) is related to the time delay of the signal reflected from the target τ:

$$\tau = \frac{2r}{c} \tag{3.5}$$

To derive the analytical expression on the beat-frequency [62], for simplicity, it will only be considered the case of a transmitted up-chirp with duration T and bandwidth BW. The signal received from the target s_r is a delayed copy of the transmitted signal s_t in equation 3.4:

$$s_r(t) = A_r cos(2\pi f_c(t-\tau) + \pi\frac{BW}{T}(t-\tau)^2) \tag{3.6}$$

Where A_r is the amplitude of the received signal. In the mixing process the transmitted and received signals are multiplied together and, using trigonometric identities, the output of the mixer is the signal s_m:

$$\begin{aligned} s_m(t) = &\frac{A_t A_r}{2} cos(2\pi f_c t + \pi\frac{BW}{T}t^2 - 2\pi f_c(t-\tau) - \pi\frac{BW}{T}t^2(t-\tau)^2) + \\ &+\frac{A_t A_r}{2} cos(2\pi f_c t + \pi\frac{BW}{T}t^2 + 2\pi f_c(t-\tau) + \pi\frac{BW}{T}t^2(t-\tau)^2) \end{aligned} \tag{3.7}$$

The low pass filter removes the second term in equation 3.7, which frequency is about twice f_c, generating the beat signal s_b:

$$s_b(t) = \frac{A_t A_r}{2} cos(2\pi f_c \tau + 2\pi \frac{BW}{T} t\tau - \pi \frac{BW}{T} t^2) \tag{3.8}$$

The beat-frequency is finally calculated by the derivative of the cosine argument:

$$f_b = \frac{1}{2\pi}\frac{d}{dt}(2\pi f_c \tau + 2\pi \frac{BW}{T} t\tau - \pi \frac{BW}{T}\tau^2) = \frac{BW}{T}\tau = \frac{BW}{T}\frac{2r}{c} \tag{3.9}$$

If the target is moving with a radial velocity $\pm v_r$, the range of the target changes over time and can be expressed as:

$$r(t) = r_0 \pm v_r t \tag{3.10}$$

Where r_0 is the initial range to the target. From equation 3.5, the delay τ in this case is $\tau = \frac{2r_0}{c} \pm \frac{2v_r t}{c}$, therefore the beat frequency is calculated as:

$$f_b = \frac{1}{2\pi}\frac{d}{dt}(2\pi f_c(\frac{2r_0}{c} \pm \frac{2v_r t}{c}) + 2\pi \frac{BW}{T} t(\frac{2r_0}{c} \pm \frac{2v_r t}{c}) - \pi \frac{BW}{T}(\frac{2r_0}{c} \pm \frac{2v_r t}{c})^2) \tag{3.11}$$

Thus, after taking the derivative and considering that the target velocity is much less than c, the beat frequency is:

$$f_b = \frac{BW}{T}\frac{2r_0}{c} \pm f_c \frac{2v_r}{c} \tag{3.12}$$

The first component in equation 3.12 depends on the range to the target, and the second component on the Doppler shift. Finally, if N consecutive chirps are transmitted and received an additional term appears in the calculation of f_b because the target is moving

during the n^{th} chirp. The time delay is: $\tau = \frac{2r_0}{c} \pm \frac{2v_r(t+NT)}{c}$ and thus:

$$f_b = \frac{BW}{T}\frac{2r_0}{c} \pm f_c\frac{2v_r}{c} \pm BW\frac{2v_r}{c}N \tag{3.13}$$

Figure 3.6 shows the transmitted and received FMCW waveforms in the case of a single moving target. The beat frequency f_b and time delay τ are indicated.

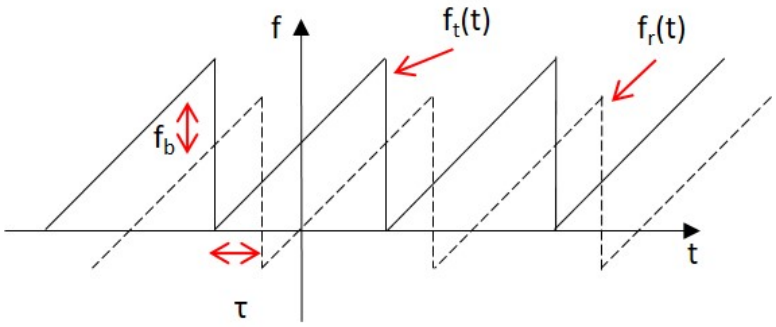

Fig. 3.6 Transmitted and delayed/Doppler shifted received signals

The spectral analysis of the beat-frequency gives the information on range and Doppler characteristics of a target. The processing is based on FFT: a first FFT is applied to a single chirp to extract the range information and a second one to N_c consecutive chirps to process the Doppler information. The accuracy, that it is possible to achieve in the measurement of the range and velocity, depends on the precision of the measure of the f_b. The accuracy of the range measurement is consequence of duration in time in which f_b is constant: $\frac{T}{2} - \tau \approx \frac{T}{2}$, the resolution of the measurement of $\Delta f_b = \frac{2}{T}$ determines the range resolution:

$$\Delta r = \frac{c}{2BW} \tag{3.14}$$

The number of points $M \geq \frac{f_b}{2T}$ of the first FFT, which is direct consequence of the Nyquist sampling theorem, determines the maximum unambiguous range, from 3.8:

$$r_{un} \geq \frac{cM}{4BW} \tag{3.15}$$

At the output of the second FFT there are N discrete samples, if the chirp duration T is such to avoid range/Doppler ambiguity, the maximum unambiguous Doppler shift is within $\geq \frac{1}{2T}$ and thus the Doppler resolution $\frac{1}{N_c T}$ and the velocity resolution:

$$\Delta v = \frac{\lambda}{2N_c T} \tag{3.16}$$

As for CW waveforms the sampling frequency determines the highest measurable velocity, for FMCW, this is determined by the frequency of repetition of consecutive chirps (chirp repetition frequency, CRF).

Finally, if the target is stationary during the duration of a certain number of chirps K, it is possible to increase the signal to noise ratio (SNR) by integration of processed data obtained from measurements with consecutive sweeps. The integration can be coherent, in which case spectra of different measurements are summed using both magnitude and phase and then the range profile obtained taking the absolute value of the summation, or non-coherent, when only the magnitudes of spectra are summed together. Using 3.8 the final range profile obtained in this case can formally, be expressed as:

$$R(r) = \mid \sum_{k=1}^{K} \int_0^T w(t)s(t)e^{j2\pi f \frac{cTf}{2BW}} df \mid^2 \tag{3.17}$$

Where $s(t)$ is the signal after mixing and $w(t)$ a window function used to lower the sidelobes as described in 3.2.1

3.2.3 SFW waveform

A stepped frequency wave (SFW) consist in N successive narrowband pulses transmitted at a fixed pulse repetition frequency (PRF), with fixed length T_s and which frequencies are linearly increased from pulse to pulse with the same increment ΔF (Figure 3.7).

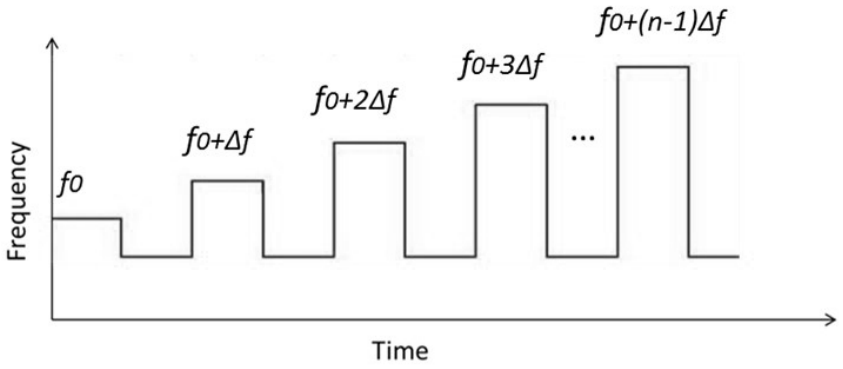

Fig. 3.7 Stepped frequency waveform

The SFW removes the requirements of pulsed waveforms for both wide instantaneous bandwidth and high sampling rates, by sampling near-steady state reflectivities as the target is illuminated at discrete frequencies stepped pulse to pulse [8]. Although the instantaneous bandwidth is narrow, being the inverse of the pulse width, the total bandwidth BW is wide, being N times the frequency step size: $BW = N\Delta F$. As for FMCW waveforms, the range resolution Δr is inverse proportional to the total bandwidth, in this case it is:

$$\Delta r = \frac{c}{2BW} = \frac{c}{2N\Delta F} \tag{3.18}$$

Therefore, the range resolution can be increased by either increasing N or increasing ΔF. The coherent processing interval, the time in which the targets returns are collected and processed coherently, is $CPI = \frac{N}{PRF}$.

As opposed to pulsed waveforms, the pulses within one CPI have different carrier frequencies and the target return from a pulse at a specific frequency is the magnitude of the target reflectivity at that frequency. Therefore, the collection of these samples is a

frequency spectrum and the received signals can be processed by converting frequency domain target reflectivity data to time domain signal using inverse fast Fourier transform (IFFT) and obtain a high range resolution profile (HRRP) of the target. The frequency induced by the phase shift from pulse to pulse (f_p) depends on two components: the rate of change of the carrier frequency and the Doppler shift caused by the target relative motion; if the latter can be neglected during the CPI, the frequency can be expressed as:

$$f_p = PRF\frac{2r}{c}\Delta F \tag{3.19}$$

From 3.19 the maximum range can be derived when the f_p is equal to the PRF:

$$r_{un} = \frac{c}{2\Delta F} \tag{3.20}$$

As for the CW waveforms, in this work SFW have been generated through vector network analysers and the scattering parameters measured in the frequency domain. The output data are S_{21} parameters with one sample for each frequency step which are processed through IFFT codes. The scene range profile can be expressed formally, using 3.5 as:

$$R(r) = \mid \sum_{k=1}^{K} \sum_{f_n=f_s}^{f_e} W(f_n) S_{21}(f_n) e^{j2\pi f_n \frac{2r}{c}} \mid^2 \tag{3.21}$$

Where, f_s and f_e are the start and the end frequencies of the SFW, $W(f)$ is the Fourier transform of a window function used to reduce the sidelobes and the summation refers to the integration of K measurements. In fact, in order to reduce the noise floor, either the IF BW should be reduced, as explained in section 3.2.1, or an integration of multiple measurements should be performed as explained in section 3.2.2. However both methods lead to a significant increase of the acquisition time. Therefore an effort has to been made to choose the optimal IF bandwidth and integration number. For

example a series of tests were made on a Fieldfox Keysight VNA to estimate the acquisition time (sweep time + sweep recovery time + saving time) and noise floor reduction with respect to the reference IF of 10 kHz bandwidth with 1 measurement average. The results, shown in 3.1, suggest that in this case to have a good noise floor reduction of around 20 dB, the best performances in terms of time duration would be to use 3 KHz IF BW and 10 averages. It must be noted that some of the values in the table are not what simple theory might predicts, because of our lack of knowledge of the actual VNA processing.

Table 3.1 Effect of IF BW and averaging on acquisition time and noise floor level respect to the reference IF of 10 kHz

IF BW	Number of coherently integrated measurements	Noise floor reduction (dB)	Acquisition time increase factor
100 Hz	1	19	31
	10	31	316
	20	33	19631
1 KHz	1	9	20
	10	21	24
	20	24	69
3 KHz	1	4	1.5
	10	18	16
	20	21	32

Regarding the Doppler measurements of moving targets, the Doppler resolution is approximately the inverse of the total duration of the waveform and thus the velocity resolution is:

$$\Delta v = \frac{\lambda \Delta F}{2N} \tag{3.22}$$

The range-Doppler resolution product is:

$$\Delta r \Delta v = \frac{\lambda c}{4N^2} \tag{3.23}$$

This shows that in order to improve both resolution, the number of pulses in the waveform can be increased and/or the wavelength can be reduced.

As for FMCW waveforms the highest measurable velocity is determined by the frequency of repetition of consecutive full waveforms (sweep repetition frequency, SRF) and thus by the acquisition time of the S_{21} parameter from the single sweep (sweep repetition interval, SRI). Coming back to the example discussed in the section 3.2.1 on the radial velocity of arms swing, at 79 GHz the SRI should be 330 μs and 83 μs at 300 GHz, but this is far away the capability of modern VNA which acquisition time is mainly dictated by the saving time, not less than 500 μs. Therefore, the method used in this work to measure the μD produced by a walking human is based solely on CW waveforms, and SFW are used for range measurements.

3.2.4 Physical beam mapping

As explained in section 2.6, 2-dimensional images of a scene can be obtained with several methods. All of them aim to develop resolution profiles in both range and cross-range. The method used in this work to obtain the reflectivity map of the scene and the image of road targets is based on physical beamforming. The image is generated by using narrow beam antennas which illuminate a small portion of the scene and scan the scene electronically or mechanically, the radar utilises a FMCW or SFW waveform to generate range profiles that are then placed one after the other in the order they have been collected. The image scanning angle θ is n times the angle subtended by the antennas aperture beam, θ_n, with n the number of positions of the antennas while

scanning. The image can be described by the function:

$$I(r,\theta) = R(r,\theta_1), R(r,\theta_2)...R(r,\theta_n) \tag{3.24}$$

The final image is comprised by a map that shows the backscatter power received by resolution cells, whose dimensions are defined by the range and cross-range resolutions. In the case of this work, the radar antenna rotates to scan the scene and the map assumes the curved form in Figure 3.8, the lines of constant range and cross-range describe respectively a set of radial lines and concentric circular arcs disposed about the radar antenna.

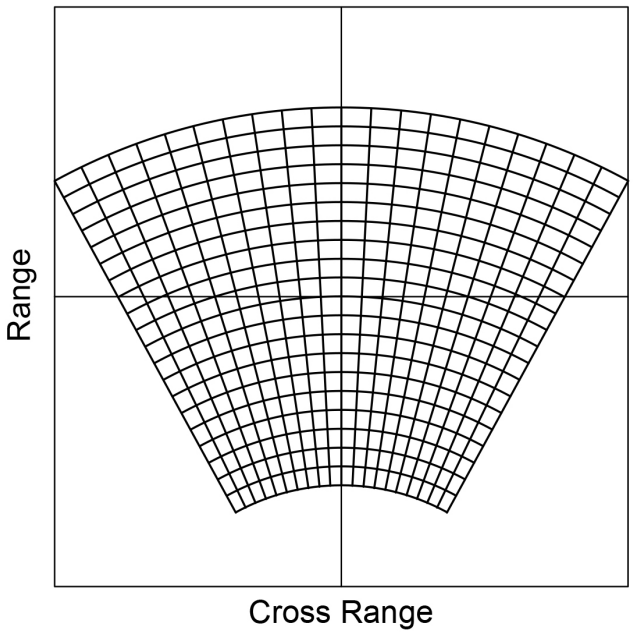

Fig. 3.8 Curved image map from rotating scanning imaging antennas

The range resolution is defined by the waveform of the transmitted signal, while, as shown in Figure 3.9, the resolution achievable in cross-range is directly proportional to the 3dB beamwidth θ^{-3dB} of the radar antennas and can be approximated as:

$$\Delta\theta = r\theta^{-3dB} \tag{3.25}$$

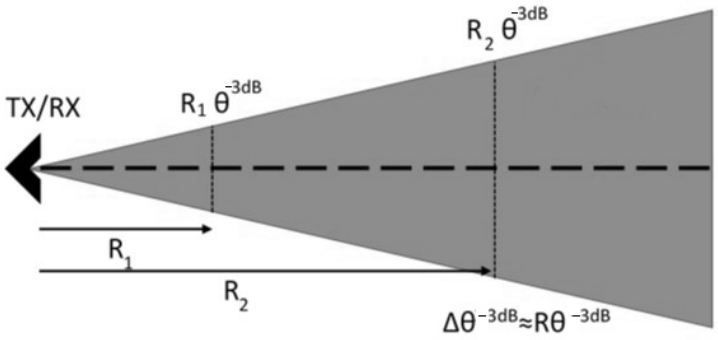

Fig. 3.9 Angular resolution for a monostatic radar

From 3.25 it is clear as the cross-range resolution degrades with the increase of the distance from the radar. This method, in fact, gives good results at short ranges, as for automotive application, but cannot be used to produce images of objects located at ranges further than a few tens of meters. Moreover, the overlap of the antenna beam from measurements at two different angles improves the SNR because the contributions are summed together, however the cross-range resolution is not improved. In order to improve the cross-range resolution several methods are used for long range applications and recently extended for automotive applications based on SAR [48] or Doppler beam sharpening (DBS) [63].

3.3 Characterisation of the atmospheric attenuation in road scenarios

The radar equation [64] provides a measure of the signal to noise ratio (SNR) required to detect a target at a certain range, relatively to the transmitted power, the target RCS and the radar system parameters. In the radar equation in free space in equation 3.26, which symbols meanings are summarized in Table 3.2, it is highlighted the term relative to the atmospheric attenuation.

$$SNR = \left(\frac{P_t G_r G_t \sigma_0 \lambda^2}{(4\pi)^3 r^4 k_b T_0 B_n F_n L_s} \right) \frac{1}{L_{atm}} \tag{3.26}$$

Table 3.2 Symbols in the radar equation

Symbol	Meaning
P_t	Transmitted power
P_r	Received power
G_t	Transmitting antenna gain
G_r	Receiving antenna gain
σ_0	Radar cross section in free space
λ	Wavelength
r	Range
k_b	Boltzmann's constant
T_0	Standard temperature (290K)
B_n	Receiver bandwidth
F_n	Receiver noise figure
L_s	System losses
L_{atm}	Atmospheric losses

Attenuation of radio waves in the earth atmosphere consists of attenuation in atmospheric gases (oxygen and water vapour) and attenuation due to particles of precipitation (such as rain, fog or snow) present in the atmosphere. If the absorption by atmospheric gases has been characterized and summarized in the well known graph in Figure 2.1, attenuation during precipitation, especially in the low-THz band lacks of experimental data. In this work we concentrated in the investigation through experimentation of attenuation of EMW due to rain and snow for ranges typical of automotive scenarios: up to 200 meters.

The method used for experimentation consists in measuring the attenuation by comparing the signal received from a reference target, located at the reference range, in the condition of clear air (absence of precipitation), with the signal received from the same target during the precipitation. The reference signal is measured before and after the rain event and a average received powers calculated, to minimize the influence of humidity and temperature on the measured attenuation. From 3.26 the term on the right in brackets is constant to all the measurements, thus it cancels when calculating the ratio between the received power in the reference measurement and the received power in the precipitation measurement. The measurements are made using FMCW or SFW waveforms. In order to reduce any RCS fluctuation which may arise by the integration of the power received from the range cells occupied by the reference target, a narrow bandwidth is chosen, so as to produce a range resolution big enough to include the entire target in one resolution cell (40 meters).

The measurements needs to be taken simultaneously for all the systems working at the different frequency bands, that are aimed to be compared, to have a precise estimate of the attenuation in the same weather conditions. Moreover, the radar measurements are taken at varying precipitations fall rates and combined with a simultaneous measurement of the precipitations fall rate by a disdrometer (Theis Clima Precipitation Monitor [65]). The disdrometer produces results averaged over an integration time of one minute. The 1-minute integration time is commonly adopted as a standard time interval in propagation

studies. Therefore, the radar measurements results are obtained by averaging the number of chirps (K_{1m}) for which the total length is one minute. The atmospheric attenuation is simply calculated from the maximum magnitude of the target in the range profiles obtained from the reference (R_{ref}) and the precipitation (R_p) measurements:

$$L_{atm} = \frac{\sum_{k=1}^{K_{1m}} R_{ref,k}(r_{ref})}{R_p(r_{ref})} \tag{3.27}$$

Where r_{ref} is the range at which the reference target is located.

The results are presented using scatter plots of the 1-minute attenuation measurements over rainfall rates, and a least mean squares fit to the highest measured attenuation calculated.

3.4 Radar signatures of road actors

There are a number of reasons for the experimental characterization of the signatures of road targets and each has a different influence on the way the measurements are carried out. These are:

- Knowledge of the electromagnetic scattering characteristics of targets
- Acquire diagnostic data
- Acquire information for targets identification
- Build a database
- Develop models for simulators

The primary function of any radar system is target detection. For the development of automotive radars, there is the need to define the maximum range and the SNR required to detect any road target of interest. Therefore, it is fundamental that the knowledge of the reflection characteristics of such objects, like the average value of the backscatter

wave intensity and its fluctuation in range and at different aspect angles. One of the aims of the research is the recognition based on high resolution radar images of road targets, in this sense the collection of diagnostic data means the identification of the main scattering centers of a target and the reconstruction of its sizes. Another method for target identification is based on the extraction of features based on the micro-Doppler signatures, although models of for these signatures are already advanced, measurements to validate such models are essential. The building of database of road target signatures is becoming increasingly necessary, as algorithms for target classification are based on machine learning, which require a huge numbers of data to train their classifiers. Finally, the development of automotive test environment simulators require the generation of virtual radar targets, which reliability can only be possible if based on real targets measurements.

In the next sections, the methodologies to achieve the radar signatures, necessary to fulfill these requirements, will be illustrated.

3.4.1 The radar cross section

The formal definition of radar cross section, as it is used in the radar equation 3.26, assumes that the target scatters electromagnetic energy equally in all directions. Since this is a characteristic of a large metal sphere, the RCS of any target can simply be seen as the the projected area of a large metal sphere that would reflect a wave of the same intensity, therefore it is like that the actual target is replaced by this fictitious sphere [42]. This assumption involves that the target is fully illuminated by the radar antenna's beam, as would be the sphere. Moreover, after the received signal is processed the target should occupy only one resolution cell to appear as a point-like target, as it would be for a sphere. Therefore, in order to measure a target RCS in the traditional way, the radar system should be provided with wide beam antennas and the waveform should have a narrow bandwidth. Moreover, the formal definition of RCS involves a

limiting process in which the distance to the target should tend to infinite [42]. However, this is not the case of automotive scenarios, the RCS signature is intended here to refer more to the methodology of measurements rather then on its strict definition. In static RCS ranges, the distance radar-target is fixed and the footprint of the antenna beam on the target is stationary. Fluctuations of the backscatter signal can arise if the relative position and orientation of the target scattering centers along the LOS change. These fluctuation can exhibit high variation if the aspect angle of the target relative to the radar change even with a fraction of a degree. Therefore, the targets needs to be measured as functions of aspect angle, with the aid of rotating platforms (turntables), and the result are patterns with the amplitude of the echo, usually in the decibel scale, plotted in a polar or Cartesian format versus the azimuth angle (example in Figure 3.10).

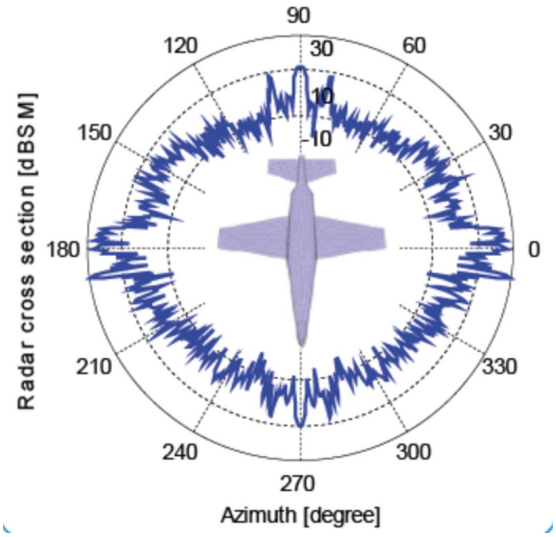

Fig. 3.10 Example of polar plot of the RCS vs azimuth angle of a simulated aircraft [66]

The RCS signature obtained through measurements with wide beam (WB) antennas and narrow bandwidth (NBw) waveforms, for each azimuth angle ϕ is obtained considering the maximum magnitude of the target backscatter in the range profile:

$$\sigma^{uncal}_{WB,NBw}(\phi) = \mid R(r = r_t, \phi) \mid \tag{3.28}$$

Where r_t is the range at which the target is located, that is identified by comparison with a measurement of the background (no target present in the test range).

3.4.2 RCS calibration

In 3.28 the notation *uncal*, for uncalibrated, refers to the fact that the measurement results needs to undergo a calibration process. There are a number of reasons to require a calibration of the target backscatter power, as cited early, one refers to the failure of satisfying the far-field criterion in its strict definition. Moreover, the backscatter intensity is defined by the propagation and attenuation losses as well as system characteristics such as system losses and circuitry mismatch which may be not known a priori, as well as possible uncertainties caused by multipath propagation.

For dynamic test ranges the calibration has to be performed starting from the radar range equation and measuring all the parameters. However, for static ranges it is possible to use a simple calibration by substitution procedure. A measurement of a reference target, with known analytical RCS, is collected with it replacing the target under test. At a fixed frequency the only quantity that varies in the radar equation is the RCS of the target, in fact the wavelength, the antennas gains, range and losses are fixed and can be represented by a single constant. When the reference target is measured, effectively this constant of proportionality is measured and thus the calibration just consists in measuring this constant for all the frequencies of the transmitted waveform. There are some targets which analytical RCS is well known, like metal plates, cylinders, corner reflectors. However the one used in this work is the smooth metal sphere. This is an isotropic target for the monostatic radar so that there is no need for the alignment of the sphere with respect to the antennas. Moreover, according to the Mie's solution the monostatic RCS is constant in the optical scattering region, which is of interest for this work, and only depends of the radius of the sphere as explained in 2.5.1 and it is independent on frequency, thus in this case the only one measurement is required. In

conclusion, the calibrated RCS signature of a target is:

$$\sigma_{WB,NBw}(\phi) = \sigma_{the,sp} \frac{R(r = r_t, \phi)}{\mid R_{sp}(r = r_{sp}, \phi) \mid} \tag{3.29}$$

Where $\sigma_{the}^{sp} = \pi a^2$ is the analytical RCS of a sphere, with radius a, in the optical region and $R_{sp}(r = r_{sp}, \phi)$ the measured reflection from the sphere.

3.4.3 High resolution range profile

The high resolution range profile (HRRP) is obtained, depending on the transmitting waveform used, with eq. 3.17 or 3.21, and gating the whole scene range profile within the regin occupied by the target. HRRP is a one dimensional signature of a target which gives information on the position in range of the most significant scatterers constituting a target (example in Figure 3.11).

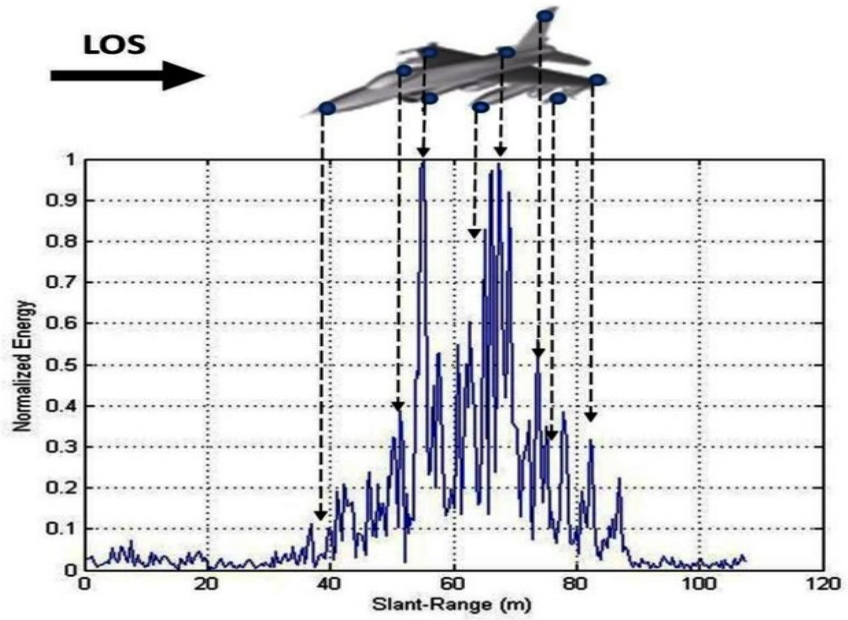

Fig. 3.11 Example of high resolution range profile of a simulated aircraft [67]

These information can be used for automatic target recognition. When a waveform with large bandwidth is used (in this work it is in the order of some GHzs and the range resolution is less than 10 cm), the target is not a point, but a range profile related to the

scatterers distribution. The range profile is comprised of many range resolution cells, each of them still contains the echoes of many scatterers and its complex amplitude is the sum of these scatterers. Now, if the wavelength is small compared to the range cell size, the phase variation caused by changes of aspect, of any of the scatterers present in the resolution cell, will cause a change in the complex amplitude of the cell. Therefore, in order to use HRRP for example for target classification, measurements at different aspect angles with increments as small as possible are required.

The range profiles obtained from measurements of a target placed on a turntable and always in the main lobe of wide beam antennas, at different azimuth angles, $R(r,\phi)$ can be used as a signature of a target. The plot of the range profiles vs azimuth with a color scale proportional to the backscatter signal amplitude (example in Figure 3.12) will produce characteristic signatures for different targets and can be used for classification purposes.

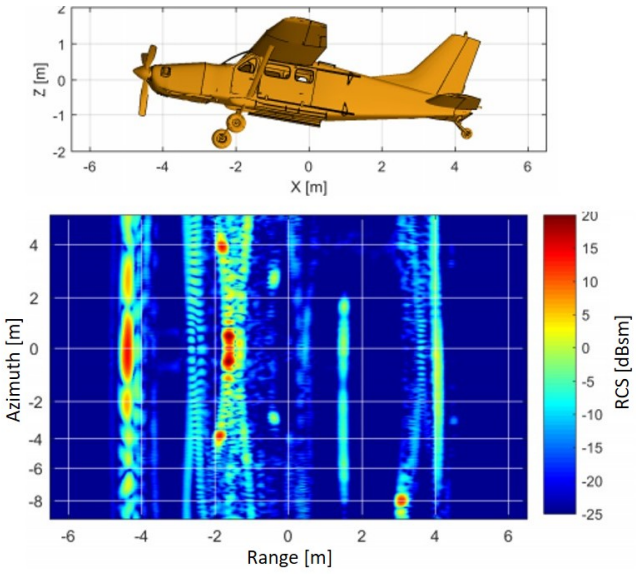

Fig. 3.12 Example of high resolution range vs azimuth profile of a simulated aircraft [68]

Moreover, the range spread at different aspect angles, as the target is rotated, can be used to estimate its dimensions, for instance, it will be shown later in this thesis, how it is possible to reconstruct the contour of a target by using the position of the first

resolution cell occupied by the target in the range profiles. From the range vs azimuth data it is possible to calculate the RCS of the target in two ways, which will lead to similar (not equivalent) results:

- The signal bandwidth can be reduced after the data collection and before the processing, to obtain a range resolution low enough to contain all the target in one range cell. This is achieved by applying to the sampled signal, a bandpass filter centered at the signal center frequency and with the reduced bandwidth. Subsequently the windowed signal is processed through Fourier transform:

$$R(r) = \sum_{m=0}^{M} s(i) W_L e^{-j\frac{2\pi}{M}mr} \tag{3.30}$$

  Where M is the number of samples of the original signal with bandwidth Bw, W_L is the window function centered at $\frac{N}{2}$ and with length $L = M\frac{Bw_1}{Bw}$, being Bw_1 the reduced bandwidth. In this way all the echoes from the target scatterers are summed together and the target appears with on peak in the range profile. The uncalibrated RCS can be calculated using 3.28 and then calibrated with the same procedure used for the narrow band RCS with 3.29.

- The range profile can be integrated within the region that it occupies and the RCS calculated. By comparison with a background measurement, a range gating can be applied to the range profile to isolate the target echoes and integration of the backscatter power from all the cells performed. The integral range profile (R_i) is defined as:

$$R_i(\phi) = \frac{\int_{r_s}^{r_e} R(r,\phi)dr}{r_e - r_s} \tag{3.31}$$

where r_e and r_s are the start and end range resolution cells enclosing the reflection from the target. The calibrated RCS calculated in this way can be expressed as:

$$\sigma_{WB,WBw}(\phi) = \sigma_{the,sp}\frac{R_i(\phi)}{R_{i,sp}(\phi)} \tag{3.32}$$

where $R_{i,sp}(\phi)$ is the integral range profile of the calibration sphere.

3.4.4 High resolution images

High resolution radar images (HRI) (example in Figure 3.13) are obtained with the methodology of the physical beam mapping (section 3.2.4), gating the scene image within the region occupied by the target. HRI have been used as 2D signatures of road targets.

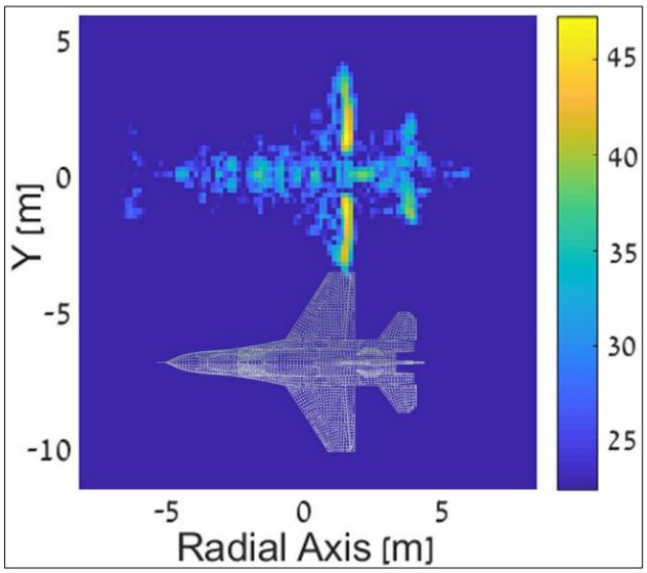

Fig. 3.13 Example of a high resolution radar image of a simulated aircraft at 2.5 GHz with 0.2m range and cross-range resolutions [69]

These signatures are clearly characteristics for each target and are the basis for identification and classification of road objects based on machine learning algorithms [70]. Moreover, they give important information on the sizes and position and identification of the scatterers that contribute the most to the target reflections, information that is es-

sential for developing reliable target models for automotive environment simulators [71]. For both these reason it is important to collect images of targets at different aspect angles. High resolution images have been produced using physical beamforming techniques, and therefore with an FMCW radar transmitting signals with wide bandwidth and scanning narrow beam antennas, and rotating the target in azimuth. As for HRRP data, the RCS of a target can be estimated from imaging data $I(r,\theta,\phi)$, by integrating the range and cross-range profiles, to form the integral image $I_i(\phi)$:

$$I_i(\phi) = \frac{\int_{r_s}^{r_e}\int_{\theta_s}^{\phi_e} I(r,\theta,\phi)drd\theta}{(r_e - r_s)(\theta_e - \theta_s)} \tag{3.33}$$

where θ_s and θ_s are the start and end angular cells enclosing the reflection from the target. Subsequently, the appropriate calibration, with the integral image from the reference target $I_{i,sp}$, is applied:

$$\sigma_{NB,WBw}(\phi) = \sigma_{the,sp}\frac{I_i(\phi)}{I_{i,sp}(\phi)} \tag{3.34}$$

The integration of the image along the range is done with the method illustrated in section 3.4.3. To have a comparison with the RCS estimated from measurements using wide beam antennas, the integration along cross-range is done after a transformation of the curved two-dimensional map described by the scanning narrow beam antennas (see section 3.2.4) into a rectangular coordinate system, which we would have using a wide beam antenna.

As shown in Figure 3.14, in fact, in the far-field region, the wavefront of a wide beam antenna is plane and orthogonal to the radar LOS. The wavefront of the narrow beam antenna is also plane, but as the antenna is rotating the LOS describes a circular wavefront. Therefore, the loci of constant range describe a set of lines orthogonal to the direction of wave propagation for a wide beam antenna. However, using scanning narrow beam the lines of constant range are circular arcs.

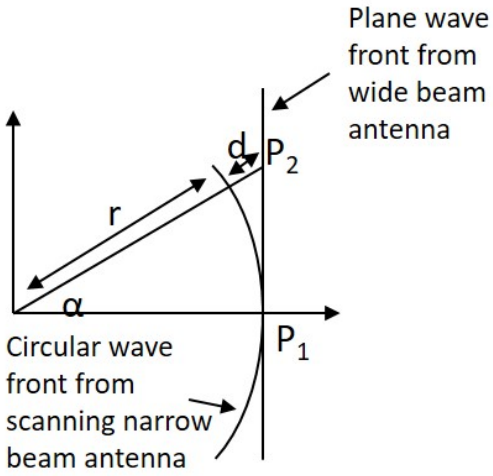

Fig. 3.14 Method used for azimuth integration of narrow band measurements

From the sketch in Figure 3.14, scatterers located in the points P_1 and P_2 are at the same range using wide beam antennas and thus the backscatter signals b_1 and b_2 from these two points are physically integrated in the total backscatter b_{int}; using narrow beam antennas, to achieve the same result, the backscatter from the scatterers at ranges r and $r+d$ are integrated:

$$\begin{aligned} b_{int} = b_1(P_1) + b_2(P_2) = b_1(r) + b_2(r+d) \\ r+d = \frac{r}{cos(\alpha)} \end{aligned} \tag{3.35}$$

where α is the angle subtended by the direction of propagation of the plane wave radiated by the virtual widebeam antenna and the directions of propagation of the narrow beam antenna at each scanning angle.

3.4.5 RCS statistics

As mentioned, one of the objectives for RCS measurements is to determine the detectability of a target. Since the detection is a statistical process, there is a need to build appropriate statistical models for the target fluctuations. The RCS values at different aspect angles, over 360^o, are used to make a histogram which represent their probability

of occurrence, generating a probability density function (PDF), $P(\sigma)$, and the related cumulative distribution function (CDF), which is a measure of the fraction of total data below a given RCS value:

$$CDF(\sigma) = \int_{-\infty}^{\sigma} P(x)dx \tag{3.36}$$

From the PDF and the CDF the following statistics of results measurements have been extracted: the mean, the standard deviation, the median and the dynamic range.

- The mean σ_m is calculated with the classic method of average of a data set: the first statistical moment. It can be calculated using linear or dB values of the RCS:

$$\sigma_m = \frac{\int_0^{2\pi} \sigma P(\sigma)d\sigma}{2\pi} \tag{3.37}$$

  The mean value is useful when comparing the RCS results obtained at different frequency bands and also with those reported in literature.

- The standard deviation σ_{sd} is the simplest measure of fluctuations and is calculated as:

$$\sigma_{sd} = \frac{\sqrt{\int_0^{2\pi} (\sigma - \sigma_m)^2 P(\sigma)d\sigma}}{2\pi} \tag{3.38}$$

- The median is the value of RCS for which the empirical $CDF_e(\sigma) = 0.5$

- The dynamic range is calculated for the CDF between 0.1 and 0.9, to exclude the less probable RCS values, in the following way:

  1. The probability distributions of known statistical models, which are listed in Table 3.3, is build by calculating the parameters from a maximum likelihood estimate of the RCS values fitted against the PDF

Table 3.3 Probability distribution models used to fit the measured RCS data

Model	Probability distribution	Parameters
Swerling 1/2 [72]	$P(\sigma) = \frac{1}{\sigma_m} e^{-\frac{\sigma}{\sigma_m}}$	σ_m
Swerling 3/4 [72]	$P(\sigma) = \frac{4\sigma}{{\sigma_m}^2} e^{-\frac{2\sigma}{\sigma_m}}$	σ_m
Gamma	$P(\sigma) = \frac{\beta^\alpha \sigma^{\alpha-1} e^{-\beta\sigma}}{\Gamma(\alpha)}$	α, β
Weibull	$P(\sigma) = \frac{k_w}{\lambda_w}(\frac{\sigma}{\lambda_w})^{k_w-1} e^{-(\frac{\sigma}{\lambda_w})^k_w}$	k_w, λ_w
Log-normal	$P(\sigma) = \frac{1}{\sigma}\frac{1}{(ln(\sigma))_{sd}\sqrt{2\pi}} e^{-\frac{(\sigma-(ln(\sigma))_m)^2}{2((ln(\sigma))_{sd})^2}}$	$(ln(\sigma))_m$, $(ln(\sigma))_{sd}$

2. The empirical PDF from RCS data $P_e(\sigma)$ is compared with the PDFs obtained for the known statistical models $P_f(\sigma)$, by calculating the error of fit:

$$e_f = \sum_i (\frac{P_e(\sigma) - P_e(\sigma)}{P_m(\sigma)})^2 x100\% \tag{3.39}$$

3. The PDF of the statistical model with the lowest e_f is used to calculate a CDF_f

4. The dynamic range is found for $CDF_f(\sigma) = 0.1$ and $CDF_f(\sigma) = 0.9$

3.4.6 Micro-Doppler signatures

Micro-Doppler (μD) signature of road targets are achieved by processing through STFT backscatter signals from moving targets, obtained by transmitting CW waveforms. The representation of the signal processed through STFT can be made using spectrograms [52]. A spectrogram reveals the variation over time of the spectrum of a time-domain signal $s(t)$ and represents the magnitude squared of the STFT:

$$\mu D(\phi) = |STFT(t, f, \phi)|^2 \tag{3.40}$$

where the dependence with ϕ describes the orientation of motion of the main body of the target in respect to the radar line of sight.

In this work the investigation of μD is mainly focused on human signatures. Human motion, defined as gait, is characterised by different types of movement of individual body parts. During a walking cycle the motion of the individual scatterers comprising the human body is characterised by periodic movements and can be regarded as vibrations [73]. The signal received from a vibrating point scatterer is:

$$s_r = Ae^{j2\pi f_c t + \psi(t)} \tag{3.41}$$

where A is the amplitude of the received signal, f_c the transmitted carrier frequency and the phase $\psi(t)$ can be modelled, considering a vibration with amplitude A_v and frequency f_v, as:

$$\psi(t) = \frac{4\pi A_v}{\lambda} sin(2\pi f_v t) \tag{3.42}$$

thus, the Doppler frequency induced is calculated as:

$$f_d(t) = \frac{1}{2\pi}\frac{d\psi(t)}{dt} = \frac{4\pi}{\lambda} A_v f_v cos(2\pi f_v t) \tag{3.43}$$

From 3.43 it can be concluded that the μD signature in a spectrogram of a vibrating point scatterer is a sinusoidal-like pattern. The final μD signature for the human gait is the linear superposition of the Doppler shifts from all the individual point scatterers and the same period of the sinusoids characterise the gait duration and walking speed and are therefore used as parameters for classification. This behaviour is illustrated by a number of models developed in literature, the most famous, the Boulic-Thalman human model [73] is an empirical model based upon the motion of an average human being. An example spectrogram of the simulated radar return signal for a CW waveform is shown in Figure 3.15.

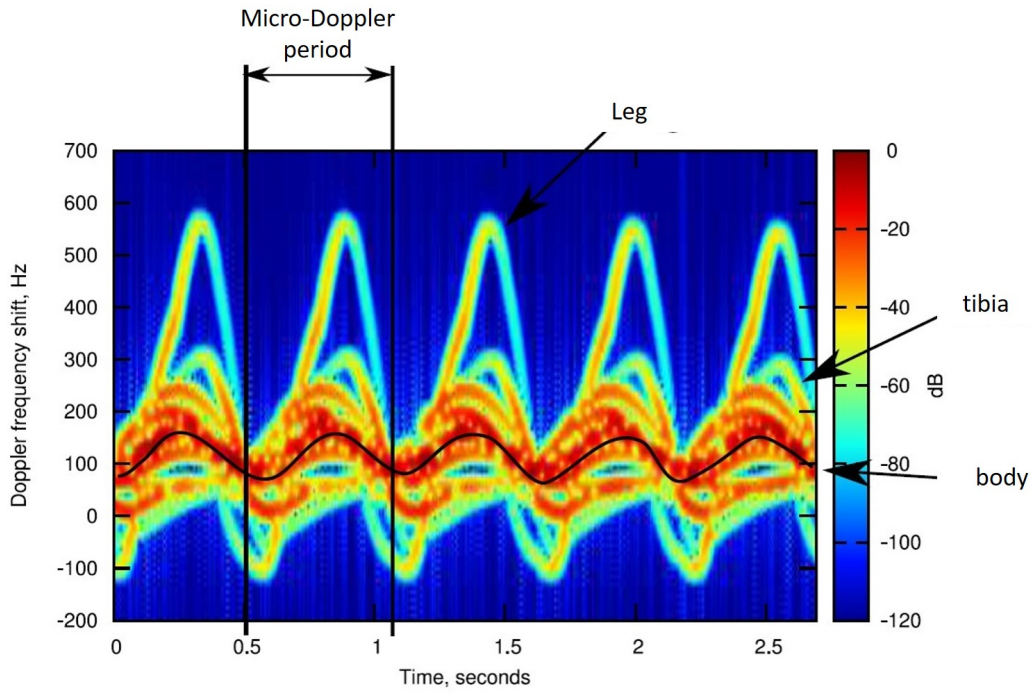

Fig. 3.15 Spectrogram of micro-Doppler signal provoked by walking human [74]

The body parts of the human describe sinusoidal patterns in the spectrogram with the period and different velocities.

3.5 Radar systems

Since there was not specifically designed radar for the doctoral work, the experimental studies were made using different types of available equipment. Two classes of radar systems have been used to collect data necessary to characterize the atmospheric attenuation and road targets at Low-THz frequencies and at the automotive standard frequencies. The first class is based on VNAs, to generate CW and SFW waveforms, with square wide beam or pencil beam horn antennas and frequency up-down converters. The second class is constituted by FMCW radar systems and fan-beam horn antennas. In the following sections the various systems are presented.

3.5.1 CW and SFW radars

Three different VNAs were used to generate CW and SFW waveform, they were chosen depending on the type of measurement. Carrier frequency, sampling frequency and portability were the distinguishing characteristics for the choice of the VNA. CW and SFW radars were used to collect data to produce reflectivity and μD signatures, the antennas used for these measurements were square horn antennas with 10° or 20° 3dB beamwidth in both E and H plane, except for those used for the atmospheric measurements where high gain antennas were needed for longer range operation.

24 GHz CW and SFW radars

The 24GHz radars, used for reference purposes, are based on a VNA at which are directly connected transmitting and receiving square horn antennas with 20° 3dB beamwidth in both E and H plane, with an operational bandwidth from 20 to 25GHz. The antennas are collocated in elevation, and separated horizontally by 15 cm. For the reflectivity measurements a Keysight Fieldfox portable VNA with frequencies ranging from 30 kHz to 26.5 GHz was used thanks to its portability. However, the sampling frequency achievable with this VNA was not high enough to measure the μD produced by a

walking or cycling human, therefore, for these measurements a PNA-X with frequencies ranging from 900 Hz to 120 GHz was used. Figure 3.16 shows photo of the two Fieldfox portable VNA and horn antennas and the key parameters are summarized in Table 3.4.

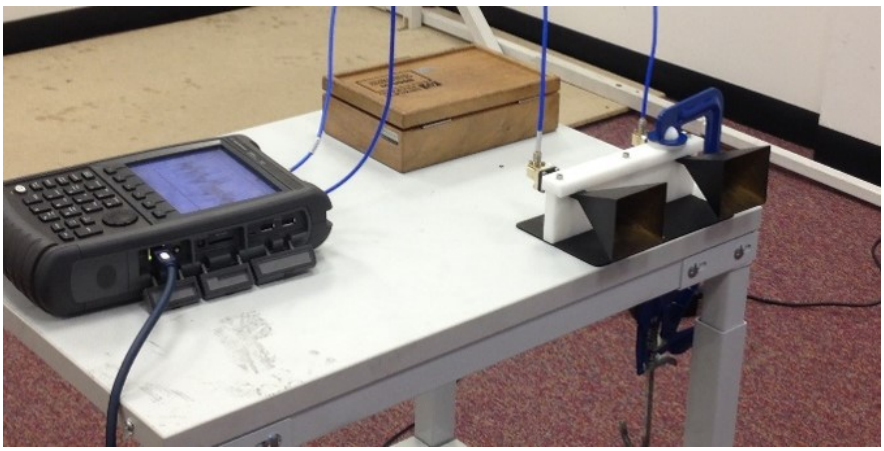

Fig. 3.16 Photo of the SFW 24 GHz radar system

Table 3.4 Parameters of the 24 GHz CW and SFW radars

Parameter	CW	SFW
Network Analyser	PNA-X	Fieldfox
Center frequency, GHz	24	24
Max bandwidth, GHz	0	5
Output power, dBm	10	10
Antennas type	Square horn	Square horn
Antennas 3dB beamwidth (azimuth/elevation),deg	20/20	20/20
Antennas gain, dBi	18	18
IF Bandwidth, KHz	10	1
Sweep repetition frequency, KHz		0.4
Max sampling frequency, KHz	8	

300 GHz CW and SFW radar

The 300GHz CW and SFW radar is based on a Keysight PNA-X which transmits at frequencies up to 20GHz and up and down converters developed by VivaTech Company [75] in collaboration with MISL. Stepped-frequency signals are swept from 10 GHz at the PNA, up converted to 292 GHz and transmitted out by the Tx antenna. The reflected signal is received by the identical Rx antenna, converted back down to 10 GHz band by a down-converter and recorded at PNA. The converters and the PNA are synchronised by a 10 MHz rubidium frequency standard reference. Square horn antennas with 10° 3dB beamwidth in both E and H plane were used for the reflectivity and μD measurements. For the atmospheric measurements pencil beam antennas were used because of its high gain, which was needed to illuminate a target at 200m range. In both configurations, the converters are placed in a quasi-monostatic configuration, as shown in the photo of the system in Figure 3.17. Figure 3.18 shows an outline of the system and in Table 3.5 the parameters of the system are summarized.

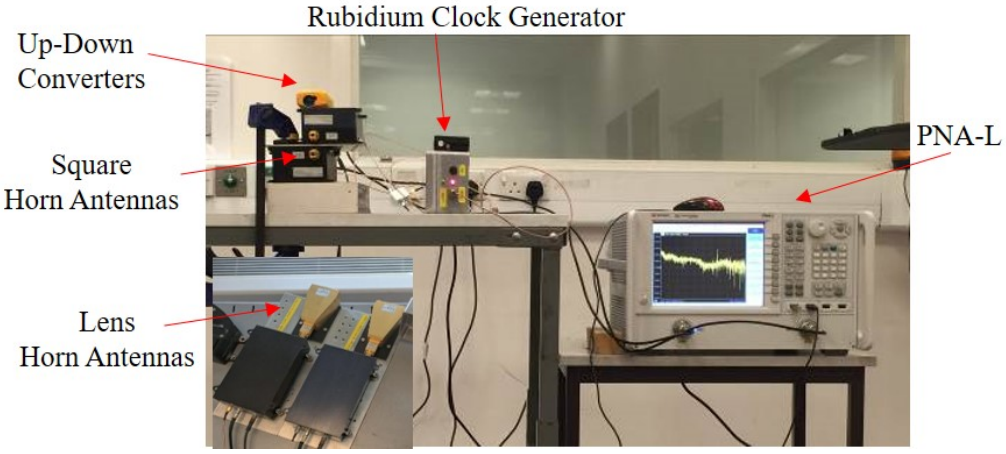

Fig. 3.17 Photo of the CW and SFW 300 GHz radar system

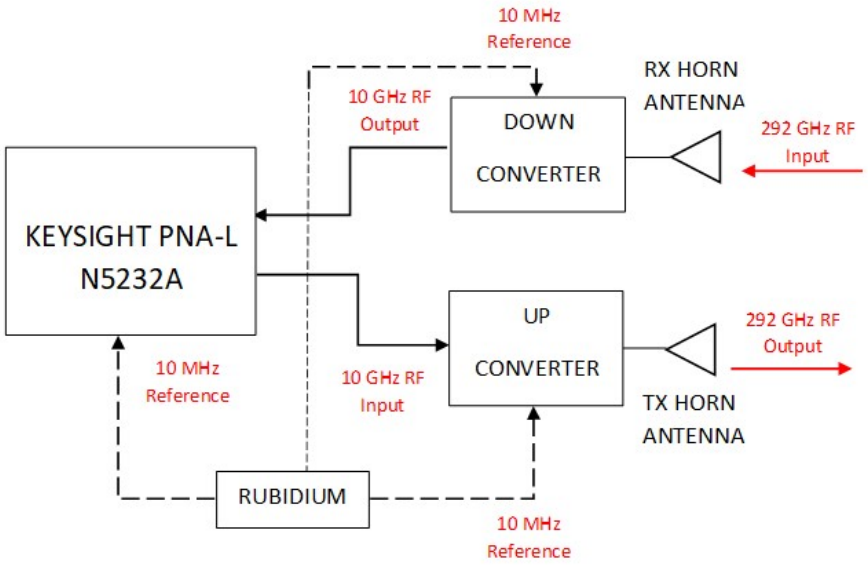

Fig. 3.18 Outline the CW and SFW 300 GHz radar system

Table 3.5 Parameters of the 300 GHz CW and SFW radar

Parameter	CW	SFW
Center Frequency, GHz	292	292
Max bandwidth, GHz	0	16
Output power, dBm	-17	-17
Antennas type	Square horn	Square horn Pencil beam
Antennas 3dB beamwidth (azimuth/elevation),deg	10/10	10/10 1.6/1.2
Antennas gain dBi	24	24 30
IF Bandwidth, KHz	10	1
Receiver noise figure, dB	14	14
Sweep repetition frequency, kHz		0.8
Sampling frequency, KHz	8	

3.5.2 FMCW radars

Four FMCW radars were used in the experiments. A 77GHz Off-the-shelf radar, developed by Celsius Tech, was used for collecting data for the atmospheric attenuation measurements, due do its long range operation. A 150GHz radar with wide beam antennas was used for the targets reflectivity measurements. Two systems at 79 and 300 GHz with scanning imaging antennas were used to collect data to produce high resolution images of vehicles. The 79, 150 and 300GHz systems have been developed at MISL (University of Bimingham) in collaboration with ELVA [76].

77 GHz FMCW radar

The Frequency Modulated Continuous Wave (FMCW) radar operating at 77 GHz has 300MHz operational bandwidth, 10dBm output power and Offset Cassegrain twist reflect antennas with 36dBi gain [77]. A photo of the radar is shown in Figure 3.19. Parameters of the radar are reported in Table 3.6.

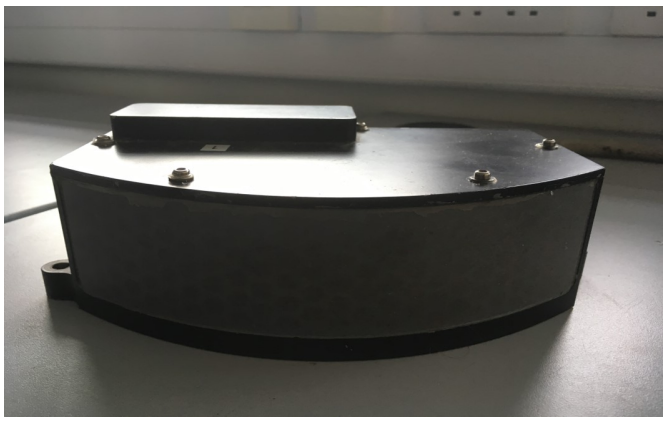

Fig. 3.19 Photo of the FMCW 77 GHz radar

Table 3.6 Parameters of the 77 GHz FMCW radar

Parameter	FMCW
Center frequency, GHz	77
Max bandwidth, GHz	0.3
Output power, dBm	10
Antenna type	Offset Cassegrain twist reflect
Antennas 3dB beamwidth (azimuth/elevation),deg	1.8/8
Antennas gain, dBi	36

150 GHz FMCW radar

The 150GHz FMCW radar has an operational bandwidth of 5GHz (76-81 GHz) and output power of 11dBm. This radar was used for RCS and HRRP measurements of road targets, therefore the antennas used were square horn with 10° by 10° 3dB beamwidth both in azimuth and elevation, Figure 3.20 shows how the antennas are collocated in azimuth. The block diagram illustrated in Figure 3.21 is similar to the one of the 79GHz radar. In this case a 7.5GHz signal is up-converted to 150GHz through the use of a multiplier with factor of 20 and the received echo is mixed with the transmitted signal through an IQ mixer and sampled with the use of a picoscope [78]. Table 3.7 summarize the main parameters of the radar.

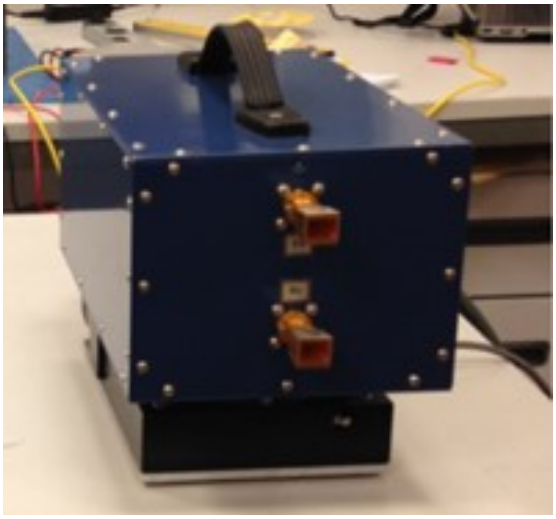

Fig. 3.20 Photo of the FMCW 150 GHz radar

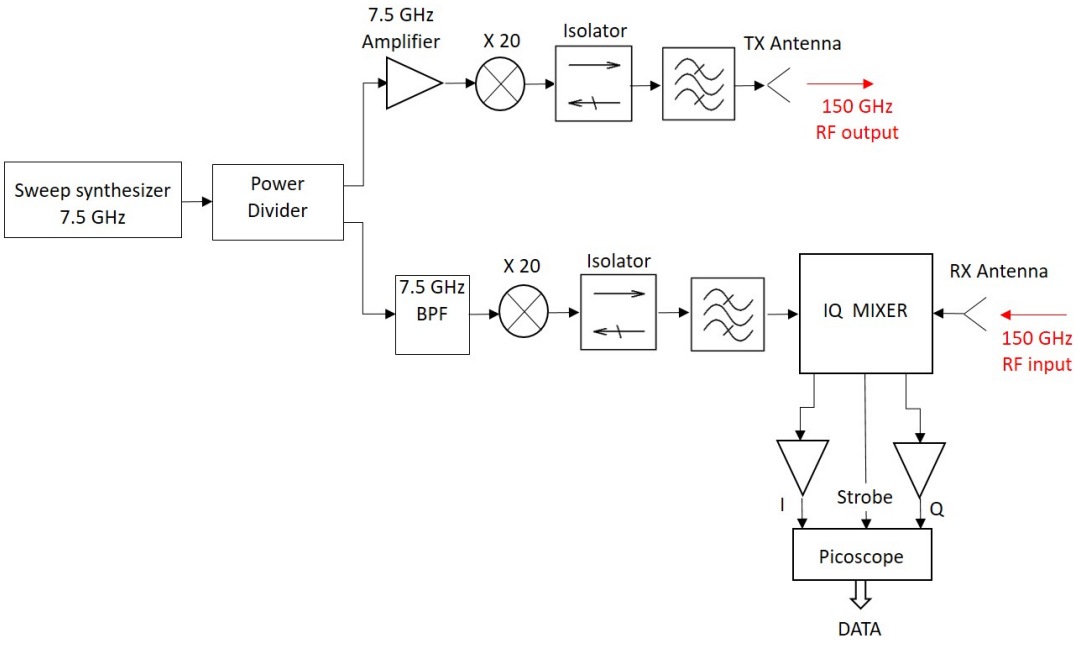

Fig. 3.21 Outline of the FMCW 150 GHz radar

Table 3.7 Parameters of the 150 GHz FMCW radar

Parameter	FMCW
Center frequency, GHz	147.5
Max bandwidth, GHz	5
Output power, dBm	11
Antennas type	Square horn
Antennas 3dB beamwidth (azimuth/elevation),deg	10/10
Antennas gain, dBi	24
Receiver noise figure, dB	11
Sweep time, ms	1.2
Sweep repetition interval, ms	11.8

79 GHz FMCW radar

The 79GHz FMCW radar has an operational bandwidth of 5GHz (76-81 GHz) and output power of 15dBm. The antennas, used to obtain images of vehicles, are rectangular horn antennas with narrow beamwidth in azimuth and relative wide beam in elevation. As shown in the block diagram in Figure 3.22 a 13GHz signal is up-converted to 79GHz through the use of a multiplier and the received signal from the target, mixed with transmitted signal through an IQ mixer, is sampled with the use of a picoscope [78]. Table 3.8 outlines the main parameters of the system.

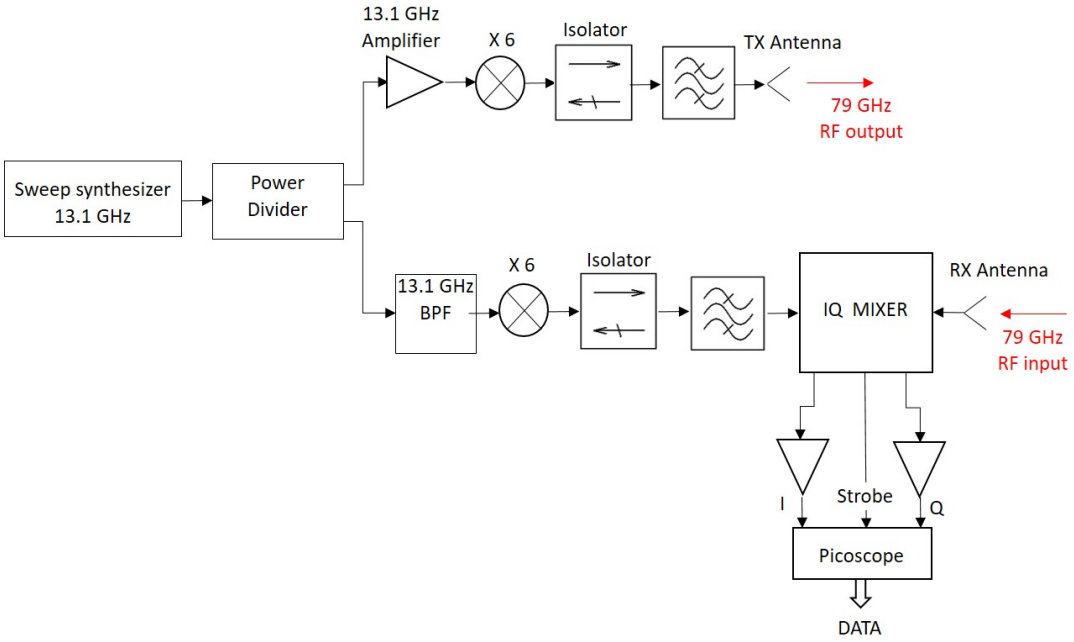

Fig. 3.22 Outline of the FMCW 79 GHz radar

Table 3.8 Parameters of the 79 GHz FMCW radar

Parameter	FMCW
Center frequency, GHz	78.5
Max bandwidth, GHz	5
Output power, dBm	15
Antennas type	Rectangular horn
Antennas 3dB beamwidth (azimuth/elevation),deg	1/7
Antennas gain, dBi	29
Receiver noise figure, dB	10
Sweep time, ms	1
Sweep repetition interval, ms	4.3

300 GHz FMCW radar

The 300GHz FMCW radar was used to produce high resolution images of vehicles. It can provide a high bandwidth, up to 20GHz, which a range resolution up to 7.5mm. However the transmitted power is less than the other imaging system (79GHz), providing, therefore, smaller dynamic range. Rectangular horn antennas with 1° in azimuth and 7° in elevation supply the fine azimuth resolution required to produce high resolution images. The block diagram of the radar is shown in Figure 3.23, in this case a 7.5GHz signal is firstly up-converted to 150GHz with a multiplier with a factor of 20 and a second up-conversion is performed with a doubler. The received echo at 300GHz is mixed with the signal at 150GHz obtained after the first up-converter, through a second harmonic mixer. The output from the mixer is finally sampled with a picoscope. Table 3.9 outlines the main parameters of the system.

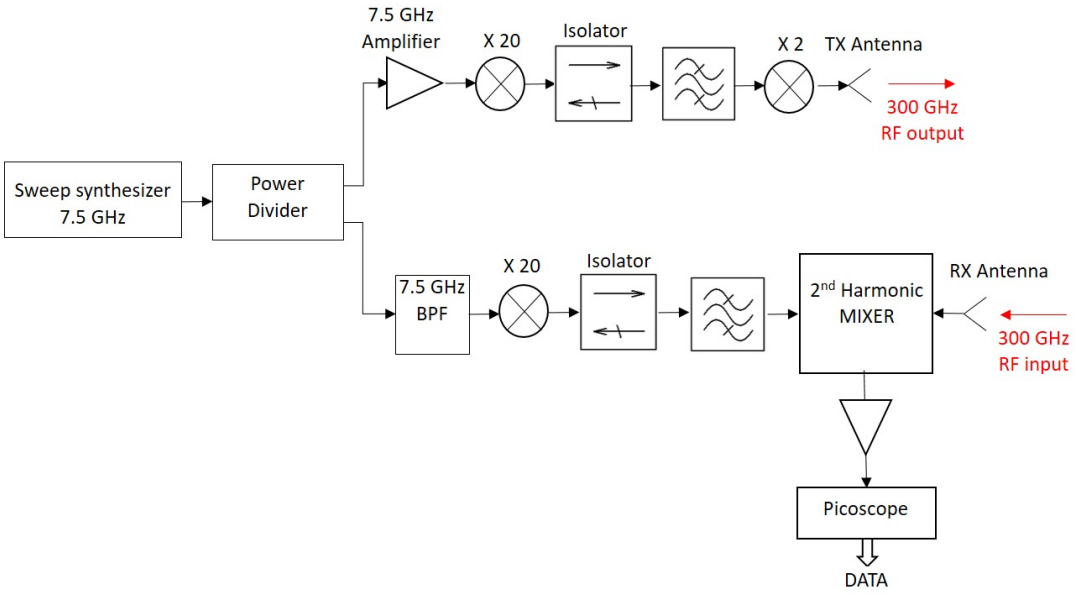

Fig. 3.23 Outline of the FMCW 300 GHz radar

Table 3.9 Parameters of the 300 GHz FMCW radar

Parameter	FMCW
Center frequency, GHz	292
Max bandwidth, GHz	20
Output power, dBm	-3
Antennas type	Rectangular horn
Antennas 3dB beamwidth (azimuth/elevation),deg	1/7
Antennas gain, dBi	30
Receiver noise figure, dB	15
Sweep time, ms	1
Sweep repetition interval, ms	4.3

Figure 3.24 shows a photo of the 79 GHz and 300 GHz FMCW radars mounted through a metallic frame on a rotating platform to scan simultaneously the scene.

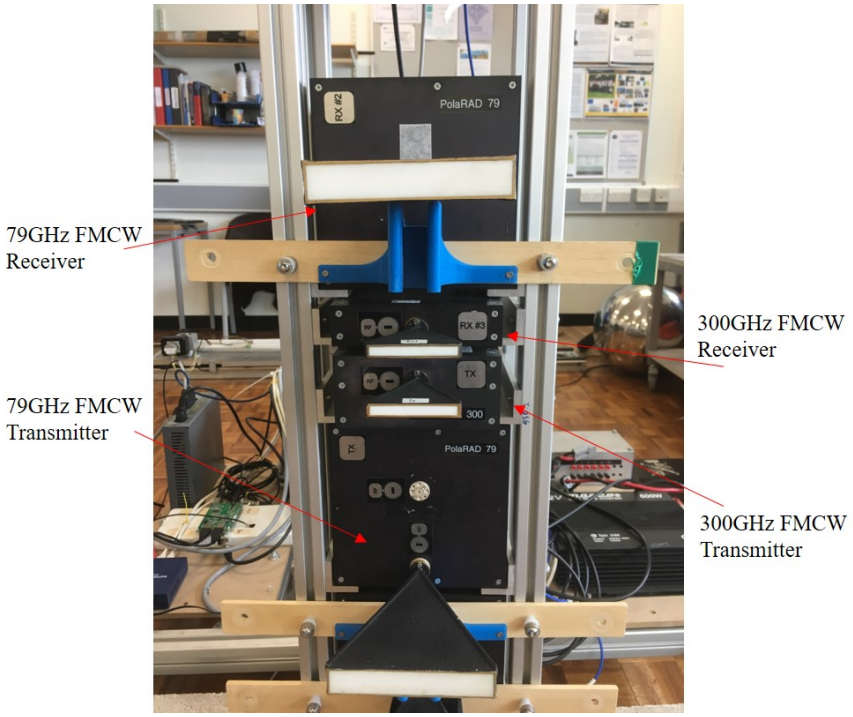

Fig. 3.24 Photo of the FMCW 79 GHz and 300 GHz radar system

3.6 Experimental sites

The first objective of this work is the characterization of the performances of low-THz sensors in terms of propagation and scattering in an automotive environment. Therefore, experimentation carried out in practical outdoor scenarios are essential, as well as characterization of a practical road environment. However, in particular regarding RCS measurements, characterization of targets in a clutter-free environment and without any interaction with the test range, where possible, is desirable, hence the need for measurements in anechoic chambers. In the next sections, the test ranges used for experimentation are described and characterized.

3.6.1 Site for atmospheric attenuation measurements

For the measurements of atmospheric attenuation in presence of rain and snow, the radars, in monostatic configuration, are placed at an open window in the fifth floor of the Gisbert Kapp building at the University of Birmingham. Wetness or snow accumulated on the radome results in reducing transmissivity due to reflection and absorption by the water on the radome, as explained in [79]. Therefore, to evaluate the attenuation caused solely by the rain precipitation, the radars are set 0.5 m inside the open lab window and kept dry at all times with no radome present.

The reference target is a nearby high rise building (Muirhead tower), used because of its large RCS. The Muirhead tower is a 16-storey building with a height of approximately 195m above mean sea level and the radar is placed approximately 160m above mean sea level. All the radar antennas are aligned to be at the same LOS to the reference target and are placed approximately 25m above the local ground level to render negligible any ground reflections or scattering due to the ground cover or low lying buildings present between the LOS. This setup gives a unobstructed two-way path length of 320m between the antennas and target with only rain or snowfall across the antenna beams. The radars used in the measurements are the 77GHz FMCW radar 3.5.2 and the 300GHz

SFW radar with pencil beam antennas 3.5.1, for both radar the SBR of the reflection from the Muirhead tower was over 30dB.

An aerial image showing the location of the radars and the target is shown in Figure 3.25.

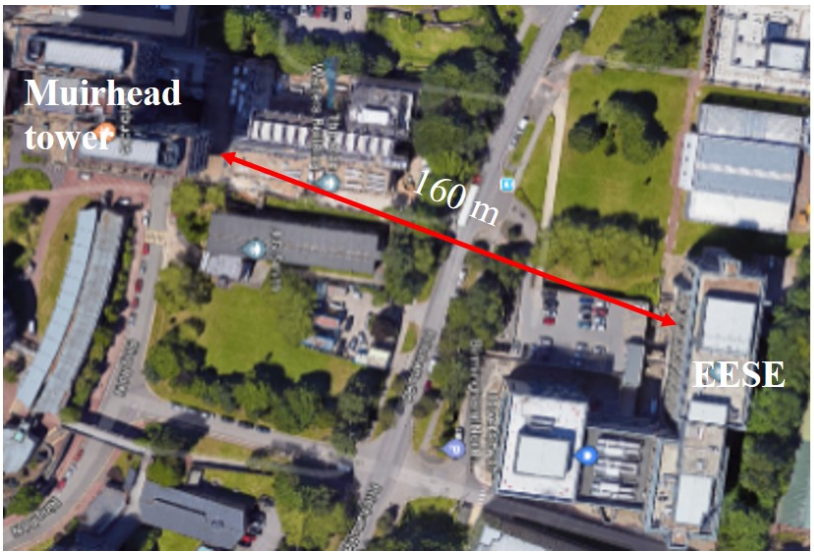

Fig. 3.25 Photo showing the location of radar and reference target (Google maps)

Photos of the reference target (Muirhead tower) taken during a snowfall event and of the disdrometer used to measure the precipitation fall rates are shown in Figure 3.26.

(a)

(b)

Fig. 3.26 Photo of the reference target (a) and disdrometer (b) used for attenuation measurements

3.6.2 Indoor test range

Part of the RCS measurements and the μD experiments have been performed in a controlled indoor environment, a room with $3x7.5x2.5m^3$ (width x length x height) of open space. In order to reduce any multipath reflection, the targets have been placed in an 'anechoic' space where Persian high-pile woollen rugs are used as low-THz wave absorbers, as demonstrated in [80], such carpets exhibit high absorption for EMW in the low-THz band. A photo of the facility is shown in Figure 3.27.

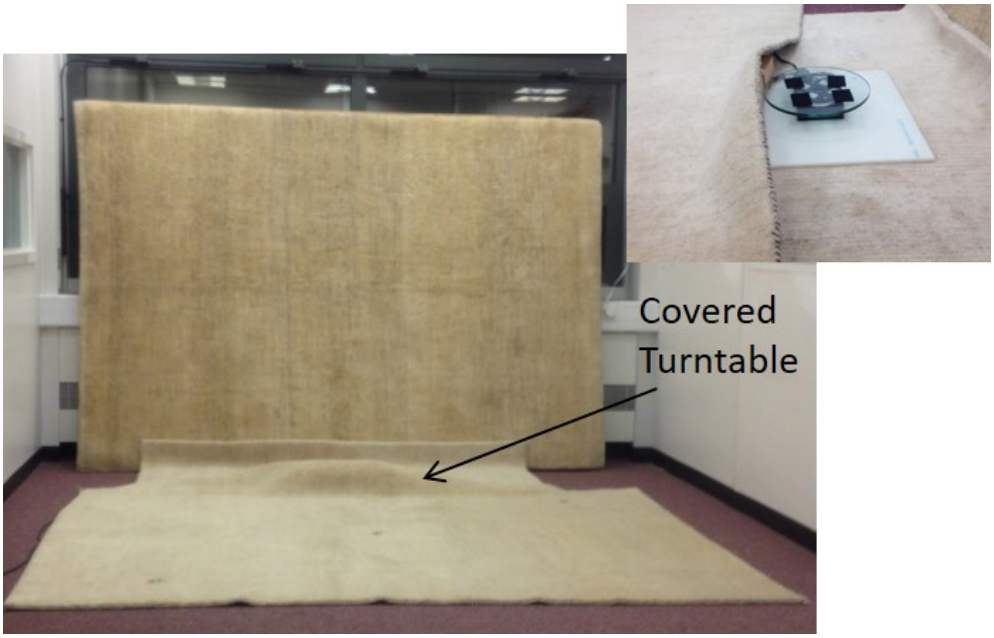

Fig. 3.27 Indoor test range

As mentioned before, one of the objectives of the RCS measurements is to look at the fluctuations of RCS at different aspect angles. Thus the targets are placed on a computer-controlled turntable to acquire backscatter data at 360 orientations of the object, with respect to the radar, without changing the experimental setup. Depending on the frequency band of the measurements, absorbers are placed in front of the turntable to avoid reflections from it, as shown in Figure 3.27. The rotation of the turntable and the data acquisition are controlled by a software written in Matlab. After initialisation,

the code enters in a loop in which the angular position is set, the radar acquisition starts and the backscatter data are streamed to a hard disk.

A square horn antennas with a 3dB beamwidth of 10° produce a footprint of 1.3m at a range of 7m from the radar, thus in order to ensure the condition of beam filling, measurements with wide beam antennas were possible for all the targets whose dimensions do not exceed 1.3m. Moreover, to avoid reflections from the ground before the target is reached by the antennas main beam, the height of the antennas above the ground has to be adjusted to have the radar LOS (line of sight) in the direction of the middle height of the target, as shown in the sketch in Figure 3.28.

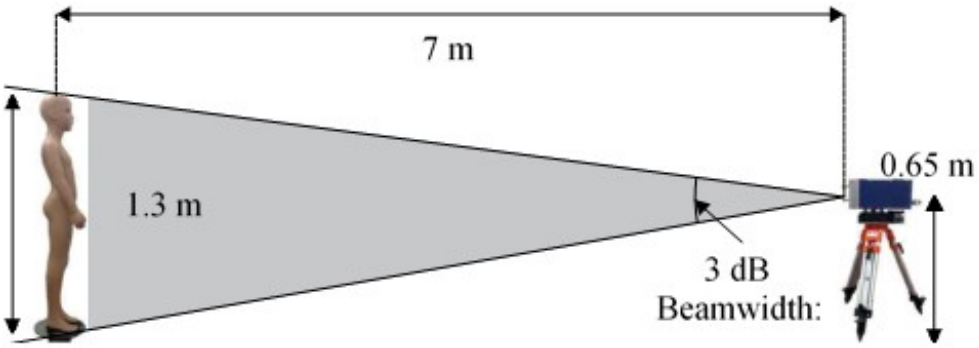

Fig. 3.28 Sketch showing the illumination of a 10°x10° beamwidth antenna on a target

3.6.3 Real road test range

When it is not possible to perform indoor measurements of RCS because of the sizes of the target under test, we need to measure the target outdoor. This is the case of the measurement on cars carried out in this work. These measurements were taken in a paved carpark, which is shown in the photo in Figure 3.29.

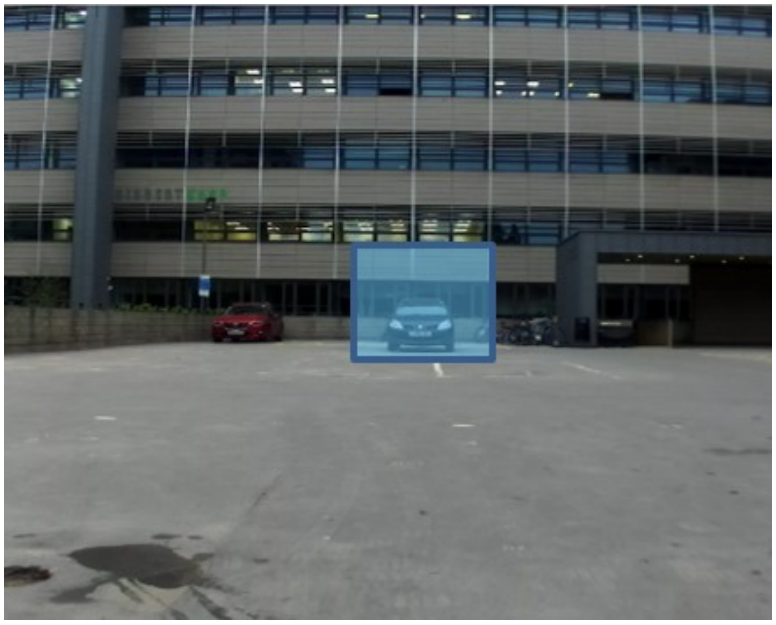

Fig. 3.29 Photo of the outdoor test range used for RCS measurements of cars

The distance between radars and target is 22 meters, to assure the complete illumination by the main beam of a 10° square horn antenna. In Figure 3.30 a sketch one of the experimental setups is shown.

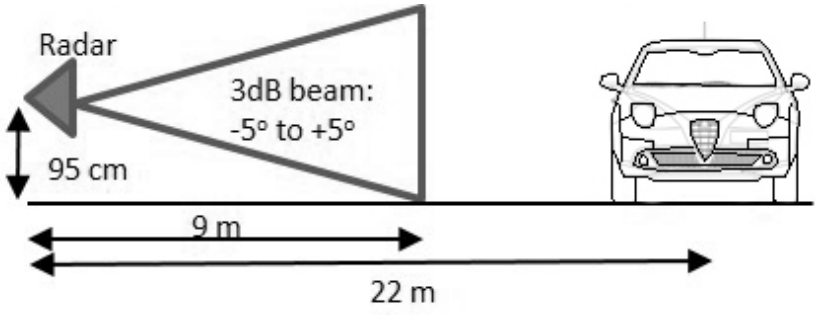

Fig. 3.30 Sketch of the experimental setup used for RCS measurements of cars

The height of the radar antennas above the ground, 0.9m, is chosen to be in LOS with the middle height of the car. With this configuration it is not possible to avoid that the radar antennas beam hits the ground before reaching the target. The ground represents the most pervasive electromagnetic feature of outdoor ranges and cannot be eliminated, so its influence on target reflectivity has to be analysed and taken into account in the design of radar systems for target detection in real road scenarios. In the

next section, a model of multipath generated by a paved ground is developed and the influence of frequency of the transmitted waveform on target reflectivity analysed.

3.7 Effect of the road ground plane on target reflectivity

In presence of a ground plane the target is illuminated by two waves, one which propagates directly from the transmitting antenna and one arriving from the reflection of the ground. The energy reflected from the target propagates back to the receiving antenna via the same paths. Thus, as shown in Figure 3.31 (a), the ground reflected ray generates an interference pattern due to the phase change given by the different lengths of the direct (D) and indirect (I) paths, which are the source of four possible roundtrip propagation paths as indicated in Figure 3.31 (b).

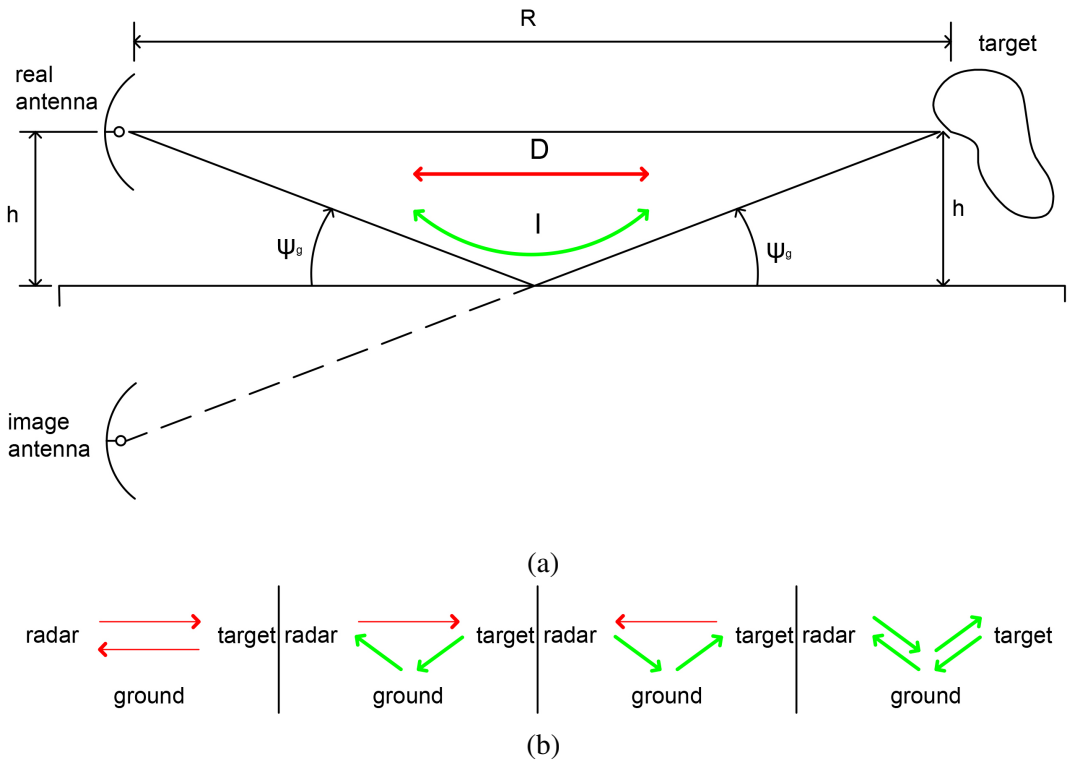

Fig. 3.31 Geometry for 4-ray path model (a) and possible wave roundtrips (b)

The radar equation in 3.26 can be rewritten taking into account the interference pattern by including a propagation factor (F_p) by multiplying it by the target RCS in a free space environment:

$$P_r = \left(\frac{P_t G_r G_t \lambda^2}{(4\pi)^3 R_{max}^4 k T_0 F_n L_s L_{atm}} \right) \left(\sigma_0 F_p^4 \right) \tag{3.44}$$

For automotive application, the interference pattern can be just considered for a vertical plane along the LOS and for simplicity it can be assumed that the transmitting and receiving antennas have identical radiation pattern and subtend a negligible bistatic angle at the target.

In this circumstance and using the geometry in Figure 3.31 (a), the propagation factor is identical in transmission and reflection and it is defined as the amplitude ratio between the signal in free space and the signal in presence of the ground: [22]:

$$F = \mid \frac{S_D + S_I}{S_D} \mid = \mid 1 + \Gamma e^{j\Delta\delta} \mid \tag{3.45}$$

where Γ is the reflection coefficient of the ground and $\Delta\delta$ is the phase difference between direct and direct paths, from the geometry taken into account:

$$\Delta\delta = \frac{2\pi}{\lambda}(I - D) = \frac{2\pi}{\lambda} \left(\sqrt{d^2 + (2h)^2} - d \right) \tag{3.46}$$

The propagation factor in the radar equation 3.44 is raised to the fourth power because it combines two identical factors for transmission and reflection and each of them is squared to form a power ratio.

The reflection coefficient can be decomposed to take into account the electrical properties (Γ_g) and the roughness of the (Γ_r) of the ground. The derivation of the reflection coefficient here is made under the conditions that the interface between the two media is infinite, the ground is perfectly flat and the incidence wave is plane. Although this conditions are ideal, they may be deemed acceptable for short range automotive

radars as the antennas beam footprint on the ground is usually relatively small. Moreover in the calculations, a practical case is considered by including the roughness of the asphalt, which is a key parameter to compare the effect of the multipath, generated by the ground plane, on targets reflectivities, measured at Low-THz frequencies and at lower frequencies

Γ_g depends on transmitted wave polarization, antennas grazing angle (ψ_g) and indirectly on frequency through the surface relative permittivity (ε_r). Γ_g is approximated using the Fresnel reflection coefficient derived for an interface between free space and a paved surface, considering a horizontal polarization:

$$\Gamma_g = \frac{sin\psi_g - \sqrt{\varepsilon_r - (cos\psi_g)^2}}{sin\psi_g + \sqrt{\varepsilon_r - (cos\psi_g)^2}} \tag{3.47}$$

Γ_r, defined as surface roughness reflection coefficient is an empirical parameter which depends on the grazing angle, the root mean square surface height irregularity and frequency [53]:

$$\begin{aligned} \Gamma_r &= e^{-z} I_0(z) \\ z &= 2\left(\frac{2\pi h_{rms} sin\psi_g}{\lambda}\right)^2 \end{aligned} \tag{3.48}$$

where I_0 is the modified Bessel function of zero order.

Defined $\sigma_g = \sigma_0 F_p^4$ the the measured reflectivity of the target in presence of ground plane the amplitude of the interference pattern can be expressed as:

$$\frac{\sigma_g}{\sigma_0} = F_p^4 = \mid 1 + \Gamma_g \Gamma_r e^{j\Delta\delta} \mid^4 \tag{3.49}$$

Results of simulations for the model described by 3.49 are now illustrated for the measurement setup carried out in this work, described in the previous section, the parameters in 3.46 , 3.47 and 3.48 for this particular scenario are summarised in Table 3.10.

Table 3.10 Parameters of the 4-ray path propagation model

Parameter	Symbol	Value
Antennas height above the ground	h	$0.9m$
Target distance	d	$22m$
Asphalt permittivity	ε_r	3.18 [81]
Asphalt rms surface height irregularity	h_{rms}	$0.5mm$
Grazing angle	Ψ_g	5°

Plots of the amplitude of the interference pattern versus range using the free-space and the 4-ray path propagation model, at 79 GHz and 300 GHz, are shown in Figure 3.32.

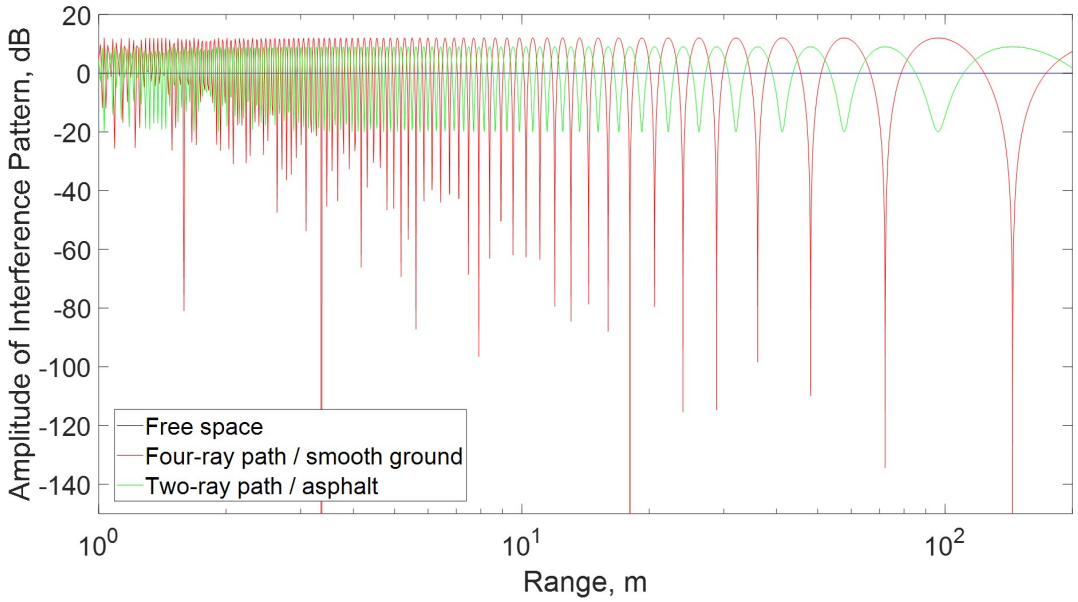

(a)

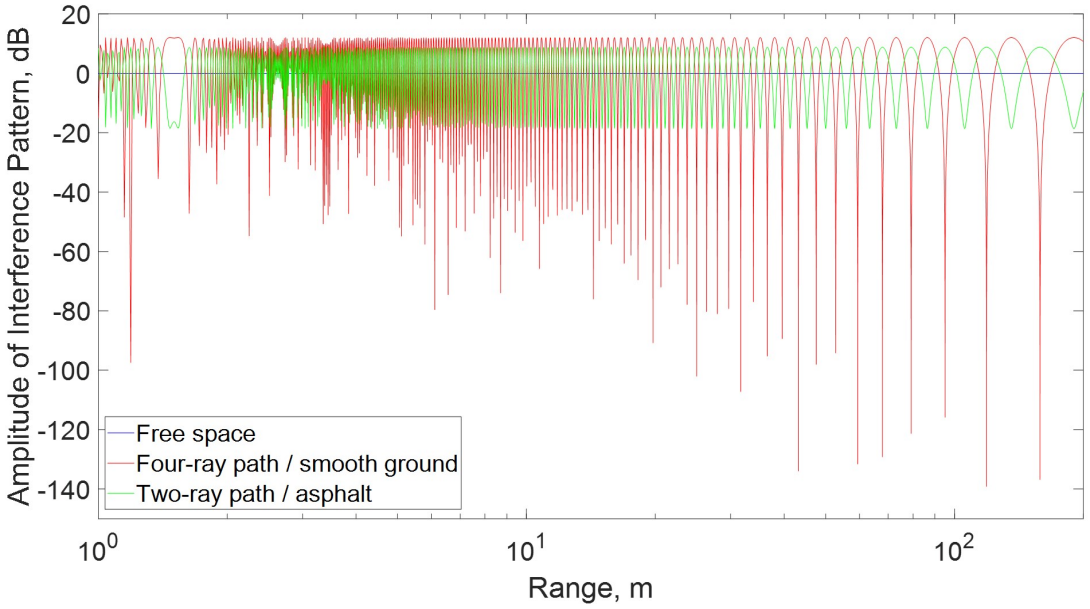

(b)

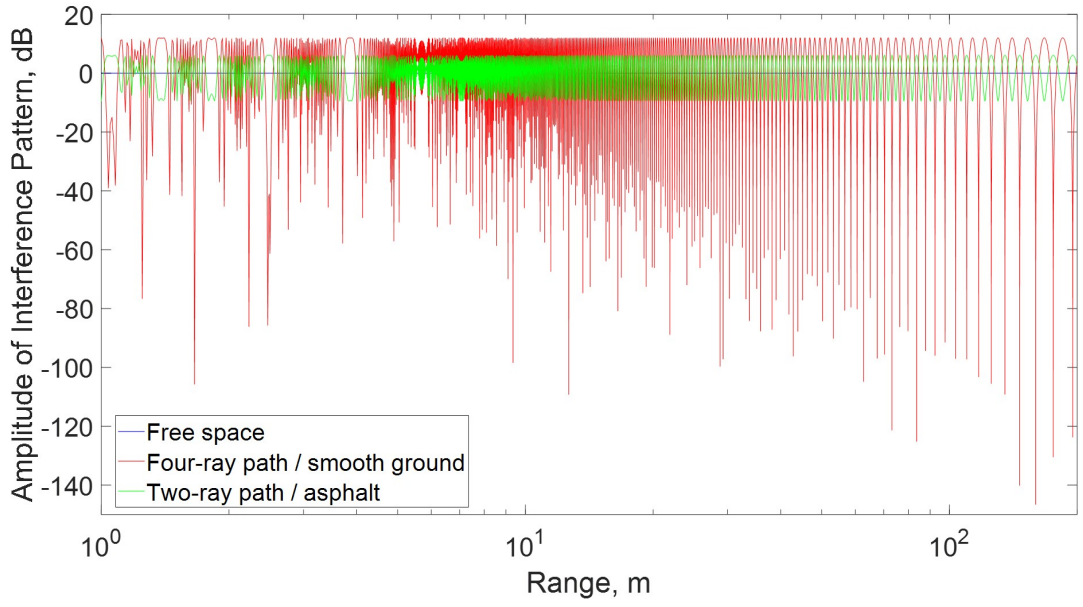

(c)

Fig. 3.32 Interference pattern with smooth ground and asphalt at 24(a), 79(b) and 300(c) GHz, and comparison for automotive ranges

The model shows that the oscillation caused by the constructive and destructive interferences of the four rays produces a considerable variation of the target reflectivity. Moreover, at low frequencies, the interferences calculated using the reflection coefficient

of asphalt have an amplitude close to the ones that consider the ground as a smooth and nearly perfectly conductive ground, and the nulls cause a high attenuation. In contrast, at 300 GHz the wavelength is of the order of the asphalt roughness and thus, the scattering from ground is diffuse, producing less interferences amplitudes, which still introduce fades but with much less amplitude variations in comparison with the 24 and 79 GHz counterpart. As described in Figure 3.33, where a comparison of the interference pattern in presence of paved road is shown at the automotive ranges (up to 200m), multipath losses affect the received power by introducing nulls at distances proportional to the wavelength and the range.

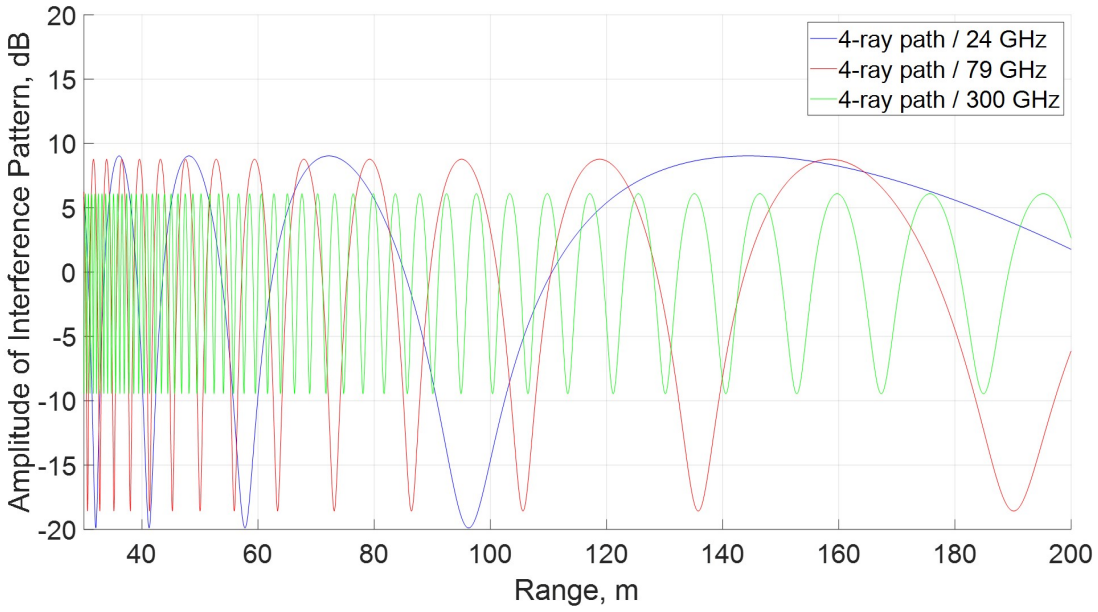

Fig. 3.33 Comparison of interference patterns with asphalt at 24, 79 and 300 GHz, for automotive ranges

The oscillation of the interference pattern is particularly relevant to the detection capability of automotive sensors: at 24 and 79 GHz the road object can be located at the range corresponding to the nulls causing a high drop of the reflected signal and therefore a missing detection. This phenomena has been observed in standard 77 GHz ACC radar operation. By contrast, at low-THz frequencies, the distance between the nulls is smaller and the attenuation is lower, this will produce low reflectivity only

for the scatterers of the target present in correspondence to the nulls, nevertheless the overall target can still be detected.

In Figure 3.34 the four-ray propagation model is shown for the measurement range under test ($22m$) at 300GHz it can be seen that the nulls in the interference pattern are spaced at approximately $20cm$, while at 24 GHz there is only one deeper null.

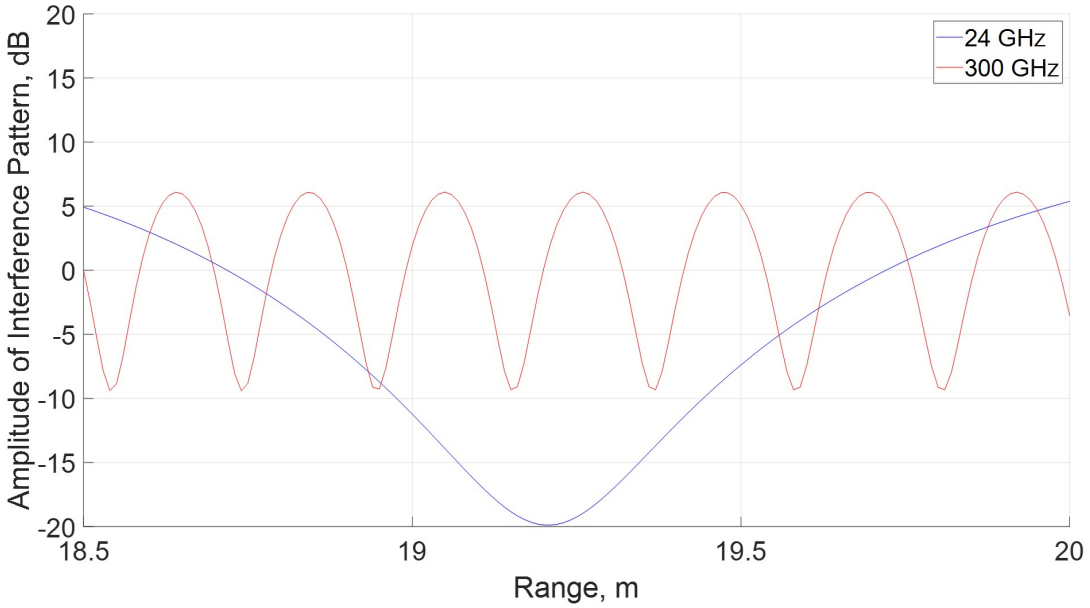

Fig. 3.34 Comparison of interference patterns with asphalt at 24 and 300 GHz, for the range used in the measurements of car

To illustrate this effect, the car in Figure 6.2 was placed on a computer controlled turntable and its reflectivity measured at 24 GHz and 300 GHz, using widebeam antennas and with a range resolution of 3 cm, for 180 aspect angles. Figure 3.35 shows the range profiles versus azimuth angle of the front of the car (as highlighted in (a)), with a colour scale proportional to the received power.

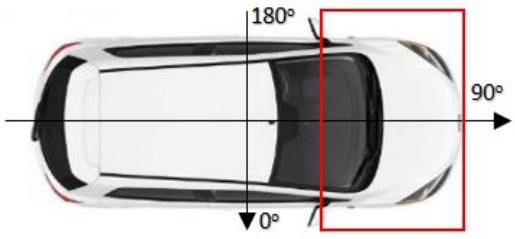

(a)

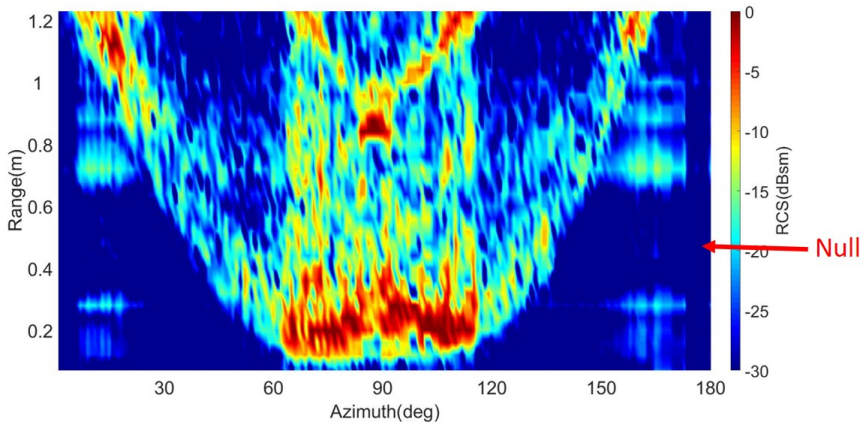

(b)

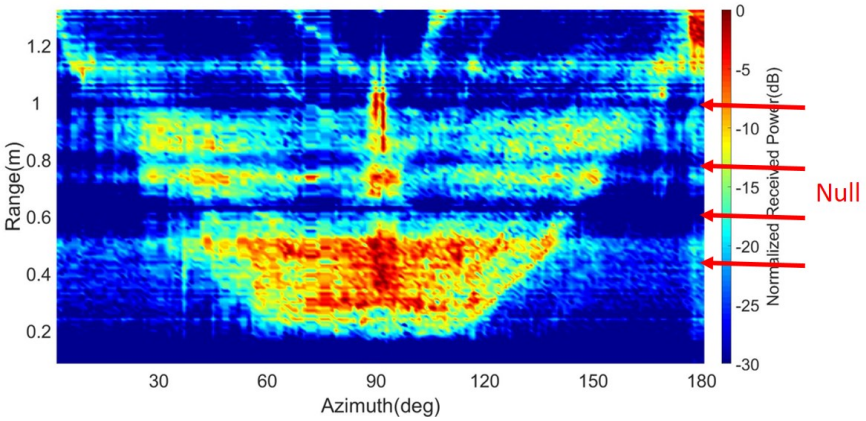

(c)

Fig. 3.35 Sketch of the rotation angles and beam illumination of the car placed on a turntable (a). Received power vs azimuth angle at 24(b) and 300(c) GHz

The range profiles at $300GHz$ (Fig. 3.35(c)) show that the much lower backscatter from the range cells, corresponding to the nulls in the propagation model, produces the low power stripes (blue) at constant ranges. How it can be seen in the plot the nulls are spaced of about 20cm, as predicted from the model. In contrast at $24GHz$ (b) only one blue stripe can be seen looking at the sidelobes placed at about 50cm.

3.8 Summary

This chapter illustrates the methodology used for the experimental investigation of low-THz automotive radar performances and the methods of characterization of outcomes. Firstly, the waveforms and processing typically used for automotive radar are presented in details. Table 3.11 summarises the type of automotive radars classified depending on the waveform used.

Table 3.11 Automotive radar waveforms

Waveform	Processing	Range resolution	Doppler resolution
CW	STFT	None	$\Delta f_d = 1/T_w$
FMCW	FT	$\Delta r = \frac{c}{2BW}$	$\Delta f_d = \frac{1}{N_c T}$
SFW	IFT	$\Delta r = \frac{c}{2N\Delta F}$	$\Delta f_d = \frac{\Delta F}{N}$

T_w: time window duration. T: Chirp duration. BW: Bandwidth.
N_c=Number of chirps. N: Number of frequency steps. ΔF: Frequency increment

Secondarily, the methodologies of characterization of atmospheric attenuation and road targets are shown. Thirdly, the radar systems employed in the experimentation are illustrated in detail. Table 3.12 summarises the key parameters of the radars. It includes the type of waveforms and antennas selected to collect data for characterising the attenuation through atmospheric precipitations and for obtaining signatures reflectivity and μD signatures of typical road targets. Table 3.13 is a complementary table to 3.12 in which are indicated the parameters necessary to obtain the various target signatures, discussed in this chapter. Finally, the experimental sites designed for the experiments are described and characterized.

Finally, the influence of the road ground plane on targets reflectivity is discussed.

Table 3.12 Parameters of the radar systems used in the experiments

Frequency, GHz	Waveform	Max Bandwidth, GHz	Output Power, dBm	Antennas Gain, dBi	Antennas 3dB Beamwidth (azimuth/elevation), degree
24	CW SFW	0 5	10	18	20/20
77	FMCW	0.3	10	36	1.8/8
79	CW FMCW	0 5	10 15	20 29	20/20 1/7
150	FMCW	5	11	24	10/10
300	CW	0	-17	24	10/10
	SFR	16		38	1.6/1.2
	FMCW		-3	18	1/7

Table 3.13 System parameters used to obtain targets signatures

	Classic RCS	HRRP	HRI	μD
RCS symbol	$\sigma_{WB,NBw}$	$\sigma_{WB,WBw}$	$\sigma_{NB,WBw}$	
Antennas beam	Wide	Wide	Narrow	Wide
Waveform type	FMCW/SFW	FMCW/SFW	FMCW/SFW	CW
Bandwidth	Narrow	Wide	Wide	Null

Narrow beam antennas, degree: 1/7. Wide beam antennas, degree: 10/10 or 20/20
Narrow bandwidth, GHz: 0.3 or 0.4. Wide Bandwidth, GHz: 5 or 16

Chapter 4

Attenuation of low-THz waves

4.1 Overview

As shown in Figure 4.1, attenuation losses of signals transmitted by automotive radars occur fundamentally in three media: the car's surface component behind which the radar's antennas are installed and may be used as radome, contaminants accumulated on the radome, the atmosphere.

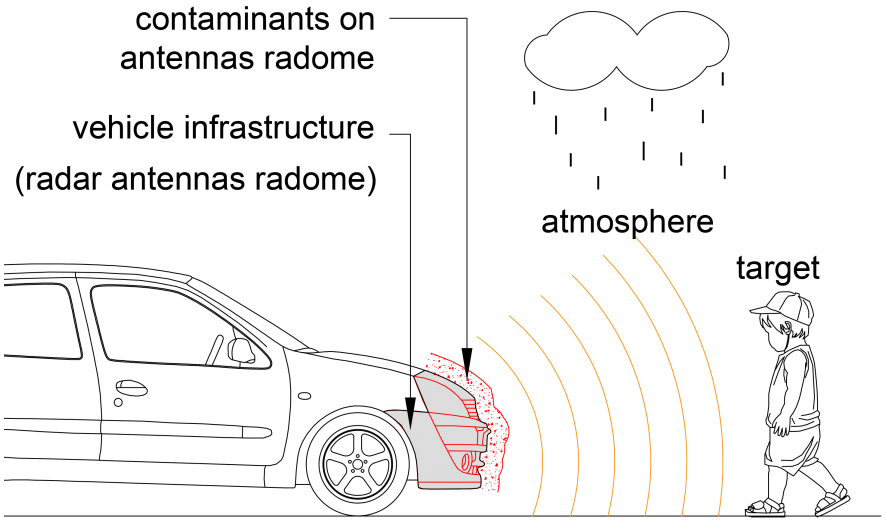

Fig. 4.1 Attenuation mediums for automotive radars

Focus of this chapter is the analysis of the results obtained in a research study, currently carried out at MISL, aimed to characterise the attenuation of EMW propagating through these three critical areas for low-THz radars. The chapter combines original results obtained by the author regarding the attenuation of low-THz waves in the atmosphere exposed to adverse weather conditions, as well a review of works undertaken at MISL as part of the project TRAVEL [82]. In the following sections, firstly there is a summary of the findings on transmissivity of low-THz waves through automotive bumper and headlight cover material, published by Ms Xiao in [83]. Secondarily, results on attenuation of low-THz signals due to radome contamination published by Dr. Norouzian in [79, 84–87], are shown. Thirdly, two sections illustrate the results obtained in the study of atmospheric attenuation of low-THz waves due to rain and snow precipitation, these results are published in [88–90].

4.2 Transmission through automotive bumpers and headlight covers

The design constraints for modern cars require the invisible integration of radar sensors behind different types of plastic cover such as the bumpers or headlight covers [91]. The influence of radar signal propagation through such covers has to be taken into account by radar designers. Several studies can be found in literature on the characterization and optimisation of radar covers for sensors operating at 79 GHz. A bumper is typically a stratified medium, consisting on a plastic substrate and some layers of paint. In [92] the influence of material and painting of bumpers was investigated by characterising their dielectric parameters. The study reports that the plastic material and the majority of paint typically used for bumper provide low attenuation at 79 GHz, less than 3 dB, with an increase when high permittivity paints are used, some metallic paint were found with permittivity values as high that they would prohibit the operation

of a 79 GHz sensor. However, absorptive losses are not the only issue for the radar performances, which are strongly affected by the reflections from the bumper, causing reduction of the dynamic range and interference. Impedance matching of multilayer structures is therefore necessary. The optimization of stratified radome at mm-wave frequencies was studied by Fitzek [93], if the layers are made with materials with high permittivity, like in the case of car bumpers, the classic quarter-wave transformer cannot be used, different approaches are proposed by the same author, such as substrates with embedded antireflection media [93], frequency selective surfaces [94] or other metamaterial structures [95].

These studies demonstrate how the knowledge of transmission and reflection performances, as well as the electric characteristics of automotive radar covers are essential for the design of effective sensors. Therefore, a comprehensive study, including experimentation and mathematical modelling, at low-THz frequencies was undertaken at MISL [83, 96]. Attenuation through bumpers with various paint types and headlights were conducted at 77 GHz, to have a comparison of performances with the current automotive radars, and at low-THz frequencies, 300 GHz. Table 4.1 summarises the experimental results of the measurements for a normal incident angle of the radar's antenna beam to the samples. The results are expressed in terms of transmissivity, the ratio between the power transmitted through the sample and the power transmitted in free space. These results are also confirmed by an analytical model based on multi-layer structures and Fresnel's theory. A detailed explanation of the measurement methodology and theoretical modelling can be found in [83, 96].

Table 4.1 Transmissivity of automotive radar covers

Type of plastic	Paint classification	Sample thickness, mm	Transmissivity, dB 77GHz	300GHz
PP, E/P	Solid black	2.87	-0.5	-1.9
PP, E/P	Solid white	3.72	-0.7	-2.1
PP, E/P	Solid white	3.33	-1.5	-2.4
PP, E/P	Solid white	3.02	-2.0	-2.7
PP, E/P	Metallic gold	3.15	-1.0	-3.1
PP, E/P	Metallic grey	3.26	-2.0	-2.7
PP, E/P	Pearlescent red	3.25	-1.0	-2.5
PP, E/P	Pearlescent red	3.33	-0.2	-1.3
PP, E/P	Pearlescent green	3.27	-0.6	-1.3
PUR	Pearlescent white	3.34	-5.8	-7.4
PC	Headlight-cover	3.20	-0.4	-2.4

PP: Polypropylene
E/P: Ethylene / Propylene
PUR: polyurethane

Overall, the loss through the bumpers increases from 77 GHz to 300 GHz, however the signal reduction is always no more than 2 dB for polypropylene (PP) and polyurethane (PUR) automotive bumpers, both considering solid and metallic paints. A analogous result was also found for a plastic headlight cover. Moreover, the transmissivity was measured by changing the incident angle between the samples and radar beam to simulate the real case scenarios of a radar scanning behind the bumper. Shorter wavelength produce higher variation of the transmissivity when changing the incident angle, because of the higher variation of the electrical thickness. This result indicates a requirement for high precision positioning of the radar behind the cover at higher frequencies.

4.3 Attenuation through contaminated radome

In the presence of adverse weather conditions the antenna radome becomes wet or it is covered with a thin layer of water, ice or dirt and the transmission and reflection characteristics of the radome can vary. Contaminants interact with EMW and can produce its attenuation up to complete signal blockage and sensor failure. The study of signal attenuation due to radome contamination needs to be addressed to generate the requirements for radome design and packaging in a vehicle as well as the loss dependence on the radar signal carrier frequency.

In literature, the attenuation due to contaminants present on the antenna's radome is mainly limited to the study of water and at frequencies below 100 GHz. All these studies, show a considerable loss even with a very thin layer of water and a strong dependentance on the frequency. In [97] considerable transmission losses through uniform layers of water are calculated and in [98] measurements of a radome covered by a water layer with a thickness of approximately 1.5 mm at 20 GHz, show transmission loss of 20 dB. [99] reports attenuation between 9 and 14 dB caused by a thin layer of rainwater on the radome of a 94 GHz radar, from results of measurements carried out over two years at varying precipitation rates. Attenuation due a uniform layer of water has been recently studied also in the optical region, [100], measurements and simulations show strong attenuation even with a very thin layer of water. Coming to automotive applications, experiments carried out at the Robert Bosch GmbH, [101] and compared with a theoretical model based on Fresnel theory, reveals that, the existence of a water film on the surface of the antenna lens or its radome is the primary cause for weak performance of radar sensors, operating at high frequencies in rainy and snowy weather conditions. Measurement results at 76.5 GHz show a loss of about 30 dB due to a water layer of 1 mm thickness. In [102] the influence of a thin water layer on automotive radar operating in a wide frequency interval 75-85 GHz is studied and

results show losses from 6 dB to 20 dB, strongly depending on the thickness of the water film.

Published information on the impact of radome contaminants on wave propagation is absent for the Low-THz bands. At MISL comprehensive theoretical and experimental studies on the loss effect of many common contaminants that occur in automotive practice, were made at Low-THz frequencies. The study regards water, ice, sand, diesel, gasoline and fallen leaves. The measured two-way transmission losses through these contaminants are summarised in Table 4.2 and confirmed by theoretical models. A detailed explanation of the measurement methodology and theoretical modelling can be found in [79, 84–87].

Table 4.2 Two way signal reduction on a contaminated radome, dB [90]

		Frequency band, GHz		
Contaminant		77	150	300
Water (0.45mm)	Pure	30 [101]	29	38
	Salty (3.5%)	23.2	22	31
	Dirty	no data	34.6	40
Sand (size: 0.2 mm)	Dry	no data	≈ 0	10
(Thickness: 1mm)	Moist (10%)	no data	12.6	26
Ice (1mm)		0.4	1.4	3.2
Diesel (1mm)		0.6	0.8	1.1
Gasoline (1mm)		1	1.4	1.5
Leaf (0.37mm)	Fresh	30	34	40
	Dry	≈ 0	≈ 0	4
Water droplet	10%	no data	2	2
(coverage area in %)	20%	no data	4	1.6

The highlight of the results shown in the table is the strong dependence of EMW degradation, at every frequency band, with the presence of water or when other contaminants containing water cover the entire radome surface.

The high reduction of a signal passing through water is caused by the absorption of energy of the EMW because of the alignment of the polarised water molecules in the presence of an electric field. Water on the radome can be in the form of a thin layer or as droplets distributed over the radome.

Losses due to a layer of water depend mainly upon the thickness of the layer and are scarcely influenced by other chemicals that may contaminate it, as well as by the percentage of salt contained. Losses due to droplets distributed on the radome are the most common case in real scenarios and have a less detrimental effect on the wave propagation in comparison with a uniform layer of water. Losses are influenced by the droplet size, density and distribution. Results in [79] show that the propagation at sufficiently short wavelengths does not degrade the performance of the radar radomes significantly. This is attributable to the fact that gaps between droplets have an electrical dimension larger than the wavelength, increasing the transmissivity through a screen of randomly distributed droplets. Such effect demonstrates one of the advantages of the low-THz band for outdoor applications, as this requirement is achievable with very short wavelength signals.

The study of losses due to a random distribution of sand particles on the radome shows, for dry sand, negligible loss at 150 GHz, at 300 GHz, probably due to resonance effects, losses are consistent. The signal reduction at every frequency, dramatically increases with the presence of water mixed to sand. Moreover, as shown in [85] attenuation is lower when produced by mixture of finer particles and water, which is also the most practical case. The signal reduction due to the presence of a uniform layer of ice is significantly lower compared to the same thickness of water. As explained in [84] the result is due to water and ice different molecular structures. Ice molecules are locked into a crystal structure and thus will not align with an electric field. Diesel

and gasoline do not produce significant reduction of the EMW [86]. Moreover, if on one hand, gasoline has a stronger absorption coefficient in comparison with diesel, on the other hand, in practice, it evaporates very quickly, due to its weak molecular dispersion, almost cancelling the chances of forming gasoline film on the radome. The study of signal reduction due to leaves attached to the radome [87] shows that while the leaves themselves are transparent to EMW, the presence of water in it constitute the main issue for the radar signal. The measured signal reduction through fresh leaves, in fact, is equivalent to the reduction through a uniform layer of water with a thickness of 0.5 mm.

4.4 Atmospheric attenuation due to rain precipitation

The study of EMW propagation in different weather conditions for radars operating at Low-THz frequencies is significant for the future development of Low-THz outdoor applications. The most common precipitation occurring in Europe is rain, which is well known to be the cause of the most of the attenuation for potential automotive radars operating at frequencies above 100 GHz [103]. The presence of rain in the atmosphere causes the reduction of the intensity of an EMW propagating through it, due to absorption inside the raindrops and scattering by them. This study aims to determine an empirical model for different rainfall rates and find out how the switch to the current automotive frequency of 77 GHz to low-THz frequencies affects the radar maximum detection range.

Attenuation due to rain at frequencies between 30 and 350 GHz has been subject of study since 1975 when Sander [104] published results of measurements collected over two years and determined the attenuation coefficient as a function of rainfall rates at 52, 90 and 150 GHz. The results show that higher attenuation caused by heavy rainfalls in the whole frequency range between 52 and 150 GHz differs only by 20%. In [105] and [106] measurements results at 37, 57, 97 and 103 GHz were used to develop models of the raindrop size distribution. The rain attenuation statistics for a

wireless link at 120 GHz were studied in [107] and results show good agreement with the International Telecommunications Union Radio-communication Sector (ITU-R) prediction model [17]. The same conclusion was drawn in [108] for measurements results of rain attenuation in tropical regions at 120 GHz and in [109] for results at 355.2 GHz through rainfall rates up to 25 mm/hr. An improved semi-empirical method for the prediction of rain attenuation in earth space and terrestrial links is proposed in [110]. The model uses the full rainfall rate distribution to predict the attenuation distribution.

The sparsity of experimental work at Low-THz frequencies on rain attenuation validate the importance of further studies to support the future development of outdoor applications. It is expected that the increase of the rainfall rate causes higher attenuation due to the occurrence of bigger raindrops. Moreover, for the same rainfall rate, it is expected to observe a signal reduction higher as the frequency increase, because the raindrops are electrically bigger at a higher frequency.

In this work, the attenuation was measured simultaneously at 77 GHz and 300 GHz as a function of rainfall rate throughout one year. The rainfall rate measured by laser disdrometer and expressed in mm/hr, is equivalent to the accumulated depth of rainwater in a gauge over a time interval of one minute. Two radar systems operating at the frequency under investigation are co-located in the experimental setup described in Sections 3.3 and 3.6.1, providing the same propagation path. In the next section, experimental results are shown and a model based on the ITU-R theoretical model extrapolated.

4.4.1 Experimental results

Figure 4.2 shows the measured specific attenuation at 77 GHz and 300 GHz. Here the term 'specific' indicates that the results are obtained from measurements in a specific location (UK) and may be different if the experimentation would be carried out in different regions of Earth.

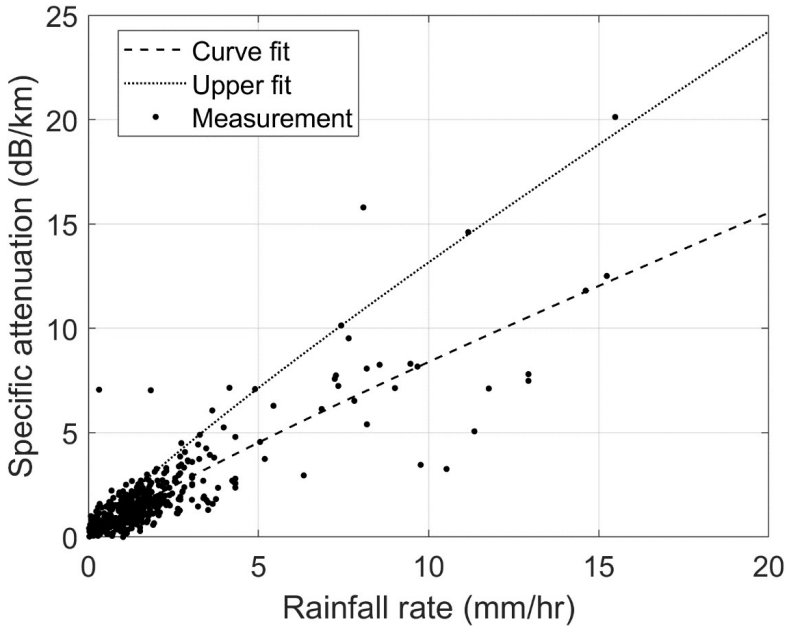

(a)

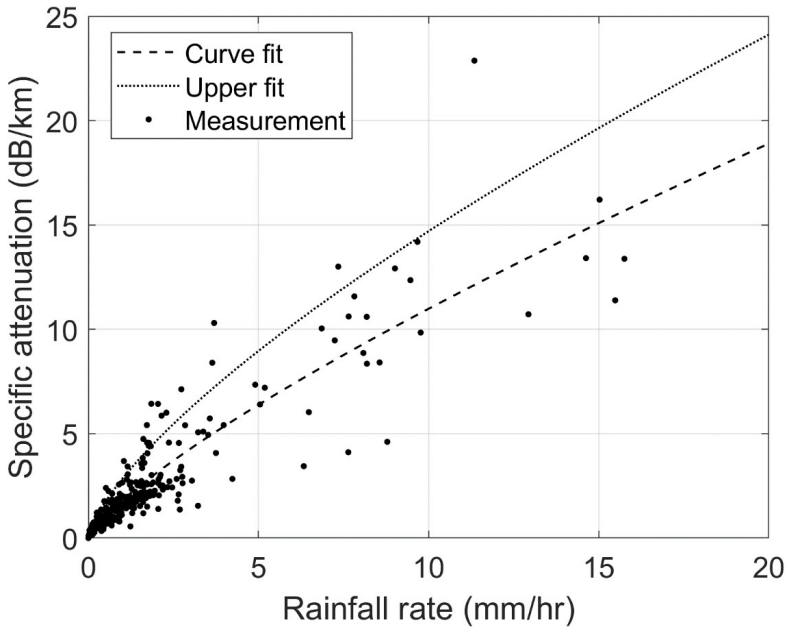

(b)

Fig. 4.2 Measured attenuation due to rain precipitation at 77 GHz (a) and 300 GHz(b) [88]

Overall, results at both frequencies exhibit higher attenuation with the increase of the rainfall rates, as expected due to the presence of larger raindrops at the higher

rainfall rates. The attenuation per kilometre is only slightly higher at 300 GHz than at 77 GHz.

The ITU-R prediction model expresses the rain attenuation A_r as a function of the rainfall rate R_r through a power law relation:

$$A_r = kR_r^{\alpha} \tag{4.1}$$

where the coefficients k and α are empirical parameters that only depend on the frequency and EMW polarization and do not take into account the raindrop size distribution. Based on the ITU-R model, the coefficients k and α were extracted from the measurements results by fitting a power law equation to the data, using a least mean square algorithm, the coefficients obtained are: $k = 1.6286$, $\alpha = 0.6296$ at 77 GHz and $k = 1.1320$, $\alpha = 0.7177$ at 300 GHz.

In [88] a model of rain attenuation based on Mie scattering theory and the drop size distribution, measured with the laser disdrometer and fitted against common statistical distribution models, is derived. The measurements results, shown here, best agree with the ITU-R recommendation at 77 GHz whereas at 300 GHz, the calculation based on Mie scattering and the Weibull distribution exhibits a slightly better fit to the measured data.

Now, there are several measured data points that exceed the curve fitted to the measured data. For the estimation of the maximum range of operation of the radar system, the additional propagation attenuation needs to be modelled as a link margin, therefore, an upper bound it is also calculated by fitting a least mean squares to the measured specific attenuation which exceeds the theoretical prediction calculated by Mie scattering theory. The curves obtained are also shown in Figure 4.2.

4.5 Atmospheric attenuation due to snowfall

The second precipitation, typical of automotive scenarios, studied was snowfall. Attenuation due to snow precipitation is the result of extinction by individual snowflakes. In our study carried out to analyse the absorption in ice [84], it was found that ice produces very low attenuation, therefore the attenuation through the single snowflake is mostly produced by scattering. Measurements during snow storms show that attenuation due to falling snow is difficult to characterise. Snow precipitation is comprised of crystalline ice water; the crystals can have many different shapes and sizes with maximum diameters of 15 mm. The fall velocity is smaller than for raindrops and more regular, this is expected to cause more attenuation to EMW as a higher amount of water is present in the atmosphere for a given amount of time. A classification that may be taken is based on the amount of free water associated with them. In this work, two categories are considered, dry and wet, which are identified depending on the ambient temperature and humidity. The measured specific attenuation through snowfall is analysed and presented as a function of the snowfall rate. Very few studies can be found in the literature regarding the influence of snow on the EMW propagation at either the standard 77 GHz automotive frequency or in the low-THz band. In 1977 a research conducted at the Ballistic Research Laboratory (BRL), USA, on attenuation of 140 GHz signals through different precipitations [111], shows the results of measurements on wet snow. The measured attenuation was in general 3 times higher than rain precipitation at the same rate, for example with a snowfall rate of 1.2 mm/hr the maximum attenuation was 5.5dB/km higher. A second publication by the BRL in 1988 [112] shows results at 95, 140 and 217 GHz with a snow mass concentration of 1 g/m^3, the attenuation increases with the rise of frequency, from 2 dB/km to 9 dB/km. A more recent study [113] provides results from a satellite link at Ka-band, the attenuation with dry or wet snow rarely exceed 2 dB at these frequencies.

Snow attenuation through various intensities of wet and dry snowfall was measured at 77 GHz and 300 GHz during several snowfall events from the 8^{th} to the 11^{th} of December 2017 and from the 14^{th} and 28^{th} of February 2018. The experimental methodology is analogous to the one used for the rain precipitation characterisation and explained in Sections 3.3 and 3.6.1, the laser disdrometer can also measure the snowfall rate. Temperature and relative humidity are monitored as they influence characterisation of the snow and because the snow can suddenly turn to rain and vice versa. The reference signal with clear air is measured close to the snow events, just before and after. This is because changes in relative humidity can result in a variation of the signal amplitude. The next section reports the experimental results obtained.

4.5.1 Experimental results

Figure 4.3 shows specific attenuation through dry snow at 77 GHz and 300 GHz. In figure 4.4 the specific attenuation is, instead, shown for wet snow at both frequencies.

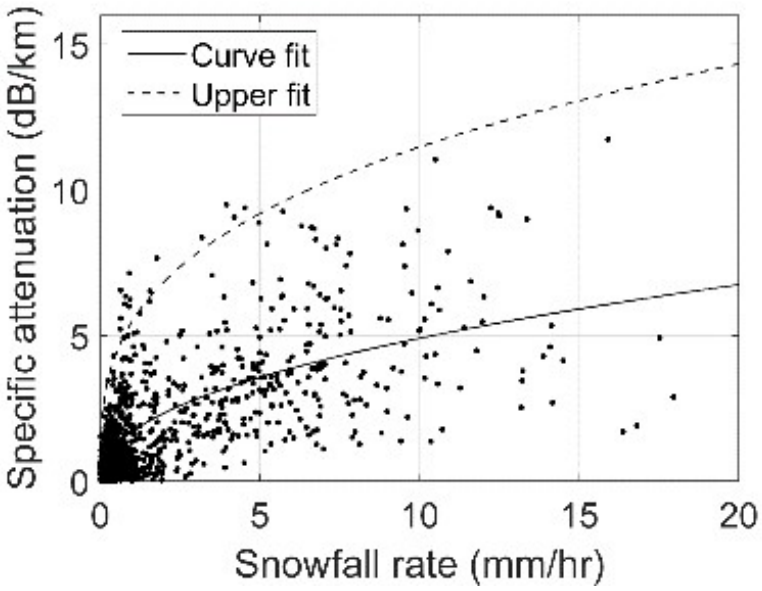

(a)

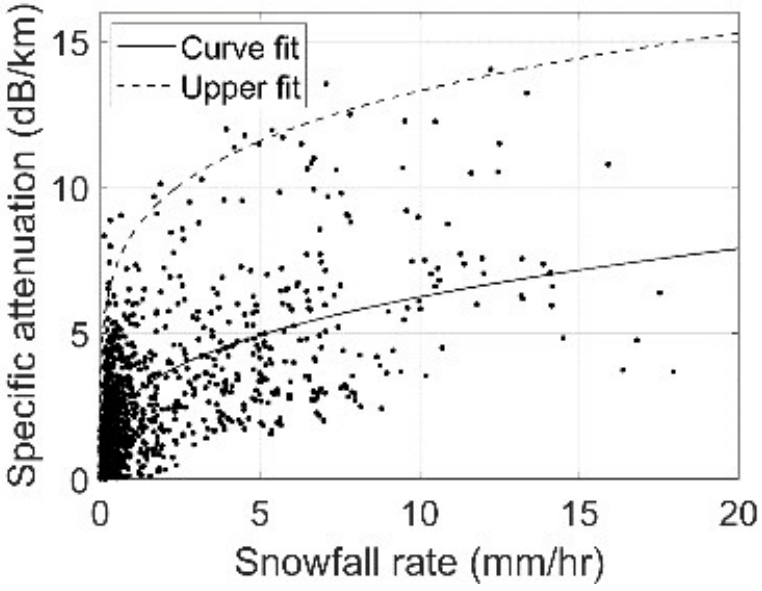

(b)

Fig. 4.3 Measured specific attenuation due to dry snow precipitation at 77 GHz(a) and 300 GHz(b) [89]

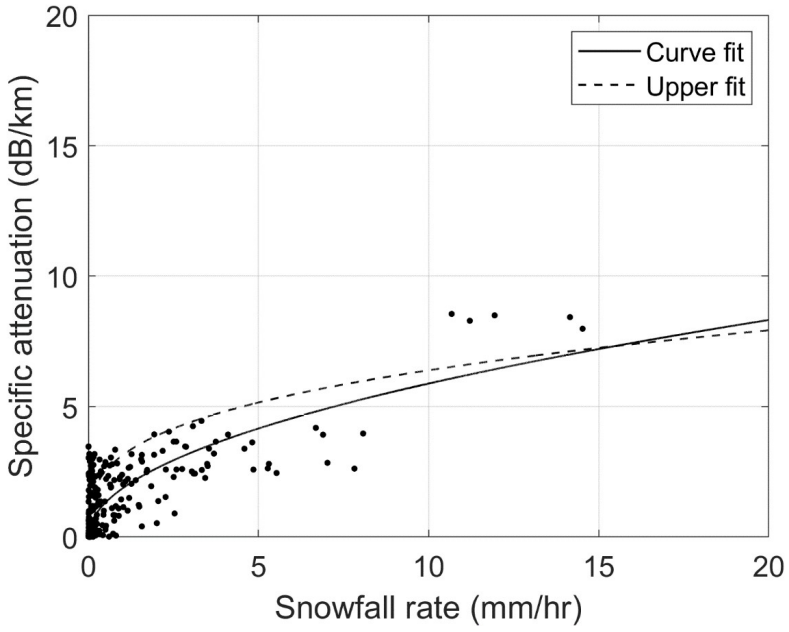

(a)

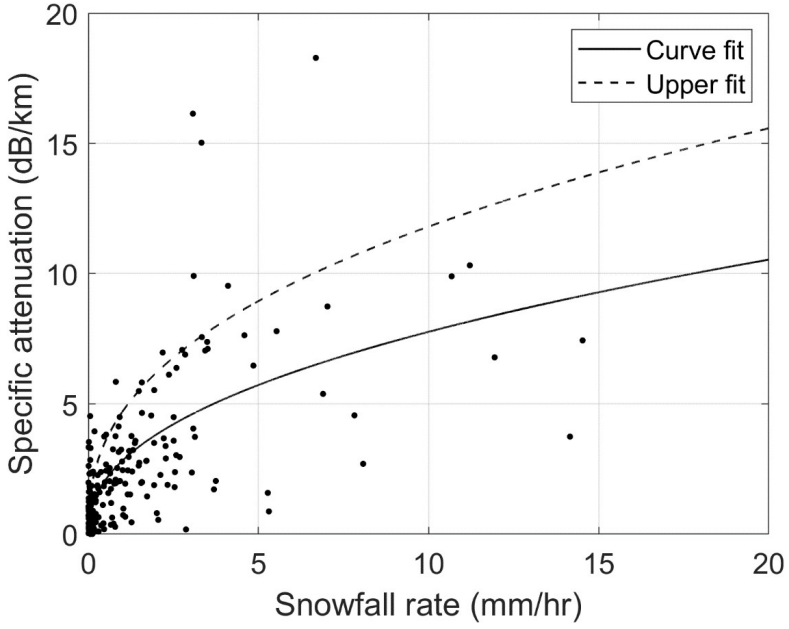

(b)

Fig. 4.4 Measured specific attenuation due to wet snow precipitation at 77 GHz(a) and 300 GHz(b) [89]

As for the study of rain attenuation, using the same power law relation of the ITU-R, a least mean square fit is obtained for the median values and the upper bound. Overall,

for all the measured specific attenuation through all the snow storms the attenuation increases with the increase of snowfall rate. In general, at 300 GHz attenuation is 2-3 dB higher than at 77 GHz. Comparison between the median least squares fit for dry and wet snowfall shows slightly higher attenuation through wet snowfall. This result is consequence of the increase of water content in snowflakes and therefore of the absorption rate, and by the increase of the size of snowflakes and reduction of their fall rate. The difference between the fitted curve to the median values and to the highest values exhibit higher variability for dry snow. There may be a number of factors inducing this results, all related to the different characteristics of the dry and wet snow which are not fully understood at this stage. The spatial non-uniformity of the snowfall along the path or during the observation time may be higher for dry snow, or the reference target reflectivity may be different when there is dry snow accumulated on it. Moreover, the classification as dry or wet snow, based on ambient temperature, may be inaccurate.

4.6 Comparison of atmospheric attenuation in presence of different precipitations

The plots in Figure 4.6 show a summary of the findings of the experimental characterization of the atmospheric attenuation in presence of adverse weather conditions of low-THz waves and standard automotive frequency signals. The results are accompanied with values for clear air and fog extrapolated from the plots in Figure 4.5.

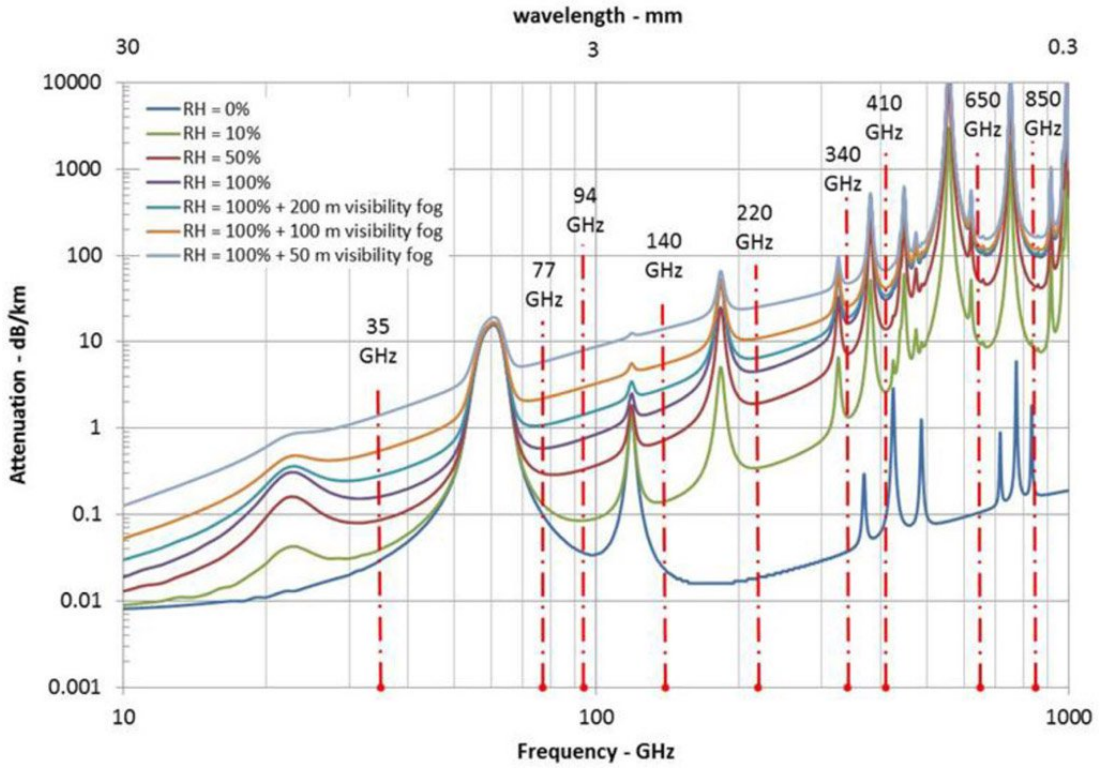

Fig. 4.5 Atmospheric attenuation curves from 10GHz to 1THz under various levels of relative humidity (RH) and fog [114]

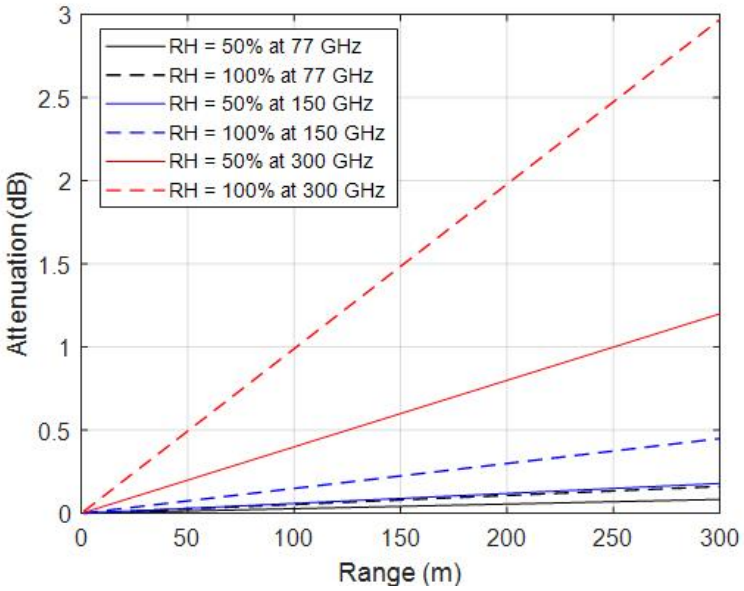
RH = 50% at 77 GHz
RH = 100% at 77 GHz
RH = 50% at 150 GHz
RH = 100% at 150 GHz
RH = 50% at 300 GHz
RH = 100% at 300 GHz
Attenuation (dB)
Range (m)
0
0.5
1
1.5
2
2.5
3
0
50
100
150
200
250
300

(a)

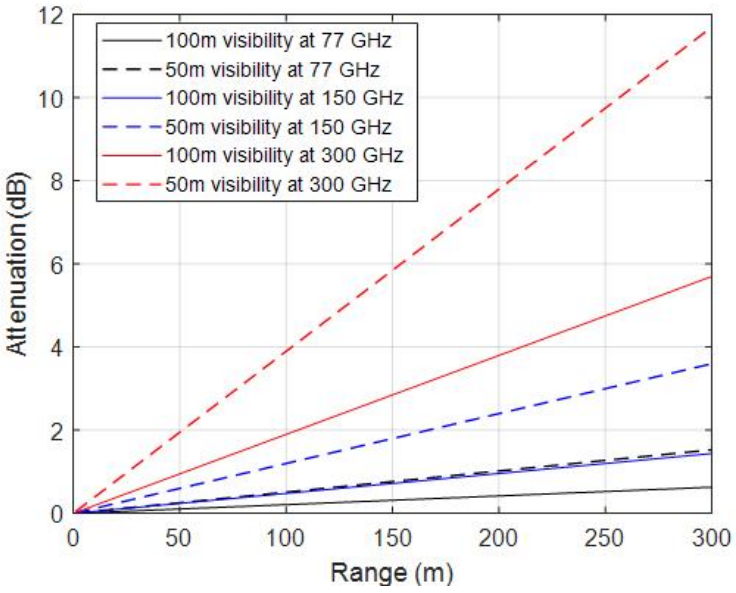
100m visibility at 77 GHz
50m visibility at 77 GHz
100m visibility at 150 GHz
50m visibility at 150 GHz
100m visibility at 300 GHz
50m visibility at 300 GHz
Attenuation (dB)
Range (m)
0
2
4
6
8
10
12
0
50
100
150
200
250
300

(b)

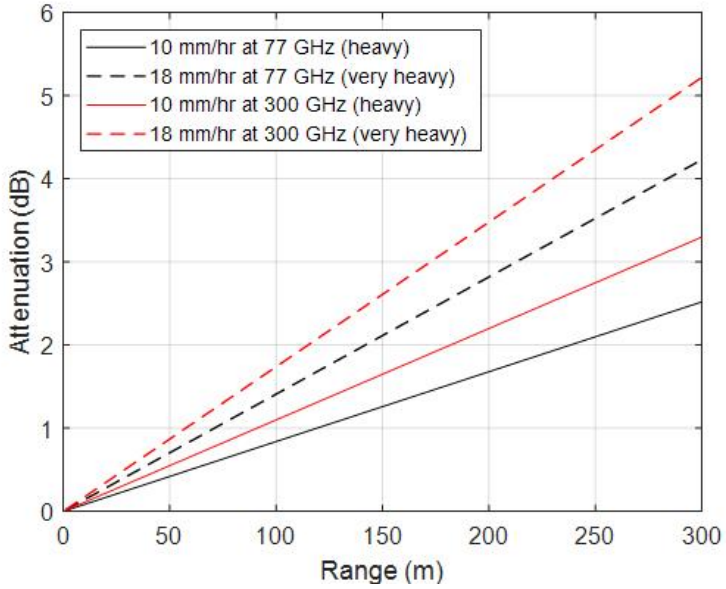

(c)

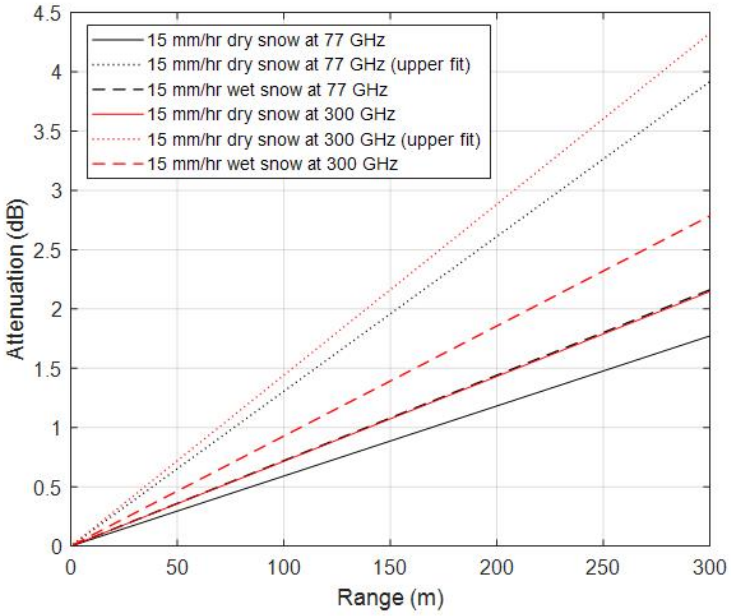

(d)

Fig. 4.6 Attenuation in clear air (a), fog (b), rain (c) and snow (d) [90]

The EMW attenuation is illustrated for the automotive standard frequency of 77 GHz, as reference, and at the Low-THz frequencies, for ranges up to 300 m. Attenuation in clear air with relative humidity (RH) of 100% shows a loss of 3 dB over a range of

300 m at 300 GHz. The presence of water in the atmosphere as a result of complex weather conditions, such as rain, fog and snow introduce higher attenuation as the EMW is absorbed and/or scattered when interacts with the precipitation particles. As expected, the smaller specific attenuation for both frequencies is observed for dry snow due to lower absorption coefficient in dry snowflakes. The maximum difference between attenuation at 300 GHz and 77 GHz corresponds to extremely dense fog which reaches about 10 dB at 300 m. For rain and snow, the loss difference is lower and it is within 3 dB between the two frequency bands.

Finally, coefficients for a theoretical model, based on the ITU-R power law model, are extracted from the atmospheric propagation results and summarised in Table 4.3. The coefficient are calculated using a least-mean square algorithm for the median and upper bound values of attenuation.

Table 4.3 Power law fit for precipitation measurements

Precipitation	Fit	$A_r = kR_r^{\alpha}$	$77GHz$	$300GHz$
Rain	Median	k	1.08	1.81
		α	0.89	0.78
	Upper bound	k	1.73	2.84
		α	0.88	0.71
Dry snow	Median	k	1.7	2.85
		α	0.46	0.34
	Upper bound	k	5.49	8.39
		α	0.32	0.2
Wet snow	Median	k	1.86	2.82
		α	0.5	0.44
	Upper bound	k	3.13	4.7
		α	0.31	0.4

4.7 Summary

This chapter reports results on the analysis on attenuation losses in the low-THz band, through the component behind which the radar's antennas are installed, contaminants accumulated on the radome and the atmosphere in presence of adverse weather conditions. Installing the radar behind bumpers or headlights would produce only 2 dB difference in attenuation by increasing operating frequency from 77 GHz to 300 GHz.

Attenuation due to particles on the antennas radome or in the atmosphere along the EMW propagation path affect the maximum detection range of Low-THz radars even for the relative short range of operation for automotive applications (300 m). A comprehensive study of different contaminants on the antennas radome was undertaken at MISL and results summarised in Section 4.3. As expected, it was found that the presence of water in the contaminants is the most significant cause of attenuation and its effect is in general more detrimental at higher frequencies. However, analysis of the most common scenario, with water droplets distributed on the radome, shows lower attenuation at the shorter wavelength, due to EMW transmission through gaps between the droplets.

Sections 4.4, 4.5 and 4.6 report experimental results of the atmospheric attenuation in presence of adverse weather conditions. Compared to standard automotive frequencies (77 GHz), Low-THz frequencies do not introduce dramatic increase of the attenuation through atmosphere over the range of operation of automotive radars (up to 300 m). The maximum difference between attenuation at 300 GHz and 77 GHz corresponds to extremely dense fog which reaches about 10 dB at 300 m range. For rain and snow, the loss difference is within 3 dB between two frequency bands.

Chapter 5

Signatures of pedestrians in the Low-THz band

5.1 Overview

Road accident statistics show that pedestrian detection and recognition are the two most challenging problems that have to be considered in the development of automotive safety systems. According to the global status report on road safety, 2015 by the World Health Organization, more than 25% of all road traffic deaths are among pedestrians and cyclists [115]. In order to assess the capability of automotive radars for pedestrian detection and identification, the knowledge of the way the human body reflects electromagnetic waves is essential. In particular, it is indispensable to estimate the human RCS to evaluate the maximum range at which a pedestrian can be detected and its motion characteristics, in terms of micro-Doppler signature, to identify the pedestrian among other detected targets. While μD signatures have been investigated in several studies over the past years [116, 117], the literature lacks studies on the reflectivity of humans.

Regarding Low-THz frequencies, there are no reported studies on either RCS or μD signatures of humans. In the following sections, firstly it will be presented a comprehensive study on pedestrian RCS carried out at the MISL and published in [118–

120]. Secondarily, results of μD signatures of humans subjects at Low-THz frequencies, plublished in [120, 121] will be shown and analysed.

5.2 Radar Cross Section of pedestrians in the Low-THz band

Studies of the RCS of the human body are reported mostly for medical applications, and at frequencies up to 10 GHz [122–124]; Yamada [125] measured the pedestrian RCS at the standard automotive frequency of 76 GHz with a narrow bandwidth, the average RCS was found to be about $-8dBsm$ with a range of fluctuation of about $20dB$. A comprehensive study undertaken at the European Microwave Signature Laboratory (EMSL) [126] established a reference library of RCS signatures in the automotive radar bands of 24 GHz and 79 GHz. The observed RCS averages in the two frequency bands are quite close and they do not show significant differences. The mean RCS is around $-8dBsm$ for an adult male and $-11dBsm$ for a child. The use of large bandwidth shows the potential to obtain robust RCS signatures that can be used for classification purposes.

In the next sections, experimental results on pedestrian RCS at 150 GHz and 300 GHz will be shown and compared with the standard automotive frequency of 24 GHz, at which computer simulated results will also be shown. The work presented in the following sections was published in [118].

For ethical, health, safety and technical reasons, it is not possible to arrange prolonged measurements with a real human subject. Furthermore, such measurements do not guarantee the reliability of the results due to an issue with the required repeatability. Instead, the use of human dummies is a standard approach for the characterisation of pedestrian detection performance for automotive sensor performance analysis [127]. In our studies a child dummy was selected as the representative of the class of road

actors who are (i) most at risk on the road, and (ii) the most challenging object to detect due to their small physical size compared to that of an adult and less predictable behaviour, resulting in a higher variation of the aspect angles over the car reaction period. We assume that the ability of radar to detect children should guarantee the detection of adults. Moreover, since it was not possible to involve a real child in the experimentation, adult mannequin and human targets were used for preliminary tests to assess the accuracy with which the RCS of a mannequin can represent that of a human.

5.2.1 Target selection

In order to assess the accuracy with which the RCS of a mannequin can represent that of a human, initially a comparison of reflectivities of a human subject and a mannequin was performed. To match the size of the human measured, a mannequin of adult size was used for this test. The material of the mannequin is the same plastic material as of the child mannequin which is used in the main RCS measurements presented in the following sections Figure 5.1(a) and (b) shows the set-up of measurements at 150 GHz where the range is chosen so that the man and the mannequin both fill the antenna beams, their sizes are similar and both wore the same clothes. In Figure 5.1(c) the high resolution range profiles (HRRP), normalised to the maximum value of the received power, for both subjects are plotted and the calculation of the integrated gated profiles, calculated using 3.31, shows a difference of 0.5 dB.

(a) (b)

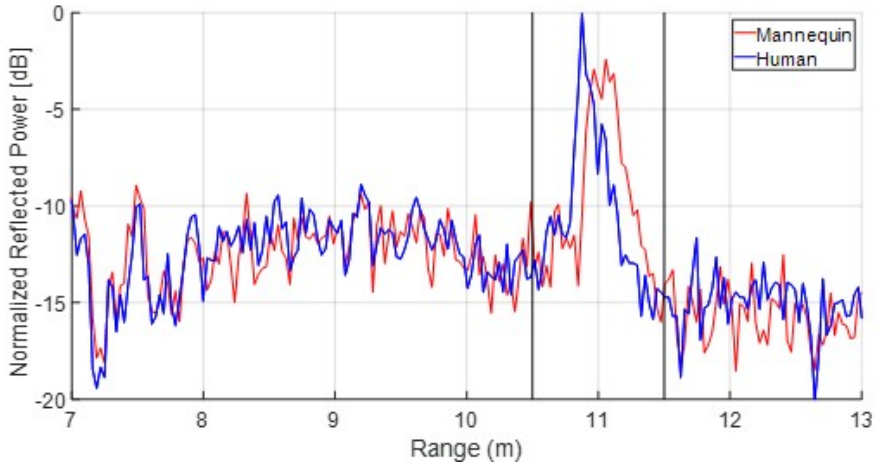

(c)

Fig. 5.1 Comparison of reflectivities between human and mannequin. (a), (b) Experimental setup, (c) HRRP of the mannequin and human

Similar agreement between returns from both targets was observed for other aspect angles, which allows the conclusion that, at the frequencies of interest, it is possible to estimate the RCS of human wearing clothes using a mannequin of the same size.

Next, an analysis of the difference in the reflectivity of a human with and without clothes was carried out to see the effect that this has on detectability. The setup of the experiment made at 300 GHz is shown in Figure 5.2(a) and (b). In Figure 5.2(c) representative range profiles of the human subject with and without a cotton T-shirt are shown.

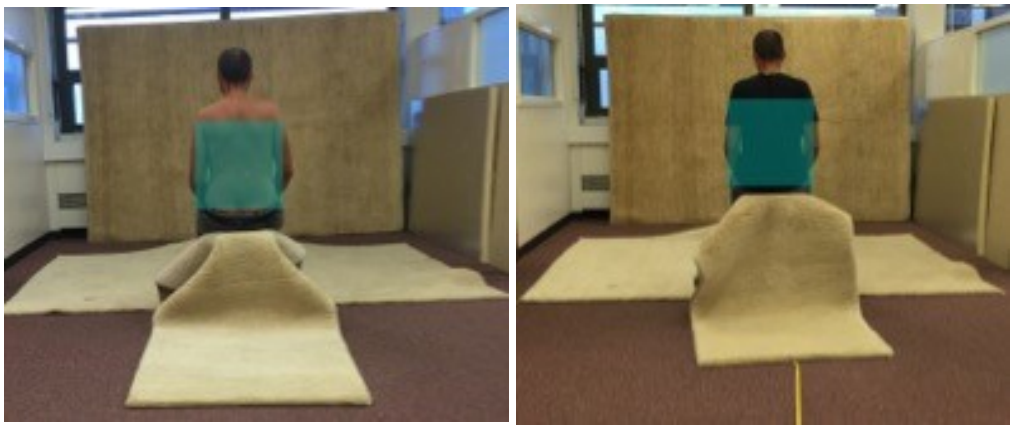

(a) (b)

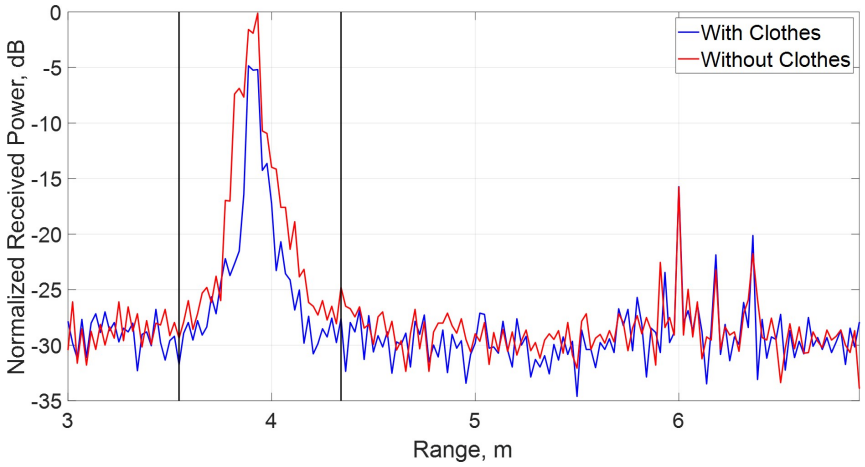

(c)

Fig. 5.2 Comparison of reflectivities between human skin and clothes. (a), (b) Experimental setup, (c) HRRP of human with and without clothes

The signal received from the targets, shows that the reflectivity of the human skin is about 3 dB higher than the reflectivity of fabric. Therefore, since even light clothes reduce the human reflectivity, effect of different kinds of common clothes on pedestrian's RCS was investigated and presented next, in Section 5.2.8.

5.2.2 Measurements methodology

The primary objective of the measurement campaign was the collection of pedestrian returns to characterize pedestrian reflectivities at the frequencies of 150 and 300 GHz

using 5 GHz bandwidth and to compare the results with the existing results reported at lower frequencies, namely at 24 GHz and 77 GHz. Secondly a comparison of results of measurement with two different bandwidths: 300 MHz (current automotive standard) and 5 GHz, was carried out.

The measurements were performed in the indoor site described in Section 3.6.2, the target was placed in a controlled environment in an anechoic space built with low-THz absorbers, high-pile woollen rugs, placed to cover the floor and the wall behind the target. Table 5.1 summarize the key parameters of the systems and setup used for the data collection in the three frequency band considered in this study. The 24 and 300 GHz systems are SFW radars (Section 3.5.1) the 150 GHz radar is the FMCW radar shown in Section 3.5.2.

Table 5.1 Parameters for the pedestrian RCS measurements

Parameter	24GHz Radar (Section 3.5.1)	150GHz Radar (Section 3.5.2)	300GHz Radar (Section 3.5.1)
Output power, dBm	0	11	-17
IF Bandwidth, KHz	3	1	3
# of integrated measurements	10	10	10
Antennas gain, dBi	20	24	24
Antennas Beamwidth, deg (Azimuth/Elevation)	20/20	10/10	10/10
Distance from the target, m	3.5	7	7
Sweep Bandwidth, GHz	5 0.3	5	5 0.3
Range resolution, cm	3 50	3	3 50

The square horn antennas used in the 150 and 300 GHz systems, with both azimuth and elevation 3 dB beamwidth of 10° illuminate the entire mannequin placed 7 m away from the antennas, without reflections from the ground. For the measurements at 24 GHz square horn antennas of 20° 3dB beamwidth were used, the mannequin was kept at the same position but the radar was moved 3.5 m towards the mannequin to ensure the same beam filling by the mannequin and to avoid main beam reflections from the ground before target. Figure 5.3 shows the setup for the measurements, where the footprint of the radar on the mannequin is highlighted.

(a) (b)

Fig. 5.3 Setup for RCS measurements of a child mannequin. Turntable covered with low-THz absorber (a) and 24 GHz VHP-2 pyramidal absorber (b)

Figure 5.4 shows the range profiles of the child mannequin where is highlighted the start and end range gating (r_s and r_e) of the region enclosing the target.

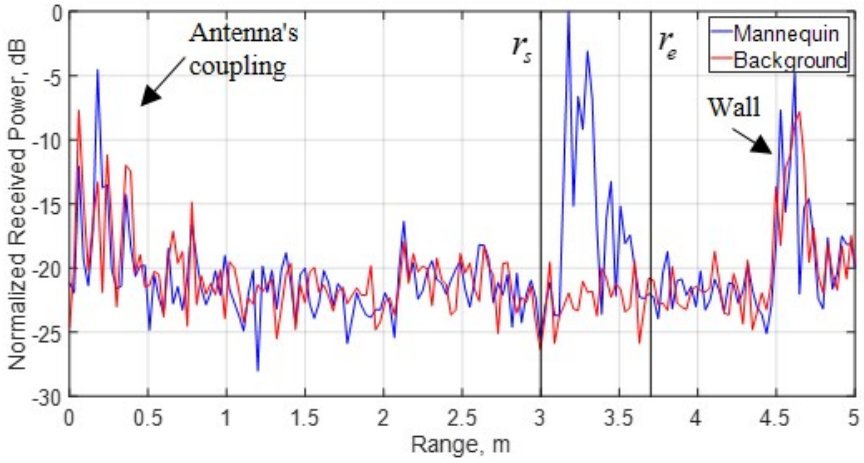

(a)

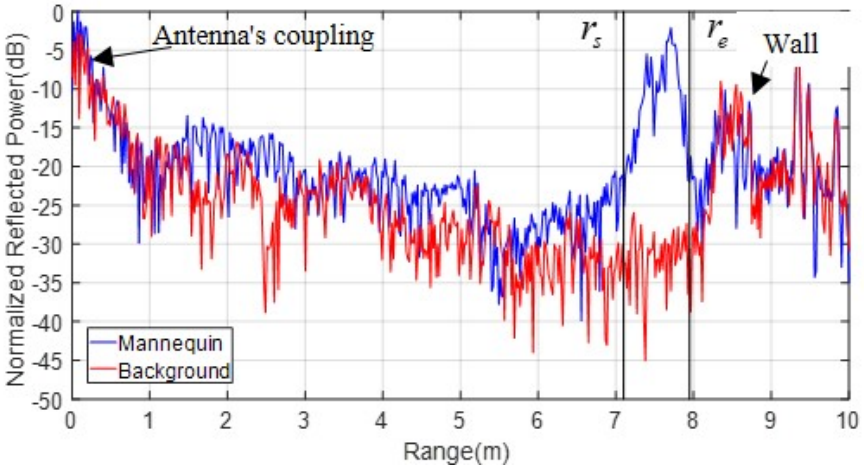

(b)

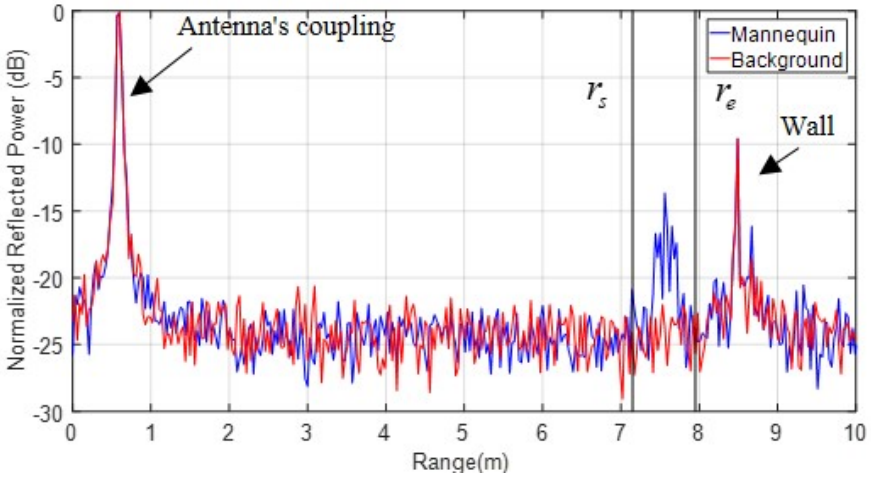

(c)

Fig. 5.4 Range profiles of a child pedestrian with 5GHz bandwidth at (a) 24 GHz, (b) 150 GHz and (c) 300 GHz

The repeatability of the results and the experimental setup used in the RCS measurements was assessed by two tests. Firstly, the short-term repeatability of the setup, aimed to assess the stability of the radar system and environment, was estimated by measuring the received power from the target during the same day once every hour for 10 hours, without modifying the setup. Secondly, a long-term repeatability of the results was determined by comparing the results of measurements made under the same conditions but on different days, so that a setup disassembly and re-assembly was made in between. The setup repeatability was assessed comparing the integral range profile R_i of the mannequin at one aspect angle. Results have demonstrated a very high repeatability: it was found that at 300 GHz the standard deviation of the average measured RCS is about 0.9 dB for the short-term assessment and for the long-term assessment it is 1.9 dB.

5.2.3 RCS calibration with metal sphere

A polished steel sphere with a radius of 18 cm (RCS=-9.9 dBsm) was used as reference target to perform the RCS calibration procedure explained in Section 3.4.2. A smooth sphere is an isotropic target for monostatic radars, so that there is no need for the alignment of the sphere with respect to the radar. Moreover, due to the fact that the polished metallic sphere represents a point-like reflector any measurement uncertainty that can arise due to the effect of non-planar returns to the antenna is reduced. As shown in Figure 5.5 the calibration sphere is suspended by a thin woollen string of very low reflectivity from the ceiling, to avoid the use of any support that could interact with the reflection from the target.

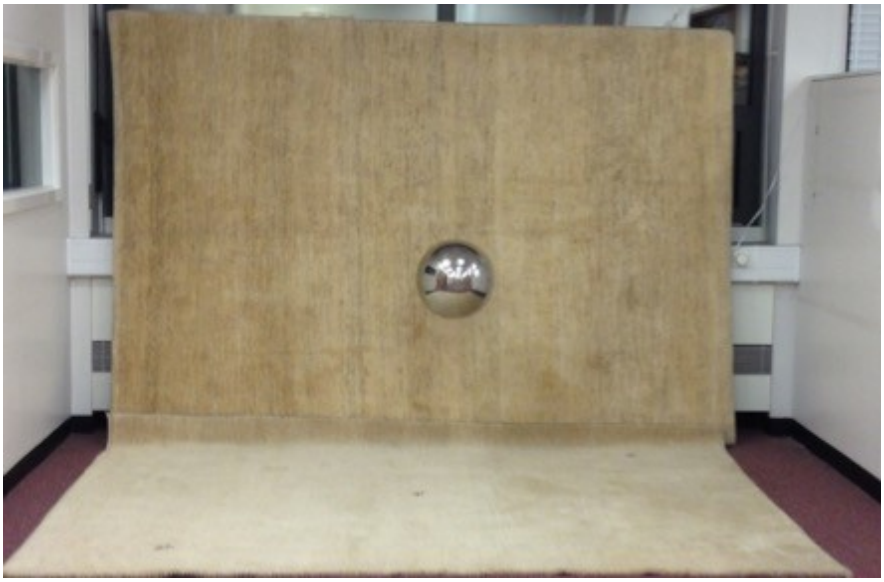

Fig. 5.5 Setup for the measurement of a calibration sphere

Measurements of the calibration sphere were also used to define the type of integration to perform among multiple measurements, to increase the signal to background ratio (SBR). Firstly, the number of range profiles from consecutive measurements to integrate was chosen to be 10, according to Table 3.1, to provide a trade-off between noise floor, required sensitivity, and acceptable acquisition time. Secondly, the type of integration was chosen. Ideally, coherent integration, which leads to a higher processing gain, should be applied. However due to the phase instability caused by the phase noise generated by the electronic components used in our low-THz systems, after a series of tests on a reference target it was concluded that non-coherent integration should be used instead for our experiments to improves the SBR. For example, at 300 GHz with 5GHz bandwidth, about 8 dB improvement of the SBR is shown (Figure 5.6) after non-coherent integration of 10 returns from a calibration sphere.

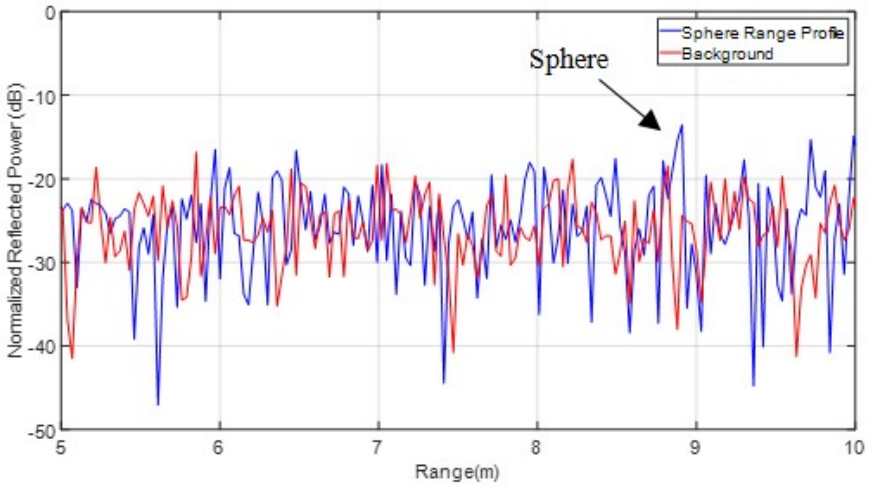

(a)

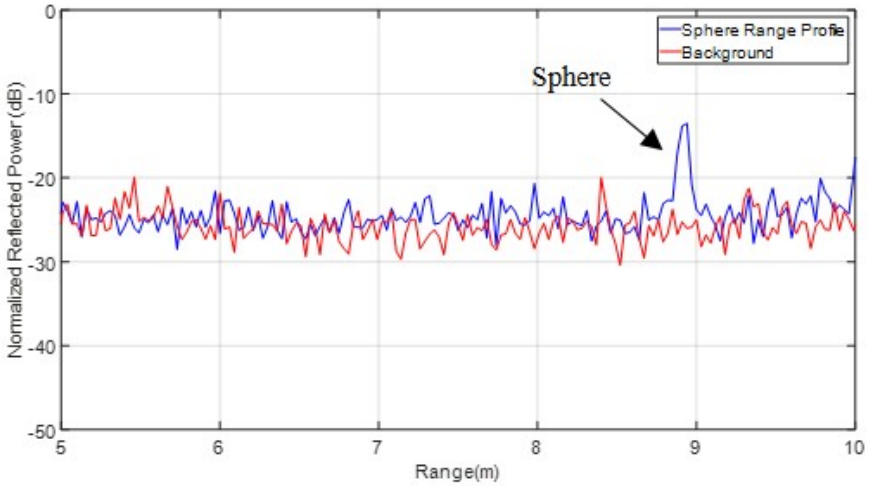

(b)

Fig. 5.6 HRRP at 300 GHz of a calibration sphere with coherent (a) and non-coherent (b) integration of 10 measurements

Finally, Figure 5.7 shows the range profiles of the sphere after non-coherent integration at 24, 150 and 300 GHz. The plots demonstrate one strong return from the specular point on the sphere.

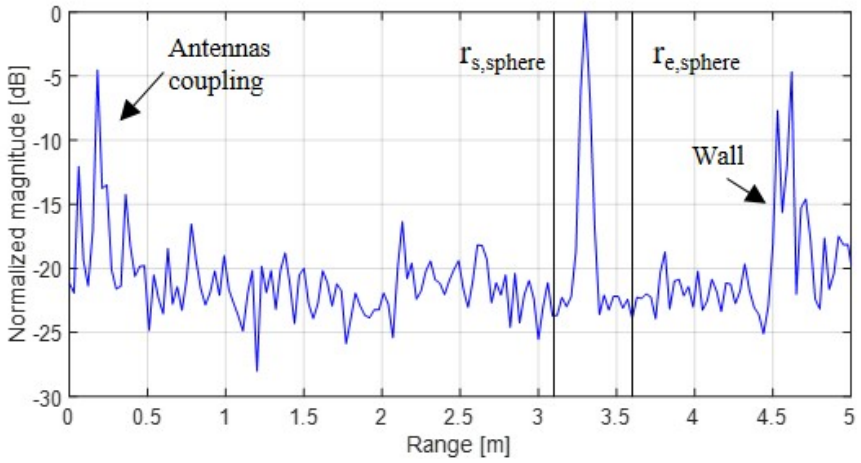

(a)

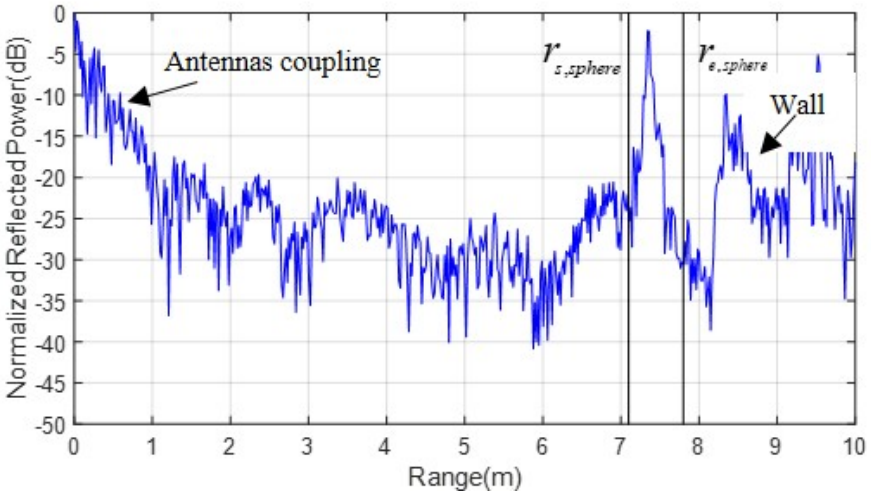

(b)

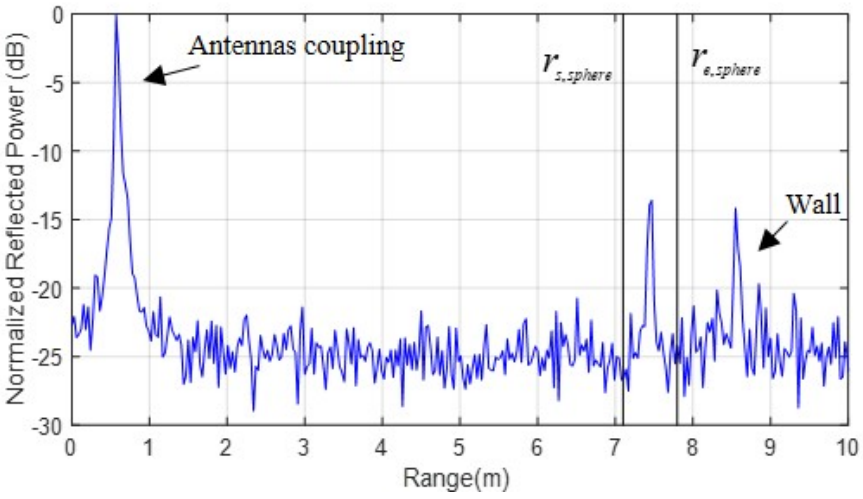

(c)

Fig. 5.7 Range profiles of a calibration sphere measured at (a) 24 GHz, (b) 150 GHz and (c) 300 GHz

5.2.4 High resolution range profiles

High resolution range profiles are obtained through the methodology described in 3.4.3. An example of HRRP at 300 GHz versus azimuth angle is shown in Figure 5.8(a).

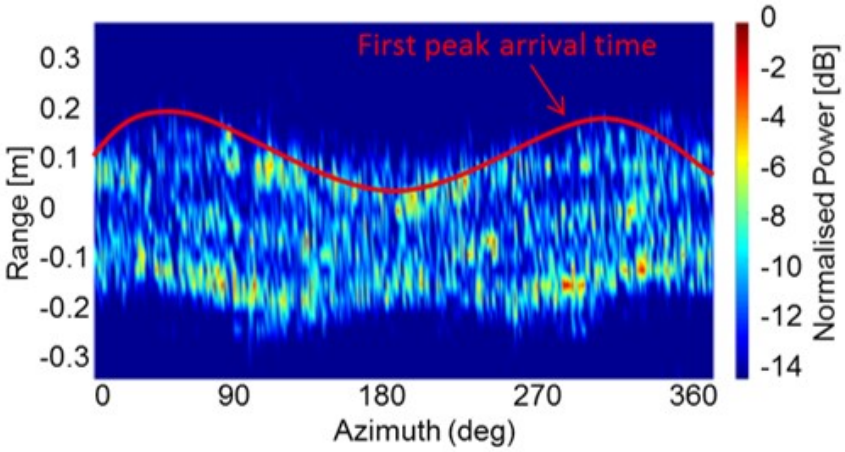

(a)

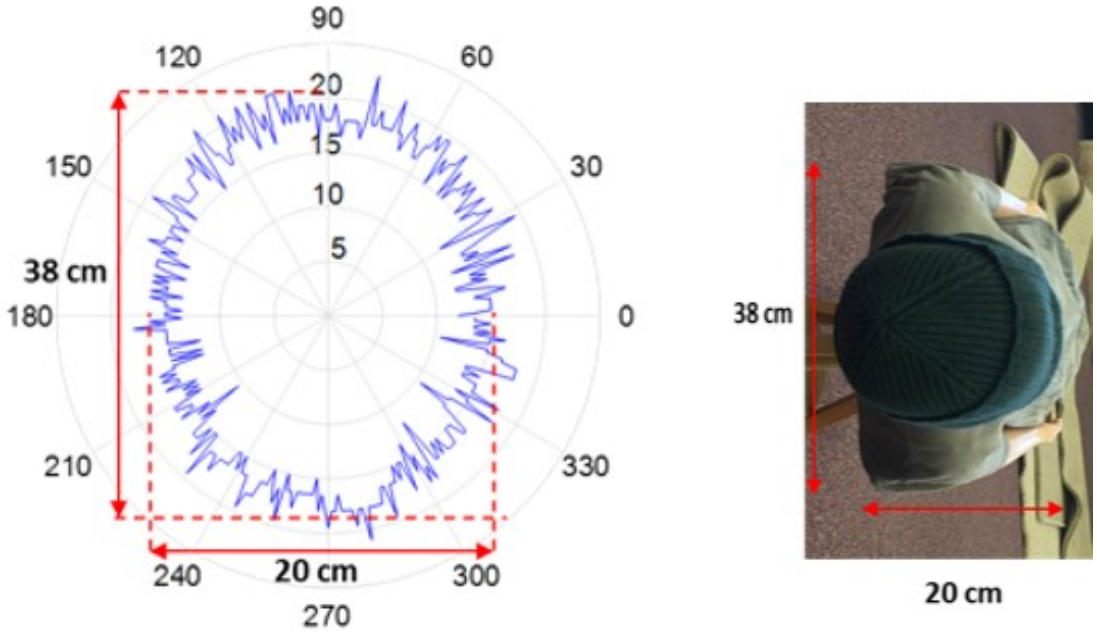

(b)

Fig. 5.8 Contour reconstruction of a child mannequin. (a) Position of the first peak in the HRRP for each azimuth angle; (b) contour reconstruction from the position of the start arrival times

This result highlights the fact that using a wide bandwidth and, therefore, a very fine range resolution of 3 cm, even the small target can be modelled as a set of closely-

spaced scattering centers distributed in range, outlining the shape of the target, which is observed as the range spread in the Figure 5.8(a). The range spread of a target represents a feature which can be used for classification purposes, in particularly for estimation of the dimensions of the object. For example, by estimating the range spread and its start point in the HRRP at each measured aspect angle, it is possible to reconstruct the contour of the target as illustrated in Figure 5.8(b), even though ambiguously as the vertical spread cannot be evaluated due to the lack of vertical resolution measurement setup.

Target range profiles versus azimuth, $R_i(\phi)$ (Eq. 3.31) measured at three frequencies with 5 GHz bandwidth are shown in Figure 5.9. As expected all three demonstrate nearly the same range spread of the target which determines the same sinusoidal behaviour associated with the changing of the aspect angle. However with the frequency increase the pattern becomes more uniform indicating higher sensitivity of the surface to the wavelength, in fact rather specular scattering is observed at 24 GHz, while more diffuse scattering on the target surface is obtained at 150 GHz and 300 GHz. In fact, as surface becomes rough at higher frequencies we can expect relatively similar level of returns from all the resolution cells occupied by the target [21] (13 range bins in the case of the mannequin at the azimuth position of 90°), which define the more 'continuous' pattern compared to the 'discrete' one at low frequency.

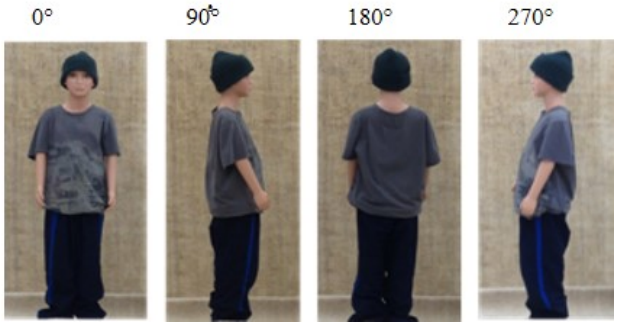

(a)

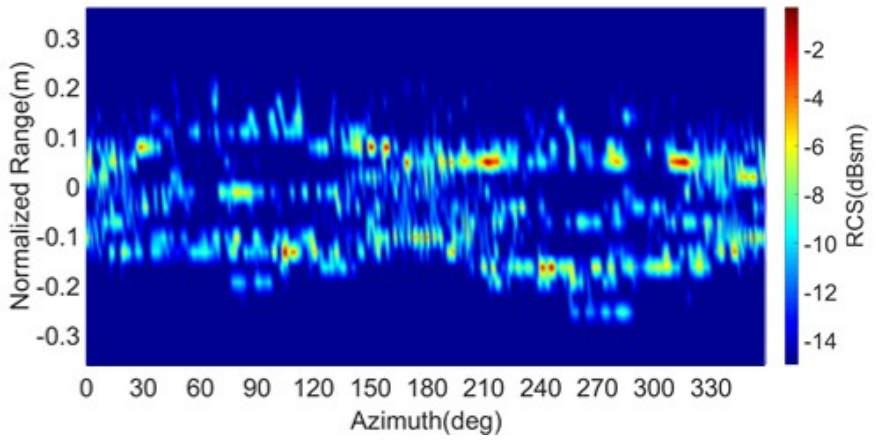

(b)

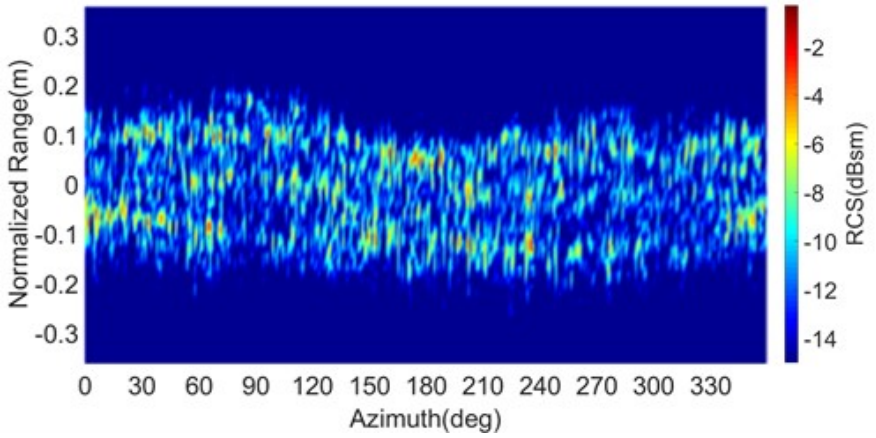

(c)

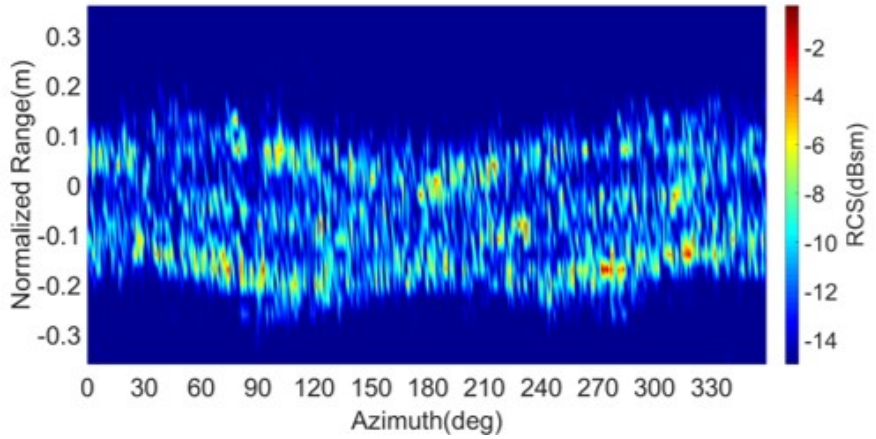

(d)

Fig. 5.9 Aspect angle of the child mannequin rotating on the turntable corresponding to the front, rear, left, and right azimuth positions (a). Child pedestrian HRRP vs azimuth for 24 (b), 150 (c) and 300 (d) GHz Bands

5.2.5 RCS estimation

The polar plots of the calibrated average RCS versus azimuth with wide and narrow bandwidths, $\sigma_{WB,NBw}(\phi)$ (Eq. 3.29) and $\sigma_{WB,WBw}(\phi)$ (Eq. 3.32), are shown in Figure 5.10.

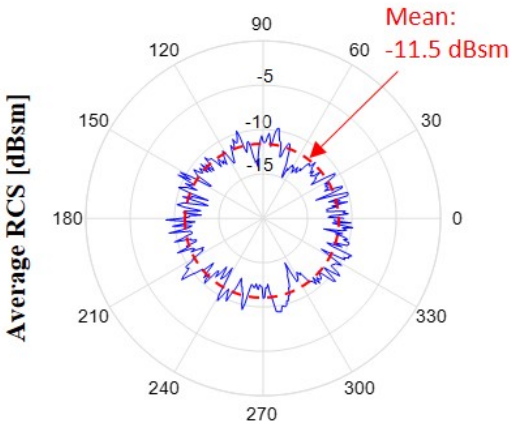

24 GHz – BW 5 GHz

(a)

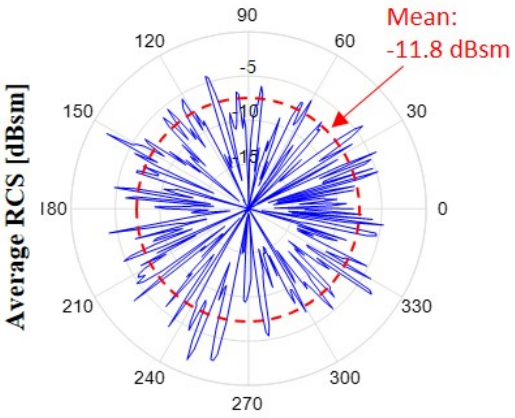

24 GHz – BW 300 MHz

(b)

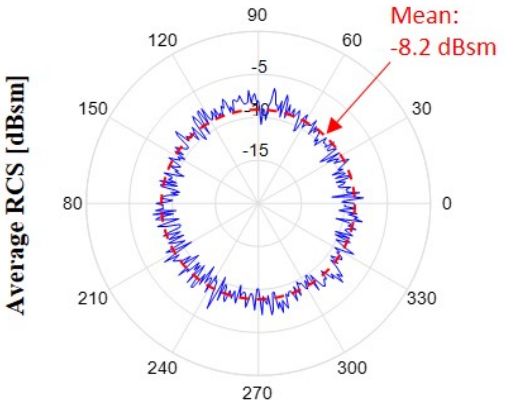

300 GHz – BW 5 GHz

(c)

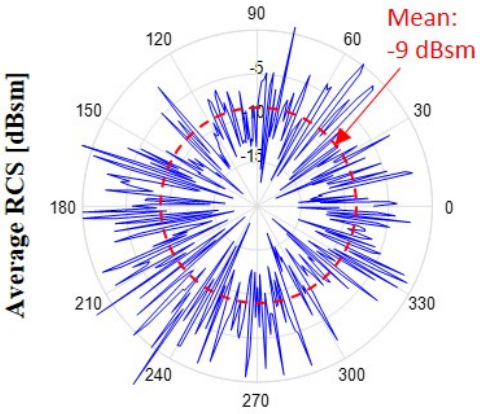

300 GHz – BW 300 MHz

(d)

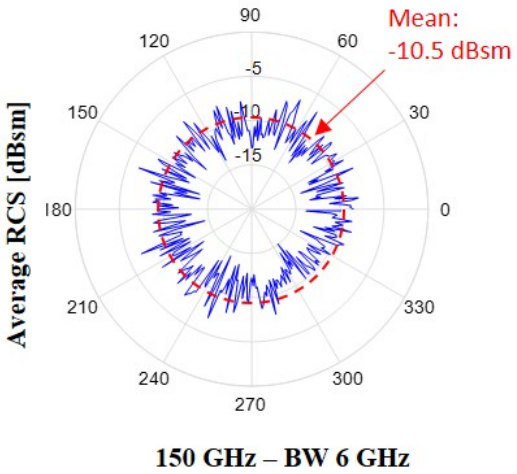

(e)

Fig. 5.10 Polar plots of the calibrated RCS vs azimuth angles at 24GHz with 5GHz (a) and 300 MHz (b) bandwidth. At 300GHz with 5GHz (c) and 300 MHz (d) bandwidth. At 150GHz with 6GHz bandwidth (e)

It can be seen that for 5 GHz bandwidth at all frequencies the average RCSs of the measured child mannequin do not depend significantly on the aspect angle and with the increase of the frequency the pattern becomes smoother, so that the variance of the intensity of returns decreases. Yet, the variance is less than 10 dB for all frequencies, in contrast to the results obtained with narrow band signals where it is larger than 20 dB. Overall the results indicate the advantage of using a wide bandwidth and high frequencies to reduce target fluctuation typical for traditional radar. Moreover, it can be noticed a slightly increase of the mean RCS with the raise of the frequency.

5.2.6 RCS fluctuation statistics

Figure 5.11 shows the histograms and CDFs of the average RCS as a function of aspect angles, for the different bands and bandwidths measured.

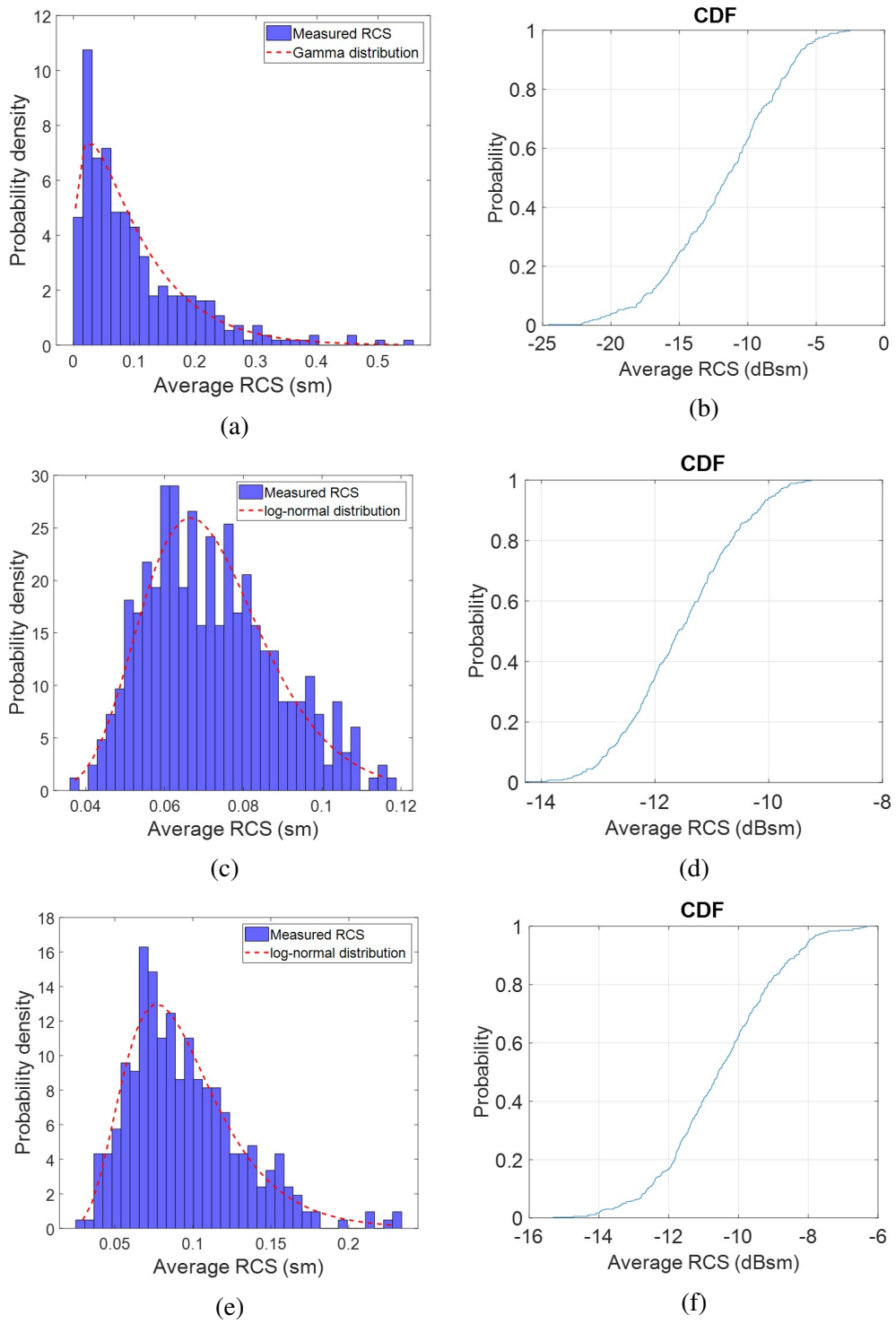

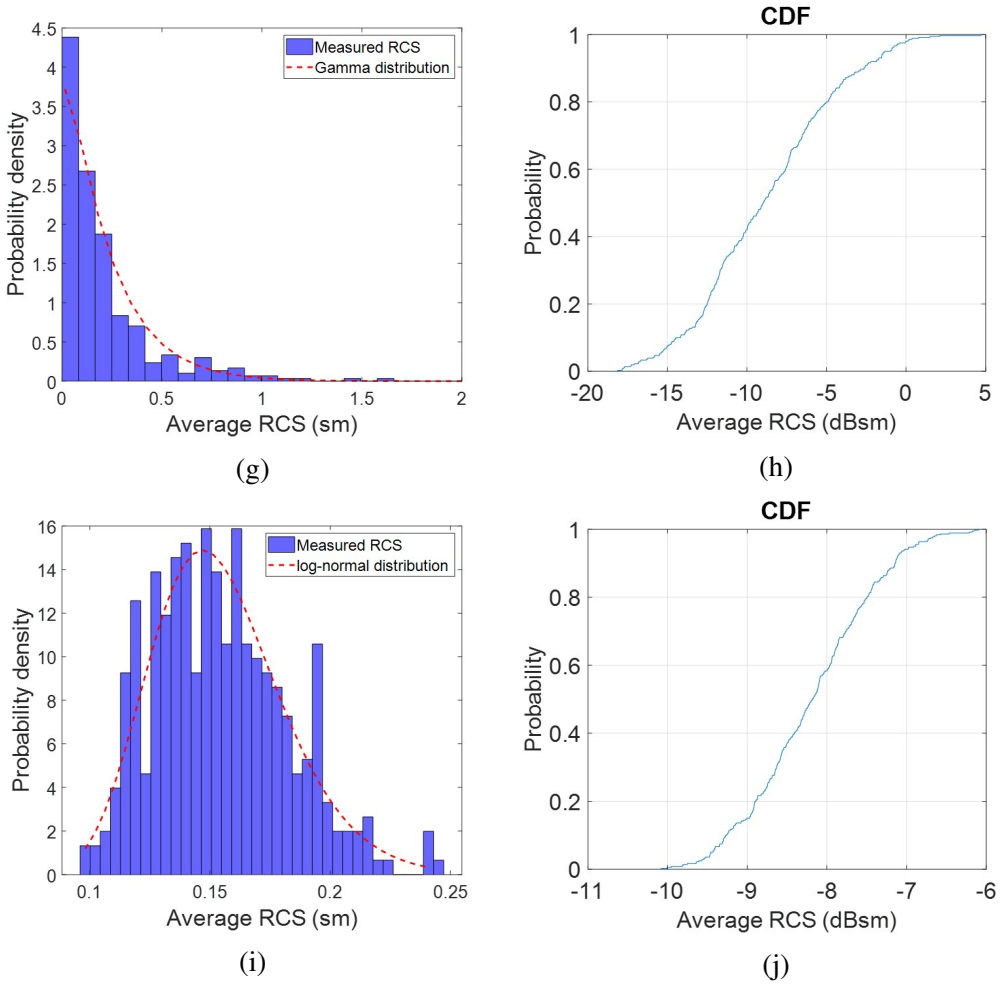

Fig. 5.11 Statistics of the child pedestrian RCS vs azimuth angles. Histograms at 24GHz with 300MHz (a) and 5GHz (c) bandwidth, CDFs at 300GHz with 300MHz (b) and 5GHz (d) bandwidth. Histogram at 150GHz with 5GHz bandwidth (e), CDF at 150GHz with 6GHz bandwidth (f). Histograms at 300GHz with 300MHz (g) and 5GHz (i) bandwidth, CDFs at 24GHz with 300MHz (h) and 5GHz (j) bandwidth

Following the methodological analysis illustrated in Section 3.4.5, the probability distribution models best fitting the measured distributions are identified by calculating the errors of fit summarized in Table 5.2.

Table 5.2 Error of fit for the child pedestrian RCS against different distribution models

Distribution model	Frequency GHz	Bandwidth GHz	Parameters (Table 3.3)	Error of fit % (eq. 3.39)
Swerling 1/2	24	0.3	$\sigma_m = 0.25$	0.075
		5	$\sigma_m = 0.14$	5.045
	150	5	$\sigma_m = 0.77$	2.96
	300	0.3	$\sigma_m = 0.22$	0.103
		5	$\sigma_m = 0.15$	6.02
Swerling 3/4	24	0.3	$\sigma_m = 0.25$	1.24
		5	$\sigma_m = 0.14$	3.41
	150	5	$\sigma_m = 0.77$	1.37
	300	0.3	$\sigma_m = 0.22$	8.79
		5	$\sigma_m = 0.15$	4.54
Gamma	**24**	**0.3**	$\alpha = 1.35, \beta = 0.19$	**0.038**
		5	$\alpha = 19.98, \beta = 0.007$	0.037
	150	5	$\alpha = 7.43, \beta = 0.1$	0.13
	300	**0.3**	$\alpha = 1.11, \beta = 0.2$	**0.046**
		5	$\alpha = 31.16, \beta = 0.005$	0.23
Weibull	24	0.3	$k_w = 0.26, \lambda_w = 1.16$	0.41
		5	$k_w = 0.15, \lambda_w = 4.67$	0.95
	150	5	$k_w = 0.86, \lambda_w = 2.77$	1.46
	300	0.3	$k_w = 0.22, \lambda_w = 0.99$	0.19
		5	$k_w = 0.17, \lambda_w = 5.64$	1.83
Log-normal	**24**	0.3	$(ln(\sigma))_m = -1.8, (ln(\sigma))_{sd} = 0.97$	1.04
		5	$(ln(\sigma))_m = -2.01, (ln(\sigma))_{sd} = 0.23$	**0.008**
	150	**5**	$(ln(\sigma))_m = -0.33, (ln(\sigma))_{sd} = 0.37$	**0.019**
	300	0.3	$(ln(\sigma))_m = -2.02, (ln(\sigma))_{sd} = 1$	1.44
		5	$(ln(\sigma))_m = -1.89, (ln(\sigma))_{sd} = 0.18$	**0.17**

The best fit is the Gamma distribution for the measurements with narrow bandwidth and the log-normal for the wide bands. These results are direct consequence of the different variance of the RCS vs aspect angle for different range resolutions. In contrast with low resolution waveforms, high resolution produces similar values of the average returns at different aspect angles. Wanting to confine the analysis to the classic Swerling models, results show that for the wideband measurements the distribution approaches the Swerling Case 3 fit while for the narrowband measurements it is closer to the Swerling Case 1 model. This result is expected considering the nature of the human target, being comprised of multiple scatterers with one usually being dominant, which would indicate a Swerling 3 target, however with a coarse resolution these scatterers are not distinguishable across aspect because conglomerated and averaged into one cell, producing a Swerling 1 distribution.

Statistics obtained from the histograms and CDFs are summarized in Table 5.3.

Table 5.3 Child pedestrian RCS statistics

Frequency GHz	BW GHz	Mean dBsm	Standard deviation, dB	Median dBsm	Dynamic range, dBsm (see Section 3.4.5)
24	0.3	-11.82	4.21	-11.58	[-17.25 -6.3]
	5	-11.45	0.98	-12.79	[-12.65 -10.18]
150	5	-10.53	1.62	-10.58	[-12.83 -8.45]
300	0.3	-8.8	4.34	-8.97	[-18.13 -2.95]
	5	-8.99	0.78	-8.18	[-10.16 -8.06]

The mean and median values show that overall there is no significant differences between narrow and wide bandwidth measurements. Moreover, the values obtained in the measurements are close to that reported in literature, in particular to the results of measurements at 24 and 77 GHz reported in [126]. Finally, results of standard

deviations and dynamic ranges indicate the advantage of using a wide bandwidth and high frequencies to reduce target fluctuation typical for traditional radars.

5.2.7 24 GHz child pedestrian RCS computation

The simulation is a conventional approach to validate the results of measurements and, therefore, to justify the chosen methodologies. The computer simulation technology (CST) microwave studio (MWS) [128] allows the calculation of the monostatic RCS of electrically large objects using the method of moments. However, due to the complexity of the realistic human model at very short wavelengths corresponding to low-THz frequencies, and the fact that electrical properties of material including clothes are not always known at such frequencies, it was used the expedient to attempt simulations at the lower standard automotive frequency, for instance, 24 GHz, to compare results of simulation with results of measurements at this frequency and, then, to contrast these characteristics to that measured at low-THz frequencies of interest. Additionally, it will justify the chosen methodology so that further work can be done at higher-frequency bands with confidence. The first step is to evaluate the accuracy of the simulated result versus mesh size. For this purpose, a reference object, a perfect electric conductor (PEC) sphere of radius of 18 cm, was simulated at 24 GHz. According to Mie theory (Section 2.3.6), reflection from a sphere with radius of 18 cm with respect to 1.25 cm wavelength corresponds to the optical scattering region. Figure 5.12 shows the convergence of the simulated results to the RCS theoretical value as the mesh sizes in the simulation reduce in respect to the wavelength, the convergence is found with an accuracy of 0.1 dBsm when the mesh cell size is lower than $\frac{\lambda}{8}$.

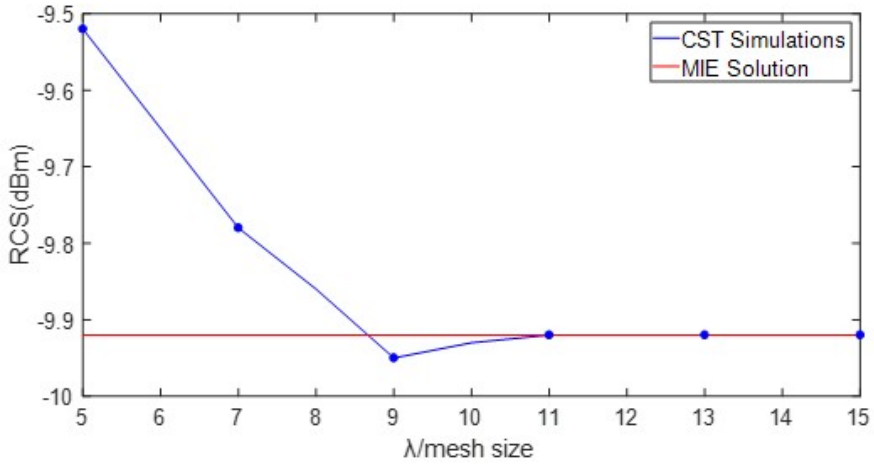

Fig. 5.12 Comparison between theoretical and simulated RCS of a sphere

Taking this result into account, a mesh size of $\frac{\lambda}{10}$ was chosen for simulations using a model corresponding to a body of a child of the same physical size as the mannequin used in experiments (Figure 5.13(a)). For the simulation PEC was used as a material of the body and its effect on the RCS is discussed later in this section. In Figure 5.13(b), the comparison of RCS calculated in CST with that measured at 24 GHz is shown. For the measurements the bandwidth of 300 MHz of the signal is chosen, defining range resolution of $0.5m$, so that the whole body is confined within one resolution cell.

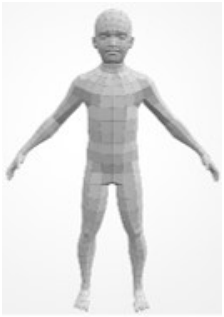

(a)

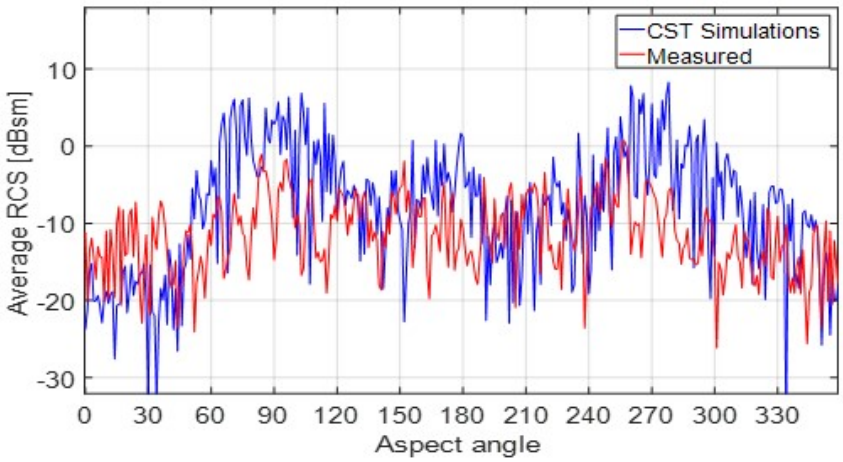

(b)

Fig. 5.13 (a) CST model of a child mannequin. (b) Comparison between full-wave simulated RCS and measured RCS of a child mannequin

While RCS patterns with respect to aspect angle are similar, the average power level of the simulated RCS within the azimuth angle range 50–340° is about 4 dB higher than that of the measured RCS. This discrepancy is likely due to the differences in surface material reflectivities of PEC and plastic body covered by clothes. Moreover, the higher level of measured RCS in this angular range might be due to the difference of geometrical features such as chin and eye cavities, acting as corner reflectors, of the mannequin and body built in CST. An analysis on the reflectivity of the CST child model shows that the difference of the amplitude using PEC material and dry skin material, with a dielectric constant of 18.99 and a conductivity of 22.84 S/m [129], is 6 dB; therefore, the measured average reflectivity of the mannequin stands between these two extremes, i.e. 4dB lower than the value obtained using PEC in the simulations.

Simulations at 300 GHz, where the wavelength is 12.5 smaller than at 24 GHz would require over 1 billion mesh cells for electrically accurate representation of a human. Moreover, without the exact knowledge of electrical–physical properties (dielectric permittivities, conductivities etc.) and material parameters (texture, density and thicknesses) of pedestrians' clothes, the results of the simulation may differ significantly from actual values, and therefore will lead to inaccurate estimation of actual reflectivities. For this reason, in this work, the key method of the RCS evaluation is based on measurements.

5.2.8 Effect of clothing

An additional set of measurements was carried out to assess the impact of clothing on the reflectivity. All the results presented in the previous sections were obtained with the mannequin wearing 100% cotton clothes. Two other sets of measurements were made with a mannequin cladded in (i) a 100% woollen jumper and (ii) a high-viz jacket, made of 100% of polyester. Calculated global RCS averages, summarized in Table 5.4 and Figure 5.14 show that at 24 GHz there is very little difference in the reflectivities

of different clothing; this seems due to the fact that at relatively low frequencies the clothes are almost transparent to electromagnetic waves. The variability due to clothing increase with the rise of the frequency and at 300 GHz the RCS of the mannequin wearing high-viz jacket is 3 dB higher than that of the woollen jumper. This result confirms the finding that a woollen carpets acts as absorber at mm-wave and above [80].

Table 5.4 Child pedestrian mean RCS for three types of clothes

Frequency	RCS, dBsm		
	24 GHz	150 GHz	300 GHz
Cotton t-shirt	-11.4	-10.5	-8.2
Woollen jumper	-11.9	-12.2	-11.3
High-viz jacket	-10.9	-9.4	-7.3

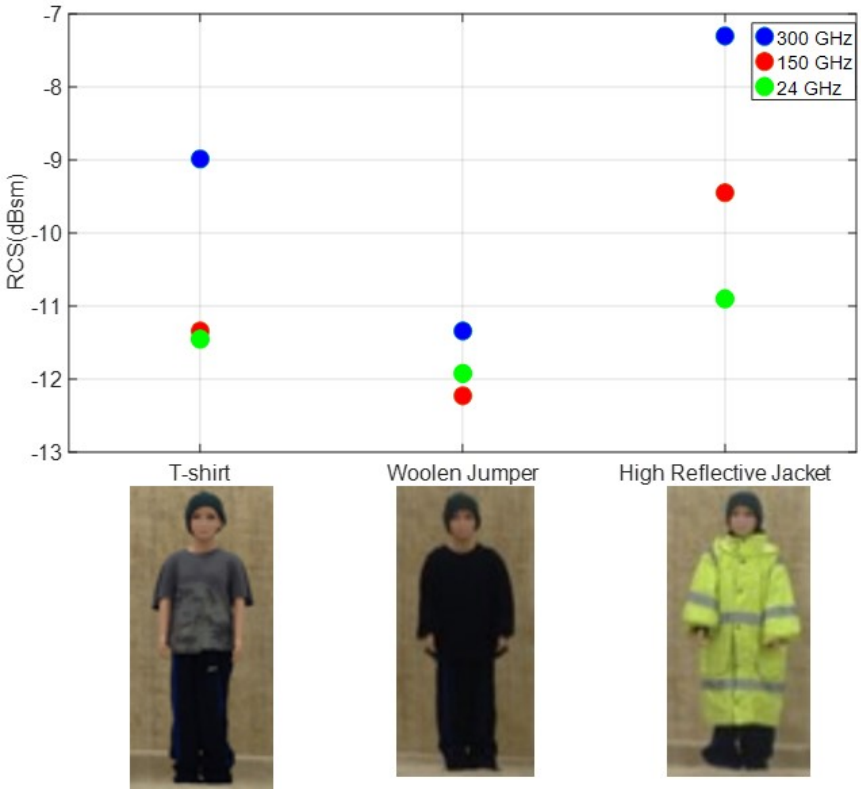

Fig. 5.14 Comparison of the mean RCS for three types of clothes worn by the child pedestrian

5.3 Motion characteristics of pedestrians in the Low-THz band

Chen [52] has been the pioneer of the micro-Doppler (μD) study of human motion, following the work of Boulic, N. Thalmann, and D. Thalmman [73] he proposed a radar signal model of the μD generated by a walking human. The model is based on empirical mathematical parameterizations, derived from biomechanical experimental data, of the body parts which are modelled as sphere, cylinders or ellipsoids. The movement of individual body parts is described by their trajectories, translations and rotations, as a function of time. Subsequently, more complex models to predict the human μD signatures were build, like in [130] using computer animation data or in [131] using motion capture sensors devices.

The time-frequency representation of the human μD could be used to detect pedestrians and classify their activity or among the other road targets. Features in the signature extracted from real radar data, such as the periodicity of the leg swing component, the frequency spread of the signature or the velocity of the bulk motion, are distinctive of human motion. Several works have been done to develop classifiers based on feature extraction. For example, in [132], a classifier of a support vector machine (SVM) using the features of target stride, frequency of the limb motion, bandwidth of a micro-Doppler, and distribution of the strength of a Doppler signal from a spectrogram, is implemented to discriminate between humans, dogs, bicycles, and cars. In [133] a μD classification method on measured data at 77 GHz is based on selecting the strongest parts of a Cadence-Velocity Diagram (CVD), which expresses how the curves in the μD repeat. The quality of the signature is therefore particularly important for the extraction of appropriate features to build robust classification algorithms.

The main goal of this study is the introduction of a potential low-THz radar for automotive application, in the following sections experimental results of pedestrians μD,

including reflectivity, in the low-THz band will be shown and compared to traditional automotive radar frequencies. The pedestrian identification itself is outside the scope of this study. The work presented in the following sections was published in [120, 121].

5.3.1 Micro-Doppler signatures

The aim of the μD measurements was the comparison between the quality of the signatures obtained with the standard mm-waves radars (24 GHz) and in the low-THz band. It is expected that by taking advantage of the defuse scattering behaviour of higher frequency waves, a clearer pattern of the μD signatures of a walking pedestrian can be obtained to provide its better identification and motion parameters estimation. Hence, although automatic target recognition algorithms would require signal length of few milliseconds, all the results in this section are shown for signals of 5 seconds duration. Measurements were carried out with the CW radars shown in section 3.5 and processed using STFT, as discussed in Section 3.2.1, Table 5.5 summarises the parameters used.

Table 5.5 Parameters of the μD measurements

	24GHz	300GHz
System parameters		
Antennas beamwidth, deg	20/20	10/10
Output power, dBm	10	-17
IF Bandwidth, KHz	10	10
Sampling frequency, KHz	2	8.3
Processor parameters		
Time window, s	0.1	0.1
Windows overlap, %	50	50

The measurements were performed in the same anechoic space used to evaluate the pedestrian RCS and described in Section 3.6.2. In this case the pedestrian is walking on the spot at a distance of 4 m and 2 m from the 300 GHz and 24 GHz antennas, respectively, these distances are enough to achieve an acceptable SNR and yet measure μD contribution from the human torso, arms and upper legs, as shown in the Figures 5.15 and 5.17. The spectrograms of the pedestrian walking on the spot towards the radar at 24 GHz and 300 GHz are shown in Figure 5.16. In order to show clearly the signatures of the different segments, the colour scale is normalised to the received power maximum value and the dynamic range limited to -40 dB. The higher noise level noticeable in the 300 GHz spectrogram is due to the lower output power of the system. Compared to the signature at 24 GHz, the one at 300 GHz show clearer patterns described by the gait cycle, with the contributions from the movement of different body segments easily identifiable. The enhanced quality of the signature at higher frequencies is not only due to the higher Doppler shift produced, which is proportional to the carrier frequency, but it is specially achieved thanks to the higher sensitivity of small wavelength to surface roughness: each segment of the human body is comprised of several distributed scatterers and each of them describes a swing movement contributing to the overall μD signature.

The advantages of low-THz frequencies in providing high quality μD signatures are particularly evident when the aspect angle between the pedestrian movement direction and the radar LOS approaches 90°, in this case performances of classification algorithms can be compromised because the measured Doppler offset from the zero frequency clutter line is diminished. Figure 5.18 shows how, while at 24 GHz it is almost impossible to identify a pattern, at 300 GHz a clear signature is produced.

All the measurement results reported in this section are compared with simulation results obtained using the method based on Boulic-Thalman human model showing good agreement.

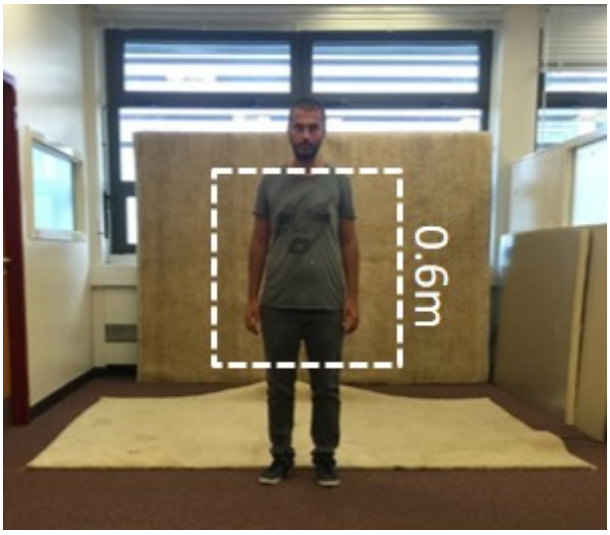

Fig. 5.15 Photo of the setup of a human walking on the spot in direction towards the radar

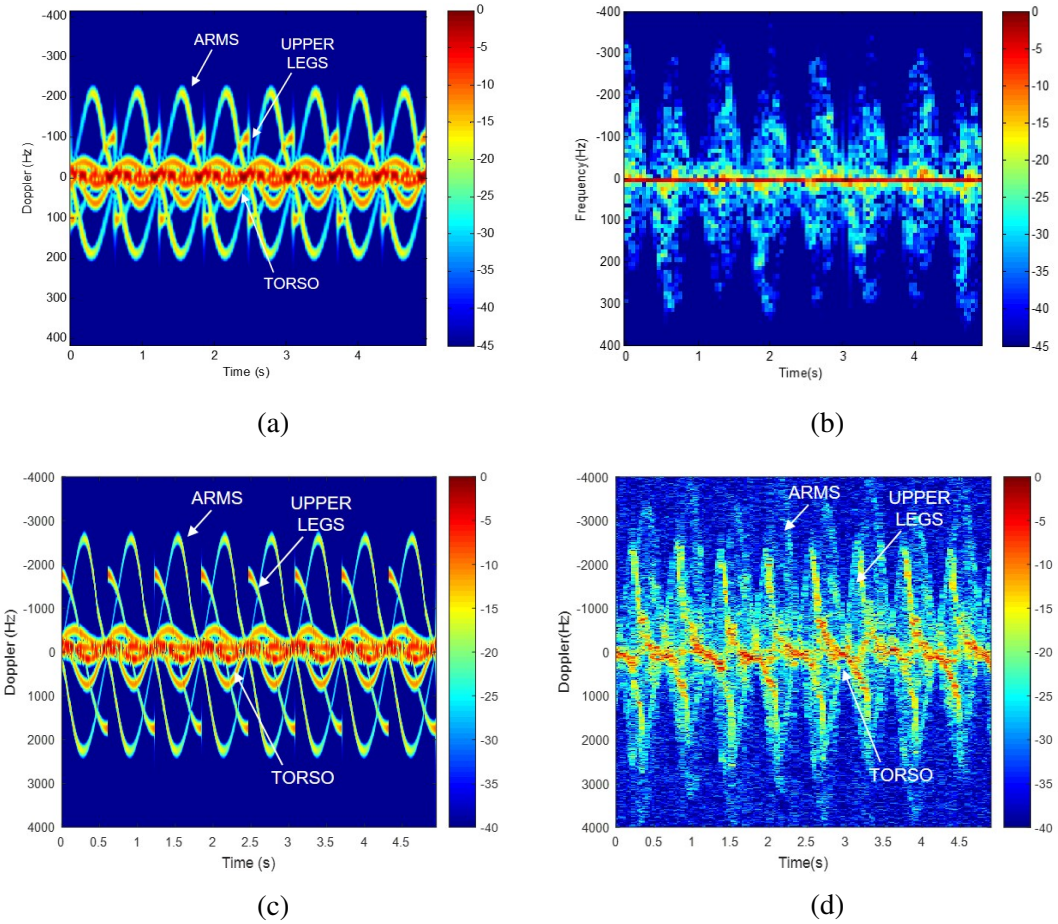

Fig. 5.16 μD signatures at 24 GHz simulations (a) and measurements (b). μD signatures at 300 GHz simulation (c) and measurements (d)

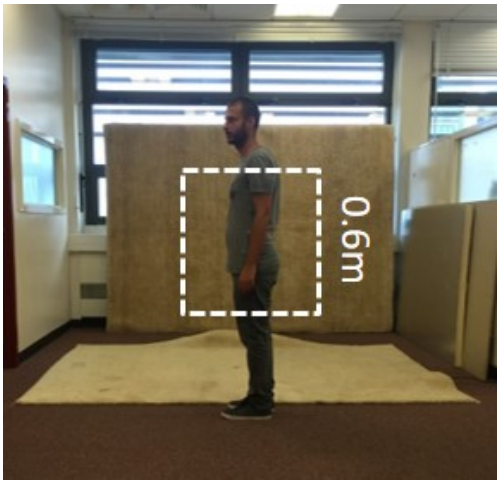

Fig. 5.17 Photo of the setup of a human walking on the spot in direction crossing the line of sight of the radar

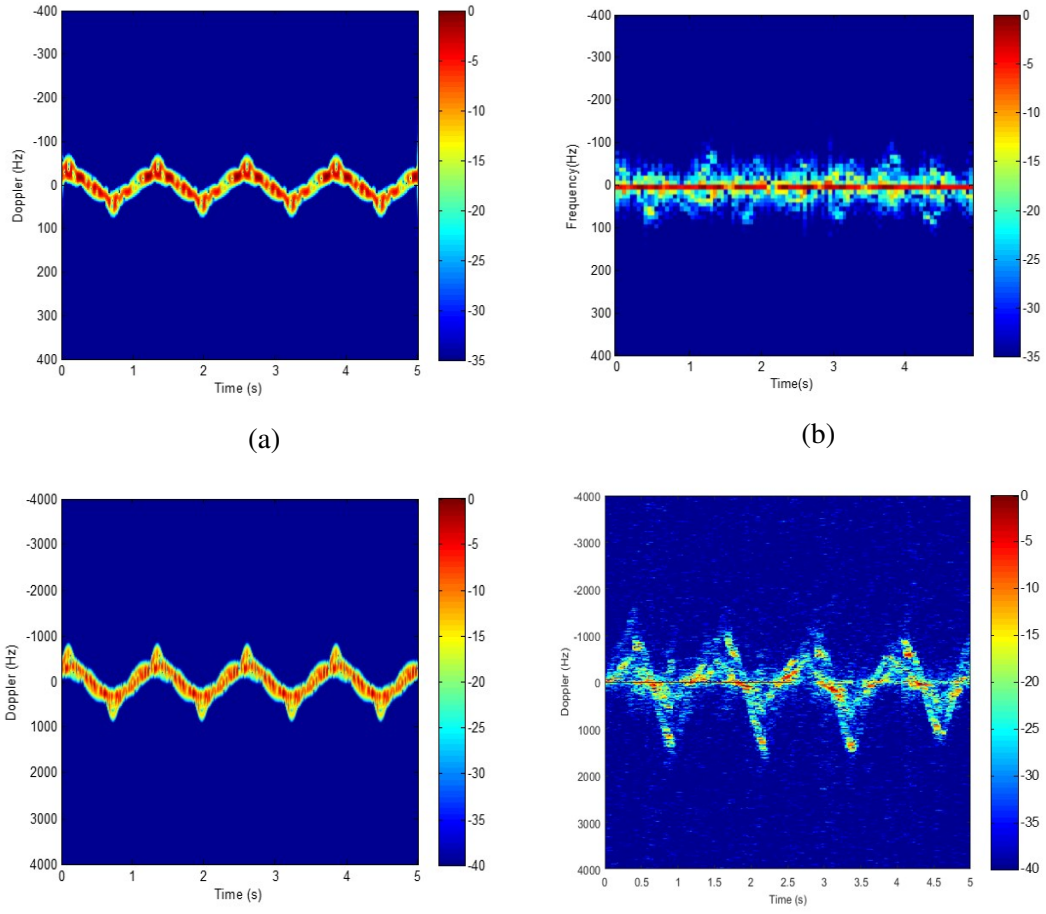

Fig. 5.18 μD signatures at 24 GHz simulations (a) and measurements (b). μD signature at 300 GHz simulation (c) and measurements (d)

5.3.2 Reflectivity analysis

For completeness of the analysis, a further set of measurements was carried out to characterize the reflectivity of the adult human at 300 GHz, in the same setup of the μD measurements. Having validated the RCS measurement methodology for the child by means of measurements and full-wave simulations at the standard automotive frequency of 24 GHz, an adult dummy is placed on the turntable at the a distance from the 300 GHz radar antennas, chosen to have the same illumination of the human body as for the subject in the μD measurements setup. A photo of the setup, with the footprint of the antennas beam on the mannequin, is shown in Figure 5.19.

Fig. 5.19 Photo of the adult mannequin RCS measurement setup

Figure 5.20 shows the range profiles of the child mannequin where it is highlighted the start and end range gating (r_s and r_e) of the region enclosing the target.

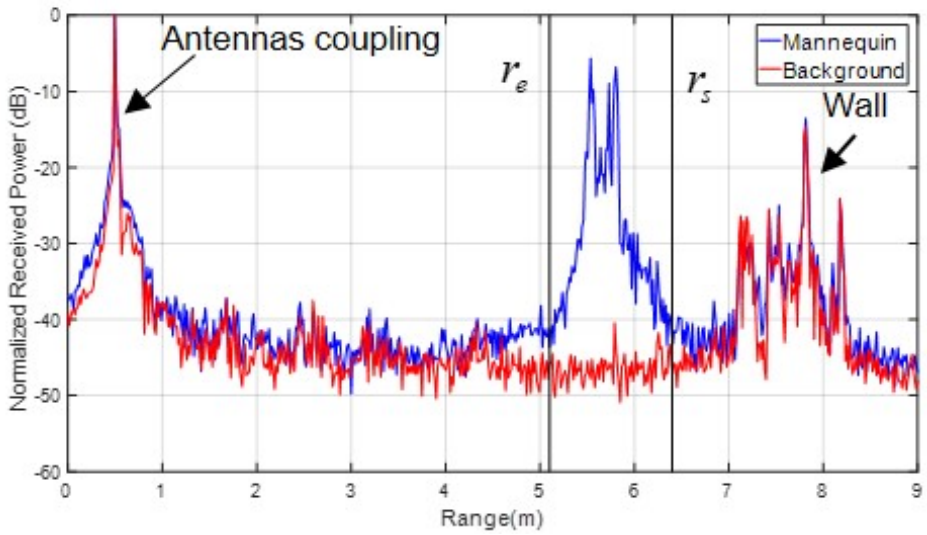

Fig. 5.20 Range profile of an adult pedestrian at 300 GHz

The range profile of the target with normalised amplitude plotted versus the azimuth angles of observation is shown in Figure 5.21(a), while Figure 5.21(b) shows the polar plot of the average RCS.

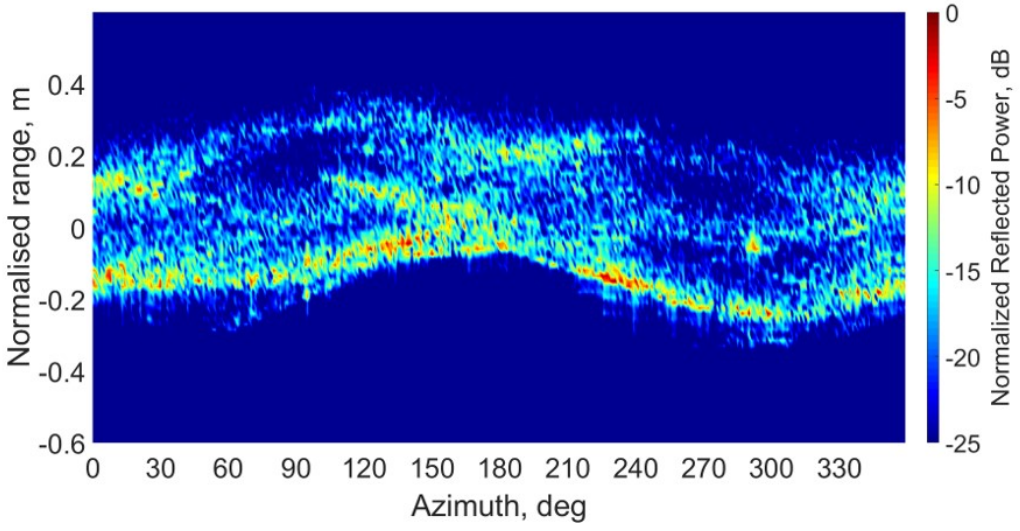

(a)

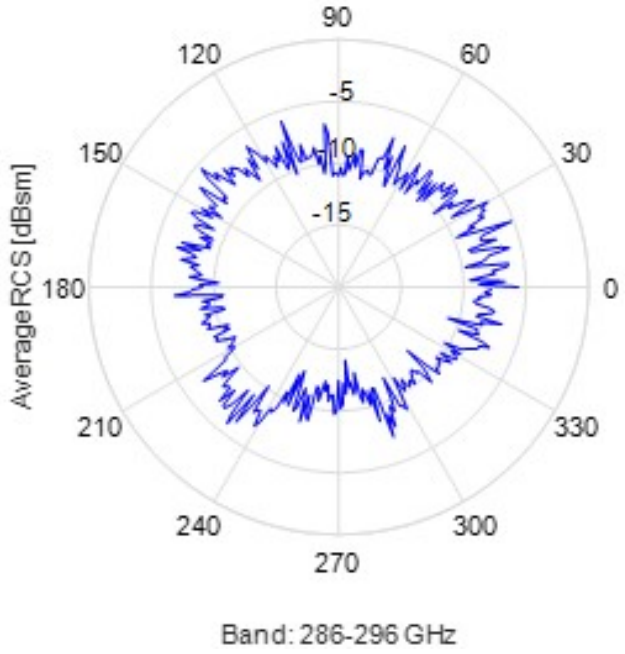

(b)

Fig. 5.21 HRRP vs azimuth (a) and RCS polar plot (b) of an adult pedestrian at 300 GHz

The RCS do not significantly depends on the aspect angle, the mean value is -7.6 dBsm and the distribution of variance has a spread of ±5 dB. This result is close to the values reported in literature for the standard automotive frequencies of 24 and 77 GHz [126]: -11.5 dBsm and -8.2 dBsm, respectively.

5.3.3 RCS and μD contributions from individual body parts

As illustrated in the previous section, a pedestrian walks as a system with different but coordinated movements of body segments. The analysis of reflectivity and motion characteristics of individual body parts can provide an improved understanding of walking human Doppler signatures, which can be particularly useful to develop models for target identification.

The use of the mannequin permitted to study the scattering contribution of RCS from different body parts. Figure 5.22 shows the pictures of the experimental setup of

measurements of torso, arms and legs for one aspect angle. The results obtained are shown in Table 5.6.

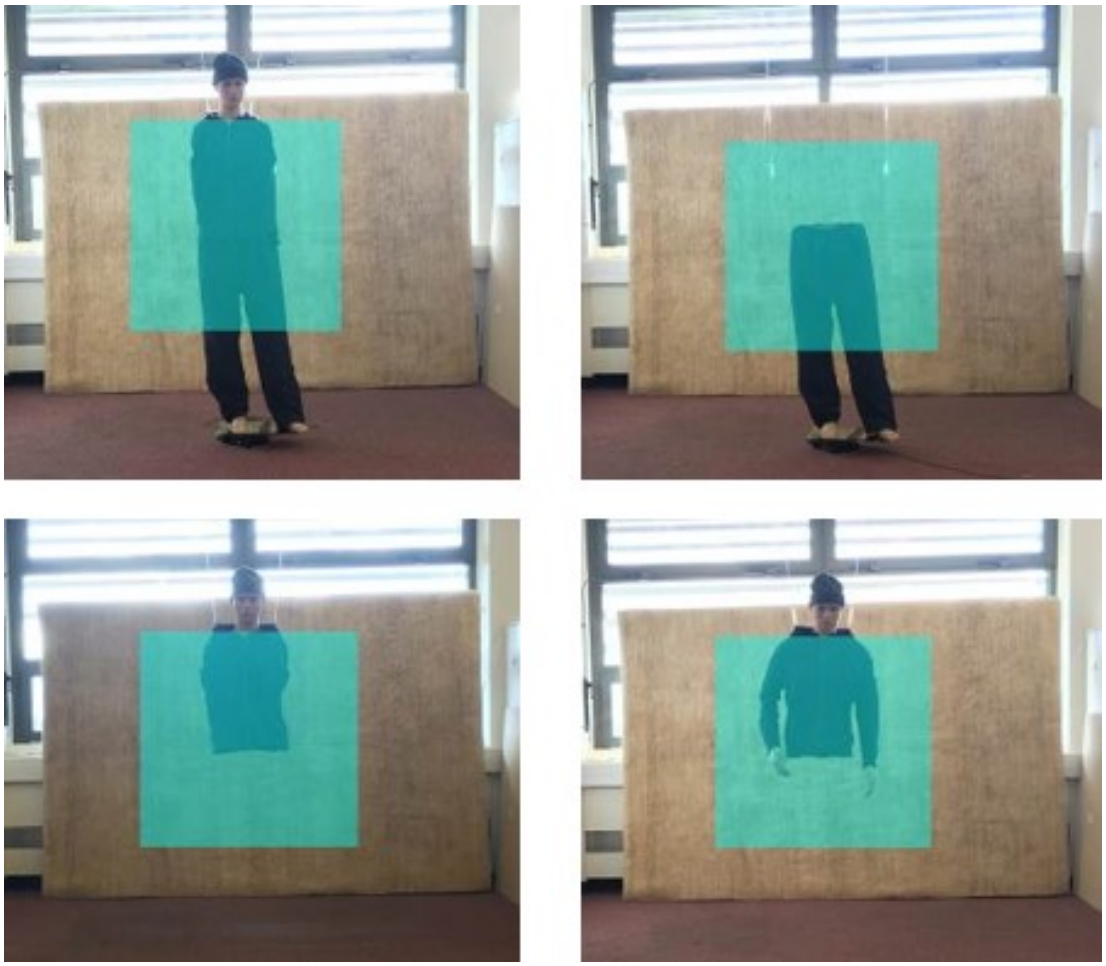

Fig. 5.22 Measurements setup of the different body parts measurements

Table 5.6 RCS of human body parts

Body part	RCS, dBsm
Torso + upper legs + arms	-7.62
Torso + upper legs	-9.73
Torso + arms	-12.01
Torso	-12.98
Upper legs	-10.32

The results show that the torso and legs dominate the reflection of the pedestrian and arms have lower RCS compared to those two parts.

Coming to the μD contribution from individual body part, the Doppler modulation produced by each segment was recorded from separate measurements: (i) human standing on the spot with only both arms swinging like in the normal walking gait (ii) the leg swing when human walked on the spot without arm swing and his torso kept stable; (iii) the swing of torso only, with no motions of arms and legs. Figures 5.23 and 5.24 (in the next pages) show the spectrograms of the body parts at 300 GHz and 24 GHz, also compared with the simulation results.

Overall, the comparison between results at the two frequencies confirm that the total pattern would be significantly clearer at 292 GHz, which shows the high potential for pedestrian detection and trajectory estimation.

The signature of arm swing, when the pedestrian is walking on the spot towards the radar, is comprised of the μD of two main segments, which can be identified in the hands (which produces the signatures with higher Doppler shift) and the shoulders, and are opposite in phase for the right and left arms. These two signatures are clearly distinguishable at 300 GHz while overlapped at 24 GHz. The same conclusion can be drown from the signature of the upper legs, at 300 GHz the μD of the hips (with higher Doppler shift) can be distinguished from the one of the knees. The sinusoidal signature produced by the torso is also very clear at 300 GHz. Regarding the μD produced by the body parts of the pedestrian crossing the line of sight, at 24 GHz is practically impossible to recognise a pattern in the signatures. Analysing the results at 300 GHz, which agree very well to the simulations, the right and left arms do not produce two patterns with opposite phase, because one of the arms is shadowed by the torso and when illuminated by the radar its radial velocity is similar to the other arm. The legs produce a quasi-triangular wave overlapped for the right and left leg, in fact while one of the legs is moving, the other is stable to sustain the body weight. The torso produces a

sinusoidal signature with a period double of the one for the pedestrian walking towards the radar, because only half of the torso is illuminated by the antennas beam.

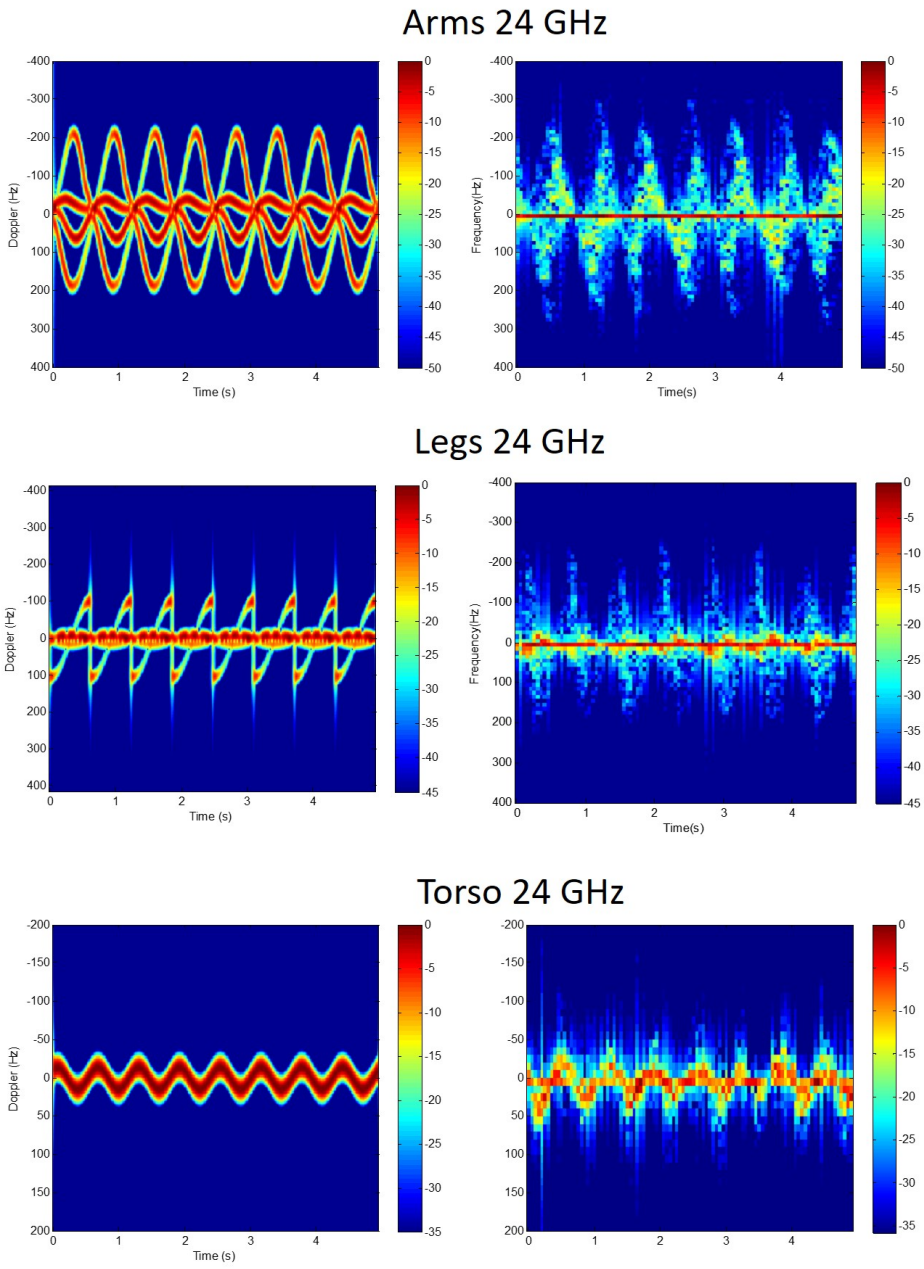

(a)

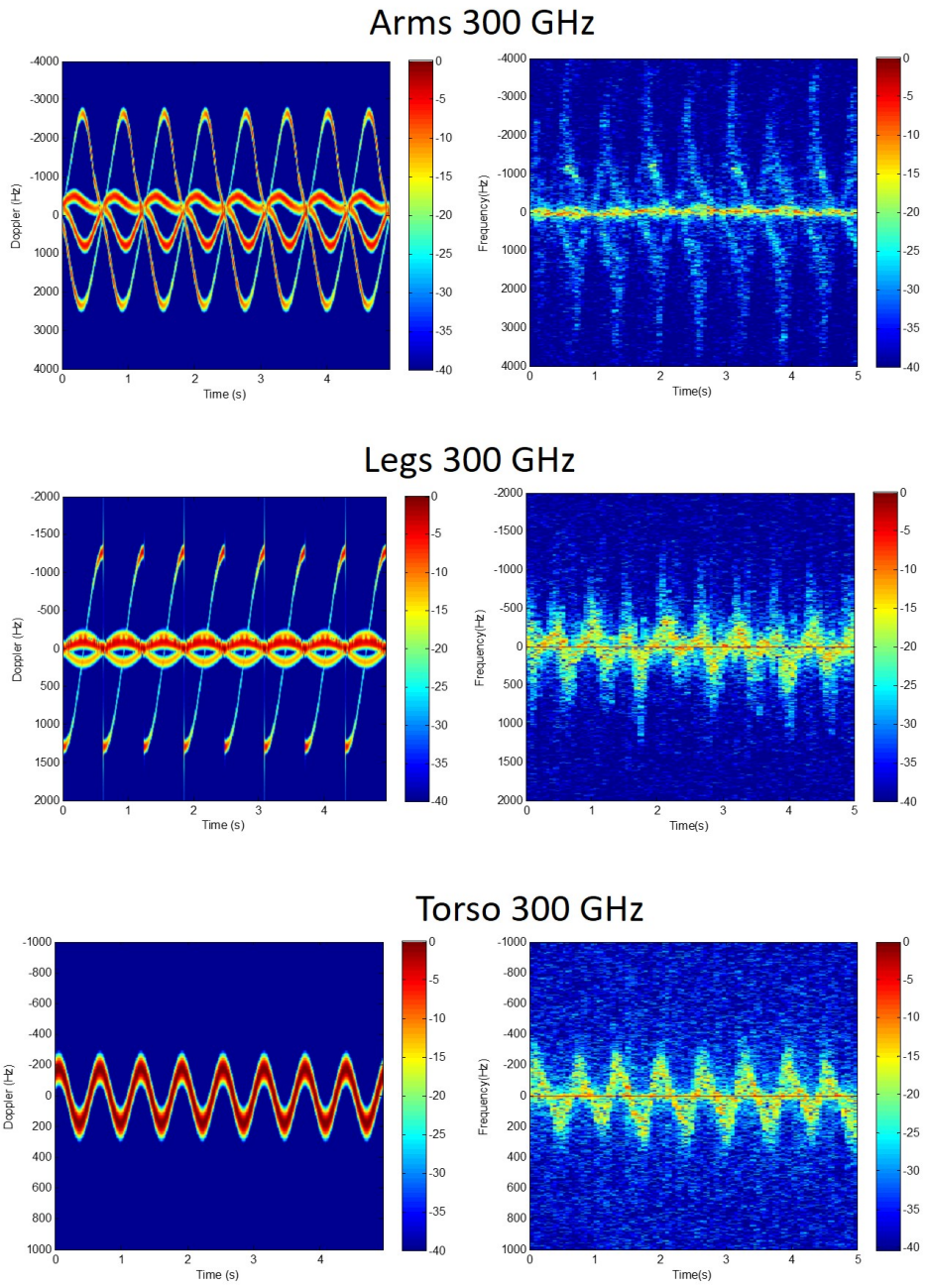

(b)

Fig. 5.23 μD signatures of different body parts of a human walking on the spot towards the radar at 24 GHz (a) and 300 GHz (b). Simulations (left) and measurements (right)

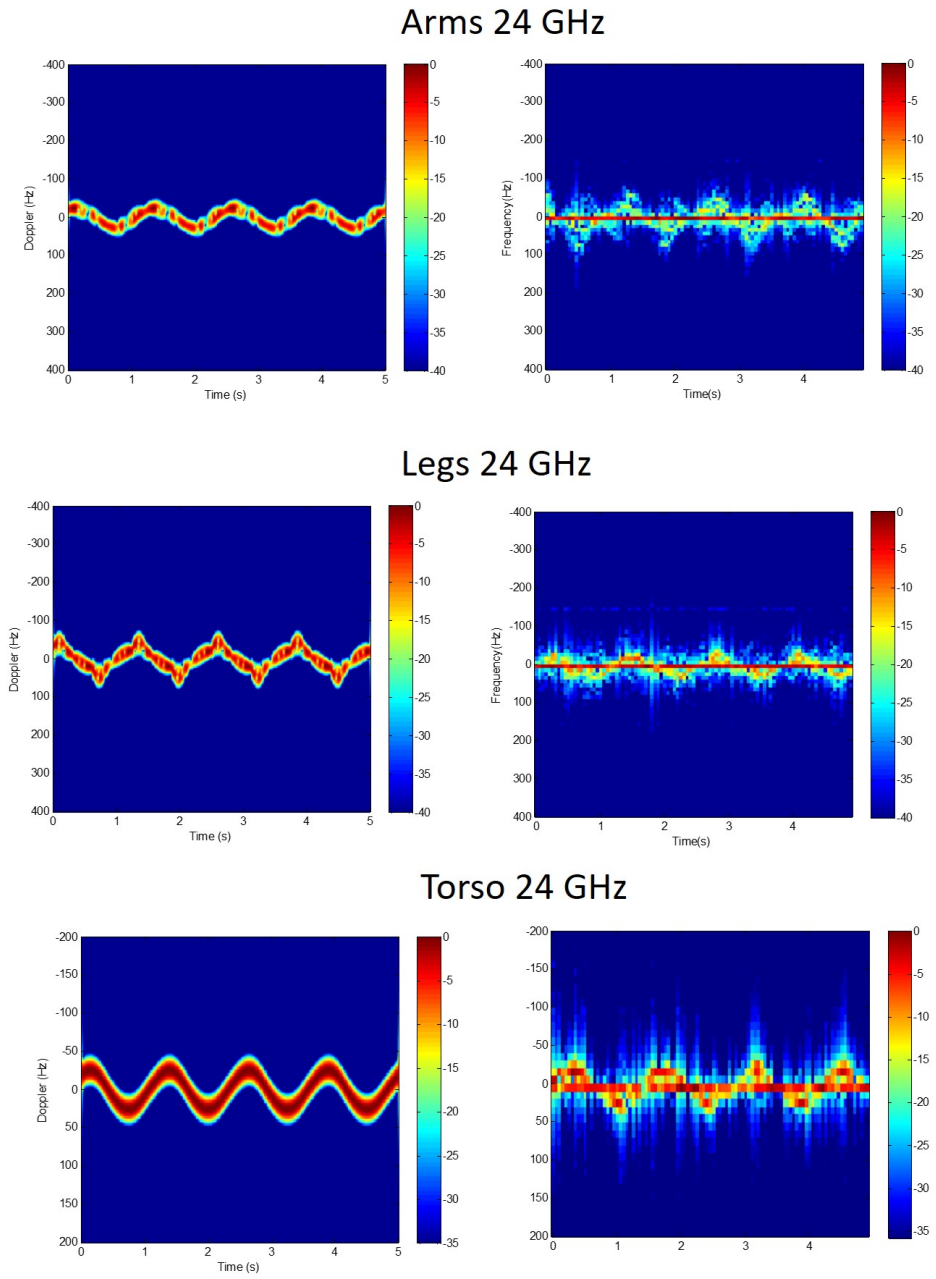
Arms 24 GHz
Doppler (Hz)
Time (s)
Frequency(Hz)
Time(s)
Legs 24 GHz
Doppler (Hz)
Time (s)
Frequency(Hz)
Time(s)
Torso 24 GHz
Doppler (Hz)
Time (s)

(a)

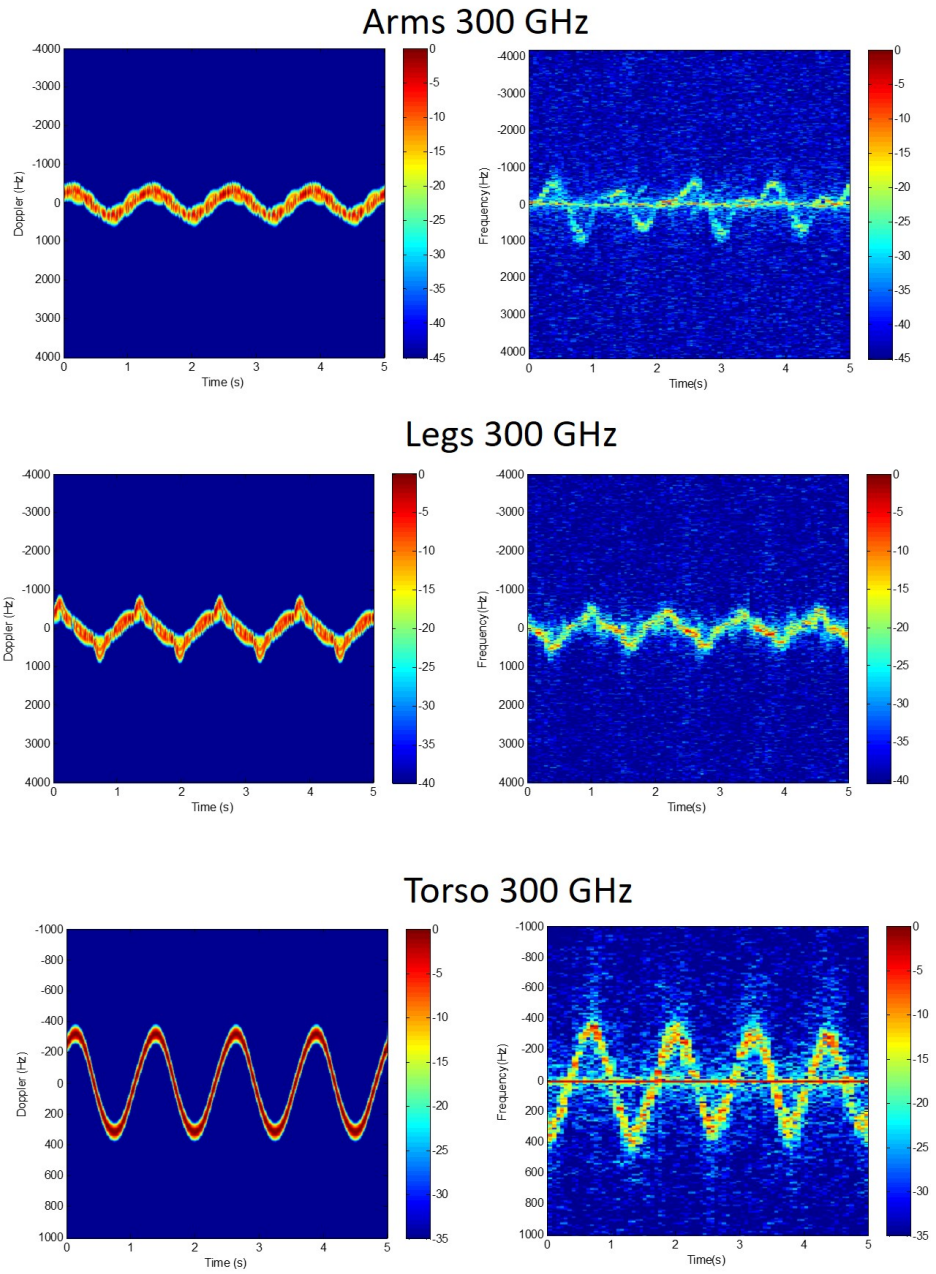

(b)

Fig. 5.24 μD signatures of different body parts of a human walking on the spot crossing the LOS of the radar at 24GHz (a) and 300GHz (b). Simulations (left) and measurements (right)

5.4 Summary

In this chapter the reflectivity and motion characteristics of pedestrian targets in the low-THz band were experimental analysed by means of RCS and micro-Doppler measurements. The analysis was carried out for the whole human body, as well as for individual body parts.

The pedestrian RCS was estimated through measurements of a child mannequin and results are presented using several indicators of reflectivities such as range–azimuth profile, polar plots and statistics of the average RCSs. The methodology employed in the test setup, the choice of the target, the calibration procedure and results obtained with full-wave simulations are presented. They permitted the collection of reliable data. The analysis of the various RCS signatures shows that the observed global average RCS in the three frequency bands, 24, 150 and 300 GHz are of similar values and in good agreement with the results reported in the literature. This is an important finding as it suggests that sensors operating at low-THz frequencies will have similar detection performances as traditional automotive sensors operating at lower frequencies. Moreover, although having about the same mean RCS, in low-THz band the RCS angular fluctuations are less pronounced, hence we can expect an enhanced probability of detection.

A qualitative analysis of the target range–azimuth profile shows that the range spread of targets in high resolution radar return is significant and can improve identification of objects in the radar image. A set of measurements carried out to assess the effect of clothes worn by pedestrians on reflectivity show that the variability of reflectivities for different clothes increases with the rise of the frequency, yet the difference between highly reflective and absorptive clothes is only a few dBs.

The micro-Doppler signatures of walking pedestrians were studied by measuring the Doppler modulations on the received signal from an adult male walking on the spot. The signature in the low-THz region shows a clearer pattern compared to the one at 24

GHz. The results, especially the ones obtained for the pedestrian crossing the line of sight of the radar, show the potential for low-THz systems to better identify features in the signatures, to be used in classification algorithms.

Finally in order to demonstrate the contribution of body parts into the μD pattern of the human gate-cycle, the reflection intensity and the μD of individual human body parts were measured. The torso and upper legs dominate the pedestrian RCS and their distinctive μD signature is clearly visible in the 300 GHz spectrograms.

Chapter 6

Signatures of cars and other road actors in the Low-THz band

6.1 Overview

The knowledge of targets reflectivity is essential during the development process of automotive sensors to provide a quantitative analysis of detection performance, to enhance the tracking stability and for classification purposes. The RCS of complex targets is sensitive to their size, shape, orientation, and material. Therefore, it is extremely important to know the individual RCS of typical vehicles and common road targets. Although the mean value of the RCS is generally used to radar system design, the RCS of such targets exhibits unique distribution characteristics as the aspect angle changes and can be used to estimate the target state including right and left turns. Moreover, to produce robust algorithms for target detection and recognition based on radar imaging, the statistical distribution of reflection for extended objects and the knowledge of fluctuation of reflectivity depending on the aspect angle of the targets is crucial.

However, currently, there are few reports related to the RCS measurement of roads actors at the standard allocated automotive bands of 24 GHz and 79 GHz and studies are

absent at higher frequencies. While the previous chapter was dedicated to pedestrians, this chapter reports the results, obtained with an analogous methodology, to characterize the reflectivity of other complex targets present in automotive scenarios at low-THz frequencies: cars, cyclists, wheelchairs and pushchairs. The results presented in this chapter are also published in [134, 135]. Firstly the results of measurements on a popular passenger car at 300 GHz and 24 and 79 GHz, to validate the experimental setup, will be presented. The measurements were carried out in a typical road environment. Secondarily, the reflectivity of other road objects in the low-THz band, namely a children's bike, a pushchair and a wheelchair, was measured in the same indoor environment used for the RCS pedestrian characterisation, presented in the previous chapter. Finally, the μD analysis of cyclists will be provided.

6.2 Signatures of passenger cars in the Low-THz band

Palubinskas and Runge [136] estimated the RCS of a passenger car in the X-band using satellite SAR data. The RCS mean was 0.5 dBsm with a standard deviation of 7.1 dB and peaks higher of 10 dBsm at the cardinal angles. Furthermore, it was shown high sensitivity of the RCS to small changes of aspect angles of up to 10 dBsm for 0.35°. Raynal et al. [137] examined the RCS probability distributions of ground vehicles across aspect and elevation angle, for HH and VV polarizations, and with different range resolutions in the Ku-band. The study reports a mean RCS of 2.6 dBsm for small civilian vehicles with standard deviation of 8.1 dB and a dynamic ranges between 1 and 15 dBsm. The vehicles RCS fluctuations across look angle were compared to the classic Swerling distributions and it is found that the best model is Swerling 1. Measurements of cars in anechoic chambers in the automotive bands of 24 GHz and 79 GHz band are reported in [138] using a wide bandwidth (4 GHz) and in [139] with narrow bandwidth (100 MHz). The values of RCS are similar in the two bands, with mean values around 3 dBsm and dynamic ranges between 0 and 20 dBsm corresponding to oblique and

cardinal angle, respectively. In [138] an analysis of the position of the main scattering centres of cars is provided. A report of NHTSA of 2013 [140] shows that the average RCS of car measured at 94GHz is also between 0 and 10 dBsm.

The aim of the experimental investigation, reported in the next sections, was the collection of reflectivity data in the low-THz band, never investigated before, and at the automotive standard frequencies, for comparison, at different aspect angles of a commercial passenger car to characterize its RCS, to get information on its extend in range and cross-range and to understand the vehicle elements that contribute most significantly to the radar reflectivity signature.

6.2.1 Measurements methodology

Objectives of the experiments were to collect reflectivity data of the car with the following systems and parameters:

- 24 GHz system using a bandwidth of 4 GHz and widebeam antennas
- 79 GHz radar with 5 GHz bandwidth and narrowbeam antennas
- 300 GHz radar with 16 GHz bandwidth and both narrowbeam and widebeam antennas

The measurements were performed simultaneously in the three frequency bands with the configuration shown in Figure 6.1.

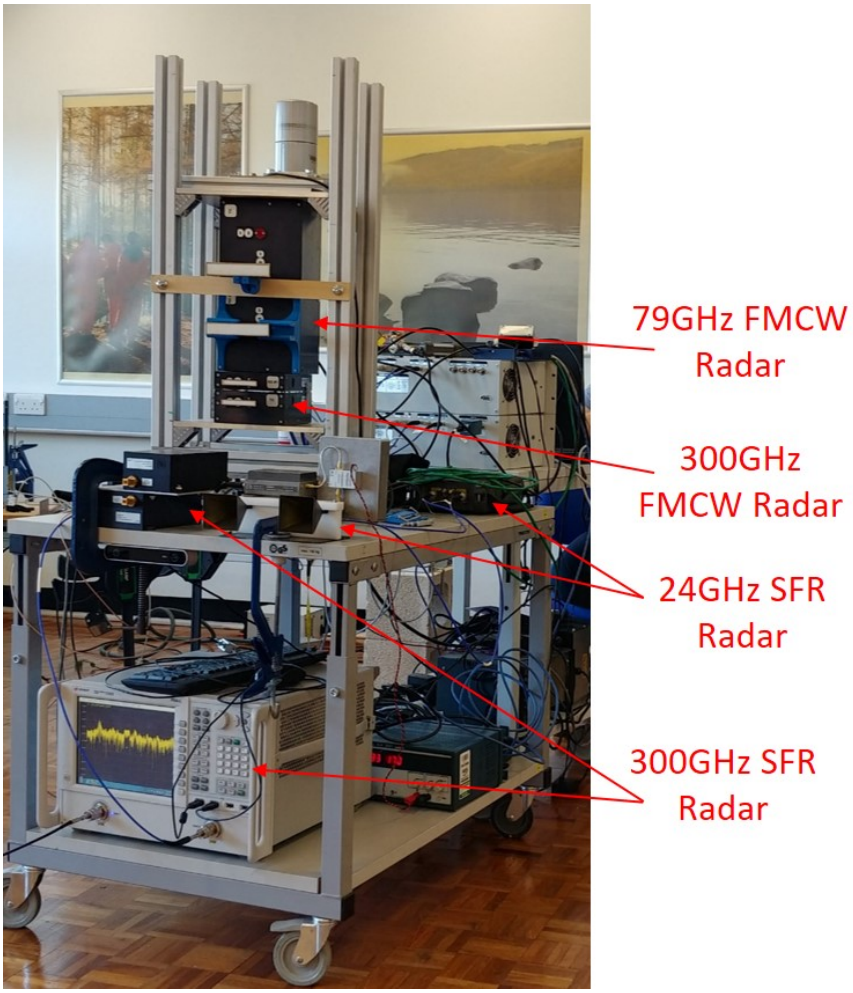

Fig. 6.1 Photo of the radars' setup for the measurements of car[1]

The 24 GHz and 300 GHz SFW radars, described in Section 3.5.1, have wide-beam antennas with 20°/20° and 10°/10° azimuth/elevation beam, respectively. The 79 GHz and 300 GHz FMCW systems (Section 3.5.2) with narrowbeam antennas, 1°/7° azimuth/elevation beam for both, are mounted on a rotating platform to scan simultaneously the scene. The radar parameters utilised in the measurements are summarised in Table 6.1.

[1]The 79 and 300 GHz FMCW scanning system on the top has been developed by Dr. E. Hoare and Dr. L. Daniel as part of the EPSRC Pathcad project, Prof. M. Gashinova (Principal Investigator)

Table 6.1 Parameters for the passenger car RCS measurements in the outdoor experimental site

Parameter	24GHz Radar (Section 3.5.1)	79GHz Radar (Section 3.5.2)	300GHz Radar (Sections 3.5.1 3.5.2)
Waveform	SFW	FMCW	SFW FMCW
Output power, dBm	10	15	-17 -3
Antennas gain, dBi	18	24	24 18
Antennas Beamwidth, deg (Azimuth/Elevation)	20/20	1/7	10/10 1/7
Distance from the target, m	23	23	23
Sweep Bandwidth, GHz	4	5	16

The bandwidths are subsequently reduced using the process in section 3.4.3 to obtain all the signatures of the car described in Section 3.4: RCS, HRRP and HRI. In Table 6.2 the sizes of the range and azimuth resolution cells are calculated depending on the bandwidths and antennas beamwidth utilised to produce the signature. As the aspect angle of the car changes respect to the radar, the car occupies a certain number of range and azimuth resolution cells, in the table the maximum number of cells occupied is indicated depending on the cells sizes. Finally, the RCS is estimated for the various combination of bandwidths and antennas' beamwidths considered.

Table 6.2 Resolution cells occupied for the various measurements parameters

Carrier frequency, GHz	24	79	300
Bandwidth, GHz	0.037		0.037
	4		4/16
		5	5/16
Range resolution cell size, m	4		4
	0.04		0.04/0.01
		0.03	0.03/0.01
Maximum number of range resolution cells occupied by the car	1		1
	106		106/426
		133	133/426
Antennas Beamwidth (Azimuth/Elevation), deg	20/20		10/10
	20/20		10/10
		1/7	1/7
Azimuth resolution cell size, m	4		4
	4		4
		0.4	0.4
Maximum number of azimuth resolution cells occupied by the car	1		1
	1		1
		10	10
Estimated RCS (see Table 3.13)	$\sigma_{WB,NBw}$		$\sigma_{WB,NBw}$
	$\sigma_{WB,WBw}$		$\sigma_{WB,WBw}$
		$\sigma_{NB,WBw}$	$\sigma_{NB,WBw}$

Two measurements campaigns were carried out, in the first the reflectivity of a Renault Clio (dimensions: 4x1.7x1.5 m (depth x width x height)) was measured for 8 aspect angles spaced by 45 degrees. The car was manually orientated towards the radars in order to avoid the use of any kind of turntable, which reflection may interact with the car or introduce direct reflections. In addition the reflectivity of a bigger car, a Land Rover (5x2x1.8 m), was measured, for comparison, orientated with its rear part in the LOS of the radar. The height of the antennas above the ground was also varied to assess its impact on the car reflectivity. In the second measurement campaign, the measurements of the Renault Clio were made for 61 non-equally spaced aspect angles of the car using only the 79 and 300 GHz FMCW radars with narrow beam antennas ($1^\circ/7^\circ$ azimuth/elevation beamwidth), to assess the repeatability of the experimental setup and obtain statistics of the fluctuation of RCS depending on aspect angles.

Figure 6.2 shows the experimental setup for one of the measured aspect angles of the car including the wide beam antenna's footprint.

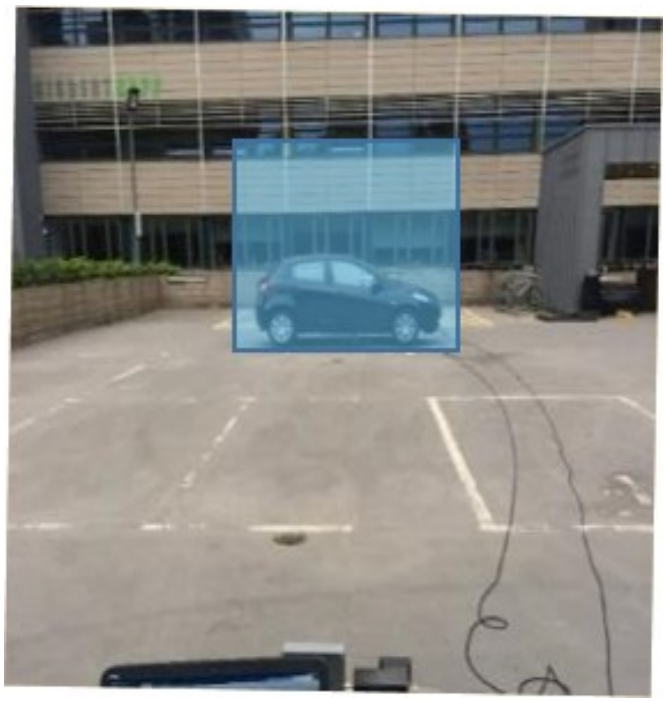

Fig. 6.2 Photo of the car

Figure 6.3 shows a sketch of the side and top views of test range for the measurements, where the range and azimuth regions enclosing the target are highlighted. In order to assure the complete illumination by the antenna beam for all the systems, the car is placed at 22 m from the radars.

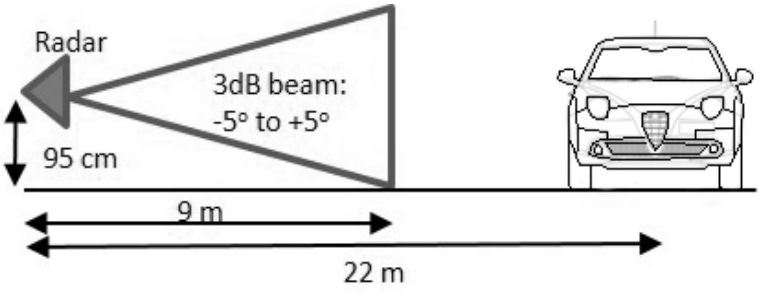

(a)

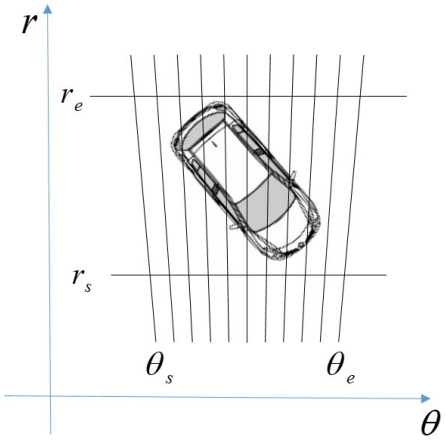

(b)

Fig. 6.3 Sketch of the experimental setup used for RCS measurements of the car. (a) side and (b) top views

Figures 6.4 and 6.5 shows examples of the scene HRRP and HRI, obtained through the wide and narrow band measurements, respectively. For all the measurements, the peak of reflection from the car is significantly higher (more than 30 dB) than the background level (i.e. the measurement of the scene without the car), within the region occupied by the target. The range profiles in Figure 6.4 highlights the reflection from the ground plane, at 24 GHz the reflection is 40 dB above the background level, significantly higher than at 300 GHz (15 dB above the noise), confirming the assumptions made in

the analysis on the effect of a paved ground plane on target reflectivity (Section 3.7): at 300 GHz the wavelength is of the order of the asphalt roughness and thus the defused scattering from the paved ground plane produces a backscattered wave with amplitude lower at 300 GHz than at 24 GHz. The reflection from the ground cannot be noticed in the images because, being spread over the azimuth cells of the image, it is below the intensity colormap threshold.

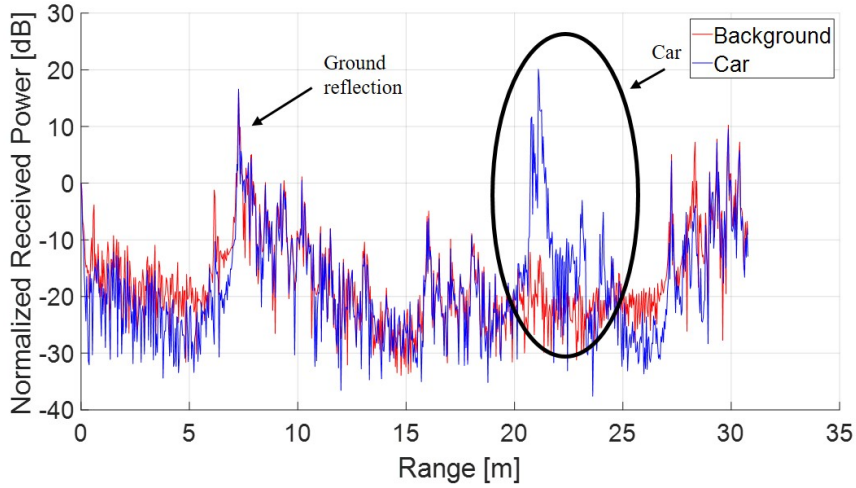

(a)

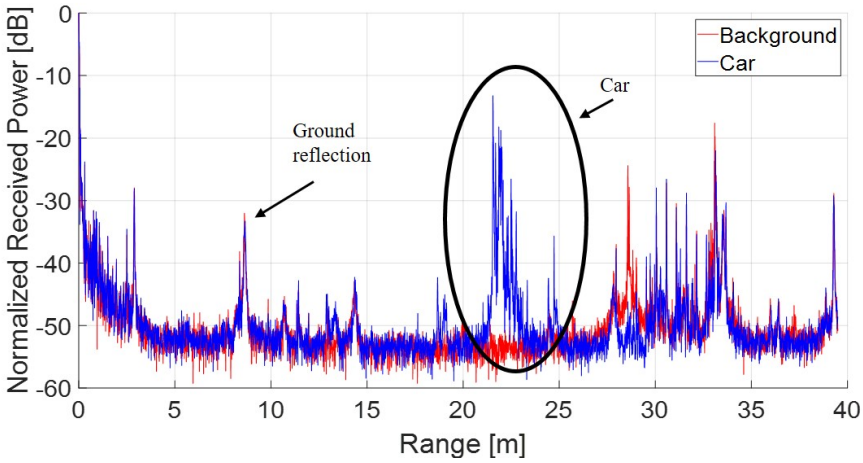

(b)

Fig. 6.4 HRRP of the setup for the measurements of a passenger car at (a) 24 GHz (BW: 4GHz), (b) 300 GHz (BW: 16GHz)

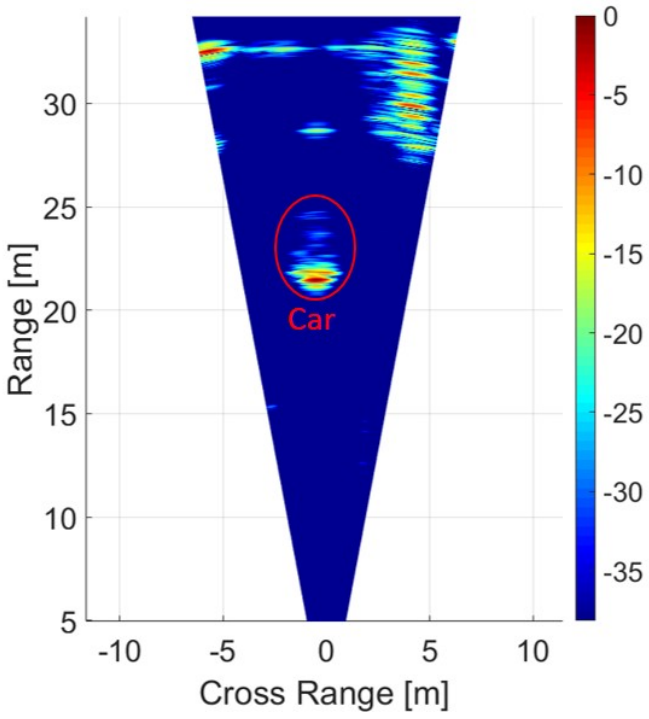

(a)

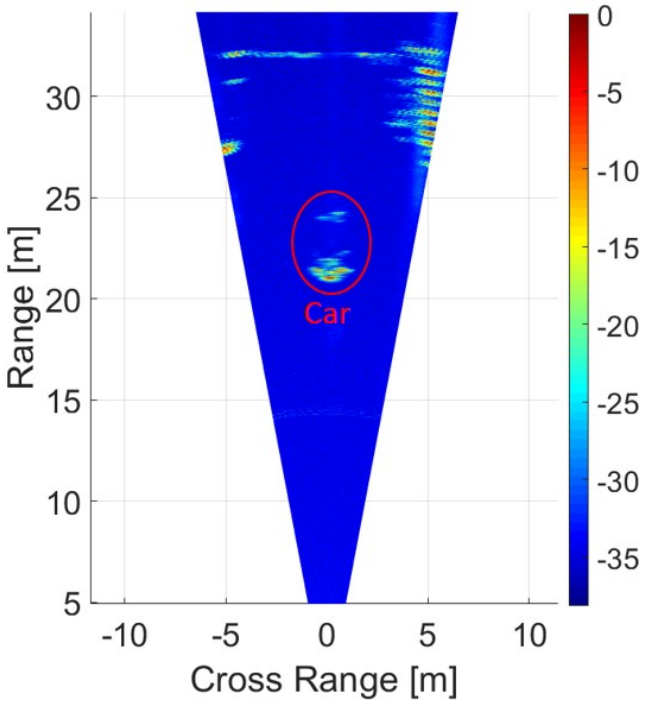

(b)

Fig. 6.5 Images of the setup for the measurements of a passenger car at (a) 79 GHz (BW: 5GHz), (b) 300 GHz (BW: 16GHz)

In order to estimate the car RCS from the radar data collected, the polished steel sphere shown in Figure 6.6 with a diameter of 50 cm was used as reference target to perform the calibration procedure explained in Section 3.4.2. The sphere is suspended to a non-reflective fibre glass pole through a suction cup (which is in the shadow region of the sphere relative to the illuminating radar).

Fig. 6.6 Photo of the calibration sphere

6.2.2 High resolution range profiles

HRRP, obtained through the methodology illustrated in Section 3.4.3, are used to identify the position in range of the main scatterers of the car. Figure 6.7 shows examples of four views of the Renault Clio's range profiles at 300 GHz, with 16 GHz bandwidth (i.e. 1 cm range resolution) and wide beam antennas.

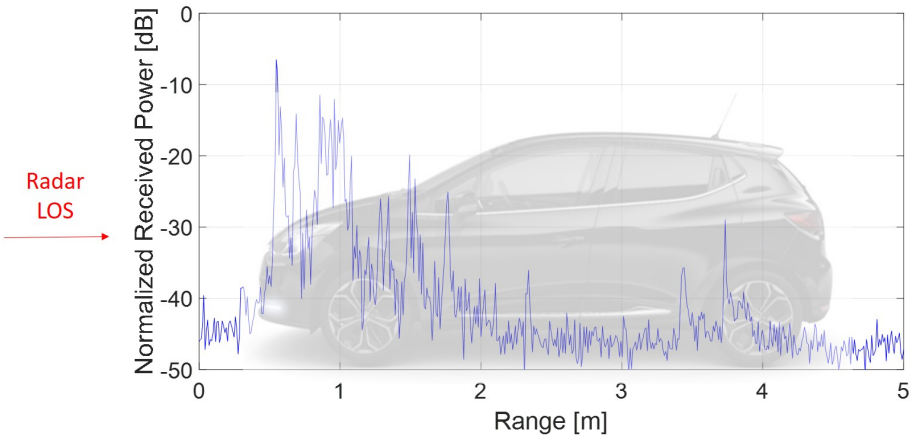
Radar
LOS
Normalized Received Power [dB]
0
-10
-20
-30
-40
-50
0
1
2
3
4
5
Range [m]

(a)

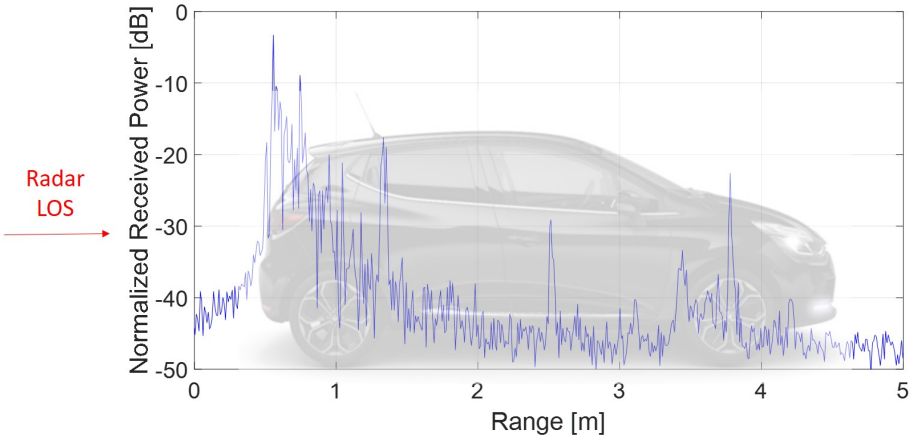
Radar
LOS
Normalized Received Power [dB]
0
-10
-20
-30
-40
-50
0
1
2
3
4
5
Range [m]

(b)

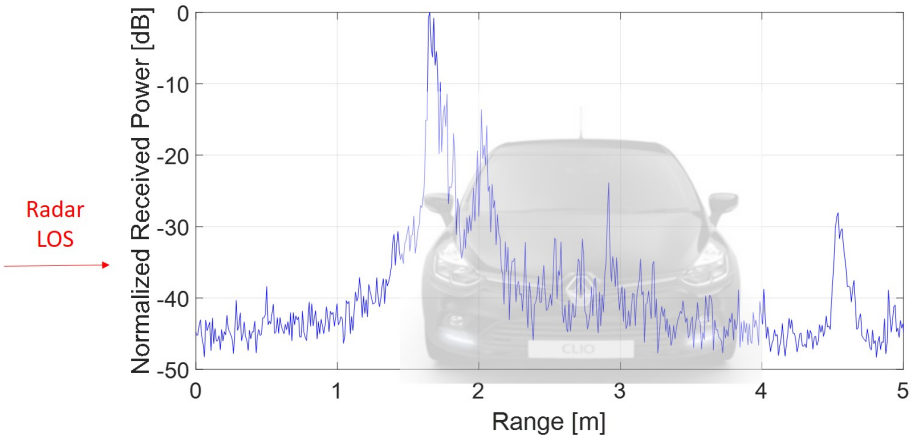
Radar
LOS
Normalized Received Power [dB]
0
-10
-20
-30
-40
-50
0
1
2
3
4
5
Range [m]

(c)

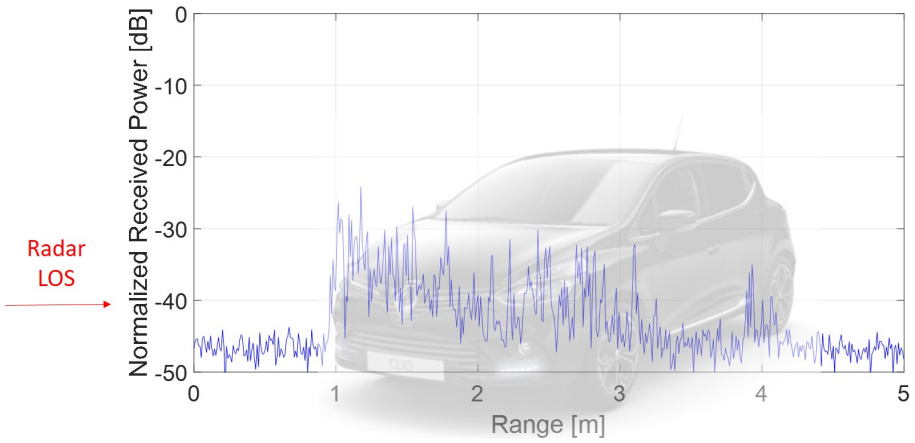

(d)

Fig. 6.7 Car range profiles, overlaid on the car picture, obtained from measurements at 300 GHz with 16 GHz bandwidth, using wide beam antennas, for 4 aspect angles: front (a), back (b), side (c) and oblique (d)

It can be seen that there are a few main scatterers contributing to the target reflectivity, from the bumper, tail, rear and front axles and wheel rims. The highest reflectivity is located for every aspect angle in the part of the car closest in range to the radar, however there are returns from the whole extend of the car resulting in the important knowledge on the size of the car.

Figure 6.8 shows a comparison the HRRPs of the car at 24 GHz (a) and 300 GHz (b) using the same bandwidth of 4 GHz (i.e. 4 cm range resolution), overlaid to a side-view image of the vehicle. As can be seen from the radar setups in Figure 6.1, the 24 GHz and 300 GHz SFW radar antennas were aligned at slightly different aspect angles of the car and therefore the scatterers of the car were not illuminated in the same way. However, the HRRPs show approximately the same sources of reflections from the car, moreover it is possible to notice the improved capability of the low-THz system, compared to the lower frequency radar, to resolve scatterer centres in range, even using the same range resolution.

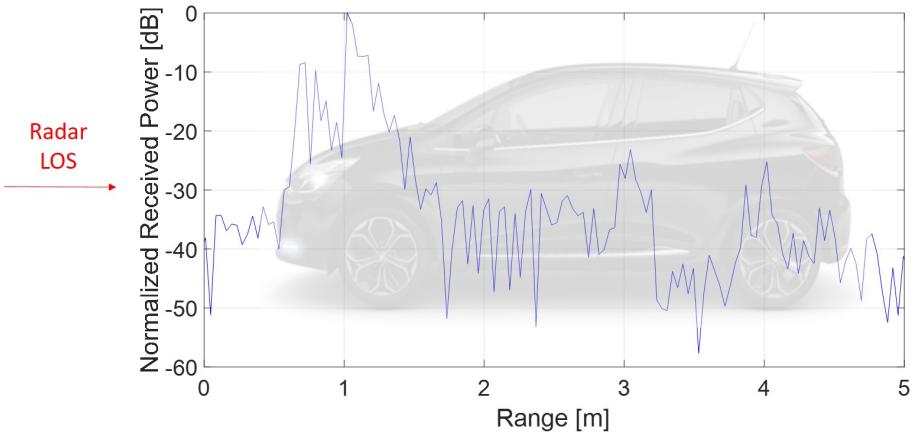

(a)

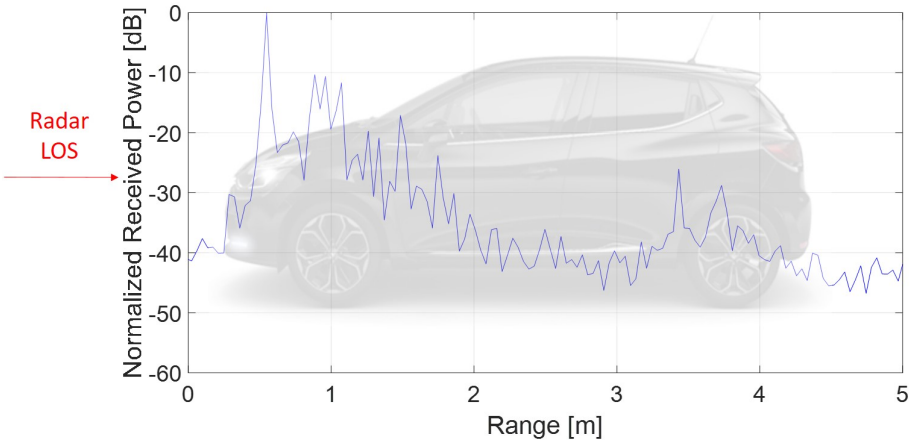

(b)

Fig. 6.8 HRRP of the car at 24 GHz (a) and 300 GHz (b) with 4 GHz bandwidth

Finally, a set of measurement was carried out with a bigger car to evaluate the difference of reflectivity between different sizes of cars, moreover the dependence of radar antennas' height above the ground on reflectivity was assessed. Figure 6.9 shows the HRRP of the rear of the Land Rover, using a bandwidth of 16 GHz, for three different heights of the antennas above the ground: 45 cm, 95 cm and 135 cm.

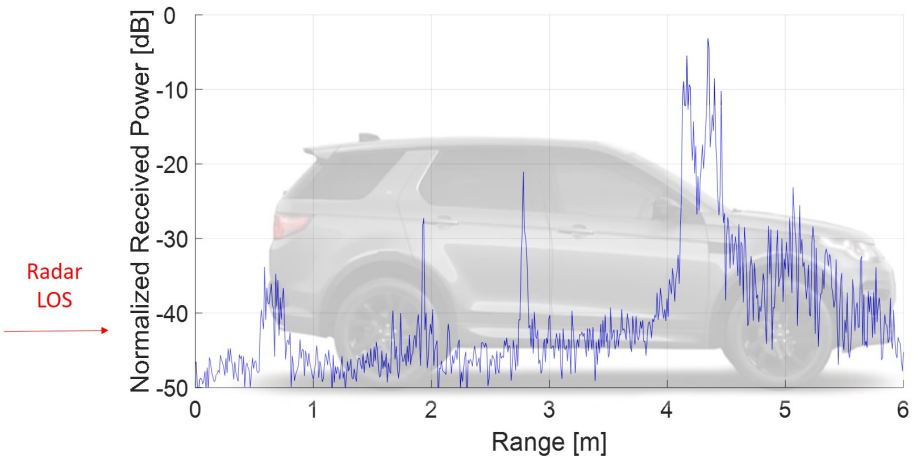

(a)

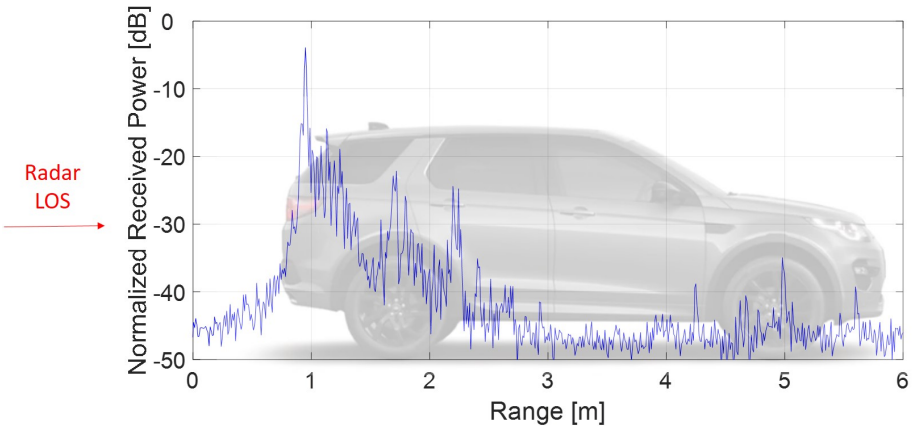

(b)

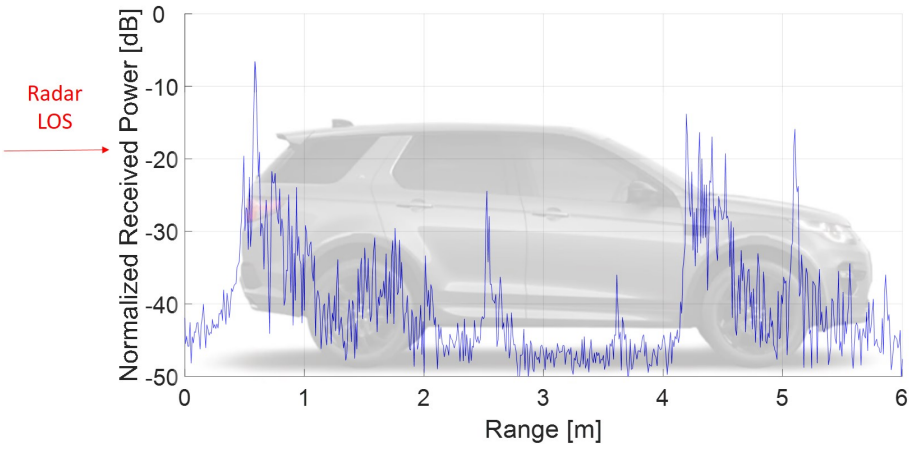

(c)

Fig. 6.9 Range profiles of the rear of a Land Rover obtained from measurements at 300 GHz with 16 GHz bandwidth, using wide beam antennas, for 3 antenna's heights above the ground: 45 cm (a), 95 cm (b) and 135 cm (c)

The calibrated average RCS is 4 dB higher to that of the smaller car, however, when the radar is in LOS to the centre height of the car (95cm), the profile shows the same sources of reflections. The variation of the radar's antennas over the ground affect the degree of intensity of reflections from these sources, when the antennas' height is 45 cm, the rear of the car is not fully illuminated by the antennas' beam and thus its reflection is low, on contrary it can be seen a very high reflectivity in correspondence of the front axle; the car reflectivity is, instead more distributed over its length when the antennas' height is 145 cm above the ground. However, the average RCS does not differ of more than 2 dBs for the three cases.

6.2.3 High resolution images

More information on the position of the main scatterers of the car in both range and cross-range, are given by the HRI shown in Figure 6.10, obtained from the measurements using scanning narrow beam antennas ($1^\circ/7^\circ$ azimuth/elevation beamwidth) and 16 GHz bandwidth. Images for four aspect angles of the car (front, back, side, oblique) are shown and a scaled stylised representation of the top view of the car is overlaid to the radar images. The extent in range and cross-range of the HRI are clearly visible and correspond to the actual sizes of the car. It is actually possible to reconstruct the contour of the car and localise the brightest scatterers of the car in correspondence of the license plate, headlights, rearview mirror, wheel rims and axes.

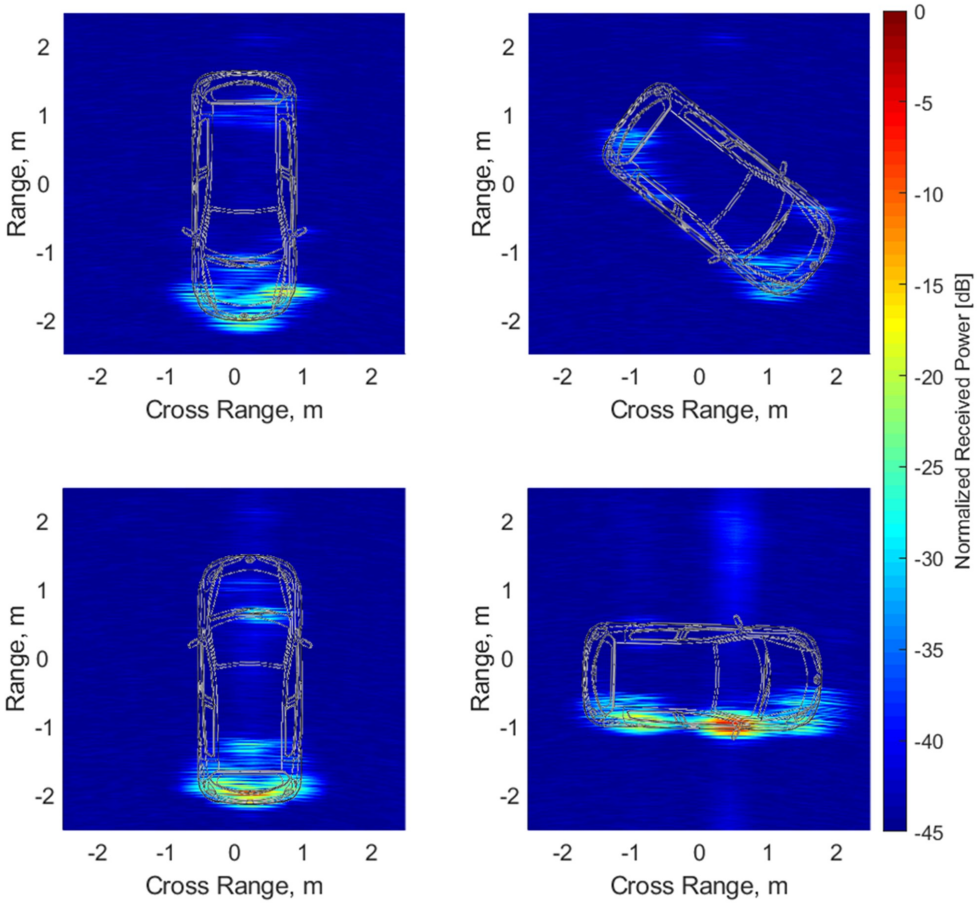

Fig. 6.10 Radar images of the car at 300 GHz with 16 GHz bandwidth

In figure 6.11 it is shown a comparison between images obtained at 79 GHz and 300 GHz, both using 5 GHz bandwidth. By looking closely at the images it is possible to see the improved image resolution achieved by the 300 GHz sensor due to presence of greater number of minor features of the target acting as corner reflectors when exposed to shorter wavelengths and the sensitivity of extremely short wavelength to target surface roughness. The images at both frequencies indicates the general dimensions of the car, however at 300 GHz the HRI exhibits more details on the position of the main scatterers in both range and cross-range. For example, the contour of the car in oblique aspect angle shows a more continuous shape, or it is possible to distinguish three different reflections from the front and the back of the car, most likely corresponding to the license plate and the headlights, where at 79 GHz these reflections are overlapped.

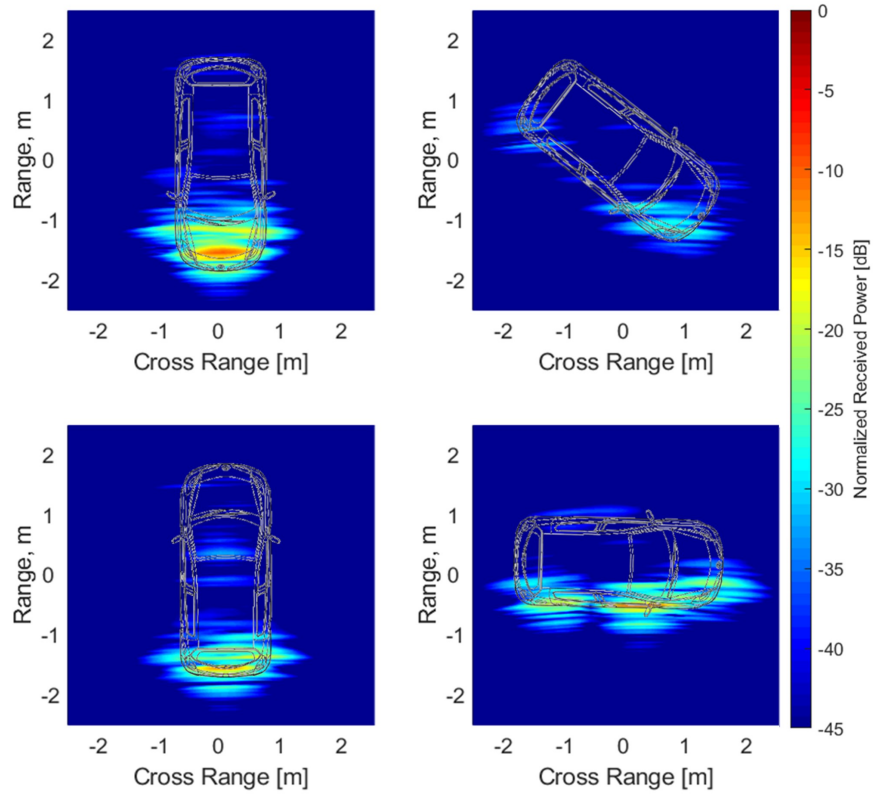

(a)

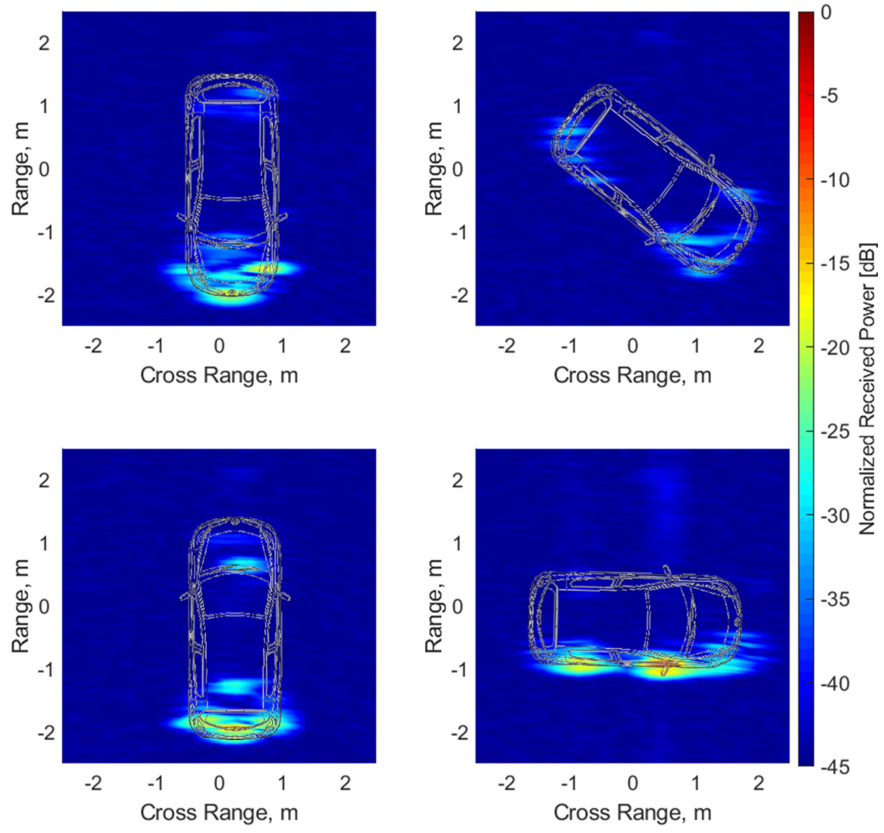

(b)

Fig. 6.11 Radar images of the car at 79 GHz (a) and 300 GHz (b) with 5 GHz bandwidth

6.2.4 RCS estimation

The calibrated RCS of the Ranault Clio, calculated with the aid of equations 3.29 and 3.32 and using the data of the first measurement campaign, are shown in Figure 6.12. The average RCS at 8 aspect angle of the car, measured in the three frequency bands, is plotted with error bars showing the difference in the RCS calculated with the different systems and bandwidths summarized in Table 6.2.

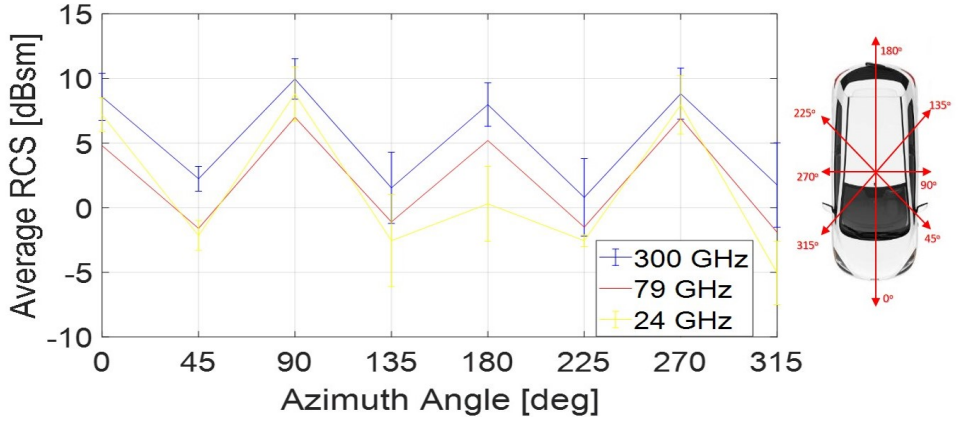

Fig. 6.12 Average RCS of the car at 8 cardinal aspect angles for different frequencies

Although the measurements were performed simultaneously, it has to be considered that the antennas were aligned at slightly different aspect angles of the car and therefore it is possible that not all the scatterers of the car were illuminated in the same way. However we can conclude that overall, the oblique angle mean RCS is between 5 and 10 dBs lower in value than the cardinal angles. The results of measurements at 24 GHz and 79 GHz are compatible with the results reported in literature for measurements carried out both in controlled [139] and real road scenarios [140], validating our experimental setup. We also observe about 3 dB rise in the mean RCS at 300 GHz in comparison with 24 GHz, this result is analogous to the one obtained for the pedestrian.

The polar plots in Figure 6.13 show the calibrated average reflectivity of the car at 79 and 300 GHz with 5 GHz bandwidth, from the second measurement campaign for 61 non-uniformly spaced aspect angles, interpolated to obtain a 360 equally spaced points in the polar plot.

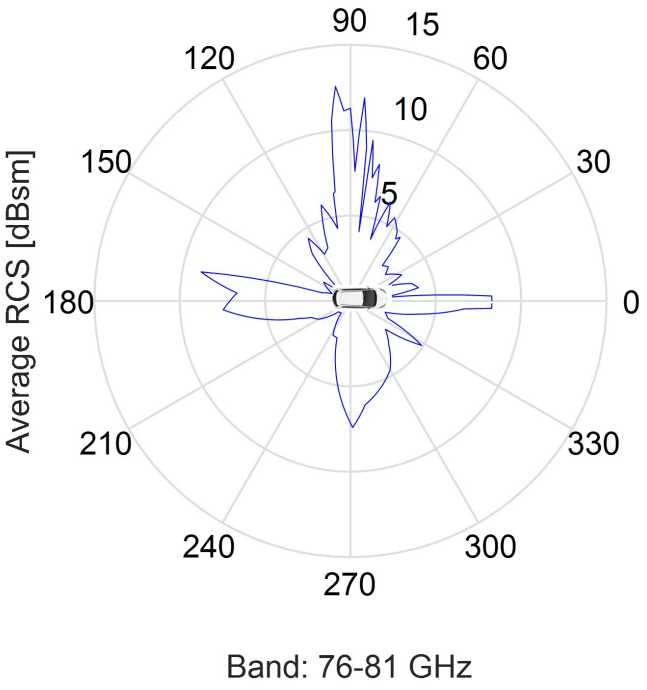

(a)

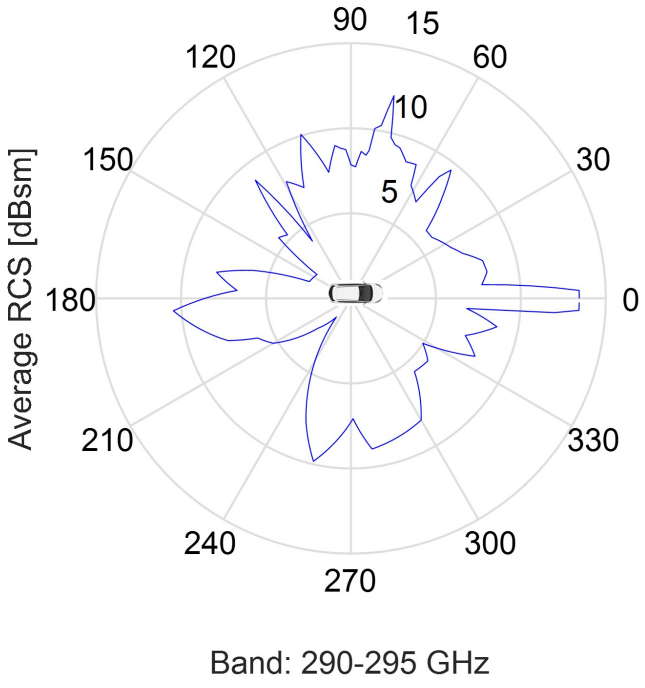

(b)

Fig. 6.13 Average RCS as a function of 360 non-uniformly spaced azimuth angles at 79 and 300 GHz

At 79 GHz (Figure 6.13 (a)), the RCS exhibit big flashes at the cardinal angles for the front, rear and sides of the vehicles, as compared to oblique angles. The oblique angle

mean RCS is roughly 10 dB lower than the cardinal angles. At 300 GHz (Figure 6.13 (b)) the RCS values at the cardinal angle are similar than those at 79 GHz, however for oblique angles, the values do not show the high decrease seen at lower frequencies. With the exception of the angle corresponding to the front of the car and a small angular sector (10°), around $\pm 30°$ in respect to the rear aspect angle, the RCS of the car is quite constant and always between 5 and 10 dBsm. Therefore, overall the RCS fluctuations due to the variation of the aspect angle of the car in respect to the radar are lower at 300 GHz than at 79 GHz. This result, which indicate an advantage of using low-THz frequencies in respect to traditional automotive frequencies, is direct consequences of the sensitivity of very small wavelengths to texture and small features of targets, which lead to the increase of observable scatterers from the car, as also observed in the HRRP (Figure 6.7) and HRI (Figure 6.11).

6.2.5 RCS fluctuation statistics

RCS statistics of cars are obtained from the measurement results of the Renault Clio for 61 non-equally spaced aspect angles using only the 79 and 300 GHz FMCW radars with narrow beam antennas. Using the methodological analysis illustrated in Section 3.4.5, the probability distribution models best fitting the measured distributions are identified by calculating the errors of fit summarized in Table 6.3.

Table 6.3 Error of fit for the car RCS against different distribution models

Distribution model	Frequency GHz	Parameters (Table 3.3)	Error of fit % (eq. 3.39)
Swerling 1/2	79	$\sigma_m = 2.62$	21.36
	300	$\sigma_m = 5.12$	19.66
Swerling 3/4	79	$\sigma_m = 2.62$	8.58
	300	$\sigma_m = 5.12$	7.15
Gamma	79	$\alpha = 3.1, \beta = 1$	8.97
	300	$\alpha = 3.97, \beta = 1.47$	2.09
Weibull	79	$k_w = 3.49, \lambda_w = 1.56$	14.76
	300	$k_w = 6.6, \lambda_w = 1.93$	4.43
Log-normal	**79**	$(ln(\sigma))_m = 0.96, (ln(\sigma))_{sd} = 0.54$	**4.26**
	300	$(ln(\sigma))_m = 1.63, (ln(\sigma))_{sd} = 0.52$	**2.02**

The best fit has been found to be the log-normal PDF for both frequencies and only considering the classic Swerling models, the car can be classified as a Swerling 3 or 4 target.

Figure 6.14 shows the PDF and CDF used to determine the RCS statistics reported in Table 3.3. The mean RCS is slightly higher at 300 GHz (3 dB difference), moreover, the coefficient of variation (standard deviation/mean) is smaller at 300 GHz than at 79 GHz, reducing, therefore, the possibility of large fluctuations of RCS with the variation of aspect angle.

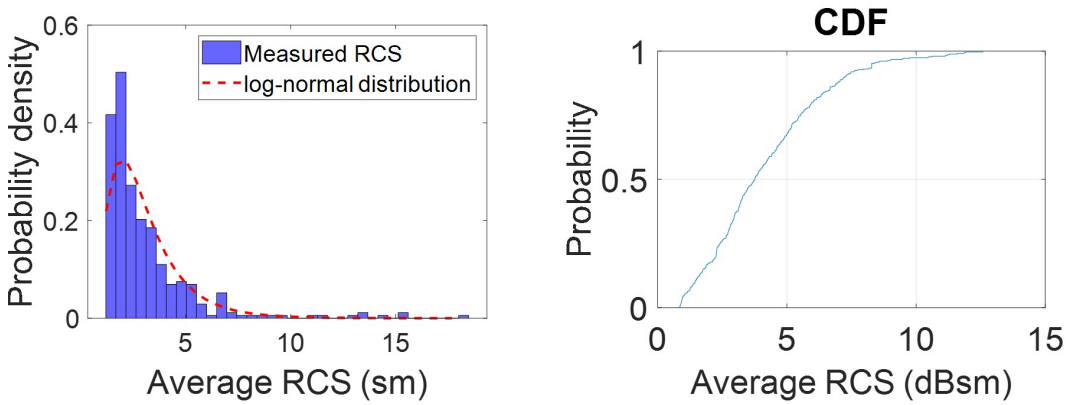

(a)

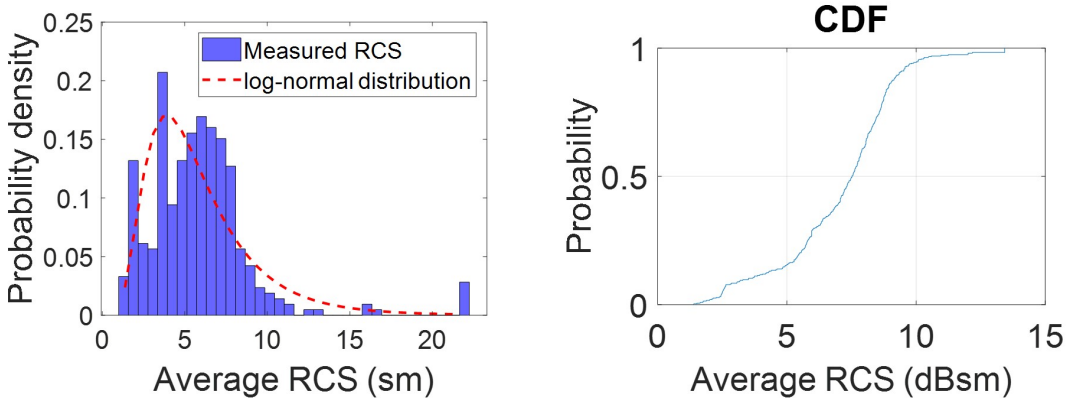

(b)

Fig. 6.14 PDF and CDF from car measurements at 79 and 300 GHz with 5 GHz bandwidth

Table 6.4 Passenger car RCS statistics

Frequency GHz	BW GHz	Mean dBsm	Standard dB	Median deviation, dBsm	Dynamic range, dBsm (see Section 3.4.5)
79	5	4.18	2.3	3.8	[1.2 9.4]
300	5	7.1	2.3	7.5	[2.5 10]

6.3 Signatures of common road actors in the Low-THz band

Detection and identification of common road actors other than pedestrian or cars is as much as fundamental for the development of radar sensors for autonomous car. In particular, cyclists are among the targets most at risk on the road, according to a report from Euro NCAP [141], although the total amount of road fatalities decreased in the last decades, the percentage of cyclist fatalities keeps increasing. However, only a limited set of reports on RCS measurements of cyclists have been reported to date, and only for the standard automotive frequencies of 24 and 79 GHz. In [142–145] the RCS of bicyclists was measured in an anechoic chambers, the mean values are around 0 dBsm at both frequencies, with a dynamic range of 20 dB, moreover the results show that the difference between manned and non-manned bikes is irrelevant. The average RCS pattern among seven bicycles without riders exhibits a rhombic shape with its major axis (i.e., strongest backscattering) being in the direction of side observation angles [144]. In the following sections results of RCS measurements of a bicycle and other road targets (wheelchair and pushchair) at low-THz frequencies and using wide bandwidths, will be presented.

As for pedestrians, the micro-Doppler produced by bicyclists is used for identification and classification purposes. In [146] distinctive signature of bicyclists μD given by the rotating wheel and the legs pedalling are shown at 77 GHz. In [147, 148] μD signatures and extreme learning machine are used to distinguish between pedestrian and the bicyclist approaching the radar from different angles. The last section of this chapter will show μD signatures of cyclists at low-THz frequencies, which are compared to the signatures obtained at the standard automotive frequencies.

6.3.1 Measurements methodology

The setup of RCS measurements of the bike, wheelchair and pushchair, is the same indoor setup used to characterise the pedestrian RCS and described in Sections 3.6.2 and 5.2.2: three radar systems operating at 300 GHz, 150 GHz and at the reference frequency of 24 GHz for comparison, are arranged in a quasi-monostatic configuration by means of two square aperture antennas collocated in azimuth and with a 3-dB beamwidth of 10 degrees. As shown in figure 6.15, the targets are in the anechoic environment built with low-THz absorbers placed to cover the floor and the wall behind them. The distance between radars and targets, 6 meters for the 150 and 300 GHz radars, and 3m for the 24 GHz system, ensures beam filling and avoids reflections from the ground before the transmitted wave reaches the target. Reflections from the target are measured at 360 aspect angles by placing it on a fully automated turntable, which is also covered with absorbers.

Fig. 6.15 Photo of the indoor experimental setup for road objects RCS measurements

Table 6.5 summarises the main parameters of the systems used for the measurements, the 24 and 300 GHz systems are the SFW radars based on VNA (Sections 3.5.1 and 3.5.1) the 150 GHz radar is the FMCW radar shown in Section 3.5.2. For all the systems, signals with a bandwidth of 5 GHz are processed through FFT, non-coherently

integrated to improve the signal to background ratio and range gating is applied to isolate the backscatter from the target.

Table 6.5 Parameters for the passenger car RCS measurements

Parameter	24GHz Radar (Section 3.5.1)	150GHz Radar (Section 3.5.2)	300GHz Radar (Section 3.5.1)
Waveform	SFW	FMCW	SFW
Output power, dBm	10	11	-17
Antennas gain, dBi	18	24	24
Antennas Beamwidth, deg (Azimuth/Elevation)	20/20	10/10	10/10
Distance from the target, m	3	6	6
Sweep Bandwidth, GHz	5	6	5

6.3.2 High resolution range profiles

Figure 6.16 shows the range profiles of three targets, a children's bike, a pushchair and a wheelchair obtained from the measurements at 300 GHz with a bandwidth of 5 GHz, for one aspect angle (shown in the photo), and the range profile of the calibration sphere.

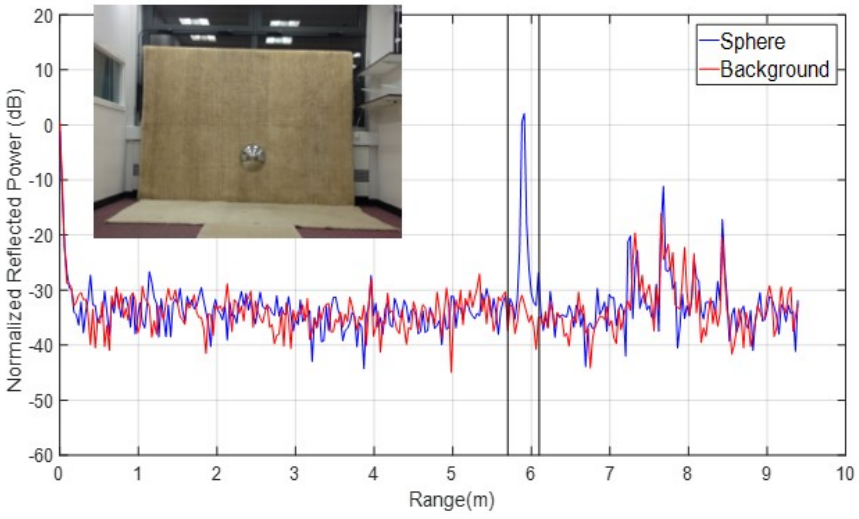

(a)

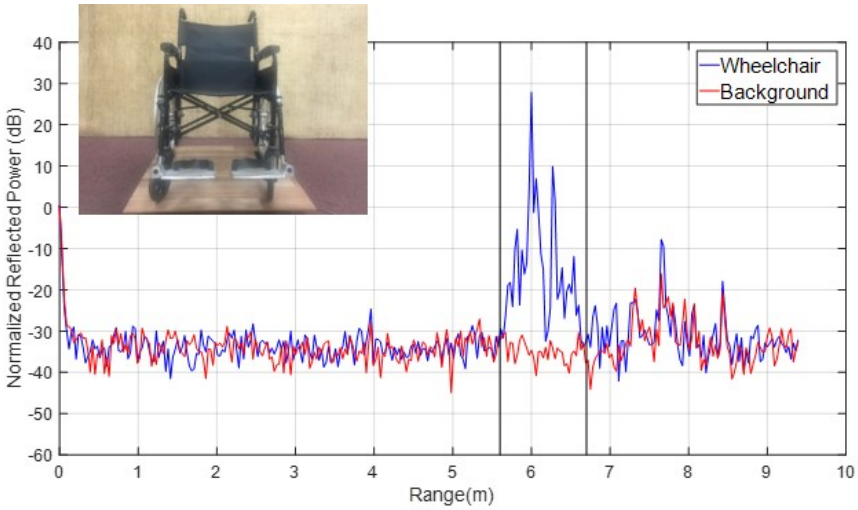

(b)

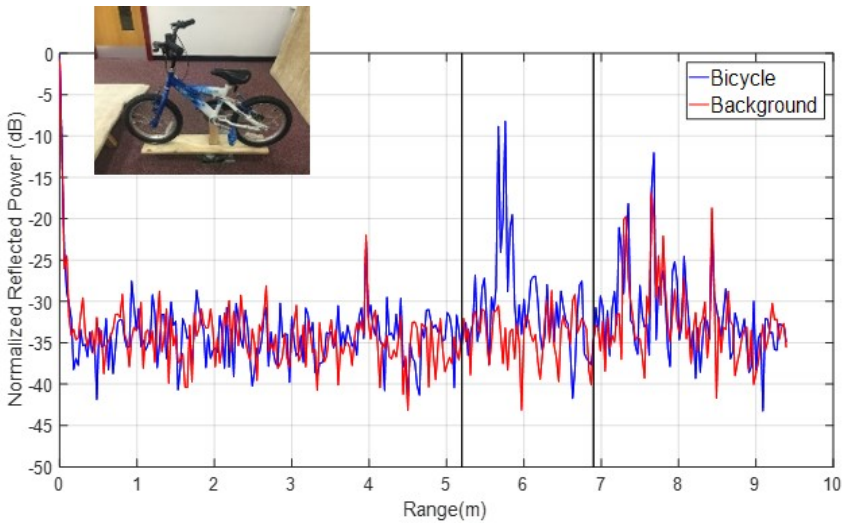

(c)

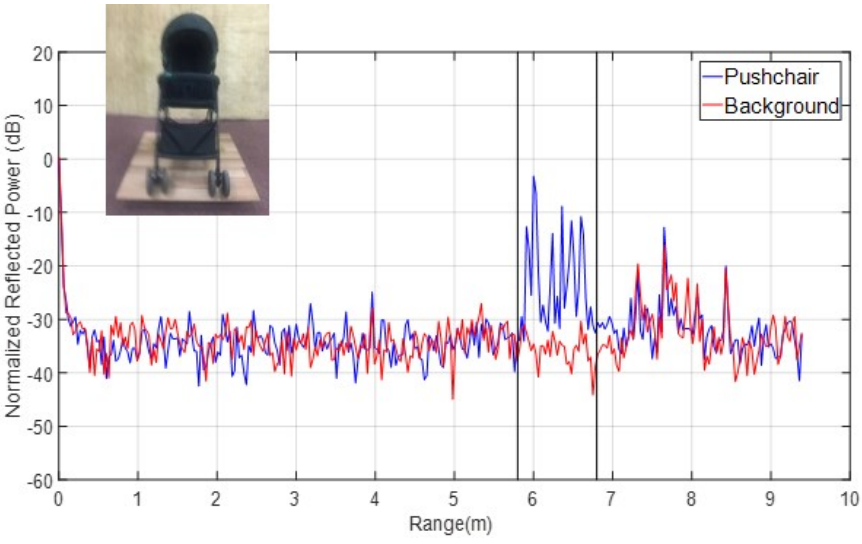

(d)

Fig. 6.16 Range profiles of the calibration sphere (a), a wheelchair (b), bike (c) and pushchair (d) at 300 GHz with 5 GHz bandwidth

For all the plots the received power is normalised in respect to the amplitude of the antenna coupling, which corresponds at the range 0 m in the plot. Vertical lines indicate the range gating applied to the processed data, the size of the gating is chosen to include all range cells occupied by the target. The extent in range measured by the radar corresponds closely to the true length of the target. This result shows that the use of a large bandwidth, in fact, gives important information on the dimensions of distributed targets as opposed to narrowband systems. The complex metallic structure of the wheelchair, with a great number of corner reflectors, results in the highest reflectivity among the three objects. The pushchair is characterized by an assemble of scatterers distributed over range and with roughly the same intensity, therefore and since its dimensions in width and depth are about the same, only the aspect angle shown in Figure 6.16 (d) was measured.

In Figure 6.17 the gated range profiles at 24 GHz and 300 GHz for the bicycle and the wheelchair are plotted across the 360 aspect angles measured.

At both frequencies, 24 GHz and 300 GHz, it can be seen that as the bike is rotated on the turntable, it produces an almost uniform distribution of scattering intensities, with the front slightly more reflective due to the presence of the handlebars. As clear from the shape of the bike, its range spread reduces at minimum when the bike is illuminated from the side. With the increase in frequency, a greater number of minor features of the target when exposed to smaller wavelengths can be seen. While at 24 GHz reflections are generated by only few scatters which constitute the target, at 300 GHz there are backscatter returns from most of the range cells occupied by the target.

The wheelchair is comprised of few bright scattering centres, which can be located by tracking them as the wheelchair rotates and can be identified in the two big back wheels and the two metallic footplates, which act as corner reflectors and which increase their backscatter intensity as the frequency rises from 24 GHz to 300 GHz.

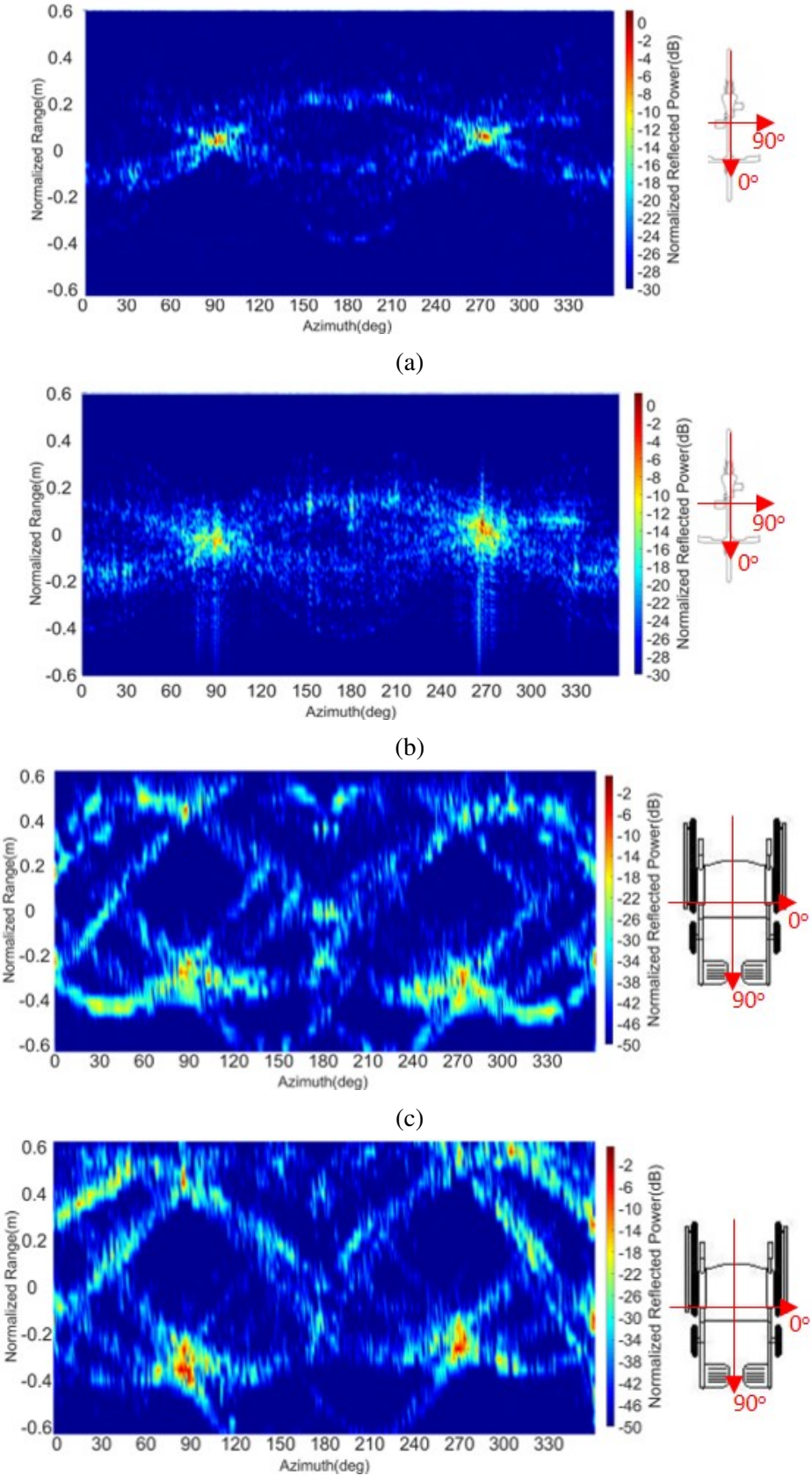

Fig. 6.17 Normalised received power vs azimuth of a bicycle at 24 (a) and 300 (b) GHz, for a wheelchair at 24 (c) and 300 (d) GHz

6.3.3 RCS estimation

In Figure 6.18 an overview of the calibrated average RCS results, $\sigma_{WB,WBw}(\phi)$ (Eq. 3.32), for all the targets measured in the indoor setup, including those of the pedestrian presented in Section 5.2.5. The results are presented with polar plots of the calibrated average RCS as a function of aspect angles.

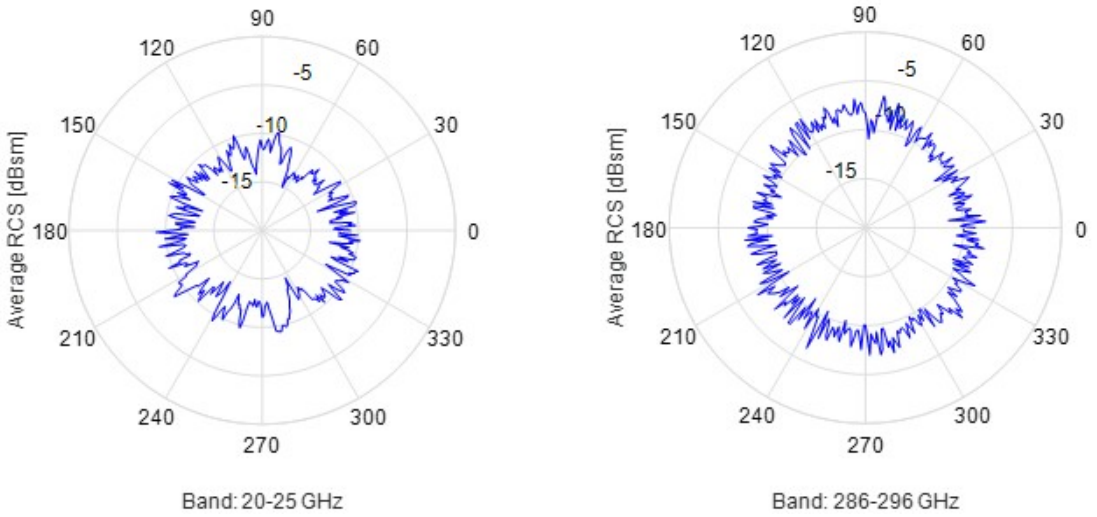

(a)

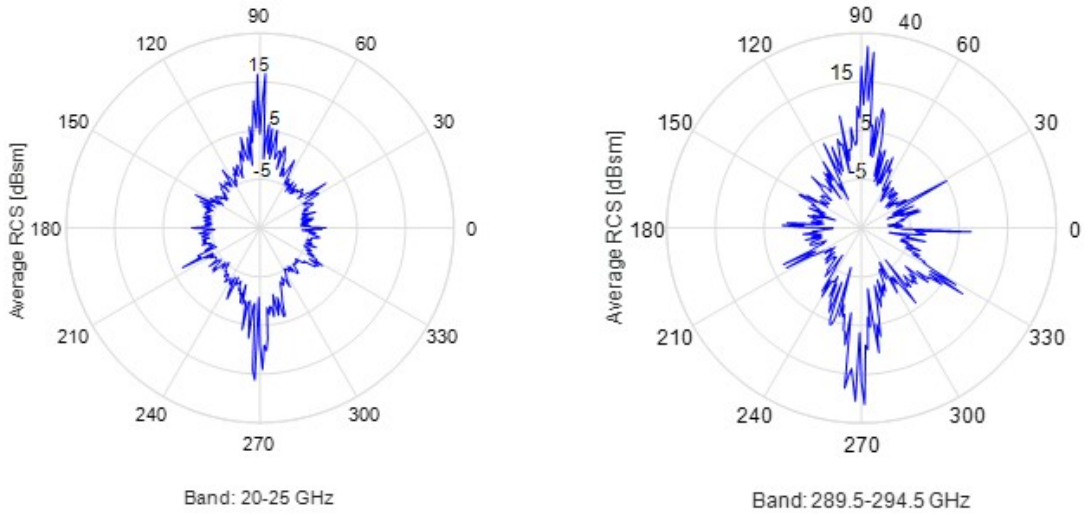

(b)

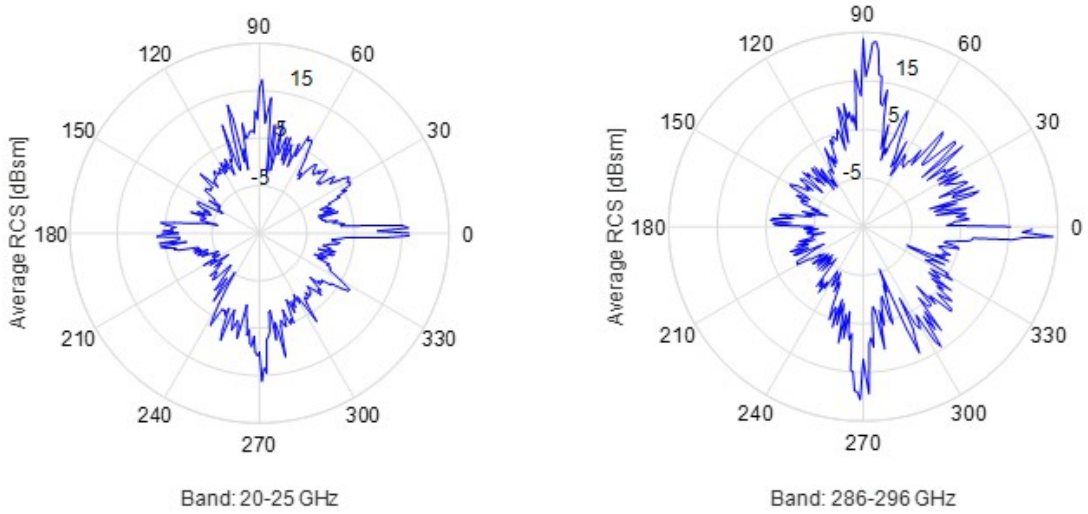

(c)

Fig. 6.18 Polar plots of the calibrated RCS vs azimuth angles for the pedestrian (a), bike (b) and wheelchair (c)

The plots show that only in the case of the pedestrian can the RCS can be considered as aspect independent. For the other targets the variation of RCS can be up to 20 dB, with flashes at the cardinal angles, as expected by observing the HRRP vs azimuth angles in Figure 6.17.

Looking at the results obtained for the pedestrian and the car, it was concluded that the rise of the frequency, from the standard automotive band to the low-THz band, entails to lower fluctuation of the RCS over aspect angles, because as the surface becomes rough with smaller wavelengths, similar level of returns from all resolution cells occupied by the target are observed. In contrast, for the bike and the wheelchair it can be observed higher fluctuations of the RCS at higher frequencies. Although this effect is not evident, it may be due to the high presence of small features in the two targets, which are not detected at lower frequencies. These features if on one hand may increase the overall RCS of the target at low-THz frequencies, on the other hand can appear or be shadowed as the aspect angle of the target relative to the radar changes, causing, therefore, fluctuations in the reflectivity.

6.3.4 RCS fluctuations statistics

The histograms and CDFs, obtained from the fluctuations of RCS over aspect angles for the bike and wheelchair and shown in Figure 6.19, highlight the influence of the different nature of reflections at 24 GHz and at low-THz frequencies on the probability distribution. A larger number of observable reflection points from the target using smaller wavelengths results in higher probability for a wider range of RCS values.

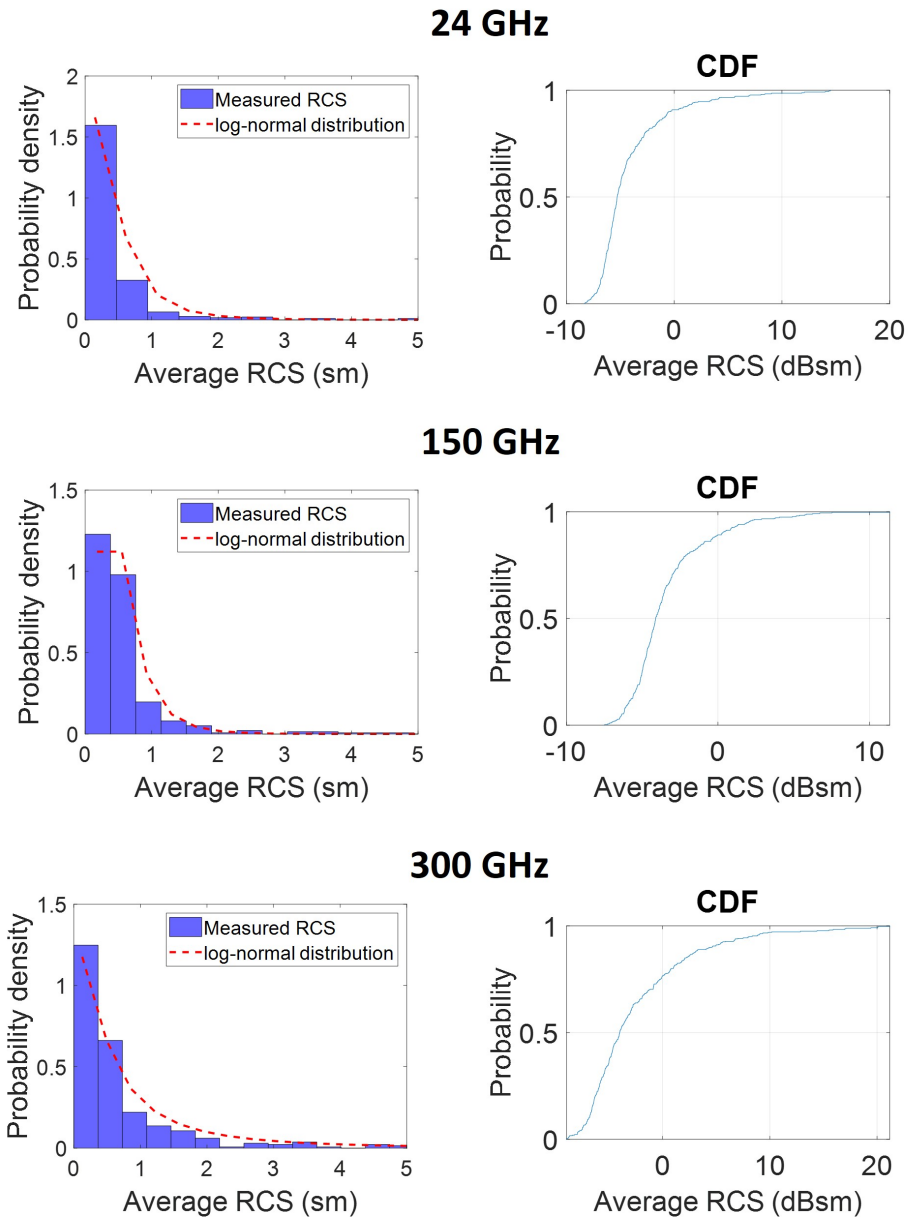

(a)

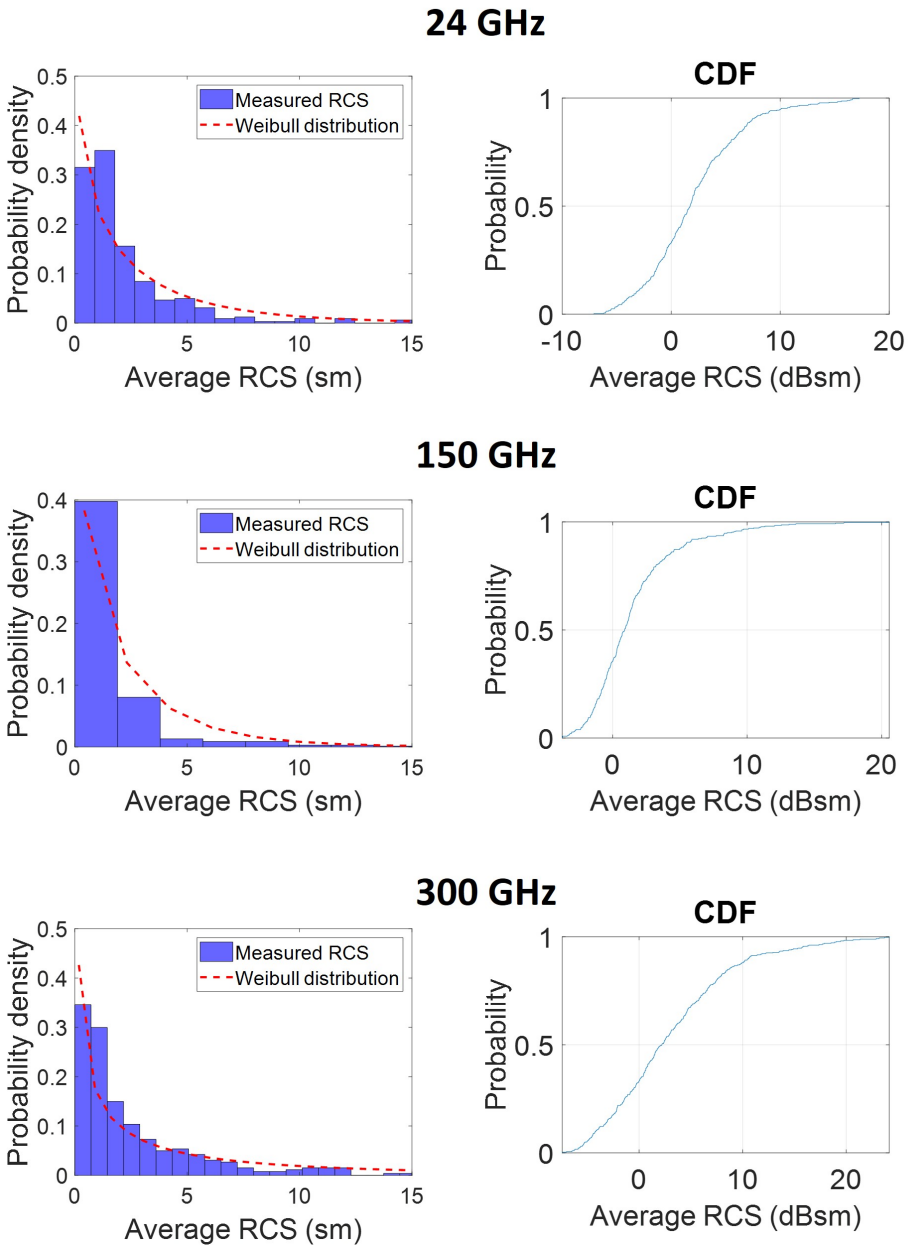

(b)

Fig. 6.19 Histograms and CDFs of the (a) bicycle and (b) wheelchair RCS vs azimuth angles

Following the methodological analysis illustrated in Section 3.4.5, the probability distribution models best fitting the measured distributions are calculated using the errors of fit summarized in Tables 6.6 and 6.7. The best fits are log-normal for the bike and Weibull for the wheelchair for all the frequency bands. Only considering the Swerling

targets model fits, both targets can, instead, be classified as Swerling 1 or 2. These results are somehow expected as bike and wheelchair are both targets comprised of multiple scatterers with none being dominant [72].

Table 6.6 Error of fit for the bicycle RCS against different distribution models

Distribution model	Frequency GHz	Parameters (Table 3.3)	Error of fit, % (eq. 3.39)
Swerling 1/2	24	$\sigma_m = 0.83$	3.02
	150	$\sigma_m = 0.62$	0.41
	300	$\sigma_m = 2.7$	1.9
Swerling 3/4	24	$\sigma_m = 0.83$	27.48
	150	$\sigma_m = 0.62$	12.7
	300	$\sigma_m = 2.7$	68.2
Gamma	24	$\alpha = 0.78$, $\beta = 1.06$	8.42
	150	$\alpha = 3.97$, $\beta = 0.34$	0.36
	300	$\alpha = 0.43$, $\beta = 6.34$	18.8
Weibull	24	$k_w = 0.63$, $\lambda_w = 0.77$	3.96
	150	$k_w = 0.65$, $\lambda_w = 1.12$	1.11
	300	$k_w = 1.17$, $\lambda_w = 0.58$	6.18
Log-normal	**24**	$(ln(\sigma))_m = -0.95$, $(ln(\sigma))_{sd} = 0.82$	**0.72**
	150	$(ln(\sigma))_m = -0.78$, $(ln(\sigma))_{sd} = 0.62$	**0.03**
	300	$(ln(\sigma))_m = -0.54$, $(ln(\sigma))_{sd} = 1.21$	**0.03**

Table 6.7 Error of fit for the wheelchair RCS against different distribution models

Distribution model	Frequency GHz	Parameters (Table 3.3)	Error of fit, % (eq. 3.39)
Swerling 1/2	24	$\sigma_m = 3.23$	2.53
	150	$\sigma_m = 2.53$	1.17
	300	$\sigma_m = 8.42$	1.12
Swerling 3/4	24	$\sigma_m = 3.23$	14.4
	150	$\sigma_m = 2.53$	17.89
	300	$\sigma_m = 8.42$	58.07
Gamma	24	$\alpha = 0.86$, $\beta = 3.77$	1.26
	150	$\alpha = 1$, $\beta = 2.52$	1.19
	300	$\alpha = 0.45$, $\beta = 18.52$	5.51
Weibull	**24**	$k_w = 2.8$, $\lambda_w = 0.83$	**0.1**
	150	$k_w = 2.24$, $\lambda_w = 0.86$	**0.006**
	300	$k_w = 4.36$, $\lambda_w = 0.59$	**0.38**
Log-normal	24	$(ln(\sigma))_m = 0.48$, $(ln(\sigma))_{sd} = 1.02$	0.59
	150	$(ln(\sigma))_m = 0.35$, $(ln(\sigma))_{sd} = 0.79$	0.1
	300	$(ln(\sigma))_m = 0.71$, $(ln(\sigma))_{sd} = 1.41$	0.4

Statistics obtained from the histograms and CDFs are summarized in Table 6.8.

Table 6.8 RCS statistics of common road objects

Target	Frequency GHz	Mean dBsm	Standard deviation dB	Median dBsm	Dynamic range, dBsm (see Section 3.4.5)
Bicycle	24	-4.1	3.6	-5.3	[-8.2 0.3]
	150	-3.3	2.7	-4.1	[-7.4 -0.34]
	300	-2.3	5.3	-4	[-8.9 4.3]
Wheelchair	24	2.1	4.4	1.7	[-7.1 8]
	150	1.5	3.4	0.9	[-3.8 6.2]
	300	3.1	6.1	2.2	[-7.4 9]
Pushchair	24	-2.5	n.a.	n.a.	n.a.
	150	-2.3	n.a.	n.a.	n.a.
	300	-1.8	n.a.	n.a.	n.a.

The mean and median values show that overall there is no significant differences between the RCS at the standard automotive frequencies and at low-THz band. The dynamic ranges show the high variation of the bike and wheelchair reflectivities as their aspect angle relative to the radar changes, the fluctuations can be up to 20 dBs, this result affirms the value of measuring the target reflectivity fluctuations over all aspect angles.

6.3.5 Micro-Doppler signature of cyclists in the Low-THz band

The investigation on the μD produced by cyclists follow a methodology analogous to the one used for the pedestrians and described in Section 5.3.1. As shown in Figure 6.20, an adult subject is cycling on spot through the aid of an exercise bike, at a distance of 3 m from the 300 GHz and 24 GHz antennas, these distance is enough to achieve

an acceptable SNR and yet measure the μD contribution from the cyclist legs. The spectrograms of the μD signatures at 2 4GHz and 300 GHz are shown in Figure 6.21.

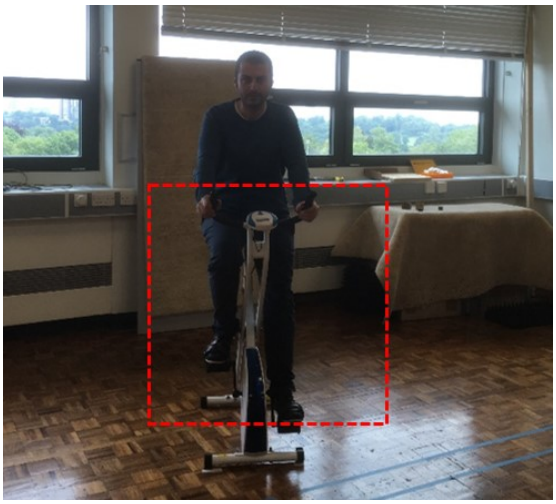

Fig. 6.20 Photo of the setup of a human cycling on spot

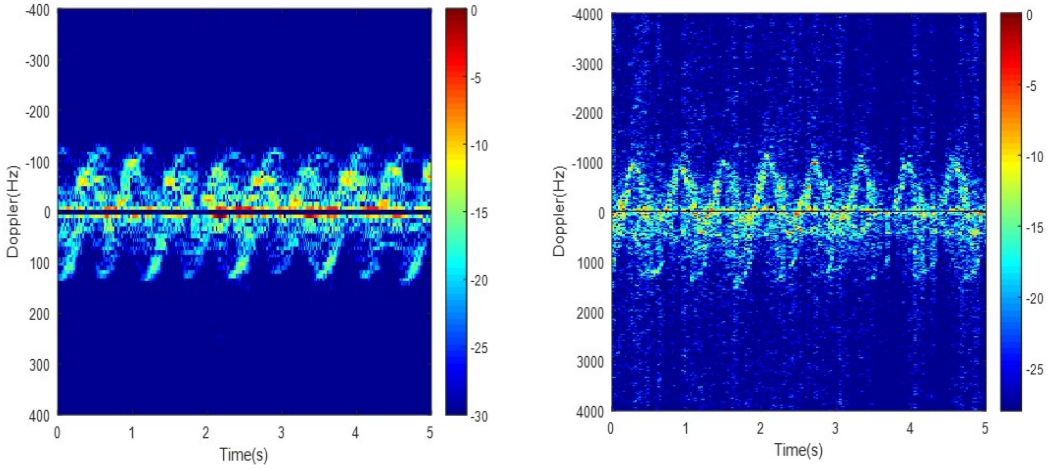

(a) (b)

Fig. 6.21 μD signature at 24 GHz (a) and 300 GHz (b) of a human cycling on spot

In real scenarios the μD signature would be comprised of overlapped signatures produced by the rotation of the wheels and the cyclist pedalling. A rotating wheel produces distinctive periodic micro-Doppler spectral lines whose fundamental frequency is related to the number of spokes and rotation rate due to the symmetrical rotation of the wheel around the axel. Each subsequent harmonic spectral line occurs an integer

multiple of the fundamental frequency and hence changes with rotation speed [146]. For the specific case of the measurements made with the exercise bike presented here, only the signatures from the cyclist legs are generated.

The leg pedalling produces two sets of overlapped sinusoidal pattern in the spectrogram, generated from left and right legs, and which are 180° out of phase because one leg moves towards the radar while the other moves away. The maximum Doppler frequency shift measured, given by the rotation of the pedal, is around 100 Hz at 24 GHz and 1000 at 300 GHz, which correspond to a maximum velocity of 0.5 m/s in both cases. The μD period is 1.2 s, determined by the velocity of the pedalling and the length of the pedal crank.

Despite of the higher noise level in the 300 GHz spectrogram, due to the lower output power of the system, the signature show a clearer pattern if compared to the one at 24 GHz. The result confirms once again that the higher number of distributed scatterers on the human body, using extremely small wavelength, produces μD signatures that can provide better identification and motion parameters estimation.

To investigate in details the μD signatures produced by the different parts of the cyclist, the low-THz system was used to validate the model proposed in [149]. The model uses the human model from the classic Boulic-Thalman model and, with the same principle, calculates the trajectories of the cyclist's body parts. The upper body is assumed to only move with the same velocity of the bicycle and micro-motions are produced by the movements of the foot and knee, which describe sinusoidal trajectories, with different phases and relative positions, as illustrated in Figure 6.22 (a). The motions of upper, lower leg and foot are calculated, based on the trajectories highlighted by the circles in the figure. The simulation results of the μD produced by their relative motions to the radar are shown in Figure 6.22 (b) (the simulations are performed considering only one leg, as their movement is symmetrical). By taking advantage of the capability of Low-THz radars to discriminate returns from close together scatterers, producing high quality μD signatures, an experiment was made at 300 GHz to validate the model. To

decompose the motions from the three different segments considered in the simulations and to increase their reflectivity, three steel trihedral corner reflectors, with an RCS of -26 dBsm, were attached to target human's right foot, right upper and lower legs, as shown in Figure 6.22 (c). The results of measurements in Figure 6.22 (d), show a very good agreement with the simulation of the model, with the μD produced by the three segments clearly distinguishable. The highest Doppler shift is produced by the foot, while the lowest is produced by the upper leg.

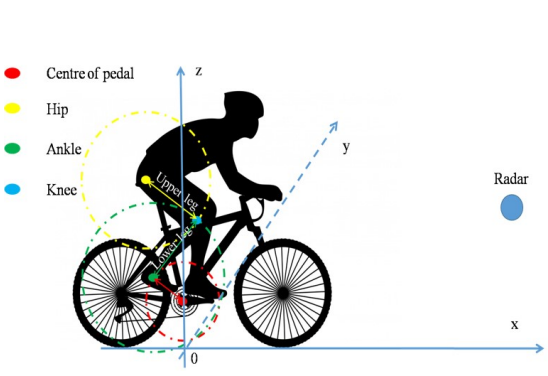

(a)

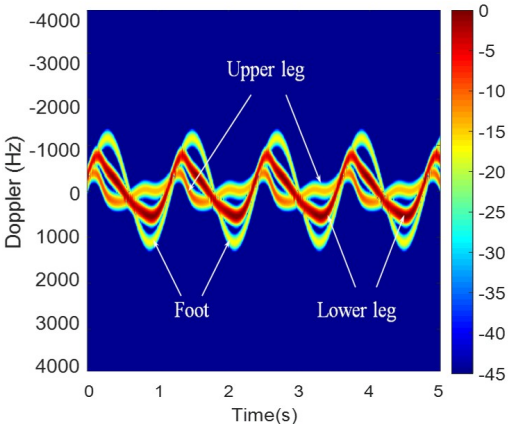

(b)

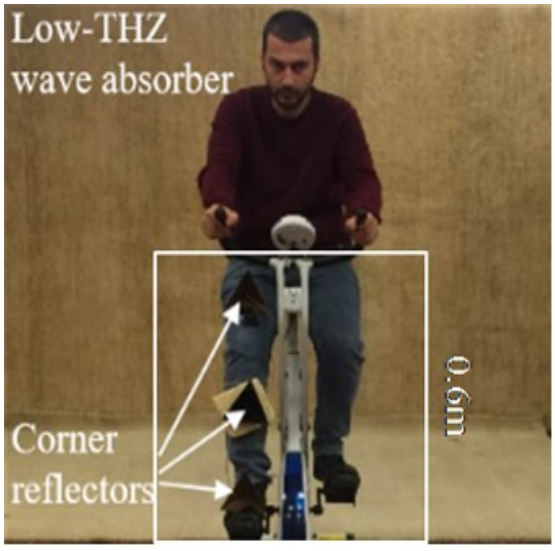

(c)

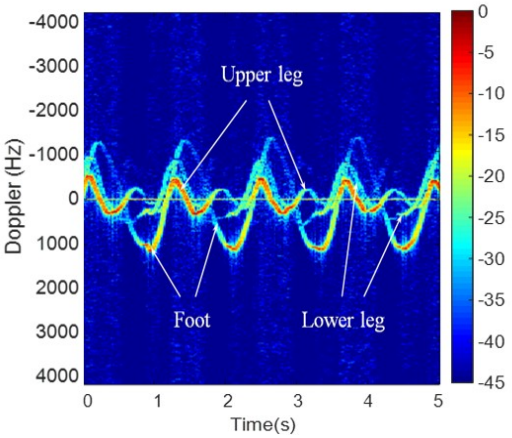

(d)

Fig. 6.22 Model (a) and simulations (b) of the μD of a human cycling on spot at 300GHz. Photo of the setup (c) and experimental results (d) to validate the model

6.4 Summary

In this chapter experimental results of the signatures of typical road targets in the low-THz band were presented and analysed. Passenger cars were measured in a typical road scenario. High resolution range profiles and images of the car show the benefit of low-THz frequencies to deliver information on the extend in range and azimuth of the car and to produce images that can be used for target identification. An investigation on the influence of radar antennas' height above the ground is also provided.

In the last section, results of measurements in a indoor controlled environment of other common target are presented, including an analysis of the micro-Doppler signatures of cyclists.

Figure 6.23 summarize the RCS values of all the road target measured with a bandwidth of 5 GHz, including those of the pedestrians presented in Chapter 5, the error bars indicate the dynamic range of the RCS fluctuations at different aspect angles (the pushchair was measured only for one aspect angle).

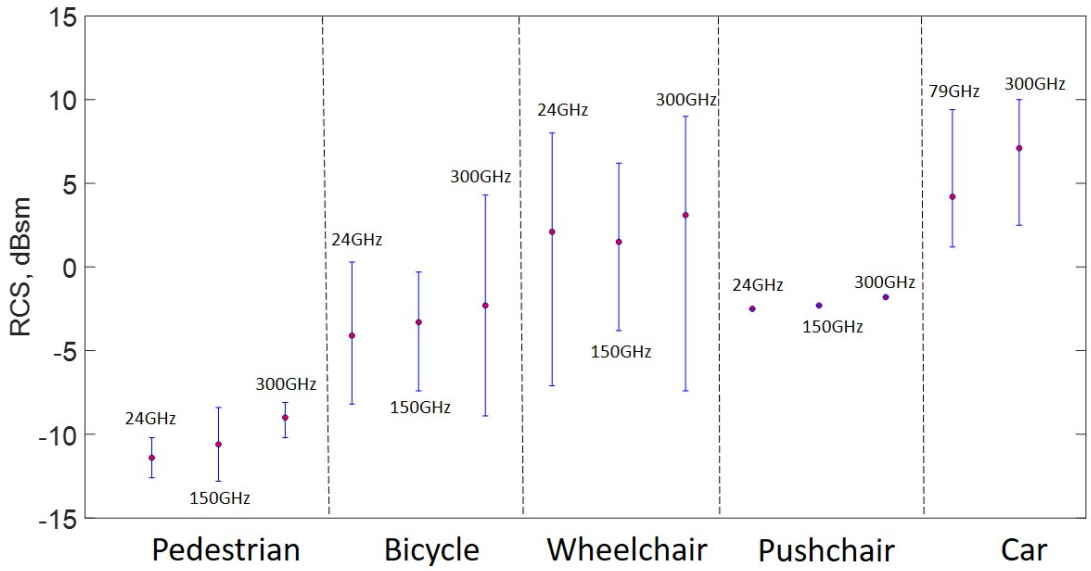

Fig. 6.23 RCS of various road targets using a bandwidth of 5 GHz

The mean RCS varies within a range of 15 dB between the target with lowest reflectivity, the pedestrian, and the most reflective target, the car. Moreover, it is

possible to notice a slight gradual increase of the mean value as the frequency increases, this is because although there is a reduction of maximum reflectivity due to the presence of more defuse scattering, the reflectivity averaged over all the resolution cells increases. By comparing the probability distributions with classic Swerling target models 1 and 3 and determine the best fit to the measured data. We found that the pedestrian and the car can be modelled as a Swerling 3 target, while the bike and the pushchair can be modelled as Swerling 1 targets. This can be explained by the fact that pedestrians and cars are comprised of multiple scatterers with one being dominant, while for the other targets no dominant scatterer can be identified [72]. As a consequence, the dynamic range of RCS values for the pedestrian and the car is smaller.

Chapter 7

Conclusions

7.1 Outcomes

The primary objective of the research work was the experimental investigation of some of the significant aspects of mmW propagation as part of a larger programme to investigate the physical aspects that characterise the propagation and reflections from targets of low-THz EMW in a road environment. The attenuation of low-THz waves in different atmospheric conditions has been investigated to show the feasibility of Low-THz (100 - 300 GHz) sensing for automotive radar in presence of adverse weather conditions. Then, the reflectivity and motion properties of typical road targets has been measured and analysed to determine the most appropriate parameters and waveforms to use in the development of low-THz radars and the generation of robust algorithms for target detection and classification.

The EMW attenuation in the atmosphere was measured and analysed for the automotive standard frequency of 77 GHz, as reference, and at the Low-THz frequencies, up to a range of 300 m. Attenuation in clear air with relative humidity (RH) of 100% shows a loss of 3 dB over 300 m range at 300 GHz. The presence of water in the atmosphere as a result of complex weather conditions, such as rain, fog and snow introduce higher attenuation as the EMW is absorbed and/or scattered when it interacts with the

precipitation particles. As expected, smaller specific attenuation at both frequencies is observed for dry snow than wet, due to lower absorption coefficient in dry snowflakes. The maximum difference between attenuation at 300 GHz and 77 GHz corresponds to extremely dense fog which reaches about 10 dB at 300 m range. For rain and snow, the loss difference is lower and it is within 3 dB between the two frequency bands.

The study of radar echo characteristics for pedestrian targets was carried out in terms of reflectivity and micro-Doppler. The pedestrian RCS was estimated through measurements of a child mannequin and results are presented using several indicators of reflectivities such as range–azimuth profile, polar plots and statistics of the average RCSs. The analysis of the various RCS signatures shows that the observed global average RCS in the three frequency bands, 24 GHz, to have a comparison with standard automotive radars, 150 GHz and 300 GHz are of similar values and in good agreement with the results reported in the literature. A qualitative analysis of the target range–azimuth profile shows that the range spread of target return is a distinctive characteristic of the pedestrian and can improve identification of the object in the radar image. A set of measurements carried out to assess the effect of clothing on pedestrian reflectivity show that although the RCS with different clothes increases with the rise of the frequency, the difference between highly reflective and absorptive clothes is anyway minimal (below 3 dB).

The micro-Doppler characteristics of walking pedestrians and cyclists, in the low-THz region shows a clearer pattern compared to the one at lower frequencies. The results show the potential for low-THz systems to better identify features in the signatures that to be used in classification algorithms. These results are particularly relevant considering pedestrians crossing the line of sight of the radar, as this is the condition under which the Doppler signature reduces to its minimum and it is scarcely usable in classification algorithms based on radar data at the standard automotive frequencies.

Passenger car reflectivities were measured in a typical road scenario. From the analysis, theoretical and experimental, of the road environment, it has been seen that the

destructive interference of the electromagnetic wave reflected from the ground plane generates nulls in the propagation pattern and thus, low reflectivity of the target in correspondence of these nulls. This effect, which may cause a missing detection for standard automotive radars, has a low impact on the road object detection at low-THz frequencies because the distance between the nulls is smaller and the attenuation is lower, thus part of the target can still be detected. The high resolution range profiles and images of the car show the benefit of low-THz frequencies to deliver information on the extent in range and azimuth of the car, on the position of the main scatterers and to produce images that can be used for target identification. An investigation on the influence of radar antennas' height above the ground shows that this parameter affects the distribution of intensity of the background signal over the car, in some cases the highest reflection can be observed in the farthest range cell from the radar, leading to wrong detection if peak detection algorithms are used.

Overall, also considering measurements of other common road actors, the RCS characteristics of targets at low-THz frequencies are similar to that at the standard automotive frequencies, with a slight gradual increase of the mean value as the frequency rises, this is because although there is a reduction of maximum reflectivity due to the presence of more defuse scattering, the reflectivity averaged over all the resolution cells increases. This is an important finding as it suggests that sensors operating at low-THz frequencies will have similar detection performances as traditional automotive sensors operating at lower frequencies.

To conclude, the research clearly indicates that the use of a frequency band up to 300 GHz is potential for all types of automotive radars, including those for long range operation, and carries a number of attractive features discussed in this thesis. Taking into account the fast growing number of cars equipped with radar and the number of radars installed on each car, it may be expected an inevitable overcrowding of the spectrum in the allocated 77 GHz band, moving automotive radar operation at frequencies well above the current standard is one of the prospective direction of development.

7.2 Ongoing and future works

Although the study illustrated in this work establish a solid basis for the development of low-THz radar systems for the new generation of automotive sensing for autonomy, there is undoubtedly further work to be done. By continuing with the study of the reflectivities of the targets that a radar needs to detect on the road, more actors, such as animals, or other objects, like road signs, have to be still analysed. The study of reflectivities, as well as the attenuation caused by the typical vegetation on the road, such as trees or bushes, is ongoing and the capability of low-THz radars to detect road cracks, bumps, pothole, curbs etc. needs to be assessed.

Next stage of the research involves higher frequencies to further improve the image resolution, the graph of atmospheric attenuation (Figure 1.3) suggests that the next atmospheric window is around 670 GHz, which fits for short range radar application, being the clear-air attenuation around 10 dB/Km. In this frequency band it is currently carried out at MISL the same study shown in this work regarding signal attenuation through the different media, radome contamination and adverse atmospheric condition, as well as the investigation of road actors reflectivities.

The high resolution range profiles, images and micro-Doppler signatures, shown in this thesis, illustrate the potentiality of low-THz radars to better identify features which can be used for targets identification. At MISL in parallel to this work, two complementary studies are carried out, aimed to develop the configurations and techniques to improve the images azimuth resolutions which significantly degrades at distances higher than 20 meters [63], and to produce identification and classification algorithms based on these images [70] as well as on high resolution micro-Doppler signatures.

Finally, the results reported in this work for the statistical characterization of road actors and the distribution of their scattering centres, are the starting point for the development of radar target simulators, for the generation of reliable test environments

with complex traffic situations, which are fundamental for low-THz automotive radar development.

References

[1] "Communication from the Commission to the European Parliament, the Council, the European Economic and Social Committee and the Committee of the Regions. On the road to automated mobility: An EU strategy for mobility of the future.," *European commission*, 2018.

[2] "Mast technology," *http://www.masttechnologies.com/automotive/*.

[3] "Radar technologies for automotive 2018 report," Yole Développement, 2017.

[4] J. Hasch, "Driving towards 2020: Automotive radar technology trends," in *2015 IEEE MTT-S International Conference on Microwaves for Intelligent Mobility (ICMIM)*, pp. 1–4, 2015.

[5] M. Gashinova, P. Gardner, and M. Cherniakov, "TASCC: Pervasive low-TeraHertz and Video Sensing for Car Autonomy and Driver Assistance (PATH CAD)," *Lead Research Organisation: University of Birmingham*, 2015.

[6] G. M. Brooker, "Mutual interference of millimeter-wave radar systems," *IEEE Transactions on Electromagnetic Compatibility*, vol. 49, no. 1, pp. 170–181, 2007.

[7] A. Stove, "Potential applications for low-tera-hertz radar," in *2015 16th International Radar Symposium (IRS)*, pp. 191–196, 2015.

[8] D. R. Wehner, "High resolution radar," *Norwood, MA, Artech House, Inc., 1987, 484 p.*, 1987.

[9] "Fraunhofer institute for telecommunications, Heinrich Hertz Institute, HHI," *https://www.hhi.fraunhofer.de/en.html*.

[10] M. Caris, S. Stanko, A. Wahlen, R. Sommer, J. Wilcke, N. Pohl, A. Leuther, and A. Tessmann, "Very high resolution radar at 300 GHz," in *2014 11th European Radar Conference*, pp. 494–496, 2014.

[11] A. G. Stove, "Linear fmcw radar techniques," in *IEE Proceedings F (Radar and Signal Processing)*, vol. 139, pp. 343–350, 1992.

[12] J. Hasch, E. Topak, R. Schnabel, T. Zwick, R. Weigel, and C. Waldschmidt, "Millimeter-wave technology for automotive radar sensors in the 77 GHz frequency band," *IEEE Transactions on Microwave Theory and Techniques*, 2012.

[13] M. Goppelt, H.-L. Blöcher, and W. Menzel, "Automotive radar investigation of mutual interference mechanisms," *Advances in Radio Science*, vol. 8, no. B. 3, pp. 55–60, 2010.

[14] G. Hakobyan, "Orthogonal frequency division multiplexing multiple-input multiple-output automotive radar with novel signal processing algorithms," *Doctoral thesis, University of Stuttgart*, 2018.

[15] D. J. Griffiths, *Introduction to electrodynamics*, ch. 9. Prentice Hall New Jersey, 2005.

[16] ITU, "Recommendation ITU-R p. 676–10, attenuation by atmospheric gases," *International Telecommunications Union*, 2013.

[17] ITU, "838-3. specific attenuation model for rain for use in prediction methods," *ITU-R Recommendations, P Series Fasicle, ITU, Geneva, Switzerland*, 2005.

[18] A. H. Cook, "Interference of electromagnetic waves.," *Interference of electromagnetic waves., by Cook, AH. Int. Ser. Monogr. Phys.(Oxford (UK): Clarendon Press), 8+ 253 p.*, 1971.

[19] ITU, "Effects of tropospheric refraction on radio-wave propagation," *Recommendations and reports of the ITU-R annex*, vol. 5, pp. 718–3, 1990.

[20] P. Beckmann and A. Spizzichino, *The scattering of electromagnetic waves from rough surfaces*, ch. 4. Norwood, MA, Artech House, 1987.

[21] B. Willetts, M. Gashinova, A. Stove, C. Constantinou, and E. Hoare, "Low-THz rough surface imaging," in *2016 European Radar Conference (EuRAD)*, pp. 394–397, 2016.

[22] E. Knott, J. Shaeffer, and M. Tuley, *Radar cross section 2nd ed*, ch. 5, 12. Artech House, 1993.

[23] J. R. Meyer-Arendt, *Introduction to Classical and Modern Optics*, ch. 16. Addison-Wesley; 4 edition, 1994.

[24] A. G. Alkholidi and K. S. Altowij, "Free space optical communications-theory and practices," *Contemporary Issues in Wireless Communications*, pp. 159–212, 2014.

[25] A. K. Panwar, A. Singh, A. Kumar, and H. Kim, "Terahertz imaging system for biomedical applications: Current status," *International Journal of Engineering and Technology IJET-IJENS*, vol. 13, pp. 33–39, 2013.

[26] D. N. Henry H. Mantsch, "Terahertz spectroscopy: The renaissance of far infrared spectroscopy," *Journal of Molecular Structure*, vol. 964, Issues 1–3, 2010.

[27] J. A. Hejase, E. J. Rothwell, and P. Chahal, "A multiple angle method for THz time-domain material characterization," *IEEE Transactions on Terahertz Science and Technology*, vol. 3, no. 5, pp. 656–665, 2013.

[28] G. P. Gallerano, A. Doria, E. Giovenale, G. Messina, A. Petralia, I. Spassovsky, K. Fukunaga, and I. Hosako, "THz-ARTE: non-invasive TeraHertz diagnostics for art conservation," in *2008 33rd International Conference on Infrared, Millimeter and Terahertz Waves*, 2008.

[29] V. Petrov, A. Pyattaev, D. Moltchanov, and Y. Koucheryavy, "TeraHertz band communications: Applications, research challenges, and standardization activities," in *2016 8th International Congress on Ultra Modern Telecommunications and Control Systems and Workshops (ICUMT)*, pp. 183–190, 2016.

[30] A. Gureev, M. Cherniakov, E. Marchetti, and I. Gureev, "Channel description in the low-THz wireless communications," in *2017 IEEE Conference of Russian Young Researchers in Electrical and Electronic Engineering (EIConRus)*, pp. 1240–1243, 2017.

[31] A. Gureev, M. Cherniakov, E. Marchetti, F. Norouzian, and I. Gureev, "Analysis of interferences in wideband low-THz wireless systems," in *2018 IEEE Conference of Russian Young Researchers in Electrical and Electronic Engineering (EIConRus)*, pp. 1734–1737, 2018.

[32] A. Gureev, I. Gureev, M. Cherniakov, E. Marchetti, and A. Bystrov, "Performance evaluation of wideband indoor wireless communication systems occupying the frequency range of 650–690 GHz," in *2019 IEEE Conference of Russian Young Researchers in Electrical and Electronic Engineering (EIConRus)*, pp. 2123–2126, 2019.

[33] M. Mikulla, A. Leuther, P. Brückner, D. Schwantuschke, A. Tessmann, M. Schlechtweg, O. Ambacher, and M. Caris, "High-speed technologies based on iii-v compound semiconductors at Fraunhofer IAF," in *2013 European Microwave Integrated Circuit Conference*, pp. 169–171, 2013.

[34] N. Orihashi, S. Hattori, S. Suzuki, and M. Asada, "Voltage-controlled sub-TeraHertz oscillation of resonant tunnelling diode integrated with slot antenna," *Electronics Letters*, vol. 41, no. 15, pp. 872–874, 2005.

[35] T. Bryllert, V. Drakinskiy, K. B. Cooper, and J. Stake, "Integrated 200–240-GHz FMCW radar transceiver module," *IEEE Transactions on Microwave Theory and Techniques*, vol. 61, no. 10, pp. 3808–3815, 2013.

[36] T. Reck, C. Jung-Kubiak, J. V. Siles, C. Lee, R. Lin, G. Chattopadhyay, I. Mehdi, and K. Cooper, "A silicon micromachined eight-pixel transceiver array for submillimeter-wave radar," *IEEE Transactions on Terahertz Science and Technology*, vol. 5, no. 2, pp. 197–206, 2015.

[37] R. Appleby and H. B. Wallace, "Standoff detection of weapons and contraband in the 100 GHz to 1 THz region," *IEEE Transactions on Antennas and Propagation*, vol. 55, no. 11, pp. 2944–2956, 2007.

[38] B. Wallace, "DARPA MMW systems programs and how they drive technology needs," *DMRC Millimeter-Wave Technology Workshop*, 2014.

[39] B. Willetts, M. Gashinova, A. Stove, C. C. Constantinou, E. G. Hoare, and E. Marchetti, "Low-THz overhead power cable signatures: The effect of surface features on low-THz reflectivities," in *2016 17th International Radar Symposium (IRS)*, pp. 1–6, 2016.

[40] L. Daniel, D. Phippen, E. Hoare, M. Cherniakov, and M. Gashinova, "Image segmentation in real aperture low-THz radar images," *2019 21th International Radar Symposium (IRS)*, 2019.

[41] "IEEE standard radar definitions," *IEEE Std 686-2008 (Revision of IEEE Std 686-1997)*, pp. c1–41, 2008.

[42] E. F. Knott, *Radar Cross Section Measurements*, ch. 4, 5, 6, 10. Van Nostrand Reinhold, 1993.

[43] P. Pouliguen, L. Lucas, F. Muller, S. Quete, and C. Terret, "Calculation and analysis of electromagnetic scattering by helicopter rotating blades," *IEEE Transactions on Antennas and Propagation*, vol. 50, no. 10, pp. 1396–1408, 2002.

[44] F. Frezza, F. Mangini, and N. Tedeschi, "Introduction to electromagnetic scattering: tutorial," *J. Opt. Soc. Am. A*, vol. 35, pp. 163–173, Jan 2018.

[45] C. Uluisik, G. Cakir, M. Cakir, and L. Sevgi, "Radar cross section (RCS) modeling and simulation, part 1: a tutorial review of definitions, strategies, and

canonical examples," *IEEE Antennas and Propagation Magazine*, vol. 50, no. 1, pp. 115–126, 2008.

[46] J. C. Leachtenauer and R. G. Driggers, *Surveillance and reconnaissance imaging systems: modeling and performance prediction*, ch. 2. Artech House, 2001.

[47] H. Iqbal, M. B. Sajjad, M. Mueller, and C. Waldschmidt, "SAR imaging in an automotive scenario," in *2015 IEEE 15th Mediterranean Microwave Symposium (MMS)*, pp. 1–4, 2015.

[48] S. Gishkori, L. Daniel, M. Gashinova, and B. Mulgrew, "Imaging for a forward scanning automotive synthetic aperture radar," *IEEE Transactions on Aerospace and Electronic Systems*, pp. 1–1, 2018.

[49] S. Madsen and H. Zebker, *Imaging Radar Interferometry*. John Wiley and Sons, 1998.

[50] Z. Jiang, J. Wang, Q. Song, and Z. Zhou, "Off-road obstacle sensing using synthetic aperture radar interferometry," *Journal of Applied Remote Sensing*, vol. 11, no. 1, 2017.

[51] S. Melo, E. Marchetti, S. Cassidy, E. Hoare, A. Bogoni, M. Gashinova, and M. Cherniakov, "24 GHz interferometric radar for road hump detections in front of a vehicle," in *2018 19th International Radar Symposium (IRS)*, pp. 1–9, June 2018.

[52] V. Chen, *The Micro-doppler Effect in Radar*, ch. 1, 2, 4. Artech House, 2011.

[53] B. R. Mahafza, *Radar signal analysis and processing using MATLAB*, ch. 1, 9. Chapman and Hall/CRC, 2016.

[54] H. Rohling and M.-M. Meinecke, "Waveform design principles for automotive radar systems," in *Radar, 2001 CIE International Conference on, Proceedings*, vol. 4, p. 1, 2001.

[55] S. M. Patole, M. Torlak, D. Wang, and M. Ali, "Automotive radars: A review of signal processing techniques," *IEEE Signal Processing Magazine*, vol. 34, no. 2, pp. 22–35, 2017.

[56] C. Sturm, E. Pancera, T. Zwick, and W. Wiesbeck, "A novel approach to OFDM radar processing," in *2009 IEEE Radar Conference*, pp. 1–4, 2009.

[57] C. Sturm, T. Zwick, and W. Wiesbeck, "An OFDM system concept for joint radar and communications operations," in *VTC Spring 2009-IEEE 69th Vehicular Technology Conference*, pp. 1–5, 2009.

[58] V. K. Ingle and J. G. Proakis, *Digital signal processing using matlab: a problem solving companion*, ch. 5. Cengage Learning, 2016.

[59] W. A. Sethares, *Rhythm and transforms*. Springer Science & Business Media, 2007.

[60] "Short time fourier transform (STFT)," *Naval Postgraduate School (NPS), http://faculty.nps.edu/rcristi/EO3404/B-Discrete-Fourier-Transform/text/3-STFT.pdf*.

[61] F. Fioranelli, "Through-the-wall detection using ultra wide band frequency modulated interrupted continuous wave signals," *Doctoral thesis, Durham University*, 2013.

[62] D. E. Barrick, "FM/CW radar signals and digital processing," tech. rep., NATIONAL OCEANIC AND ATMOSPHERIC ADMINISTRATION BOULDER CO WAVE PROPAGATION LAB, 1973.

[63] L. Daniel, A. Stove, E. Hoare, D. Phippen, M. Cherniakov, B. Mulgrew, and M. Gashinova, "Application of Doppler beam sharpening for azimuth refinement in prospective low-THz automotive radars," *IET Radar, Sonar Navigation*, vol. 12, no. 10, pp. 1121–1130, 2018.

[64] M. I. Skolnik, *Radar handbook second edition*, ch. 1. McGrawHill, 1990.

[65] "Thies Clima," *https://www.thiesclima.com/en/Products/Precipitation-Electrical-devices/*.

[66] "EMCos Consulting and Software," *https://www.emcos.com/?application-examples=radar-cross-section-of-aircraft-ia-63-pampa*.

[67] P. López-Rodríguez, R. Fernández-Recio, I. Bravo, A. Gardel, J. Lázaro, and E. Rufo, "Computational burden resulting from image recognition of high resolution radar sensors," *Sensors*, vol. 13, no. 4, pp. 5381–5402, 2013.

[68] R. F. Van Schalkwyk and J. C. Smit, "Dynamic radar cross section measurements of a full-scale aircraft for RCS modelling validation," 2017.

[69] "WiPL-D electromagnetic modeling of composite metallic and dielectric structures," *https://wipl-d.com/*.

[70] A. Stroescu, M. Cherniakov, and M. Gashinova, "Classification of high resolution automotive radar imagery for autonomous driving based on deep neural networks," *2019 21th International Radar Symposium (IRS)*, 2019.

[71] T. Dallmann, J.-K. Mende, and S. Wald, "ATRIUM: A radar target simulator for complex traffic scenarios," in *2018 IEEE MTT-S International Conference on Microwaves for Intelligent Mobility (ICMIM)*, pp. 1–4, 2018.

[72] P. Swerling, "Probability of detection for fluctuating targets," *IRE Transactions on Information Theory*, vol. 6, no. 2, pp. 269–308, 1960.

[73] R. Boulic, N. M. Thalmann, and D. Thalmann, "A global human walking model with real-time kinematic personification," *The visual computer*, vol. 6, no. 6, pp. 344–358, 1990.

[74] P. Molchanov, J. Astola, K. Egiazarian, and A. Totsky, "On micro-Doppler period estimation," in *2013 19th International Conference on Control Systems and Computer Science*, pp. 325–330, 2013.

[75] "Vivatech Millimeter Wave/THz custom solutions," *http://vivatechmmw.com/en/*.

[76] "ELVA-1, millimetre wave division," *http://www.elva-1.com/*.

[77] J. Du Preez and S. Sinha, *Millimeter-wave antennas: configurations and applications*. Springer, 2016.

[78] "Pico technology," *https://www.picotech.com/oscilloscope/5000/flexible-resolution-oscilloscope*.

[79] F. Norouzian, R. Du, E. G. Hoare, P. Gardner, C. Constantinou, M. Cherniakov, and M. Gashinova, "Low-THz transmission through water-containing contaminants on antenna radome," *IEEE Transactions on Terahertz Science and Technology*, vol. 8, no. 1, pp. 63–75, 2018.

[80] F. Norouzian, R. Du, M. Gashinova, E. Hoare, C. Constantinou, P. Gardner, and M. Cherniakov, "Monostatic and bistatic reflectivity measurements of radar absorbers at low-THz frequency," in *2016 European Radar Conference (EuRAD)*, pp. 117–120, 2016.

[81] E. S. Li and K. Sarabandi, "Low grazing incidence millimeter-wave scattering models and measurements for various road surfaces," *IEEE Transactions on Antennas and Propagation*, vol. 47, no. 5, pp. 851–861, 1999.

[82] M. Gashinova, P. Gardner, M. Cherniakov, M. Lancaster, C. Constantinou, and A. Feresidis, "TRAVEL: Terahertz Technology for Future Road Vehicles," *Lead Research Organisation: University of Birmingham*, 2014.

[83] Y. Xiao, F. Norouzian, E. Marchetti, S. Cassidy, E. Hoare, M. Cherniakov, and M. Gashinova, "Transmissivity through automotive bumpers at mm-wave and low-THz frequencies," *2019 21th International Radar Symposium (IRS)*, 2019.

[84] F. Norouzian, R. Du, E. Marchetti, M. Gashinova, E. Hoare, C. Constantinou, P. Gardner, and M. Cherniakov, "Transmission through uniform layer of ice at low-THz frequencies," in *2017 European Radar Conference (EURAD)*, pp. 211–214, 2017.

[85] R. Du, F. Norouzian, E. Marchetti, B. Willetts, M. Gashinova, and M. Cherniakov, "Characterisation of attenuation by sand in low-THz band," in *2017 IEEE Radar Conference (RadarConf)*, pp. 0294–0297, 2017.

[86] F. Norouzian, R. Du, E. G. Hoare, P. Gardner, C. Constantinou, M. Cherniakov, and M. Gashinova, "Low-THz transmission through water-containing contaminants on antenna radome," *IEEE Transactions on Terahertz Science and Technology*, vol. 8, no. 1, pp. 63–75, 2017.

[87] S. Sabery, F. Norouzian, P. Gardner, E. Hoare, M. Cherniakov, and M. Gashinova, "Signal reduction by tree leaves in low-THz automotive radar," in *2018 48th European Microwave Conference (EuMC)*, pp. 1445–1448, 2018.

[88] F. Norouzian, E. Marchetti, M. Gashinova, E. Hoare, C. Constantinou, P. Gardner, and M. Cherniakov, "Rain attenuation at millimetre wave and low-THz frequencies," *IEEE Transactions on Antennas and Propagation*, 2019.

[89] F. Norouzian, E. Marchetti, E. Hoare, M. Gashinova, C. Constantinou, P. Gardner, and M. Cherniakov, "Experimental study on low-THz automotive radar signal attenuation during snowfall," *IET Radar, Sonar & Navigation*, 2019.

[90] F. Norouzian, E. Hoare, E. Marchetti, M. Cherniakov, and M. Gashinova, "Next generation, low-THz automotive radar-the potential for frequencies above 100 GHz," *2019 21th International Radar Symposium (IRS)*, 2019.

[91] H.-L. Bloecher, A. Sailer, G. Rollmann, and J. Dickmann, "79 GHz UWB automotive short range radar spectrum allocation and technology trends," *Advances in Radio Science*, vol. 7, no. B. 3, pp. 61–65, 2009.

[92] R. Schneider, H.-L. Blocher, and K. M. Strohm, "Kokon-automotive high frequency technology at 77/79 GHz," in *2007 European Microwave Conference*, pp. 1526–1529, 2007.

[93] F. Fitzek and R. H. Rasshofer, "Automotive radome design-reflection reduction of stratified media," *IEEE Antennas and Wireless Propagation Letters*, vol. 8, pp. 1076–1079, 2009.

[94] F. Fitzek, R. H. Raßhofer, and E. M. Biebl, "Broadband matching of high-permittivity coatings with frequency selective surfaces," in *2011 German Microwave Conference*, pp. 1–4, 2011.

[95] F. Fitzek, Z. Abou-Chahine, R. H. Rasshofer, and E. M. Biebl, "Automotive radome design-fishnet structure for 79 GHz," in *German Microwave Conference Digest of Papers*, pp. 146–149, 2010.

[96] Y. Xiao, F. Norouzian, E. Hoare, E. Marchetti, M. Cherniakov, and M. Gashinova, "Modelling and experiment verification of transmissivity of low-THz radar signal through vehicle infrastructure," *IEEE Sensors Journal*, 2020.

[97] B. Blevis, "Losses due to rain on radomes and antenna reflecting surfaces," *IEEE Transactions on Antennas and Propagation*, vol. 13, pp. 175–176, January 1965.

[98] I. Anderson, "Measurements of 20-GHz transmission through a radome in rain," *IEEE Transactions on Antennas and Propagation*, vol. 23, no. 5, pp. 619–622, 1975.

[99] R. J. Hogan, D. Bouniol, D. N. Ladd, E. J. O'Connor, and A. J. Illingworth, "Absolute calibration of 94/95-GHz radars using rain," *Journal of Atmospheric and Oceanic Technology*, vol. 20, no. 4, pp. 572–580, 2003.

[100] D. Brissinger, G. Parent, and P. Boulet, "Experimental study on radiation attenuation by a water film," *Journal of Quantitative Spectroscopy and Radiative Transfer*, vol. 145, pp. 160–168, 2014.

[101] A. Arage, G. Kuehnle, and R. Jakoby, "Measurement of wet antenna effects on millimetre wave propagation," in *2006 IEEE Conference on Radar*, pp. 5–pp, 2006.

[102] N. Chen, R. Gourova, O. A. Krasnov, and A. Yarovoy, "The influence of the water-covered dielectric radome on 77 GHz automotive radar signals," in *2017 European Radar Conference (EURAD)*, pp. 139–142, 2017.

[103] M. Köhler, J. Hasch, H. L. Blöcher, and L.-P. Schmidt, "Feasibility of automotive radar at frequencies beyond 100 GHz," *International Journal of Microwave and Wireless Technologies*, vol. 5, no. 1, pp. 49–54, 2013.

[104] J. Sander, "Rain attenuation of millimeter waves at λ = 5.77, 3.3, and 2 mm," *IEEE Transactions on Antennas and Propagation*, vol. 23, pp. 213–220, March 1975.

[105] A. Maitra and C. Gibbins, "Modeling of raindrop size distributions from multiwavelength rain attenuation measurements," *Radio Science*, vol. 34, no. 3, pp. 657–666, 1999.

[106] T. Utsunomiya and M. Sekine, "Rain attenuation at 103 GHz in millimeter wave ranges," *International journal of infrared and millimeter waves*, vol. 26, no. 11, pp. 1651–1660, 2005.

[107] A. Hirata, R. Yamaguchi, H. Takahashi, T. Kosugi, K. Murata, N. Kukutsu, and Y. Kado, "Effect of rain attenuation for a 10-Gb/s 120-GHz-band millimeter-wave wireless link," *IEEE Transactions on Microwave Theory and Techniques*, vol. 57, no. 12, pp. 3099–3105, 2009.

[108] U. Kesavan, A. Tharek, A. A. Rahman, and S. A. Rahim, "Comparative studies of the rain attenuation predictions for tropical regions," *Progress In Electromagnetics Research M*, vol. 18, pp. 17–30, 2011.

[109] S. Ishii, S. Sayama, and T. Kamei, "Measurement of rain attenuation in TeraHertz wave range," 2011.

[110] L. A. da Silva Mello and M. S. Pontes, "Improved unified method for the prediction of rain attenuation in terrestrial and earth space links," in *2009*

SBMO/IEEE MTT-S International Microwave and Optoelectronics Conference (IMOC), pp. 569–573, 2009.

[111] V. W. Richard, J. E. Kammerer, and R. G. Reitz, "140-GHz attenuation and optical visibility measurements of fog, rain and snow," tech. rep., ARMY BALLISTIC RESEARCH LAB ABERDEEN PROVING GROUND MD, 1977.

[112] H. B. Wallace, "Millimeter-wave propagation measurements at the ballistic research laboratory," *IEEE transactions on geoscience and remote sensing*, vol. 26, pp. 253–258, 1988.

[113] C. Amaya, J.-M. Garcàa-Rubia, P. Bouchard, and T. Nguyen, "Experimental assessment of snow-induced attenuation on an earth-space link operating at Ka-band," *Radio Science*, vol. 49, no. 10, pp. 933–944, 2014.

[114] R. Martin, C. Schuetz, T. Dillon, D. Mackrides, P. Yao, K. Shreve, C. Harrity, A. Zablocki, B. Overmiller, P. Curt, *et al.*, "Optical up-conversion enables capture of millimeter-wave video with an IR camera," in *SPIE Newsroom*, 2012.

[115] *Global status report on road safety 2015*. World Health Organization, 2015.

[116] D. Tahmoush, "Review of micro-Doppler signatures," *IET Radar, Sonar & Navigation*, vol. 9, no. 9, pp. 1140–1146, 2015.

[117] J. A. Nanzer, "A review of microwave wireless techniques for human presence detection and classification," *IEEE Transactions on Microwave Theory and Techniques*, vol. 65, no. 5, pp. 1780–1794, 2017.

[118] E. Marchetti, R. Du, B. Willetts, F. Norouzian, E. G. Hoare, T. Y. Tran, N. Clarke, M. Cherniakov, and M. Gashinova, "Radar cross-section of pedestrians in the low-THz band," *IET Radar, Sonar & Navigation*, vol. 12, no. 10, pp. 1104–1113, 2018.

[119] E. Marchetti, R. Du, F. Norouzian, E. Hoare, T.-Y. Tran, M. Cherniakov, and M. Gashinova, "Comparison of pedestrian reflectivities at 24 and 300 GHz," in *2017 18th International Radar Symposium (IRS)*, pp. 1–7, 2017.

[120] E. Marchetti, R. Du, F. Norouzian, E. Hoare, M. Cherniakov, M. Gashinova, and T.-Y. Tran, "Radar reflectivity and motion characteristics of pedestrians at 300 GHz," in *2017 European Radar Conference (EURAD)*, pp. 57–60, 2017.

[121] R. Du, E. Marchetti, F. Norouzian, M. Gashinova, and M. Cherniakov, "Micro doppler signature of pedestrian walking on spot at low-terahertz frequencies," in *International Conference on Radar Systems (Radar 2017)*, pp. 1–4, IET, 2017.

[122] F. Schultz, R. Burgener, and S. King, "Measurement of the radar cross section of a man," *Proceedings of the IRE*, vol. 46, no. 2, pp. 476–481, 1958.

[123] R. Neely, K. Naishadham, A. Sharma, and K. Bing, "Electromagnetic human body modeling with physiological motion for radar applications," in *2012 IEEE Radar Conference*, pp. 0818–0823, 2012.

[124] E. Piuzzi, S. Pisa, P. D'Atanasio, and A. Zambotti, "Radar cross section measurements of the human body for UWB radar applications," in *2012 IEEE International Instrumentation and Measurement Technology Conference Proceedings*, pp. 1290–1293, 2012.

[125] N. Yamada, Y. Tanaka, and K. Nishikawa, "Radar cross section for pedestrian in 76GHz band," in *2005 European Microwave Conference*, vol. 2, pp. 4–pp, 2005.

[126] J. Fortuny-Guasch and J.-M. Chareau, "Radar cross section measurements of pedestrian dummies and humans in the 24/77 GHz frequency bands: Establishment of a reference library of RCS signatures of pedestrian dummies in the automotive radar bands," tech. rep., 2013.

[127] P. Vertal and H. Steffan, "Evaluation of the effectiveness of Volvo's pedestrian detection system based on selected real-life fatal pedestrian accidents," tech. rep., SAE Technical Paper, 2016.

[128] "CST-computer simulation technology," *https://www.cst.com/products/cstmws*.

[129] O. P. Gandhi and A. Riazi, "Absorption of millimeter waves by human beings and its biological implications," *IEEE Transactions on Microwave Theory and Techniques*, vol. 34, no. 2, pp. 228–235, 1986.

[130] S. S. Ram and H. Ling, "Simulation of human microdopplers using computer animation data," in *2008 IEEE Radar Conference*, pp. 1–6, 2008.

[131] B. Erol, C. Karabacak, S. Z. Gürbüz, and A. C. Gürbüz, "Simulation of human micro-Doppler signatures with Kinect sensor," in *2014 IEEE Radar Conference*, pp. 0863–0868, 2014.

[132] Y. Kim, S. Ha, and J. Kwon, "Human detection using Doppler radar based on physical characteristics of targets," *IEEE Geoscience and Remote Sensing Letters*, vol. 12, no. 2, pp. 289–293, 2015.

[133] S. Björklund, T. Johansson, and H. Petersson, "Evaluation of a micro-Doppler classification method on mm-wave data," in *2012 IEEE Radar Conference*, pp. 0934–0939, 2012.

[134] E. Marchetti, L. Daniel, E. Hoare, F. Norouzian, M. Cherniakov, and M. Gashinova, "Radar reflectivity of a passenger car at 300 GHz," in *2018 19th International Radar Symposium (IRS)*, pp. 1–7, 2018.

[135] E. Marchetti, S. Cassidy, F. Norouzian, E. G. Hoare, M. Cherniakov, and M. Gashinova, "Automotive targets characterization in the low-THz band," in *2019 20th International Radar Symposium (IRS)*, pp. 1–6, 2019.

[136] G. Palubinskas and H. Runge, "Radar signatures of a passenger car," *IEEE Geoscience and Remote Sensing Letters*, vol. 4, no. 4, pp. 644–648, 2007.

[137] A. M. Raynal, D. L. Bickel, M. M. Denton, W. J. Bow, and A. W. Doerry, "Radar cross section statistics of ground vehicles at Ku-band," in *Radar Sensor Technology XV*, vol. 8021, p. 80210E, International Society for Optics and Photonics, 2011.

[138] T. Schipper, J. Fortuny-Guasch, D. Tarchi, L. Reichardt, and T. Zwick, "RCS measurement results for automotive related objects at 23-27 GHz," in *Proceedings of the 5th European Conference on Antennas and Propagation (EUCAP)*, pp. 683–686, 2011.

[139] I. Matsunami, N. Ryohei, and A. Kajiwara, "Target state estimation using RCS characteristics for 26 GHz short-range vehicular radar," in *2013 International Conference on Radar*, pp. 304–308, 2013.

[140] W. Buller, B. Wilson, J. Ebling, L. van Nieuwstadt, and B. E. Hart, "Radar measurements of NHTSA's surrogate vehicle 'SS-V'," 2013.

[141] O. O. den Camp, A. Ranjbar, J. Uittenbogaard, E. Rosen, and S. Buijssen, "Overview of main accident scenarios in car-to-cyclist accidents for use in AEB-system test protocol," in *Proceedings of International Cycling Safety Conference*, 2014.

[142] I. Matsunami, R. Nakamura, and A. Kajiwara, "RCS measurements for vehicles and pedestrian at 26 and 79 GHz," in *2012 6th International Conference on Signal Processing and Communication Systems*, pp. 1–4, 2012.

[143] K. Geary, J. S. Colburn, A. Bekaryan, S. Zeng, B. Litkouhi, and M. Murad, "Automotive radar target characterization from 22 to 29 GHz and 76 to 81 GHz," in *2013 IEEE Radar Conference (RadarCon13)*, pp. 1–6, 2013.

[144] D. J. Belgiovane, C.-C. Chen, S. Y.-P. Chien, and R. Sherony, "Surrogate bicycle design for millimeter-wave automotive radar pre-collision testing," *IEEE transactions on intelligent transportation systems*, vol. 18, no. 9, pp. 2413–2422, 2017.

[145] E. B. Kamel, A. Peden, and P. Pajusco, "RCS modeling and measurements for automotive radar applications in the W band," in *2017 11th European Conference on Antennas and Propagation (EUCAP)*, pp. 2445–2449, 2017.

[146] D. Belgiovane and C.-C. Chen, "Micro-Doppler characteristics of pedestrians and bicycles for automotive radar sensors at 77 GHz," in *2017 11th European Conference on Antennas and Propagation (EUCAP)*, pp. 2912–2916, 2017.

[147] B. Rodriguez-Hervas, M. Maile, and B. C. Flores, "Study of the microDoppler signature of a bicyclist for different directions of approach," in *Radar Sensor Technology XIX; and Active and Passive Signatures VI*, vol. 9461, p. 94611E, International Society for Optics and Photonics, 2015.

[148] R. Du, Y. Fan, and J. Wang, "Pedestrian and bicyclist identification through micro doppler signature with different approaching aspect angles," *IEEE Sensors Journal*, vol. 18, no. 9, pp. 3827–3835, 2018.

[149] R. Du, E. Marchetti, M. Gashinova, and J. Wang, "Micro-doppler signatures of bicyclist: Modeling and experiments with mm-wave and low-THz radar," *Submitted to IEEE Access*, 2019.